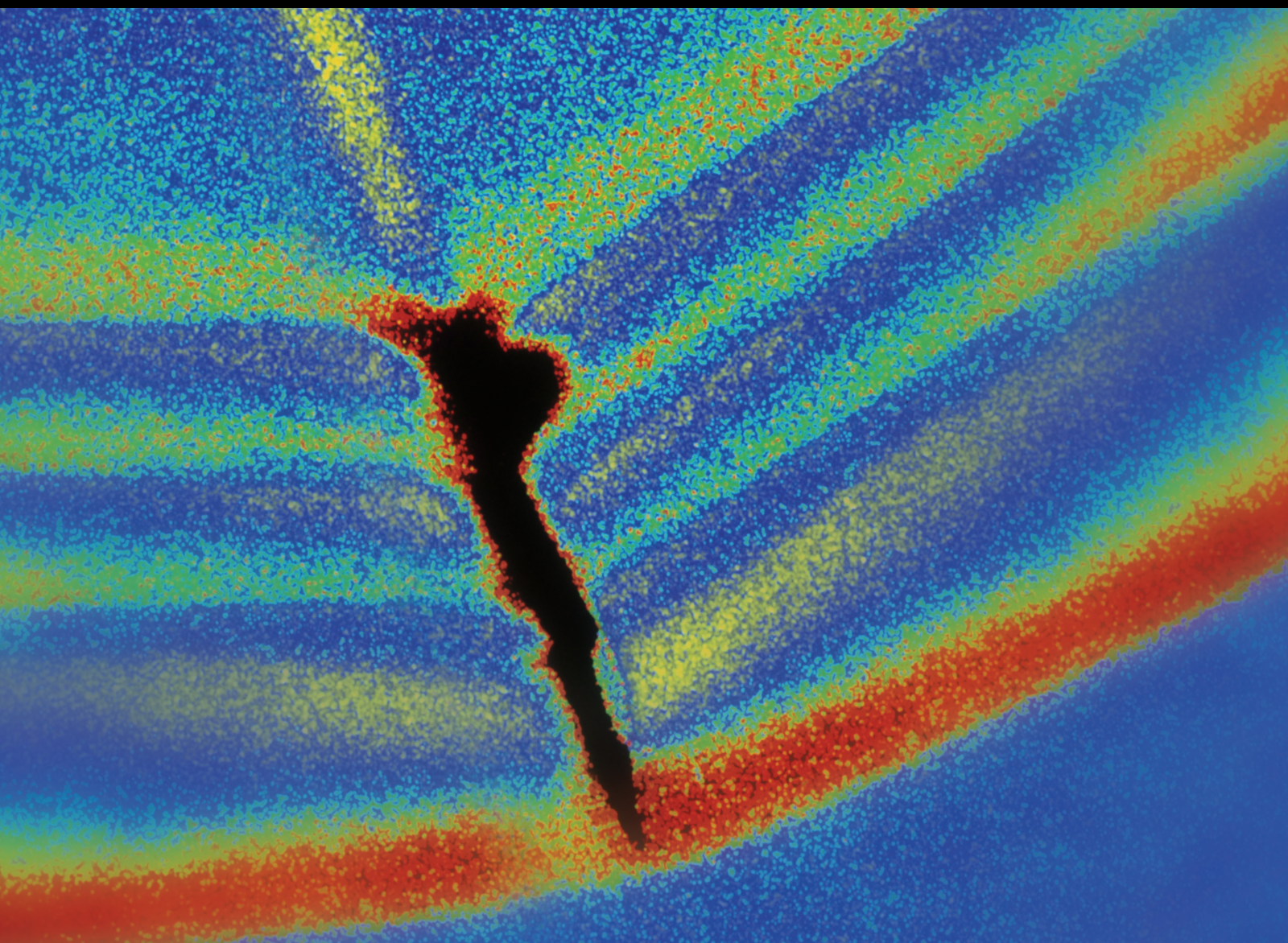


Innovative Technologies for Reducing Structural Vibrations due to Natural Events and Human Activities

Guest Editors: Nicola Caterino, Christos T. Georgakis, Ningsu Luo, and Julian Londono Monsalve





Innovative Technologies for Reducing Structural Vibrations due to Natural Events and Human Activities

Innovative Technologies for Reducing Structural Vibrations due to Natural Events and Human Activities

Guest Editors: Nicola Caterino, Christos T. Georgakis,
Ningsu Luo, and Julian Londono Monsalve



Copyright © 2016 Hindawi Publishing Corporation. All rights reserved.

This is a special issue published in "Shock and Vibration." All articles are open access articles distributed under the Creative Commons Attribution License, which permits unrestricted use, distribution, and reproduction in any medium, provided the original work is properly cited.

Editor-in-Chief

Mehdi Ahmadian, Virginia Polytechnic Institute and State University, USA

Editorial Board

Brij N. Agrawal, USA
Marco Alfano, Italy
Farbod Alijani, Canada
Sumeet S. Aphale, UK
M. Artés, Spain
Hassan Askari, Canada
Matteo Aureli, USA
Ranjan Banerjee, UK
Mahmoud Bayat, Iran
J. A. B. Villanueva, Spain
Marco Belloli, Italy
Subhamoy Bhattacharya, UK
Ivo Caliò, Italy
Antonio Carcaterra, Italy
Dumitru I. Caruntu, USA
Noel Challamel, France
Athanasios Chasalevris, UK
Ashwin Chinnayya, France
Giorgio Dalpiaz, Italy
Farhang Daneshmand, Canada
Sergio De Rosa, Italy
Dario Di Maio, UK
Longjun Dong, China
Lorenzo Dozio, Italy
M. El Badaoui, France
Mohammad Elahinia, USA
Fiorenzo A. Fazzolari, UK
Francesco Franco, Italy

Pedro Galvín, Spain
A. Gasparetto, Italy
Gianluca Gatti, Italy
Anindya Ghoshal, USA
Nere Gil-Negrete, Spain
Hassan Haddadpour, Iran
M.I. Herreros, Spain
Hamid Hosseini, Japan
Reza Jazar, Australia
Sakdirat Kaewunruen, UK
Yuri S. Karinski, Israel
Jeong-Hoi Koo, USA
G. Kouroussis, Belgium
Mickaël Lallart, France
Kenneth J. Loh, USA
Nuno M. Maia, Portugal
Giuseppe C. Marano, Italy
Laurent Mevel, France
Emiliano Mucchi, Italy
Tony Murmu, UK
S. Natarajan, India
Toshiaki Natsuki, Japan
Miguel Neves, Portugal
Coral Ortiz, Spain
Aleksandar Pavic, UK
Evgeny Petrov, UK
Antonina Pirrotta, Italy
Vitomir Racic, Italy

Carlo Rainieri, Italy
Didier Rémond, France
Francesco Ripamonti, Italy
Salvatore Russo, Italy
Edoardo Sabbioni, Italy
Jerzy T. Sawicki, USA
Onome E. Scott-Emuakpor, USA
Vadim V. Silberschmidt, UK
Kumar V. Singh, USA
Isabelle Sochet, France
Alba Sofi, Italy
Jussi Sopanen, Finland
Stefano Sorace, Italy
Narakorn Srinil, UK
Salvatore Strano, Italy
Chao Tao, China
Mario Terzo, Italy
Tai Thai, Australia
Carlo Trigona, Italy
Federica Tubino, Italy
Nerio Tullini, Italy
Marcello Vanali, Italy
Jörg Wallaschek, Germany
Zaili L. Yang, UK
Stana Živanović, UK
Lei Zuo, USA

Contents

Innovative Technologies for Reducing Structural Vibrations due to Natural Events and Human Activities

Nicola Caterino, Christos T. Georgakis, Ningsu Luo, and Julian Londono Monsalve

Volume 2016, Article ID 2181509, 2 pages

Hybrid Vibration Control under Broadband Excitation and Variable Temperature Using Viscoelastic Neutralizer and Adaptive Feedforward Approach

João C. O. Marra, Eduardo M. O. Lopes, José João de Espíndola, and Walter Antônio Gontijo

Volume 2016, Article ID 5375309, 12 pages

The Behaviour of Mistuned Piezoelectric Shunt Systems and Its Estimation

M. Berardengo, S. Manzoni, and M. Vanali

Volume 2016, Article ID 9739217, 18 pages

An Updated Analytical Structural Pounding Force Model Based on Viscoelasticity of Materials

Qichao Xue, Chunwei Zhang, Jian He, Guangping Zou, and Jingcai Zhang

Volume 2016, Article ID 2596923, 15 pages

Analysis of Free Pendulum Vibration Absorber Using Flexible Multi-Body Dynamics

Emrah Gumus and Atila Ertas

Volume 2016, Article ID 3253178, 19 pages

Performance Analysis of a Magnetorheological Damper with Energy Harvesting Ability

Guoliang Hu, Yun Lu, Shuaishuai Sun, and Weihua Li

Volume 2016, Article ID 2959763, 10 pages

Seismic Proofing Capability of the Accumulated Semiactive Hydraulic Damper as an Active Interaction Control Device with Predictive Control

Ming-Hsiang Shih and Wen-Pei Sung

Volume 2016, Article ID 6397803, 19 pages

Mechanism Analysis and Parameter Optimization of Mega-Sub-Isolation System

Xiangxiu Li, Ping Tan, Xiaojun Li, and Aiwen Liu

Volume 2016, Article ID 2605839, 12 pages

Editorial

Innovative Technologies for Reducing Structural Vibrations due to Natural Events and Human Activities

Nicola Caterino,¹ Christos T. Georgakis,² Ningsu Luo,³ and Julian Londono Monsalve⁴

¹*Department of Engineering, University of Naples Parthenope, 80143 Naples, Italy*

²*Department of Engineering, Aarhus University, 8000 Aarhus C, Denmark*

³*Department of Electrical Engineering, Electronics and Automatic Control, University of Girona, 17071 Girona, Spain*

⁴*College of Engineering, Mathematics and Physical Sciences, University of Exeter, Exeter, Devon, UK*

Correspondence should be addressed to Nicola Caterino; nicola.caterino@uniparthenope.it

Received 1 September 2016; Accepted 4 September 2016

Copyright © 2016 Nicola Caterino et al. This is an open access article distributed under the Creative Commons Attribution License, which permits unrestricted use, distribution, and reproduction in any medium, provided the original work is properly cited.

The need for effective structural control systems able to improve the performance of new and existing structures against service and extreme loads is ever growing. Indeed, over the last few decades the reduction of unwanted dynamics became a field at which intense research effort has been devoted and significant developments have been achieved by major research groups worldwide. This special issue aims at networking novel researches concerning complex and edge-technology systems and methodologies addressed to vibration control of civil structures subjected to natural actions as well as to dynamic loading induced by human activities.

M. Berardengo et al. deal with mono-modal vibration attenuation using piezoelectric transducers shunted to impedances consisting of an inductance and a resistance in series. They analyze the behaviour of mistuned electromechanical systems, demonstrating that a linear relationship between the attenuation and the logarithm of the effective coupling coefficient exists not only when a perfect tuning is given, but also when there is mistuning on either the electrical eigenfrequency or damping. Furthermore, the authors show how the loss of attenuation mainly depends on only one bias if the electrical damping is overestimated and describe how the effects of the two bias types combine with each other when the damping is underestimated. An approximated model to simulate the behaviour of mistuned shunt systems has been proposed, numerically validated via Monte Carlo simulations and then experimentally tested with two sample structures.

Earthquakes may lead to damage and collapse of colliding structures in the case of insufficient gap between adjacent structures. Q. Xue et al. propose an updated pounding force analysis method based on viscoelasticity of materials. Comparisons among proposed pounding force model and other traditional models are analyzed. Moreover, the proposed model is applied to simulate the pounding tuned mass damper (TMD) device so as to verify the validity of the model. The proposed method expands traditional Kelvin viscoelastic model to 3-parameter linear solid viscoelastic model.

Light weight, low stiffness structures potentially may suffer from wind-induced vibrations and fatigue failure. Gumus and Ertas perform theoretical analysis for a novel free-pendulum device to be adopted as a passive vibration absorber, suitable for the mitigation of large amplitude wind-induced vibrations in traffic signal structures.

J. Marra et al. deal with the development and practical implementation of a hybrid (passive-active/adaptive) vibration control system over a metallic beam excited by a broadband signal and under variable temperature. Temperature variations may affect considerably the performance of the passive control system, a viscoelastic dynamic vibration absorber. The authors show that coupling the passive device with an active-adaptive vibrations control system, based on a feedforward approach with the use of the FXLMS algorithm, leads to compensating the neutralizer loss of performance, even improving the attenuation of vibrations levels.

A magnetorheological damper with energy harvesting ability is proposed by G. Hu et al. It exploits the electromagnetic induction principle. The energy harvesting part is made of a magnet array and coils moving vertically. When the external excitation is applied, the kinetic energy is converted into electrical energy. Finite element modelling and experimental tests show good capability of the variable damper in changing mechanical behaviour according to the intensity of the feeding current, and considerable voltage output harvested with the proposed technique.

X. Li et al. deal with mega-sub-isolation system addressed to mitigate structural vibrations. The working mechanism of the mega-sub-isolation system is obtained by systematically investigating its dynamic characteristics corresponding to various structural parameters. Considering the number and location of the isolated substructures, an optimization procedure to design the isolation system is proposed, based on a genetic algorithm where base shear is assumed as objective function. The control performance of such mega-sub-isolation system is also investigated from the perspective of energy.

M.-H. Shih and W.-P. Sung improve the seismic proofing capability of an accumulated semiactive hydraulic damper, making it able to behave like an active interaction control device by means of synchronous control and predictive control methods. A full scale shaking table test is done to verify the performance of the proposed control system, leading to show that, using suitable stiffeners for the auxiliary structure at each floor, with synchronous control and predictive control, the technique guarantees high reliability and practicability for seismic proofing of buildings under excitation by external forces.

Acknowledgments

The guest editors would like to thank the authors for their contributions to the special issue and all the reviewers for their constructive reviews.

Nicola Caterino
Christos T. Georgakis
Ningsu Luo
Julian Londono Monsalve

Research Article

Hybrid Vibration Control under Broadband Excitation and Variable Temperature Using Viscoelastic Neutralizer and Adaptive Feedforward Approach

João C. O. Marra,¹ Eduardo M. O. Lopes,¹
José João de Espíndola,² and Walter Antônio Gontijo³

¹Universidade Federal do Paraná, Departamento de Engenharia Mecânica, Rua Coronel Francisco H. dos Santos, s/n, Bloco IV, Centro Politécnico, 81530-900 Curitiba, PR, Brazil

²Universidade Federal de Santa Catarina, Rua Voluntário Fernando Caldeira 87, 88085-290 Florianópolis, SC, Brazil

³Universidade Federal de Santa Catarina, Departamento de Engenharia Elétrica, LINSE, Caixa Postal 476, 88040-900 Florianópolis, SC, Brazil

Correspondence should be addressed to João C. O. Marra; joaocmarra@yahoo.com.br

Received 2 January 2016; Revised 11 April 2016; Accepted 1 June 2016

Academic Editor: Londono Monsalve

Copyright © 2016 João C. O. Marra et al. This is an open access article distributed under the Creative Commons Attribution License, which permits unrestricted use, distribution, and reproduction in any medium, provided the original work is properly cited.

Vibratory phenomena have always surrounded human life. The need for more knowledge and domain of such phenomena increases more and more, especially in the modern society where the human-machine integration becomes closer day after day. In that context, this work deals with the development and practical implementation of a hybrid (passive-active/adaptive) vibration control system over a metallic beam excited by a broadband signal and under variable temperature, between 5 and 35°C. Since temperature variations affect directly and considerably the performance of the passive control system, composed of a viscoelastic dynamic vibration neutralizer (also called a viscoelastic dynamic vibration absorber), the associative strategy of using an active-adaptive vibration control system (based on a feedforward approach with the use of the FXLMS algorithm) working together with the passive one has shown to be a good option to compensate the neutralizer loss of performance and generally maintain the extended overall level of vibration control. As an additional gain, the association of both vibration control systems (passive and active-adaptive) has improved the attenuation of vibration levels. Some key steps matured over years of research on this experimental setup are presented in this paper.

1. Introduction

In passive vibration control, the successful use of dynamic vibration neutralizers (also called dynamic vibration absorbers) is long recognized [1–4]. Particularly, it has already been shown that dynamic vibration neutralizers (DVN) of viscoelastic nature can be efficaciously designed to optimally promote vibration control over an extended frequency range and at a given temperature [5, 6]. However, as viscoelastic materials are not only frequency but also temperature dependent [2], detuning (operation away from optimal conditions) can occur, reducing the performance of

the neutralizers. A feasible alternative would then be the use of a hybrid (passive + active) vibration control scheme.

The interest in hybrid (passive + active/semiactive) vibration control systems has increased fast in the last decades [7–13], especially because it has been observed that passive and active control systems are well complementary [14, 15]. Additionally, the evolution of materials, sensors, actuators, DSP's, and signal transmission techniques has simplified implementation and increased feasibility of application in many areas of interest in vibration control.

A passive vibration control system (PVCS) usually contributes robustness, while an active vibration control system

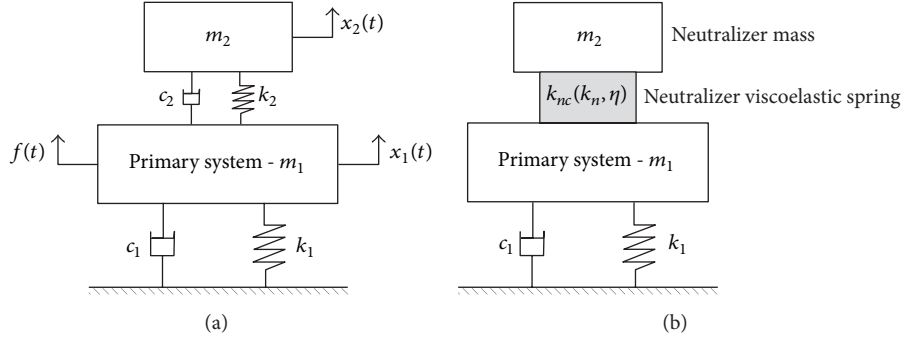


FIGURE 1: Schema of a (a) conventional (b) viscoelastic dynamic vibration neutralizer applied to a primary system.

(AVCS) contributes flexibility. Thus, the association in parallel (i.e., in the same frequency range) of these two systems permits the design of a very high performance hybrid vibration control system (HVCS), with robustness, flexibility, and reliability.

In general, passive vibration control techniques are based on fixed modifications of stiffness, mass, and/or damping characteristics of the mechanical system of concern [4, 16]. These techniques, of relatively low cost, can provide great results when working in stable environments. Their disadvantage is, exactly, the reduced flexibility when any modifications or adjustments are needed.

On the other hand, fully active vibration control techniques are based on strategies of destructive interference [17]. They are commonly implemented through sensors, actuators, and, particularly, a DSP (digital signal processor), which is able to process some input information of concern and generate the control action (based on the implemented algorithm) to be applied to the mechanical system, in order to reduce its original vibration.

In a feedback control approach, the controller works with information on the vibration of the mechanical system whereas, in feedforward control strategies, information on the disturbance is of primary interest. In the latter, the capability of adapting the controller transfer functions, according to some predefined criteria, is usually present, allowing any modifications on the excitation and/or in the mechanical system to be accounted for [18]. So, the key advantages of active vibration control techniques are flexibility and, in some cases, adaptability, at the expense of demand of external power.

In this work, a hybrid vibration control system (HVCS) is introduced and discussed, designed to attenuate vibrations in a metallic beam under broadband excitation and variable temperature. It combines a viscoelastic dynamic vibration neutralizer (VDVN), of passive nature, with components of fully active vibration control in an adaptive feedforward control approach (presented in [19]). Fundamental concepts on those elements are given below, followed by the explanation of the adopted methodology and the presentation of the results concerning the effectiveness and adaptability of the hybrid vibration control system.

It is shown that this association in parallel of a passive vibration control system (PVCS) with an active vibration

control system (AVCS) handles successfully the matter of detuning, given the adaptive nature of the AVCS. Besides, it also extends and maintains, in most cases, the overall level of vibration attenuation, over a broad frequency range. To the authors' knowledge, no such system has ever been clearly presented as done herein.

2. Fundamental Concepts

2.1. Passive Vibration Control System (PVCS). In the current application, the passive vibration control system (PVCS) consists of a viscoelastic dynamic vibration neutralizer (VDVN). As seen in Figure 1(a), in a simplified and usual form, a dynamic vibration is a secondary system (in this case, with mass m_2 , stiffness constant k_2 , and damping coefficient c_2), added to a primary mechanical system (with mass m_1 , stiffness constant k_1 , and damping coefficient c_1), the vibration of which is desired to be controlled. In Figure 1(a), $f(t)$ is the excitation on the primary system, $x_1(t)$ the corresponding vibration, and $x_2(t)$ the secondary system (neutralizer) vibration. A dynamic vibration neutralizer can be designed to work either in a tonal frequency or under broadband excitation.

It should be stressed that the use of the above DVN transforms the primary mechanical system (plant) into a two-degree-of-freedom system, the natural frequencies of which are different from those of the primary and the secondary systems alone, according to designer's interests. The damping of the DVN is related to its frequency band of action. The design parameters must be well chosen in order to attain a good control system.

In the case of a viscoelastic neutralizer (VDVN), its characteristics of stiffness and damping are determined by the viscoelastic material employed in the device [5, 6, 20]. For a single degree-of-freedom VDVN, represented in Figure 1(b) by a lump of mass m_2 and a viscoelastic spring, these characteristics can be described by the complex stiffness k_{nc} of the viscoelastic spring, which is a function of frequency and temperature and given by

$$k_{nc}(\omega, T) = k_n(\omega, T) [1 + j\eta(\omega, T)], \quad (1)$$

where $k_n(\omega, T)$ is the dynamic stiffness, $\eta(\omega, T)$ the corresponding loss factor, T the temperature, and ω the frequency.

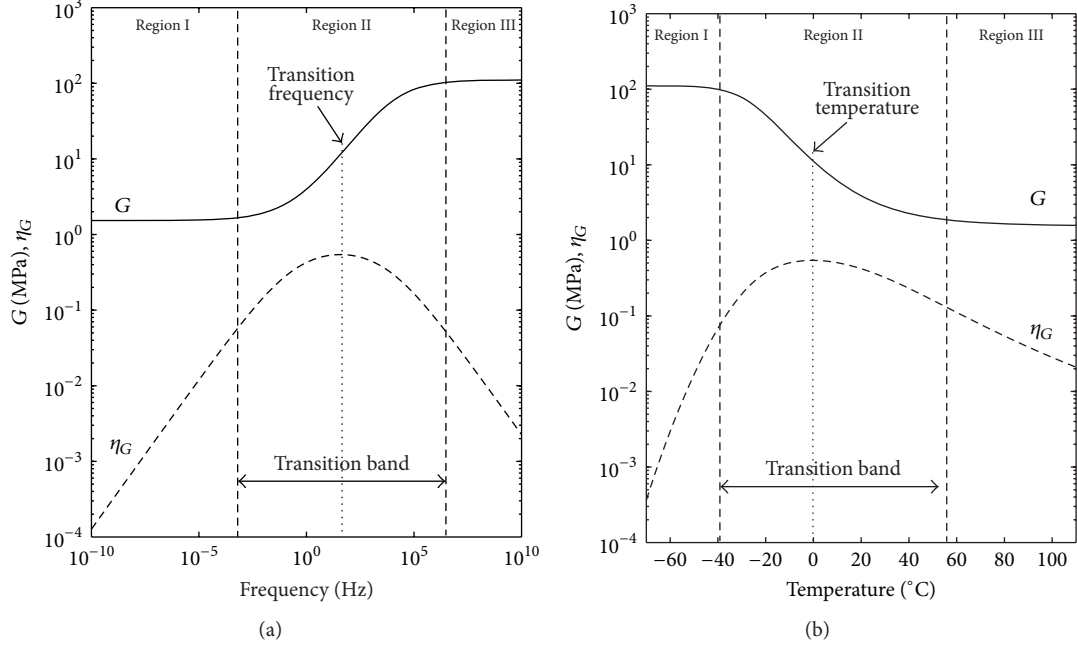


FIGURE 2: Dynamic shear modulus and loss factor as functions of (a) frequency and (b) temperature.

The stiffness k_{nc} is complex and frequency and temperature dependent because it is related to the modulus of elasticity of the viscoelastic material, which is also complex and frequency and temperature dependent. Each modulus of elasticity can be written in terms of a dynamic modulus and the corresponding loss factor, in the same way as the complex stiffness. Figure 2 shows the typical behavior of the dynamic shear modulus and the corresponding loss factor of a viscoelastic material as functions of frequency and temperature. The way the complex moduli of viscoelastic materials can be modeled by fractional derivatives and then experimentally determined can be found in [2, 21].

The single degree-of-freedom VDVN is characterized by its antiresonant frequency, Ω_n , which is such that

$$\Omega_n^2 = \frac{k_n(\omega_n)}{m_n}, \quad (2)$$

where $k_n(\omega_n)$ is the dynamic stiffness of the viscoelastic spring at the antiresonant frequency Ω_n and at a given constant temperature.

The VDVN can be designed to work, in an optimal way, in the so-called “transition band,” where the material loss factor is maximum (see Figure 2). That implies a larger frequency band in the vibration attenuation. The optimization process seeks to determine the optimal antiresonant frequency, Ω_n (which constitutes the design vector), by minimizing the Euclidean norm of the vector composed of the maximal absolute values of the principal coordinates of the primary system, over the frequency range of concern (this Euclidean norm is then the objective function).

The above optimization process, carried out by nonlinear techniques, corresponds to the reduction of the frequency

response function amplitudes of the primary system in the chosen range. It is highlighted that the VDVN is modeled in the optimization process by the concept of generalized equivalent parameters. By that concept, the compound system (primary + secondary) is described only in terms of the generalized coordinates of the primary system. The design process is fully described in De Espíndola et al. [5], Espíndola et al. [6], and Doubrawa Filho et al. [22] and is not repeated herein for the sake of conciseness.

The PVCS (VDVN), as part of the HVCS investigated in this work, is illustrated in Figure 3.

2.2. Active Vibration Control System (AVCS). An active vibration control system (AVCS) can be implemented in different ways, regarding the architecture, control algorithm, types of sensors and actuators, available signals, and operational conditions. As previously mentioned, two basic control approaches can be listed: feedback and feedforward [17]. The latter is the one employed in the present work, given that some knowledge on the primary excitation (disturbance) can be acquired.

Generally speaking, the basic components of a feed-forward control system are a sensor, which captures the input (reference) signal related to the primary excitation, a controller (or control unit), which processes the input signal according to a given algorithm and generates the output (control) signal, and an actuator, which applies the output signal in the system to be controlled. There should also be a second sensor, which captures the net response (error) signal. In the current case, the controller consists primarily of a digital finite impulse response (FIR) filter of adaptive nature. The feedforward approach usually requires the use of adaptive digital filters in order to track closely what happens to the

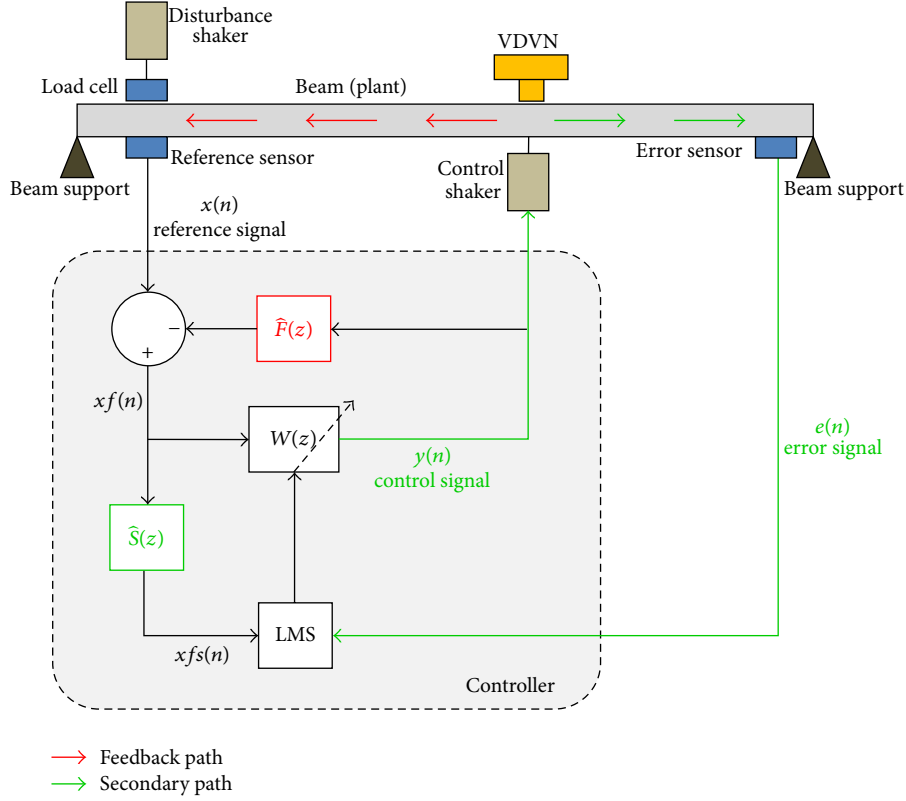


FIGURE 3: Schema of the employed hybrid vibration control system.

system (plant) and generate an efficacious control signal of destructive interference.

Finite impulse response (FIR) filters have, as opposed to infinite impulse response (IIR) filters, the important characteristic of stability; they have no poles in their transfer function. The popularity of FIR filters can also be justified by the fact that the corresponding optimal coefficients can be obtained by an objective function of quadratic nature, with a unique point of minimum. This point can be found in a prompt way through an adaptive algorithm. In the case of IIR filters, the objective function may have several local points of minimum and the algorithm may converge to any of those local points of minimum, instead of the global minimum [15, 23]. However, as FIR filters are nonrecursive structures, they can demand an excessive number of coefficients to model systems with complex transfer functions, such as vibratory systems with resonances within the frequency band of excitation. It would not be the case of IIR filters, which would require a reduced number of coefficients.

The FIR filter output (control) signal vector y is given by [23]

$$y(n) = \sum_{i=0}^{N-1} w_i(n) x(n-i), \quad (3)$$

where n is the discrete time, x is the input signal vector, N is the filter size, and w is the filter coefficient vector. In the current work, the coefficients of the adaptive FIR filter (the so-called main filter, which generates the control signal) are

obtained by a variant of the well-known LMS algorithm, the FXLMS algorithm. According to this approach, the coefficient vector is updated at each iteration by [15, 23, 24]

$$w(n+1) = vw(n) + 2\mu e(n) xfs(n) \quad (4)$$

with n being the discrete time, w the filter coefficient vector, v the so-called leaky factor, μ the adaptation step size, e the error signal, and xfs the signal vector related to the reference signal (disturbance) properly filtered by feedback and secondary filters. That explains the acronym FXLMS, which stands for filtered- x least mean square.

The AVCS, as part of the investigated HVCS, is displayed in Figure 3. In that figure, the block $W(z)$ represents the main filter, as it is the z -transform of $w(n)$, whereas the blocks $\hat{F}(z)$ and $\hat{S}(z)$ represent the feedback path and the secondary path estimation filters, respectively. It is observed that the filtered reference signal $xfs(n)$ results from the successive filtering of $x(n)$ by $\hat{F}(z)$, which gives $xf(n)$, and of $xf(n)$ by $\hat{S}(z)$.

The concept and the fundamental importance of feedback and secondary paths to the success of a practical implementation of an AVCS must be clear. The feedback path estimation filter $\hat{F}(z)$ must be inserted in the controller in order to filter the reference (input) signal $x(n)$ (which is captured by the reference sensor) from the physical vibration propagation from the control shaker to the reference sensor, through the metallic beam. Thus, a “clear” reference signal can be delivered to the controller, which is a control law requirement. The secondary path $\hat{S}(z)$ takes into account

all the dynamics inherent to the experimental setup, which includes part of the metallic beam, along with the dynamics of transducers, A/D and D/A converters, amplifiers, and analog filters. These paths are considered in the algorithm through digital FIR filters (nonadaptive), which estimate the real path dynamics (see Figure 3).

According to the design theory of Wiener filters (which are of stochastic origin), the optimal coefficients for FIR filters result from the minimization of the mean square error (MSE), or

$$\xi = E[|e(n)|^2], \quad (5)$$

where $e(n)$ is the error signal (see Figure 3) and $E[\dots]$ the expected value.

In adaptive filtering, as is the current case, the optimal coefficients can be obtained iteratively by LMS (least mean square) algorithms, regarded as practical solutions to Wiener filters [23] where the mean square error (MSE), which is the objective function, is estimated by the instantaneous value of the square of the error signal, in such a way that

$$\begin{aligned} \xi &= E[|e(n)|^2] \Rightarrow \\ \hat{\xi}(n) &= e(n)^2. \end{aligned} \quad (6)$$

Equation (4) is derived from the equation above and the consideration of the feedback and the secondary paths.

It is observed in Figure 3 that the error signal results, in this case, from the difference between the response to the disturbance shaker and the response to the control shaker (actuator). Both the reference sensor and the error sensor are accelerometers.

The advantages of LMS algorithms are simplicity, reliability, and robustness. On the other hand, a considerable disadvantage is the high dependence of the input signal power spectral density (PSD), so that the more uniform the input signal PSD, the faster the convergence.

A MIMO (multiple input multiple output) application of a very similar AVCS is implemented in an aircraft fuselage section by Marra et al. [25], where the importance of feedback path is reinforced, as well as the efficacious results of the FXLMS algorithm in an adaptive feedforward control strategy.

Another aircraft fuselage section is the plant used by Griffin et al. [26] to demonstrate the feasibility of interior cabin noise reduction via ASAC (active structural acoustic control) and ANC (active noise control) using FXLMS and PCLMS (two variants of LMS algorithm) in an adaptive feedforward approach, where significant noise reduction is obtained.

Zeng et al. [27] present the use of an adaptive feedforward control framework similar to the AVCS employed herein. It is aimed to suppress aircraft structural vibrations induced by gust perturbations, a typical case where the primary system (of aeroelastic nature) has its flexible modes shifted during operation (mass/inertia changes, different atmospheric conditions, etc.), demanding a “smart” algorithm to adapt its control actions to the new system’s behavior.

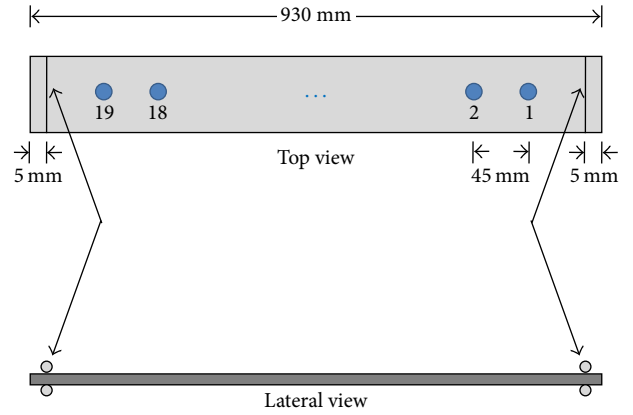


FIGURE 4: Beam schematic view.

2.3. Hybrid Vibration Control System (HVCS). The above PVCS and AVCS can be combined to form a hybrid vibration control system (HVCS). Apart from dealing with the matter of detuning of a viscoelastic device, an HVCS like this, schematically shown in Figure 3, can offer greater reliability as a global vibration control system, since, in case of failure or loss of performance of any “subsystem,” the other one can maintain some overall vibration control level. The methodology employed to implement and evaluate the HVCS is presented in the next section.

3. Methodology

The system to be controlled (primary mechanical system, or plant) is a 0.5 kg simply supported steel beam, the dimensions of which are $930 \times 23 \times 3$ mm. A schematic view of the beam is shown in Figure 4.

A previously performed theoretical and experimental modal analysis on the beam provided complete information about the dynamic behavior of the beam at all positions. It led to the selection of the modes and the frequency range of interest and also to the selection of the point in the beam where to locate both the VDVN and the control shaker. The 4th, 5th, and 6th vibration modes of the beam are chosen because they allow the design of a VDVN with a relatively small amount of mass and compact viscoelastic elements, resulting in a device of reduced size. As shown further (Figure 10), several components of the experimental setup (beam, supports, neutralizer, sensors, actuators, and others) are placed and handled inside a temperature chamber and the use of components of reduced size becomes a requirement. As to the location of the VDVN and the control shaker, point 2 in the above figure is chosen because there are no nodes of the 4th, 5th, and 6th modes at that point, as required, and also by experimental convenience.

The applied excitation signal is a white noise filtered to a band of 200 to 430 Hz. This signal, displayed in the time and frequency domains in Figure 5, only excites the vibration modes of concern of the beam, as shown in the frequency response function (FRF) of Figure 6. In that figure, the response is at point 1 and the excitation at point 19 (see

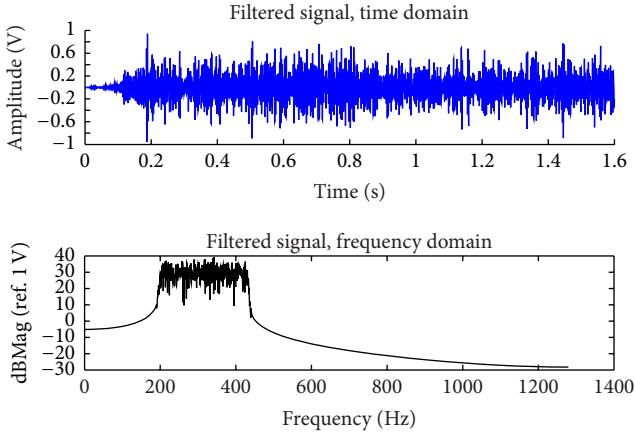


FIGURE 5: Excitation signal (filtered white noise, 200–430 Hz).

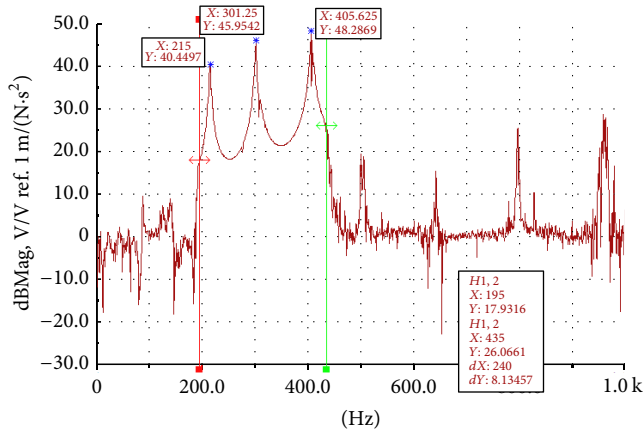


FIGURE 6: FRF (1/19) of the beam without the VDVN and excited in the frequency range of 200 to 430 Hz.

Figure 4), being the corresponding FRF indicated as FRF (1/19). This combination of response and excitation points provides clear and expressive results and is selected as the reference in this work.

The PVCS, a viscoelastic DVN with a steel lump of mass of 0.0335 kg and two elements of butyl rubber 45 Shore A, is optimally designed to act in the frequency band of 190 to 440 Hz and at the temperature of 25°C [28]. The drawings of the VDVN are displayed in Figure 7 whereas the viscoelastic material properties of the employed butyl rubber are shown in the nomogram of Figure 8. This nomogram is the standard plot for displaying dynamic properties of viscoelastic materials [2]. As mentioned earlier, the VDVN is installed at a point where there are no nodes for the vibration modes of interest. The relative positioning of the VDVN and of all the AVCS components (such as sensors and actuators) can be schematically seen in Figure 3.

The controller is based on an Analog Devices board, the EZ-KIT Lite ADSP 21161N, on which the FXLMS algorithm is implemented. Before running the control tests, identification routines for the secondary and feedback paths have to be

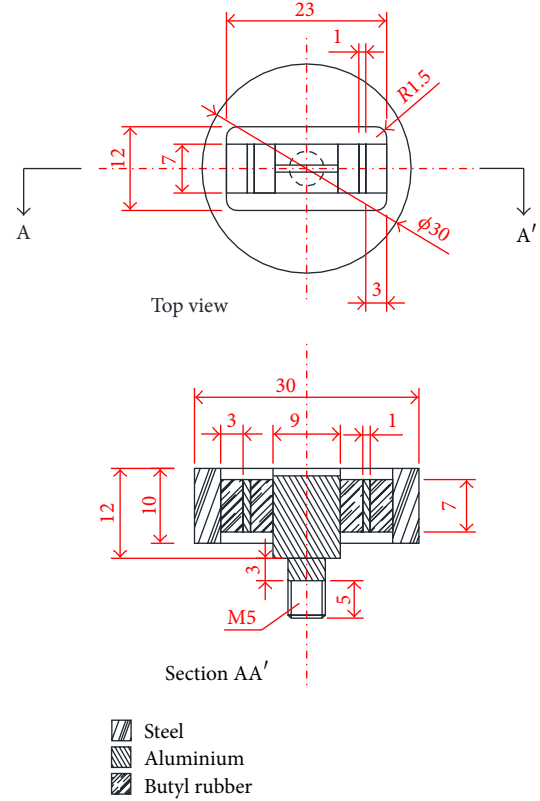


FIGURE 7: VDVN drawings (all dimensions are in millimeters).

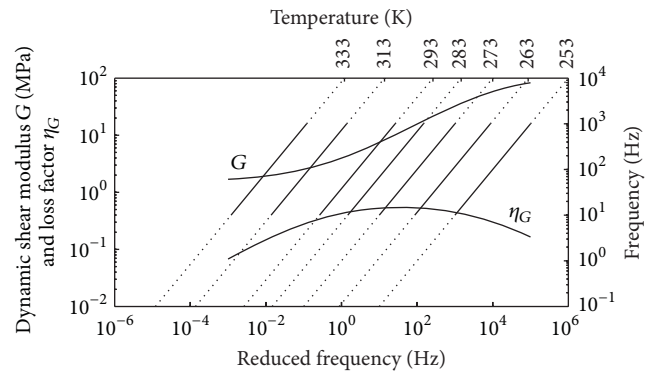


FIGURE 8: Viscoelastic material properties of the butyl rubber.

performed, in order to have the FXLMS algorithm fully implemented, as portrayed in Figure 3. Those paths are identified through offline procedures [29] and the digital filter associated with each path represents the corresponding impulsive response. These filter coefficients are loaded into the algorithm and kept constant, describing thus “static filters” during the control tests.

It should be clear, however, that the main FIR filter, $W(z)$, is not “static” like the secondary and feedback filters, but adaptive, with its coefficients being adjusted at each algorithm iteration according to (4), in an online, real time updating procedure. The use of online identification techniques for the

TABLE 1: FXLMS optimal parameters for active-adaptive vibration control.

N	N_s	N_f	ν	μ
300	500	500	0,9999995	$1,50E-06$

secondary and feedback paths, although not employed in this investigation, is also possible and has already been reported as advantageous [30].

As observed in Coan Jr. [28], in a previous implementation of an active-adaptive vibration control system, the task of tuning the FXLMS algorithm is very important and deserves special care, because of its high influence on performance. The best tuning parameters found in this work, after experimenting various alternatives, are shown in Table 1, where N , N_s , and N_f are the number of coefficients of the main filter, $W(z)$; the secondary path filter, $\hat{S}(z)$; and the feedback path filter, $\hat{F}(z)$, respectively.

In Table 1, it is observed that the main filter size (300 coefficients) is smaller than those of the secondary and feedback filters (500 coefficients). The main filter is adaptive and its coefficients have to well identify the plant's behavior at only one temperature, which is the current test temperature. That is, the main filter performance is optimized at each temperature. On the other hand, the secondary and feedback filters are not adaptive and, consequently, their performances are not optimized at each test temperature. Thus, the corresponding filter coefficients must describe satisfactorily the plant's behavior at all test temperatures without any change. That suggests that significantly smaller secondary and feedback filters can be attained if they also become adaptive. Smaller filters could improve the algorithm effectiveness as a whole.

As previously mentioned, the digital filters intend to represent the impulsive response of a specific system (for instance, the plant, the secondary path, or the feedback path). So, the more information is acquired by the digital filter about the impulsive response of the system of concern, the higher is the fidelity of such a digital model, that is, the better is the quality of identification.

Figure 9 shows that, for a given filter size, a more damped system is better identified by digital filters than a less damped one. That is due to the amount of "meaningful information" (in terms of impulsive response, $h(t)$) acquired by the digital filters regarding the system under identification; that is, it is possible to acquire more impulsive response information from a highly damped system than from a lesser damped system, as seen in Figure 9. Therefore, the main filter can have its task of representing the mechanical system (the metallic beam, in the case) facilitated by the presence of the PVCS, given the damping it introduces in the compound system and the relation between damping and length of impulsive response.

The experimental setup, which allows all the investigations regarding the vibration control systems, is displayed in Figure 10, inside the temperature chamber employed in the measurements.

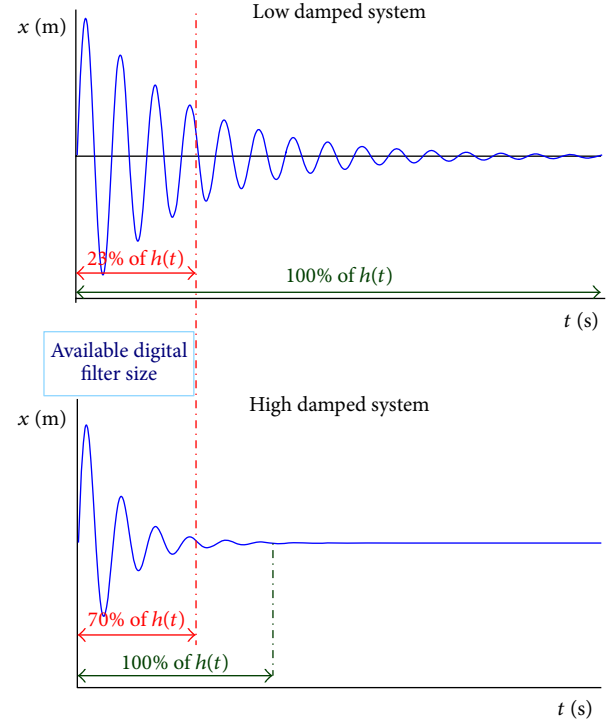


FIGURE 9: Portion of system impulsive response acquired with a given digital filter size.

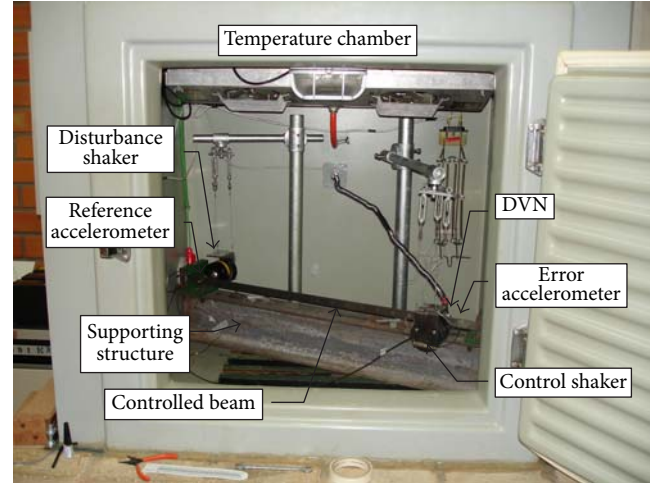


FIGURE 10: Experimental setup inside the temperature chamber.

In a first stage, for the beam alone, the ratio of the acceleration (at a point of the beam) to the disturbing force is computed, in the frequency domain. That ratio is denominated herein a response to force ratio (RFR). After installing the VDVN and maintaining exactly the same primary excitation (disturbance) applied before, it is possible to evaluate the PVCS attenuation performance by computing a response to force ratio (RFR) of the compound system (beam + VDVN).

An explanation should be given at this point. A response to force ratio (RFR) is a ratio between the response at a point in the system of concern and the disturbing force at the same or at other points, in the frequency domain [15]. This frequency function is introduced to provide a common ground in which all the attenuation performances can be compared. When only the disturbing force acts on the system (beam alone or beam + VDVN), an RFR is a frequency response function (FRF). When the disturbing force acts on the system simultaneously to another external force as, in the current case, the force of destructive interference, an RFR is no longer an FRF. Even though the RFR reveals the changes which take place in the system when the AVCS works on it and allows valid comparisons to be made with other RFRs, exactly the same disturbance force is applied on all the three experimental setups (pure beam, beam + VDVN, and beam + VDVN + AVCS).

After exclusively testing the PVCS, the AVCS is turned on, so to act on the compound system (beam + VDVN), and its additional contribution is evaluated by an RFR of the global system (beam + VDVN + AVCS), still keeping the same disturbance. All those tests are run at room temperature (around 25°C, the optimal VDVN design temperature).

The next stage is to test the adaptability of the main digital filter of the AVCS, which is carried out by varying the temperature under which the experimental setup is, inside the temperature chamber, as seen in Figure 10. By varying the temperature, it is expected that the VDVN performance deteriorates and the coefficients of the main filter are automatically adjusted in response to that, according to (4), such that the AVCS still maintains a satisfactory vibration level.

Those adaptability tests are performed at the temperatures of 5, 15, 25, and 35°C. At each test temperature, before taking the measurements, a 30-minute interval is considered to allow the temperature of the viscoelastic elements of the VDVN to stabilize. All the RFRs are computed between the error sensor location point (point 1) and the disturbance actuator location point (point 19). Those locations are shown in Figures 4 and 10.

The attenuations obtained in each test condition are calculated according to (7). This equation, introduced in this work, is used to verify the effectiveness of the vibration control systems in their actions over the whole frequency band of interest, in addition to the check in individual frequencies, as usually done:

$$\text{Att [dB]} = 20 \log_{10} \left\{ \frac{[\sum_j y_j^2(f_j)]^{1/2}}{[\sum_j x_j^2(f_j)]^{1/2}} \right\}. \quad (7)$$

In the above equation, y_j represents RFR (response to force ratio) magnitudes along frequencies f_j , when any control system is ON, that is, plant *with* any vibration control system. As to x_j , it represents the corresponding RFR magnitudes when that control system is OFF, that is, plant *without* that vibration control system. In this context, the term “vibration control system” can be applied either to the PVCS or to the HVCS, bearing in mind the primary

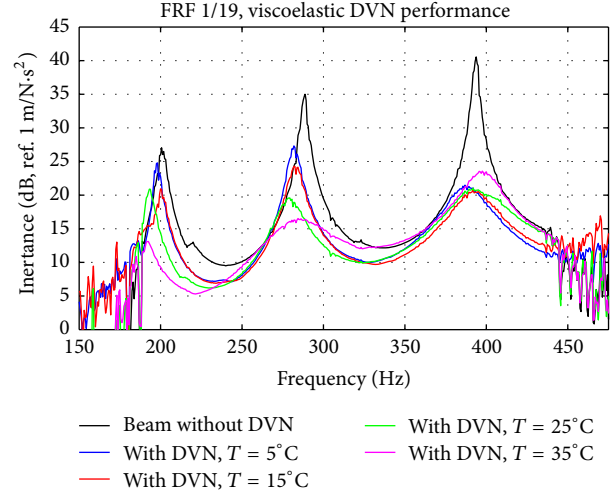


FIGURE 11: Passive vibration control system (viscoelastic DVN) performance.

TABLE 2: VDVN performance (vibration attenuation), broadband analysis.

Test temperature [°C]	RMS broadband attenuation [dB]
5	7,9
15	9,1
25	9,5
35	8,9

goal of dealing with the detuning of the PVCS. Equation (7) represents the root mean square (RMS) value of the vibration attenuation due to each particular vibration control system, in the frequency band of concern.

The corresponding results are presented below.

4. Results

The results are as follows.

4.1. Passive Vibration Control System (PVCS). Figure 11 depicts the effectiveness of the VDVN over the frequency band of interest, including the specific and characteristic reductions at the resonance peaks.

It is expected that the VDVN performance varies markedly with the temperature, due to the behavior of the viscoelastic material (see Figures 2 and 8) and that is confirmed. In a broadband analysis, which is carried out with the aid of (7), there is loss of performance when the temperature is different from the design value of 25°C, as observed in Table 2 and in Figure 11. In general, the farther the temperature from the design value the worse the VDVN broadband performance.

Considering the frequency and temperature ranges of the current application (200 to 430 Hz, and 5 to 35°C, resp.) and the frequency and temperature dependencies of a typical viscoelastic material (particularly detailed in Figure 2), it is

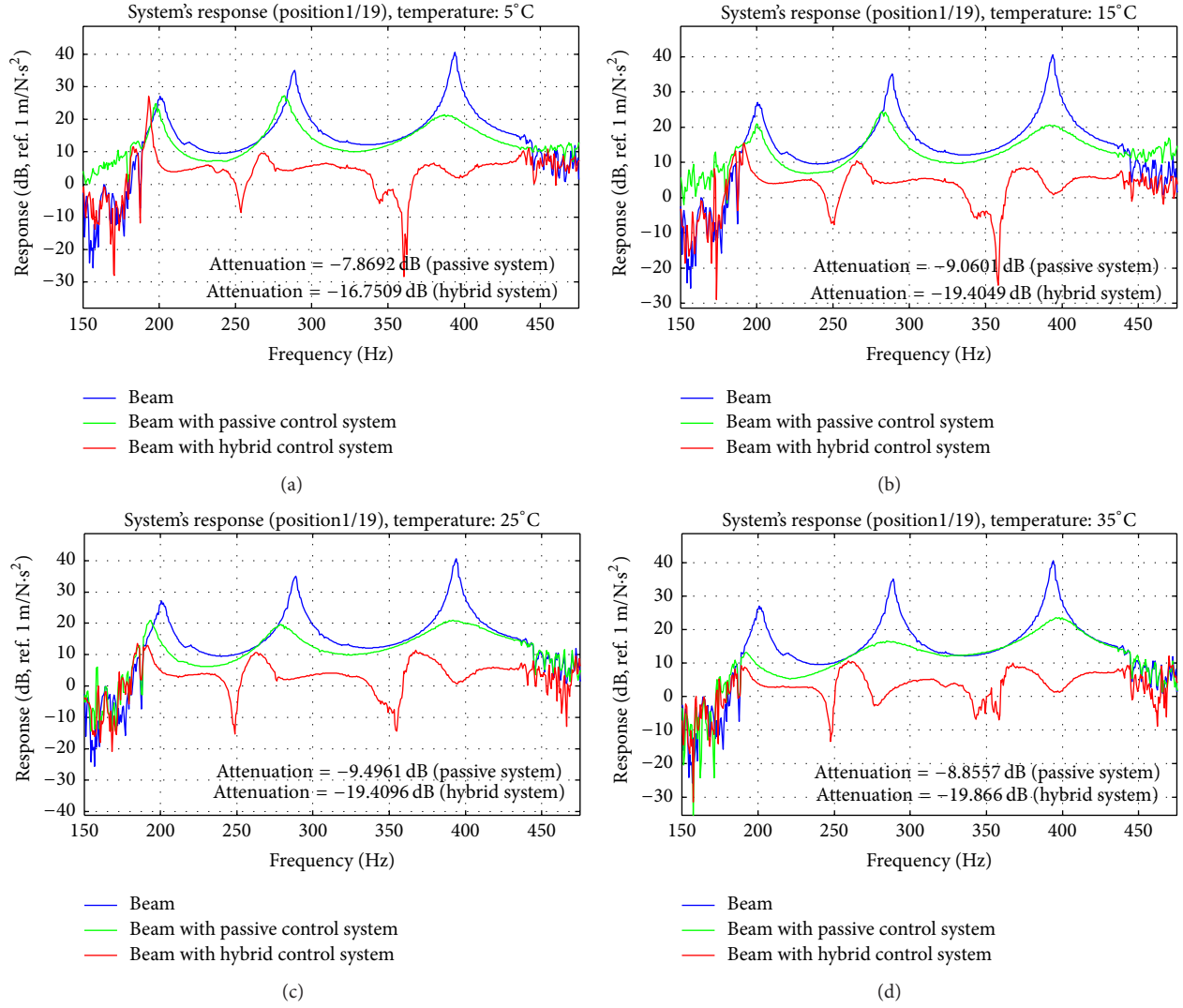
FIGURE 12: PVCS and HVCS performances at (a) $T = 5^\circ\text{C}$, (b) $T = 15^\circ\text{C}$, (c) $T = 25^\circ\text{C}$, and (d) $T = 35^\circ\text{C}$.

TABLE 3: VDVN performance (vibration attenuation), resonance peak analysis.

Test temperature [$^\circ\text{C}$]	Resonance peak attenuation (4th mode) [dB]	Resonance peak attenuation (5th mode) [dB]	Resonance peak attenuation (6th mode) [dB]
5	2,0	8,0	19,0
15	6,0	11,0	20,0
25	6,0	16,0	19,5
35	14,0	18,0	17,0

expected to observe higher VDVN sensibility to temperature than to frequency variations. This is not only the more practical but also the more revealing situation.

Focusing on the resonance peaks only, it is observed that the greatest attenuations, regarding each mode of vibration, do not occur at 25°C , as recorded in Table 3. However, it must be remembered that the viscoelastic DVN is not primarily designed for tonal action but for broadband action

and that has to do with the amount of damping in the device. In fact, for tonal passive control, an “undamped” vibration neutralizer should be used instead.

4.2. Hybrid Vibration Control System (HVCS). The results obtained with the PVCS and the HVCS (comprising both passive and the active-adaptive vibration control systems) are shown in Figure 12, for various temperatures. It can

TABLE 4: PVCS and HVCS performance (vibration attenuation related to the uncontrolled beam vibration levels), broadband analysis.

Temperature	Control system		
	Passive [dB]	Hybrid [dB]	Difference (HVCS to PVCS) [dB]
5°C	7.9	16.8	8.9
15°C	9.1	19.4	10.3
25°C	9.5	19.4	9.9
35°C	8.9	19.9	11.0

be observed in the corresponding curves that the PVCS (VDVN) generally produces a small lateral displacement of the resonance peaks, apart from the characteristic “smoothing.” These effects are typical in cases of damping addition. When the AVCS is turned on and the full HVCS is in place, drastic modifications are observed on the RFR curves, especially at the resonance peaks and at frequencies where antiresonances are introduced in those curves (there is a supplementary material, a video (in Supplementary Material available online at <http://dx.doi.org/10.1155/2016/5375309>), which shows, in real time, the AVCS actuating on the beam with PVCS, since the moment it is turned on until the final condition of the system, when the RFRs assume the shapes of Figure 12).

The marked control action at the resonance peaks after the AVCS is turned on can be explained as follows. The control signal generation is based on an online plant identification method and this makes the highest energy frequency components of the system response (the resonance frequencies) to be carried to the main filter coefficients. Thus, the control signal is generated with the same characteristics; that is, the control signal has the same highest energy frequency components as the plant response. Hence, when the control signal is reintroduced into the system (see Figure 3), its action is more efficacious exactly at the resonance peaks.

Table 4 presents the performance of the PVCS and the HVCS at each test temperature, considering the vibration attenuation at the frequency band of interest calculated according to (7), whereas Table 5 presents the attenuations at each resonance frequency, given the associated vibration mode. More expressive values are observed when considering the performance of the vibration control systems by the attenuation at the resonance peaks (see Figure 12 and Table 5). In some cases, the attenuation when the HVCS is in place is around a massive 34 dB.

Tables 4 and 5 may induce comparisons between the PVCS and the AVCS (recalling that the HVCS comprises both the PVCS and the AVCS). However, this comparison is not adequate because the AVCS always works along with the PVCS. The PVCS is applied to the metallic beam alone, but the AVCS is applied to the metallic beam with the PVCS, a “new plant” for which the mass, damping, and stiffness characteristics are different from those of the metallic beam alone. So, the PVCS and AVCS work over different plants, in such a way that their performances should not be compared.

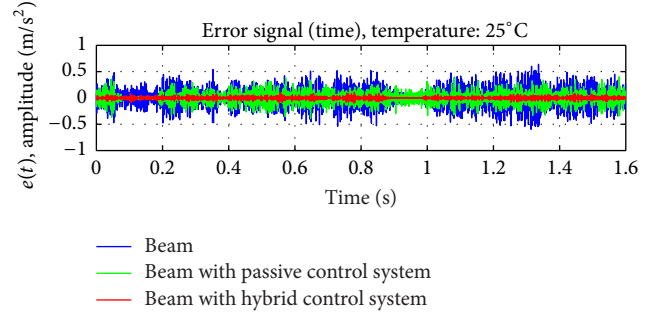


FIGURE 13: Error sensor time history.

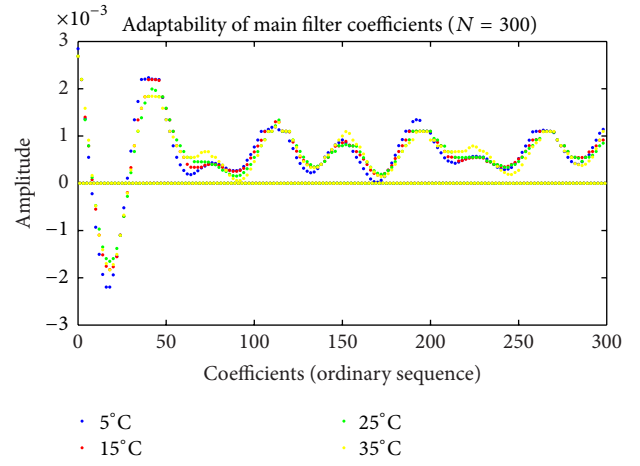


FIGURE 14: Adaptability of main filter coefficients.

Tables 4 and 5 help to illustrate (once more) the effectiveness of the VDVN (as a robust passive vibration control system) and also to demonstrate that the inclusion of the AVCS is a feasible solution for the detuning inherent to the VDVN when it undergoes temperature variations. As shown in those tables, when the AVCS works along with the PVCS (forming the HVCS), the VDVN detuning is no longer a problem, because the AVCS can compensate the VDVN loss of performance. In fact, the combination of the PVCS and the AVCS provides expressive results in terms of vibration attenuation over all the temperature and frequency ranges of operation.

The behaviors of the vibration control systems are also monitored through the error sensor signal, in the time domain, as displayed in Figure 13. Those curves reinforce the greater efficacy of the HVCS.

The adaptation capability introduced by the AVCS, as part of the HVSC, can be inferred from the above results. However, in order to make this point even more clear and help to visualize how the FXLMS algorithm handles the main filter coefficients to generate the best control signal at each test condition, the values of the main filter coefficients are traced at each test temperature. The results are presented in Figure 14, where the adaptability of the AVCS is clearly observed, in response to the changes in dynamic behavior undergone by the plant due to the temperature dependence of the VDVN.

TABLE 5: PVCS and HVCS performance (vibration attenuation related to the uncontrolled beam vibrations levels), resonance peak analysis.

Temperature [°C]	Vibration control system	Vibration mode		
		4th [dB]	5th [dB]	6th [dB]
5	<i>Passive</i>	2,3	7,7	19,3
	<i>Hybrid</i>	0,0	25,6	34,1
15	<i>Passive</i>	6,2	10,8	20,0
	<i>Hybrid</i>	11,5	24,6	32,2
25	<i>Passive</i>	6,2	15,5	19,5
	<i>Hybrid</i>	13,3	24,3	29,1
35	<i>Passive</i>	14,0	18,6	17,0
	<i>Hybrid</i>	17,8	24,7	30,6

5. Conclusions

The vibration attenuation performance and robustness of the PVCS (VDVN), as well as its expected changes in dynamic behavior under frequency and temperature variations, are verified once more. That adds to the long and successful chain of broadband applications in which the same technique for VDVN design is employed [5, 6, 20].

The adaptive behavior of the AVCS becomes well characterized when there are changes in the compound system (metallic beam + VDVN) due to the variation in temperature, confirming and extending some previous efforts of tonal nature [28]. In most cases, the filter coefficients are adjusted in such a way that the VDVN loss of performance by detuning is compensated and an extended global vibration attenuation at around 19 dB is maintained. Even when that level is not reached, a very significant effort is clearly made by the AVCS.

It is worth mentioning that the adaptive capability is very important to compensate not only system modifications but also some modeling errors or inaccuracies in design, thereby improving the applicability of the AVCS. It is understood that improvements on the quality and effectiveness of the FXLMS algorithm will be achieved if the “static” secondary and feedback filters become adaptive as well.

It is also pointed out that the damping characteristics of the mechanical system under control, altered by the insertion of the VDVN, are an important factor for the order (number of coefficients) of the employed FIR filters and for the FXLMS effectiveness. In fact, when a VDVN is inserted in a mechanical system, this system becomes more damped, with impulsive response functions of smaller nonzero length. As the AVCS is applied to this more damped plant (beam with VDVN), the FIR filters can be of reduced order. That has a direct impact on the convergence of the employed LMS algorithm.

Finally, the HVCS, comprising both the above PVCS and AVCS, reveals itself as a powerful alternative in vibration control, in which the advantages of each particular system can be well associated in order to have an adaptable, flexible, and robust global control system, of reduced cost. This association also contributes to a more reliable control system, where the responsibility is shared between its component systems and some overall vibration control level can still be maintained in case of failure of any of those systems.

Competing Interests

The authors declare that they have no competing interests.

Acknowledgments

The first author wishes to express his gratitude to the Federal University of Santa Catarina, Brazil, and Federal University of Paraná, Brazil, for all the support over the development of this work. The second author acknowledges the financial support of CNPq. A special acknowledgement must be expressed for the relevant contributions of Dr. Orlando Jose Tobias (“in memoriam”) to this work.

References

- [1] C. E. Crede, *Shock and Vibration Concepts in Engineering Design*, Prentice-Hall, Upper Saddle River, NJ, USA, 1965.
- [2] A. D. Nashif, D. I. G. Jones, and J. P. Henderson, *Vibration Damping*, John Wiley & Sons, New York, NY, USA, 1985.
- [3] B. G. Korenev and L. M. Reznikov, *Dynamic Vibration Absorbers: Theory and Technical Applications*, John Wiley & Sons, 1993.
- [4] D. J. Mead, *Passive Vibration Control*, John Wiley & Sons, 2000.
- [5] J. J. De Espindola, C. A. Bavastri, and E. M. De Oliveira Lopes, “Design of optimum systems of viscoelastic vibration absorbers for a given material based on the fractional calculus model,” *Journal of Vibration and Control*, vol. 14, no. 9-10, pp. 1607–1630, 2008.
- [6] J. J. Espindola, C. A. Bavastri, and E. M. O. Lopes, “On the passive control of vibrations with viscoelastic dynamic absorbers of ordinary and pendulum types,” *Journal of the Franklin Institute*, vol. 347, pp. 102–115, 2010.
- [7] M. A. Ahmad, A. N. K. Nasir, R. M. T. R. Ismail, and M. S. Ramli, “Comparison of hybrid control schemes for vibration suppression of flexible robot manipulator,” in *Proceedings of the International Conference on Computer Modeling and Simulation (ICCMS '09)*, pp. 356–360, Macau, China, February 2009.
- [8] H. Pu, X. Luo, W. Jiang, K. Dong, and X. Chen, “Modelling and control of hybrid vibration isolation system for high-precision equipment,” in *Proceedings of the 8th IEEE International Conference on Control and Automation (ICCA '10)*, pp. 2152–2157, Xiamen, China, June 2010.
- [9] J. L. Svensson, P. B. U. Andersson, and W. Kropp, “On the design of structural junctions for the purpose of hybrid passive-active

- vibration control,” *Journal of Sound and Vibration*, vol. 329, no. 9, pp. 1274–1288, 2010.
- [10] S.-M. Kim, S. Wang, and M. J. Brennan, “Dynamic analysis and optimal design of a passive and an active piezo-electrical dynamic vibration absorber,” *Journal of Sound and Vibration*, vol. 330, no. 4, pp. 603–614, 2011.
 - [11] M. A. Trindade, “Experimental analysis of active-passive vibration control using viscoelastic materials and extension and shear piezoelectric actuators,” *Journal of Vibration and Control*, vol. 17, no. 6, pp. 917–929, 2011.
 - [12] Y. L. Cheung, W. O. Wong, and L. Cheng, “Optimization of a hybrid vibration absorber for vibration control of structures under random force excitation,” *Journal of Sound and Vibration*, vol. 332, no. 3, pp. 494–509, 2013.
 - [13] S. Mohammadi, S. Hatam, and A. Khodayari, “Modeling of a hybrid semi-active/passive vibration control technique,” *Journal of Vibration and Control*, vol. 21, no. 1, pp. 21–28, 2015.
 - [14] M. A. Franchek, M. W. Ryan, and R. J. Bernhard, “Adaptive passive vibration control,” *Journal of Sound and Vibration*, vol. 189, no. 5, pp. 565–585, 1996.
 - [15] J. C. O. Marra, *Controle híbrido de vibrações em estruturas sob excitação de banda larga, utilizando neutralizador viscoelástico e filtro adaptativo [M.S. thesis]*, Federal University of Santa Catarina, Florianópolis, Brazil, 2007 (Portuguese).
 - [16] D. J. Inman, *Vibration with Control*, John Wiley & Sons, New York, NY, USA, 2009.
 - [17] C. R. Fuller, S. J. Elliot, and P. A. Nelson, *Active Control of Vibration*, Academic Press, New York, NY, USA, 1997.
 - [18] R. L. Clark, W. R. Saunders, and G. P. Gibbs, *Adaptive Structures—Dynamics and Control*, John Wiley & Sons, 1998.
 - [19] J. C. O. Marra, E. M. O. Lopes, J. J. Espíndola, O. J. Tobias, and W. A. Gontijo, “Hybrid vibration control applied to structures under broadband excitation using viscoelastic neutralizer and adaptive filter,” in *Proceedings of the 21st Brazilian Congress of Mechanical Engineering*, Natal, Brazil, 2011.
 - [20] C. A. Bavastrri, *Redução de vibrações de banda larga em estruturas complexas por neutralizadores viscoelásticos [Ph.D. thesis]*, Federal University of Santa Catarina, Trindade, Brazil, 1997 (Portuguese).
 - [21] J. J. De Espíndola, J. M. Da Silva Neto, and E. M. O. Lopes, “A generalised fractional derivative approach to viscoelastic material properties measurement,” *Applied Mathematics and Computation*, vol. 164, no. 2, pp. 493–506, 2005.
 - [22] F. J. Doubrawa Filho, M. A. Luersen, and C. A. Bavastrri, “Optimal design of viscoelastic vibration absorbers for rotating systems,” *Journal of Vibration and Control*, vol. 17, no. 5, pp. 699–710, 2011.
 - [23] B. Farhang-Boroujeny, *Adaptive Filters—Theory and Applications*, John Wiley & Sons, New York, NY, USA, 1998.
 - [24] S. J. Elliott, *Signal Processing for Active Control*, Academic Press, Cambridge, Mass, USA, 2001.
 - [25] J. C. O. Marra, P. J. G. Paupitz, and L. C. S. Goes, “A multichannel active-adaptive vibration control system applied to an aeronautical structure,” in *Proceedings of the International Conference on Noise and Vibration Engineering*, Leuven, Belgium, 2010.
 - [26] S. Griffin, A. Weston, and J. Anderson, “Adaptive noise cancellation system for low frequency transmission of sound in open fan aircraft,” *Shock and Vibration*, vol. 20, no. 5, pp. 989–1000, 2013.
 - [27] J. Zeng, B. Moulin, R. De Callafon, and M. J. Brenner, “Adaptive feedforward control for gust load alleviation,” *Journal of Guidance, Control, and Dynamics*, vol. 33, no. 3, pp. 862–872, 2010.
 - [28] J. Coan Jr., *Controle misto de vibrações em viga metálica por neutralizadores viscoelásticos e filtros adaptativos: caso harmônico [M.S. thesis]*, Federal University of Santa Catarina, Florianópolis, Brazil, 2005 (Portuguese).
 - [29] S. M. Kuo and D. R. Morgan, “Active noise control: a tutorial review,” *Proceedings of the IEEE*, vol. 87, no. 6, pp. 943–973, 1999.
 - [30] W. A. Gontijo, *Implementação e avaliação de desempenho de algoritmos adaptativos aplicados em controle ativo de vibrações [M.S. thesis]*, Federal University of Santa Catarina, Florianópolis, Brazil, 2006 (Portuguese).

Research Article

The Behaviour of Mistuned Piezoelectric Shunt Systems and Its Estimation

M. Berardengo,¹ S. Manzoni,² and M. Vanali¹

¹Department of Industrial Engineering, Università degli Studi di Parma, Parco Area delle Scienze 181/A, 43124 Parma, Italy

²Department of Mechanical Engineering, Politecnico di Milano, Via La Masa 34, 20156 Milan, Italy

Correspondence should be addressed to S. Manzoni; stefano.manzoni@polimi.it

Received 20 May 2016; Revised 18 July 2016; Accepted 26 July 2016

Academic Editor: Nicola Caterino

Copyright © 2016 M. Berardengo et al. This is an open access article distributed under the Creative Commons Attribution License, which permits unrestricted use, distribution, and reproduction in any medium, provided the original work is properly cited.

This paper addresses monoharmonic vibration attenuation using piezoelectric transducers shunted with electric impedances consisting of a resistance and an inductance in series. This type of vibration attenuation has several advantages but suffers from problems related to possible mistuning. In fact, when either the mechanical system to be controlled or the shunt electric impedance undergoes a change in their dynamical features, the attenuation performance decreases significantly. This paper describes the influence of biases in the electric impedance parameters on the attenuation provided by the shunt and proposes an approximated model for a rapid prediction of the vibration damping performance in mistuned situations. The analytical and numerical results achieved within the paper are validated using experimental tests on two different test structures.

1. Introduction

Vibration attenuation in light structures is a widely studied topic and often takes advantage of the use of smart materials, which are characterised by useful properties. Indeed, these materials are inexpensive when compared to other control systems, and they are characterised by low weight. This last feature is a fundamental aspect because it avoids introducing high load effects on the controlled structure. Among smart materials, piezoelectric elements (particularly piezoelectric laminates, which are used in this paper) are among the best materials to attenuate vibrations in bidimensional (e.g., plates) and monodimensional (e.g., beams) structures [1–3]. There are several control techniques for light structures that rely on this type of actuator, and one of the most attractive is the shunt of the piezoelectric element. In this case, a properly designed electrical network is shunted to the piezoelectric bender bonded to the structure. The ability of the piezoelectric element to convert mechanical energy into electrical energy and vice versa [4, 5] is used, which allows a passive attenuation of the structure's vibration. This method was initially proposed by Hagood and von Flotow [4]. This technique is extremely attractive because it is cheap, it does

not introduce energy into the system, that is, it cannot lead to instability, and it does not require any feedback signal.

When a monoharmonic control is required, the most effective shunt electric impedance consists of a resistance R and an inductance L in series [2, 4, 6–8] (resonant shunt or RL shunt). These two elements, along with the capacitance C_p of the piezoelectric actuator (i.e., the piezoelectric actuator is modelled here as a capacitance and a strain-induced voltage generator in series; see Section 2), constitute a resonant circuit, which is the electric equivalent of the mechanical tuned mass damper (TMD) [2]. Therefore, this circuit is able to damp the structural vibration corresponding to a given eigenmode as soon as its dynamic features are tuned to those of the vibrating structure.

There are several methods in the literature that explain how to select the values of R and L to optimise the vibration attenuation. Hagood and von Flotow [4] proposed two different tuning strategies based on considerations on the shape of the system transfer function and on the pole placement techniques for an undamped structure. Both these tuning methods are based on the classical TMD theory. Høgsberg and Krenk [9, 10] developed another calibration method based on the pole placement for RL circuits in series and

parallel. The values of R and L are selected to guarantee equal modal damping of the two modes of the electromechanical structure and good separation of the complex poles. Thomas et al. [11] proposed two different methods, even for damped structures, that relied on the transfer function criteria and pole placement and provided closed formulas to estimate the attenuation performance.

Although all of the mentioned tuning strategies work extremely well, one significant issue of shunt damping using RL impedances is that this type of electrical circuit is not adaptive. This in turn means that it is not possible to follow possible changes in the dynamic behaviour of either the vibrating structure (e.g., a temperature shift can change the eigenfrequency of the mode to be controlled) or the impedance itself (e.g., a temperature shift can cause a significant change in the R value [12]). Hence, this control technique often works in mistuned conditions, even when starting from a perfect tuning condition. This mistuning leads to severe worsening of the attenuation performance.

A few techniques based on adaptive circuits were proposed to overcome the limitations due to uncertainties in the mechanical and electrical quantities. Based on the single-mode control, Holkamp and Starchville developed a self-tuning RL circuit that was able to follow any change in the frequency of the mode to be controlled [13]. This technique is based on a synthetic circuit (which provides both the resistance and the inductance) consisting of two operational amplifiers and a motorised potentiometer. Despite its effectiveness, this method only considers a mistuning due to a change in the eigenfrequency to be controlled and does not consider other types of changes or uncertainties, such as ones related to electrical parameters. Furthermore, this method is active, thus losing the advantage provided by the passive shunt technique. Other recent studies by Zhou et al. [14, 15] attempted to determine methods to limit the problem of mistuning by using nonlinear elements when the disturbance was harmonic and using more than one piezoelectric actuator bonded to the vibrating structure. Although these techniques can be effectively employed, their use implies the loss of the two primary features of the resonant piezoelectric shunt: linearity (and thus ease of use) and passivity. Therefore, the analysis of the performances of traditional RL shunts in mistuned conditions still has significant relevance.

Although the problems related to mistuning are evidenced in literature [16–18], there have been few analyses on shunt robustness. These analyses are of significant interest for numerous engineering applications where electrical power is often limited or even avoided, thus preventing the use of adaptation systems for the shunt impedance (e.g., space applications). In situations where passivity is requested, it is important to analyse the behaviour of the shunted system in the presence of mistuning because it worsens the attenuation performance. Recently, Berardengo et al. [19] studied the robustness of different optimisation methods for RL circuits and determined the most robust method. Based on the outcomes of [19], this paper aims to further investigate the robustness of RL shunt damping. The word robustness is intended here as the capability of the shunt impedance to attenuate the vibrations even when in mistuned conditions.

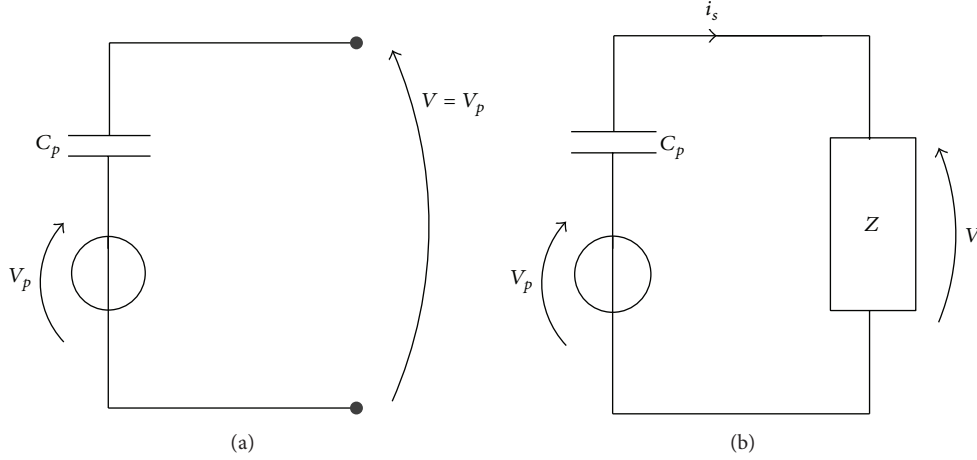
Therefore, this paper analyses the behaviour of mistuned electromechanical systems, thus depicting the relationship between the attenuation and the system parameters (e.g., coupling coefficient, mechanical nondimensional damping ratio, and eigenfrequency) in tuned and mistuned conditions. Furthermore, this paper demonstrates that the loss of attenuation primarily depends on only one bias (i.e., either the bias on the damping or the eigenfrequency of the electric resonant circuit) if the electrical damping is overestimated, whereas the effects of the two bias types (on the electrical eigenfrequency and damping) combine with each other when the electrical damping is underestimated. Based on these results, an approximated analytical model is proposed to estimate the attenuation performance with different amounts of mistuning using a small number of numerical simulations.

To summarise, the goals of this paper are to investigate how mistuned systems (which are often encountered in real applications) behave and consequently propose an approximated model that is able to predict the behaviour of the mistuned system with the least amount of numerical simulations. To reach the above goal, the authors highlight the relationship between the attenuation and all of the problem parameters and demonstrate that some of these relations can be approximated linearly in a logarithmic scale. Moreover, the authors bring to evidence the cases where the loss of performance depends on just one mistuning type (i.e., either the bias on the damping or the eigenfrequency of the electric resonant circuit), even though mistuning occurs on both, as well as the cases where both the mistuning types have an influence. All of these observations allow for the development of the mentioned approximated model for mistuned systems, which enhances the knowledge of their behaviour. Moreover, using this new simplified model, the authors demonstrate that an initially overestimated value of R is able to decrease the loss in performance due to mistuning and explain why this phenomenon occurs. Additionally, this allows for guidelines to be provided on how to tune the shunt parameters when a mistuning is expected.

This paper is structured as follows. Section 2 discusses the model of the electromechanical system used in this paper. Section 3 highlights the linear relationship between the attenuation and the system parameters, which will be employed in Section 4 to analyse the effects of mistuning and propose an approximated model to describe the attenuation performance in the presence of mistuning. Lastly, Section 5 validates the previous results using experiments.

2. Model of the Electromechanical System

As mentioned in the previous section, the goal of this paper is to study the vibration attenuation of the controlled system in mistuned conditions. Thus, the most intuitive and used index to evaluate the attenuation performance is the ratio between the maximum of the dynamic amplification modulus in uncontrolled and controlled conditions [11, 19]. Therefore, for the performance analysis, it is necessary to derive the expression of the frequency response function of the electromechanical system and thus to introduce the model used to describe its electrodynamic behaviour.

FIGURE 1: Electric equivalent of a piezoelectric actuator in open circuit (a) and shunted with impedance Z (b).

The piezoelectric actuator is modelled here as a capacitance C_p and a strain-induced voltage generator in series (Figure 1(a)). The induced voltage is V_p , whereas the voltage between the electrodes of the piezoelectric bender is V . V is equal to V_p when the piezoelectric actuator is open-circuited and null when the actuator is short-circuited. V takes different values when an impedance Z is shunted to the electrodes of the actuator (Figure 1(b)) because a current i_s flows in the circuit. Moheimani et al. [20, 21] proved that systems controlled by piezoelectric actuators shunted with electric impedances can be modelled as a double feedback loop (Figure 2(a)). The inner loop of Figure 2(a) can be observed as a controller K , which can be expressed in the Laplace domain as follows:

$$K(s) = \frac{V}{V_p} = \frac{sC_p Z(s)}{1 + sC_p Z(s)}, \quad (1)$$

where s is the Laplace variable.

Because the shunt impedance Z considered in this study is a resistance R and an inductance L (see Section 1) in series, Z can be expressed in the Laplace domain as follows:

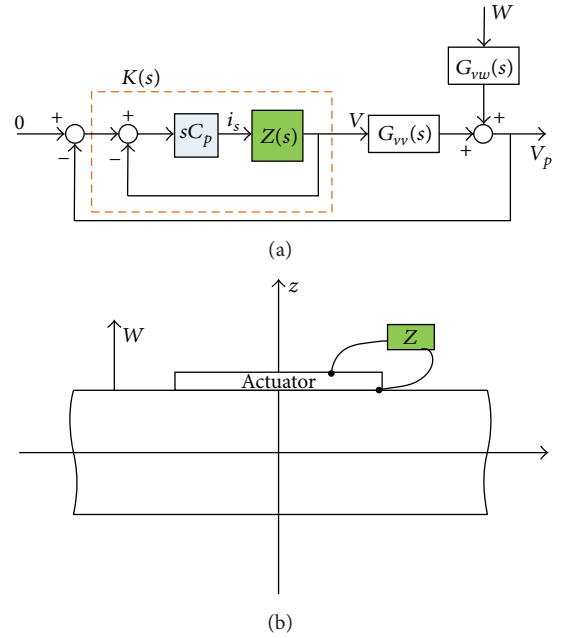
$$Z(s) = Ls + R. \quad (2)$$

The two terms G_{vv} and G_{vw} in Figure 2(a) are frequency response functions (FRFs). The former is the FRF between V and V_p , whereas the latter is between a disturbance W and V_p . These two FRFs can be expressed by the formulations in the Laplace domain [20] as follows:

$$G_{vv}(s) = \frac{V_p}{V} = \gamma \sum_{n=1}^{\infty} \frac{\psi_n \psi_n}{s^2 + 2\xi_n \omega_n s + \omega_n^2}, \quad (3)$$

$$G_{vw}(s) = \frac{V_p}{W} = \frac{\gamma}{\bar{K}} \sum_{n=1}^{\infty} \frac{\Phi_n(x_F) \psi_n}{s^2 + 2\xi_n \omega_n s + \omega_n^2},$$

where ω_n is the n th eigenfrequency of the structure with the piezoelectric bender short-circuited; ξ_n is the associated nondimensional damping ratio; Φ_n is the n th eigenmode

FIGURE 2: Feedback representation of the shunt control (a) and a structure subject to disturbance W and damped using a piezoactuator shunted to an electric impedance Z (b).

of the structure (scaled to the unit modal mass); $\Phi_n(x_F)$ represents the value of the n th mode at the forcing point x_F ; ψ_n is a term depending on the curvature of the n th mode in the area of the piezoelectric patch [20, 21], which assumes different formulations for mono- and bidimensional structures; and γ and \bar{K} are two parameters based on the geometric, mechanical, and electrical features of the structure and the piezoelectric actuator. The method for calculating ψ_n , γ , and \bar{K} for different possible configurations (e.g., monodimensional and bidimensional structures, symmetric and antisymmetric configuration of the piezoelectric actuator) can be found in [19].

The closed-loop FRF between disturbance W (Figure 2(a)) and V_p can be expressed as follows:

$$T_{vw}(s) = \frac{V_p}{W} = \frac{G_{vw}(s)}{1 + K(s)G_{vv}(s)}. \quad (4)$$

Then, the closed-loop FRF between W and the transverse displacement z of the structure (Figure 2(b)) in a given point x_M , which describes the behaviour of the system damped by the shunt, can be expressed as follows:

$$\begin{aligned} T_{zw}(s)|_{x=x_M} &= \frac{z(x_M)}{W} = G(s)|_{x=x_M} \frac{T_{vw}(s)}{G_{vv}(s)} \\ &= G(s)|_{x=x_M} \frac{G_{vw}(s)}{1 + K(s)G_{vv}(s)} \cdot \frac{1}{G_{vv}(s)}, \end{aligned} \quad (5)$$

where $G(s)$ is the FRF between V and z [19], which can be given as follows:

$$G(s, x_M) = \frac{z(x_M)}{V} = \bar{K} \sum_{n=1}^{\infty} \frac{\Phi_n(x_M) \psi_n}{s^2 + 2\xi_n \omega_n s + \omega_n^2}. \quad (6)$$

Based on the aforementioned theoretical approach (see (5)), the formulation of T_{zw} can be rearranged to achieve a compact expression. Thus, the eigenfrequency ω_p and the nondimensional damping ratio d_i of the electric network (composed by the series of C_p , L , and R) [19] can be conveniently defined as follows:

$$\omega_p = \frac{1}{\sqrt{LC_p}} \quad (7)$$

$$d_i = \frac{R}{2} \sqrt{\frac{C_p}{L}}. \quad (8)$$

By substituting (2), (7), and (8) into (1), the controller K can be expressed as a function of these two quantities as follows:

$$K = \frac{s(s + 2d_i\omega_p)}{s^2 + 2d_i\omega_p s + \omega_p^2}. \quad (9)$$

For single degree of freedom systems, the FRF T_{zw} as a function of the electrical eigenfrequency and damping can be derived by substituting (9), (6), and (3) into (5) as follows:

$$T_{zw}(s, x_M) = \Phi_n(x_M) \Phi_n(x_F) \cdot \frac{s^2 + 2d_i\omega_p s + \omega_p^2}{(s^2 + 2d_i\omega_p s + \omega_p^2)(s^2 + 2\xi_n \omega_n s + \omega_n^2) + \gamma \psi_n^2 (s + 2d_i\omega_p)}. \quad (10)$$

This formulation is valid for both beams and plates as well as for any layout of the piezoelectric actuator (e.g., single actuator, two colocated actuators) [19]. It should be noted that if the poles of this FRF are calculated considering the piezoelectric actuator in open-circuit condition ($i_s = 0$, $Z = +\infty$), then the expression of the open-circuit eigenfrequency ω_n^{oc} can be written as follows:

$$\omega_n^{\text{oc}} = \sqrt{\omega_n^2 + \gamma \psi_n^2}. \quad (11)$$

Hence, it is possible to calculate the n th effective coupling

factor k_n (defined as $\sqrt{((\omega_n^{\text{oc}})^2 - \omega_n^2)/\omega_n^2}$, e.g., [4, 11, 22]) using (11) as follows:

$$k_n = \sqrt{\frac{(\omega_n^{\text{oc}})^2 - \omega_n^2}{\omega_n^2}} = \frac{\sqrt{\gamma \psi_n^2}}{\omega_n}. \quad (12)$$

It should be noted that k_n does not depend on the type of shunt used but is a property of the system composed of the vibrating structure and the piezoelectric actuator; k_n indicates the capability of the piezoelectric actuator, coupled to a given structure, to transform mechanical energy into electrical energy.

The performance of the controlled system in optimal conditions will depend on the tuning strategy selected to fix the values of R and L . The one considered here is found as the most robust to possible mistuning in [19]. It is based on considerations on the shape of the FRF of (10). Nevertheless, it will be shown that the results and the procedure presented in this paper are valid for all tuning strategies that lead to a nearly flat shape of the FRF around the resonance frequency (see Section 3). The tuning criterion considered here fixes the values of R and L based on the procedure briefly summarised here below:

- (i) The trend of $|T_{zw}|$ is independent of the damping factor of the electrical circuit d_i at two frequency values ω_A and ω_B (see the corresponding points A and B in Figure 3(a)) (ω is the circular frequency) for undamped systems [23]. The optimal value of ω_p (ω_p^{opt}) can be found by imposing the same dynamic amplification modulus at these two frequencies. Thus, the expression for the electrical eigenfrequency can be achieved [19] as follows:

$$\omega_p^{\text{opt}} = \sqrt{\omega_n^2 + \gamma \psi_n^2} = \omega_n^{\text{oc}}. \quad (13)$$

Then, the value of L can be found by combining (7) and (13).

- (ii) The optimal value of the damping d_i (and thus of R) is found by imposing an equal dynamic amplification $|T_{zw}|$ at two different frequencies: ω_A and a second frequency given by the square root of the arithmetic mean of ω_A^2 and ω_B^2 . This frequency is found to be equal to the electrical frequency ω_p [19]. Thus, the condition used to fix the value of d_i can be given as follows:

$$|T_{zw}|_{\omega_A} = |T_{zw}|_{\omega_p}. \quad (14)$$

This condition is convenient to tune the shunt impedance because it allows a flat trend of $|T_{zw}|$ to occur in the frequency band around the resonance (Figure 3(b)). The value of the optimal electrical damping (d_i^{opt}), which results from (14) (considering $\xi_n = 0$), can be given as follows:

$$d_{i, \xi_n=0}^{\text{opt}} = \sqrt{\frac{\gamma \psi_n^2}{2(\omega_p^{\text{opt}})^2}}. \quad (15)$$

Then, the value of R can be found using (8).

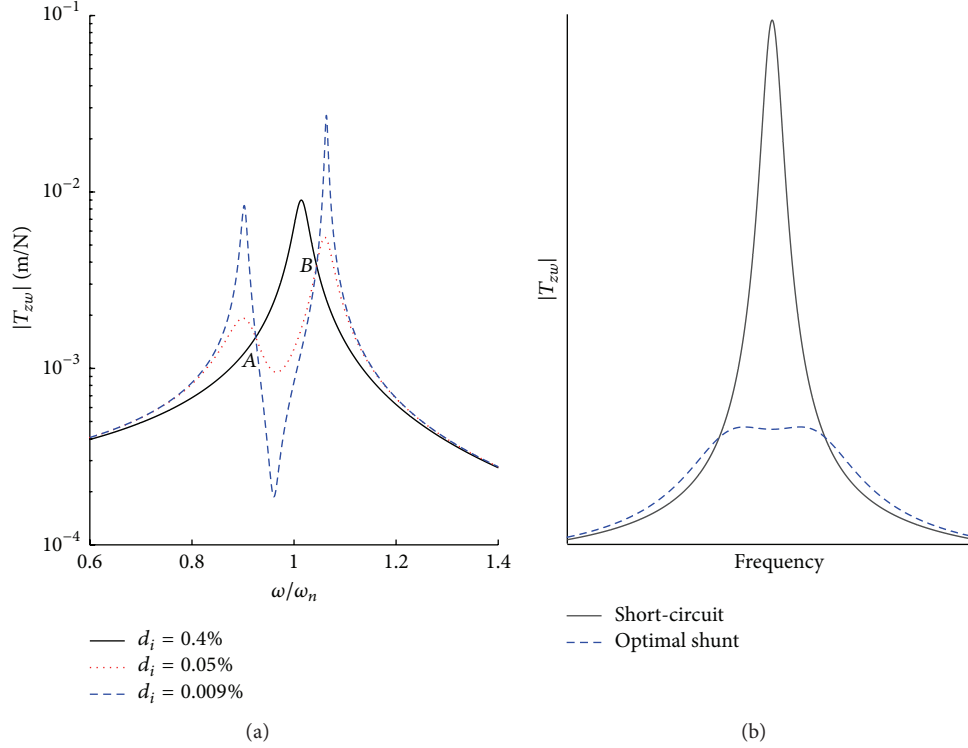


FIGURE 3: $|T_{zw}|$ for an undamped elastic structure (a) and trend of $|T_{zw}|$ for a generic system with the optimal value of d_i (b).

It should be noted that the use of (13) and (15) (which are yielded considering $\xi_n = 0$) in the case of damped systems introduces certain approximations. Nevertheless, these approximations can be assumed as negligible. In fact, according to [19], the maximum difference between the attenuation provided by (13) and (15) and the actual attenuation is less than 0.5 dB for most practical applications.

Therefore, the use of (13) and (15) can be considered reliable even with damped systems.

The behaviour of mistuned systems will be studied in the following sections. Because there are no closed formulas to describe the vibration attenuation in mistuned conditions, the maximum of $|T_{zw}|$ must be found numerically using (10). The number of variables in this equation is high: five variables, that is, ω_n , ω_p , ξ_n , d_i , and $\gamma\psi_n^2$. Hence, several simulations must be performed if a detailed description of the behaviour of different possible mistuned systems is desired (several values of ω_p , d_i , and $\gamma\psi_n^2$ for each mode considered, defined by ω_n and ξ_n). Therefore, it is essential to decrease the number of variables to be considered in the simulations to reduce the effort of this numerical study.

Therefore, Section 2.1 presents a normalisation of the system model to reduce the number of variables involved in the problem.

2.1. Normalisation of the Model. First, all of the possible values of ω_p and d_i can be defined as a function of the optimal ones ω_p^{opt} and d_i^{opt} as follows:

$$\begin{aligned} d_i &= l d_i^{\text{opt}} \\ \omega_p &= v \omega_p^{\text{opt}}, \end{aligned} \quad (16)$$

where l and v are the amount of mistuning on the electrical damping and eigenfrequency, respectively ($l = 1$ and $v = 1$ in the case of no mistuning).

Then, (10) is considered: both the numerator and the denominator are divided by ω_n^4 , and s is expressed as $j\omega$ (j is the imaginary unit). After a few mathematical rearrangements (see Appendix A), a new expression of T_{zw} in the frequency domain can be obtained. This new expression uses (13), (15), and (16) to express the electrical parameters as a function of their optimal values as follows:

$$T_{zw}(x_M) = \frac{\Phi_n(x_M) \Phi_n(x_F)}{\omega_n^2} \frac{-\varphi^2 + \sqrt{2} j \varphi k_n l v + v^2 (1 + k_n^2)}{(-\varphi^2 + \sqrt{2} j \varphi k_n l v + v^2 (1 + k_n^2)) (-\varphi^2 + 2 j \xi_n \varphi + 1) + j \varphi k_n^2 (j \varphi + \sqrt{2} k_n l v)}, \quad (17)$$

where $\varphi = \omega/\omega_n$ is the nondimensional frequency.

The advantages provided by the use of (17) will be underlined in Section 3.

3. Attenuation Performance of the Optimally Tuned Shunt

As previously mentioned, the performance of the shunt in terms of vibration attenuation can be expressed as the ratio between the maximum amplitude of the uncontrolled system FRF and the maximum amplitude of the controlled system FRF (i.e., $\max(|T_{zw}|)$; see (17)).

The FRF of the uncontrolled structure (i.e., with the piezoelectric patch in short-circuit) can be defined as follows [24]:

$$G_{zw} = \frac{\Phi_n(x_M) \Phi_n(x_F)}{(s^2 + 2\xi_n \omega_n s + \omega_n^2)}. \quad (18)$$

Therefore, the attenuation performance, denoted here as att, can be expressed as follows:

$$\begin{aligned} \text{att} &= \frac{\max(|G_{zw}|)}{\max(|T_{zw}|)} \\ &= \frac{|\Phi_n(x_M) \Phi_n(x_F)| / (2\xi_n \omega_n^2 \sqrt{1 - \xi_n^2})}{\max(|T_{zw}|)}, \end{aligned} \quad (19)$$

where, according to [11], $\max(|G_{zw}|) = |\Phi_n(x_M) \Phi_n(x_F)| / (2\xi_n \omega_n^2 \sqrt{1 - \xi_n^2})$.

The analytical expression of $\max(|T_{zw}|)$ is rather complex; thus, it is convenient to define the index attk instead of att for the case of perfect tuning ($\omega_p = \omega_p^{\text{opt}}$) as follows:

$$\text{attk} = \frac{\max(|G_{zw}|)}{|T_{zw}|_{\omega_p}} = \sqrt{\left(\frac{\max(|G_{zw}|)}{|T_{zw}|_{\omega_p}} \right)^2}. \quad (20)$$

The difference between att and attk is that, in the former case, the maximum amplitude of the controlled system FRF is considered ($\max(|T_{zw}|)$), whereas, in the latter case, the value of the system response $|T_{zw}|$ at ω_p is considered ($|T_{zw}|_{\omega_p}$). As previously mentioned, the use of attk simplifies the notation and can be used to accurately approximate the value of att. In fact, in the case of perfect tuning, $\max(|T_{zw}|) \approx |T_{zw}|_{\omega_p}$ because of the flat shape of $|T_{zw}|$ around ω_n ($\omega_p = \omega_p^{\text{opt}} = \omega_n^{\text{oc}}$ is in the frequency range where the controlled FRF has a flat shape; see Figure 3(b)) [19]. Hence, $\text{attk} \approx \text{att}$.

Based on (17), attk can be expressed as follows (see Appendix B):

$$\text{attk} = (k_n + 2\sqrt{2}\xi_n) \sqrt{\frac{(1 + k_n^2)}{8\xi_n^2(1 - \xi_n^2)}}. \quad (21)$$

Thus, the attenuation in decibels (A_{dB}) can be expressed as follows:

$$\begin{aligned} A_{\text{dB}} &= 20 \log_{10} \text{attk} \\ &= 20 \log_{10} \left[(k_n + 2\sqrt{2}\xi_n) \sqrt{\frac{(1 + k_n^2)}{8\xi_n^2(1 - \xi_n^2)}} \right]. \end{aligned} \quad (22)$$

Equation (22) only depends on two system parameters, ξ_n and k_n . Therefore, the properties of tuned systems can be studied considering only these two parameters. A similar approach is used for mistuned shunt systems (see Section 4). Hence, the normalisation proposed in Section 2.1 allows the model to be simplified, thus avoiding one of the variables (i.e., now only ξ_n and k_n are considered, whereas it would have been necessary to consider the three parameters ξ_n , ω_n , and $\gamma\psi_n^2$ without the normalisation).

It is easy to see that (22) links the achievable attenuation to the problem parameters (i.e., k_n and ξ_n). Since ξ_n is fixed, (22) allows the attenuation to be predicted as a function of the value of k_n , thus suggesting which value should be used to obtain the desired attenuation performance. In fact, it can be recalled that k_n is a function of $\gamma\psi_n^2$ (see (12)), and it can thus be modified by changing the geometrical, mechanical, and electrical characteristics of the actuator as well as its position [19]. Furthermore, k_n can be also modified by connecting several piezoelectric actuators in series/parallel [25, 26] and by using a negative capacitance [22, 27]. Therefore, the model used here is of general validity.

Equation (22) can be rearranged as follows:

$$\begin{aligned} A_{\text{dB}} &= 20 \log_{10} (k_n + 2\sqrt{2}\xi_n) + 10 \log_{10} (1 + k_n^2) \\ &\quad - 10 \log_{10} (8\xi_n^2 (1 - \xi_n^2)). \end{aligned} \quad (23)$$

Now, three different situations in terms of the k_n value can be considered:

- (1) k_n of the same order of magnitude of ξ_n (the maximum value of ξ_n considered here is 1%): this is the case of extremely stiff and damped structures and/or badly positioned actuators. In this case, (23) can be approximated as follows:

$$\begin{aligned} A_{\text{dB}} &= 20 \log_{10} (k_n + 2\sqrt{2}\xi_n) \\ &\quad - 10 \log_{10} (8\xi_n^2 (1 - \xi_n^2)). \end{aligned} \quad (24)$$

In fact, k_n is so low that $10 \log_{10}(1 + k_n^2)$ can be approximated as $10 \log_{10}(1) = 0$.

- (2) $2\sqrt{2}\xi_n \ll k_n \ll 1$: this is the typical case [19]. It is possible to make the following simplifications: $(k_n + 2\sqrt{2}\xi_n) \approx k_n$ and $1 + k_n^2 \approx 1$. Thus, for most engineering applications, (23) can be approximated as follows:

$$\begin{aligned} A_{\text{dB}} &= 20 \log_{10} (k_n) - 10 \log_{10} (8\xi_n^2 (1 - \xi_n^2)) \\ &= m_0 \log_{10} (k_n) + q_0, \end{aligned} \quad (25)$$

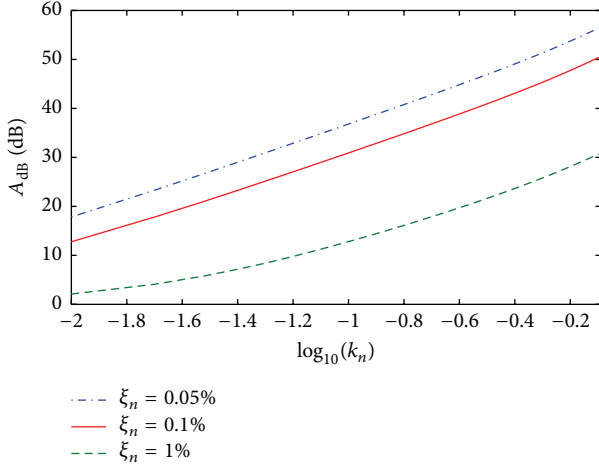


FIGURE 4: Relationship between A_{dB} and $\log_{10}k_n$ for different systems (i.e., different ξ_n values).

where $m_0 = 20$ and $q_0 = -10 \log_{10}(8\xi_n^2(1 - \xi_n^2))$. Equation (25) demonstrates a linear relationship between A_{dB} and $\log_{10}(k_n)$.

- (3) k_n close to 1: this is the case where extremely flexible structures and/or the addition of a negative capacitance are considered. Equation (23) can be approximated as follows:

$$A_{dB} = 20 \log_{10}(k_n) + 10 \log_{10}(1 + k_n^2) - 10 \log_{10}(8\xi_n^2(1 - \xi_n^2)). \quad (26)$$

Equation (26) demonstrates that, in this case, the relationship between A_{dB} and $\log_{10}(k_n)$ is no longer linear. Nevertheless, in most practical applications, a linear relation can still be used. In fact, the term $10 \log_{10}(1 + k_n^2)$ has a negligible contribution up to approximately $k_n = 0.6$. Its contribution becomes more evident, albeit small, only for higher k_n values (at $k_n = 0.8$, its contribution is approximately 2 dB). Hence, the term $10 \log_{10}(1 + k_n^2)$ can be neglected, and the attenuation A_{dB} as a function of $\log_{10}(k_n)$ can be approximated by the linear relation as follows:

$$A_{dB} \approx m_0 \log_{10}(k_n) + q_0, \quad (27)$$

where $m_0 = 20$ and $q_0 = -10 \log_{10}(8\xi_n^2(1 - \xi_n^2))$.

Figure 4 shows the linear relationship between A_{dB} and $\log_{10}(k_n)$ for different systems selected as an example. Additionally, the figure indicates that the area in which linearity is lost (corresponding to the case in which k_n is of the same order of magnitude of ξ_n , point 1 of the previous numbered list; see the left part of the green dashed line in the figure) corresponds to cases where A_{dB} is extremely low (approximately 5 dB or lower).

The linear relationship demonstrated thus far (see (25) and (27)) can lead to the following notations:

$$\begin{aligned} \log_{10} \text{attk} &\approx \log_{10}(k_n) + q_0/20 \implies \\ \text{attk} &\approx k_n (10)^{q_0/20} \implies \\ k_n &\approx \frac{\text{attk}}{\sqrt[20]{(10)^{q_0}}}. \end{aligned} \quad (28)$$

The central expression of (28) indicates that if k_n is incremented from value $f1$ to value $f2$ where $f2/f1 = g$, then the value of attk increases by a factor g , which signifies that consistent increases in attk can be achieved with moderate increases (in terms of absolute value) of k_n when k_n is low. Conversely, high increases in k_n (in terms of absolute value) produce a low increment of attk when k_n is high. Hence, an asymptotic behaviour of the attenuation performance is demonstrated.

The next section considers mistuned shunt systems.

4. Robustness of the Shunt Damping: Performance in Mistuned Conditions

Section 1 explained that, in most cases, the shunted system operates in mistuned conditions because of the uncertainty in the estimated values of the system parameters (especially electrical quantities) or changes in either the mechanical system or the electrical network. This often leads to a control performance considerably lower than that expected; thus, a robustness analysis would be useful for understanding the behaviour of the controlled system and determining a method to limit this performance reduction. Therefore, the analysis of robustness attempts to investigate the worsening of performance due to mistuning and provides formulations for its prediction.

Based on (10), (13), and (15), the mistuning can be due to errors in the estimated values of ξ_n , ω_n , and $\gamma\psi_n^2$ as well as the values of R and L . It is easy to see that all of the different reasons for mistuning can be expressed as errors in the optimal values of ω_p and d_i . Therefore, in this study, the actual values of ω_p and d_i are expressed as changes from their optimal values. Therefore, the mistuning can be easily considered in (17) by fixing l and v at values other than 1 (values lower than 1 indicate underestimation, whereas those higher than 1 indicate overestimation; see (16)). The FRF of the mistuned shunt system can thus be described by (17), and the related vibration attenuation performance is measured by the index att of (19). The attenuation in these mistuned conditions can be expressed in decibels as A_{dB}^* (see Appendix C for certain clarifications for the symbols used) as follows:

$$A_{dB}^* = 20 \log_{10} \text{att}|_{l \neq 1, v \neq 1}. \quad (29)$$

The value of A_{dB}^* can be found numerically to study the attenuation in different mistuned conditions. Thus, the values of $|T_{zw}|$ as a function of frequency must be calculated for a given situation (i.e., fixing the values of k_n , ξ_n , l , and v in (17));

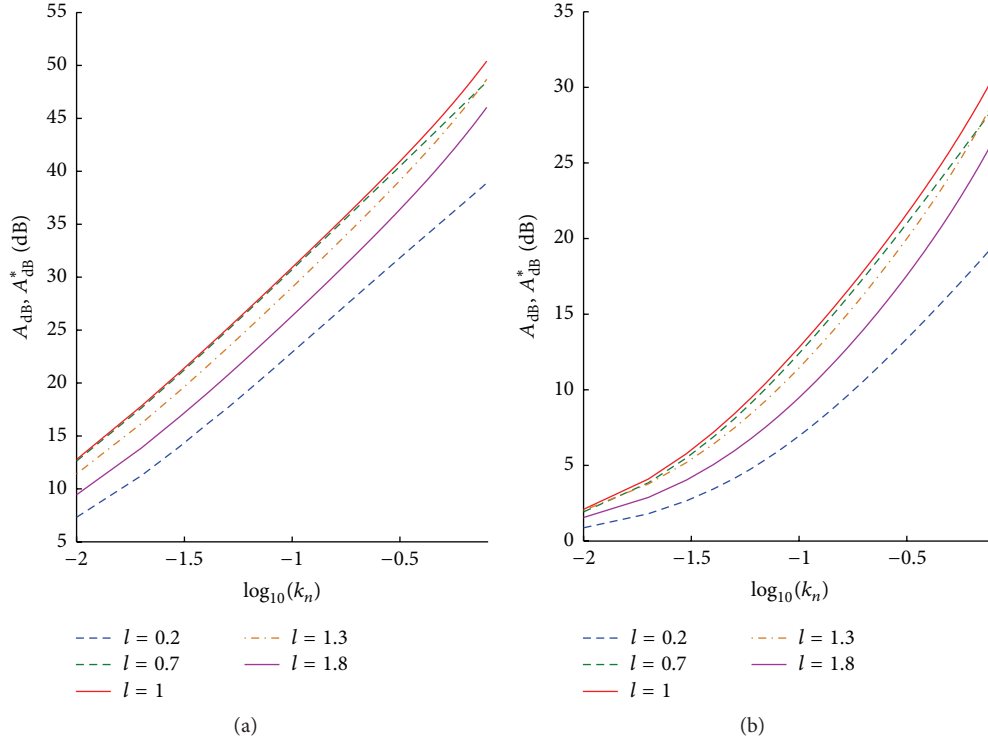


FIGURE 5: Relationship between A_{dB} or A_{dB}^* and $\log_{10}k_n$ for different ξ_n values: 0.1% (a) and 1% (b).

and then the maximum of $|T_{zw}|$ can be found numerically. Lastly, att can be calculated using (19).

Nevertheless, the number of simulations needed is often high. In fact, several different values of l and v need to be tested to consider various different possible mistuning situations. Furthermore, numerous values of k_n must be considered; in fact, it is useful to understand if an increased k_n value allows the desired attenuation performance to be achieved, even in mistuned conditions. Furthermore, according to [19] and as it will be shown in Sections 4.1 and 4.3, it is often good practice to increase the initial value of the resistance with respect to its optimal value to improve the attenuation in mistuned conditions; hence, l values significantly higher than 1 need to be tested, thus leading to a large number of l values to be taken into account. Therefore, the number of required simulations can increase substantially. For example, when N_k values of k_n , N_v biased values of ω_p , and N_l biased values of d_i have to be considered to fully study the given problem, the entire number of simulations N_s that must be performed to evaluate the attenuation in all of the possible cases results in $N_p N_v N_l$ (e.g., if N_s is equal to 10^6 , the amount of computational time to perform all the simulations becomes longer than 10 hours on a normal laptop).

Therefore, the goal of the next sections is to propose a model to describe the attenuation in mistuned conditions A_{dB}^* . Sections 4.1 and 4.2 analyse the effects of errors on d_i and ω_p , respectively. Then, Section 4.3 addresses situations where both errors (i.e., on d_i and ω_p) occur together.

4.1. Mistuning on the Electrical Damping. This section only considers mistuning on d_i . Figure 5 depicts the curves relating $\log_{10}k_n$ and A_{dB}^* for different systems and different errors on d_i (i.e., different l values and $v = 1$). These curves were found numerically using (29), (19), and (17) (see Section 4). In fact, a general analytical solution is not possible because the equations are of a high order, and thus the solution cannot be expressed through closed analytical formulas and must be calculated numerically case by case. It should be noted that the use of the normalised model of (17) still allows a decrease in the number of variables to be considered: four variables in the normalised model (i.e., ξ_n , k_n , l , and v ; see (17)) versus five variables in the nonnormalised model (i.e., ξ_n , ω_n , $\gamma\psi_n^2$, l , and v ; see (10)).

The primary property of the plots in Figure 5 is that the main effect of mistuning is to shift the curves with respect to the case of $l = 1$; however, all of these curves can still be approximated as straight lines. In fact, the lines associated with $\xi_n = 1\%$ lose their linear trend in correspondence of low values of A_{dB}^* (i.e., for approximately $A_{dB}^* < 4$ dB); nevertheless, these curves can still be considered piecewise linear. In fact, if an interval for k_n equal to one order of magnitude is considered (it is hard to change k_n for one order of magnitude [25] or more, even using negative capacitances [27]), the curves can be well approximated as lines.

The lines in Figure 5 prove that the effects of the change in the intercept are significantly higher than the effects of the change in the angular coefficient (i.e., the lines primarily shift

due to a nonunitary value of l , parallel lines). In other words, the sensitivity of the attenuation performance on the value of the coupling coefficient tends to be independent of the level of mistuning. Hence, for a given system, the improvement in the attenuation achieved by increasing the value of the coupling coefficient is the same whether the shunt is tuned or not.

The relationship between $\log_{10} k_n$ and A_{dB}^* for a given system can be expressed as follows:

$$A_{dB}^* \approx q_l^*(l) + m_l^*(l) \log_{10}(k_n) = \widetilde{A}_{dB}^*, \quad (30)$$

where \widetilde{A}_{dB}^* is the estimate of A_{dB}^* and q_l^* and m_l^* are the intercept and the angular coefficient of the line, respectively, which are both a function of l , as evidenced in (30) (see also Appendix C for certain clarifications of the symbols used). It should be noted that m_l^* is indicated as dependent on l , even if this dependency is slight (see above), for the sake of completeness.

If the trend of A_{dB}^* as a function of l is depicted for different values of k_n , a few further interesting facts can be noted (see Figure 6). All of the curves of this new figure demonstrate nearly the same features: the attenuation loss is limited for $l > 1$; furthermore, in this range of l , the rate of the loss is nearly constant. Conversely, for $l < 1$, the rate becomes increasingly larger by decreasing the value l . It is possible to approximatively state that, for $l < 0.5$, the rate of the attenuation loss increases. This result is a first sign of the benefits provided by the use of overestimated electrical damping d_i values (and thus overestimated R values). In fact, even if an overestimated d_i value causes a worsening in the attenuation performance if compared to the tuned situation, this worsening is not that high (see Figure 6); overall, if a mistuning occurs in situations where the starting d_i value is overestimated deliberately, the attenuation loss due to the mistuning is low. The use of initially overestimated d_i values will be considered again in Section 4.3.

A further interesting point is that the trend of A_{dB}^* as a function of l can be modelled as the combination of two fourth-order polynomials, one for $l < 1$ and another for $l > 1$, regardless of the system considered (see Figure 6).

The calculation for each of these fourth-order polynomials requires the knowledge of A_{dB}^* for five values of l . Therefore, for the given values of ξ_n and k_n , it is sufficient to calculate ten points (l, A_{dB}^*) using (29), (19), and (17) (i.e., five for $l < 1$ and five for $l > 1$) to determine the trend of A_{dB}^* for an extended range of l values (e.g., $l = 0.01 \div 2$, as indicated in Figure 6).

Based on (30) and Figure 6, the following procedure can be applied when the behaviour of a mistuned shunt system in a range of k_n values between k_A and k_B is studied.

- (i) Calculate five pairs (l, A_{dB}^*) using (29), (19), and (17) for $l < 1$ and $k_n = k_A$ and determine the interpolating polynomial. Then, repeat the same procedure for $l > 1$. It is now possible to know the value of A_{dB}^* for any value of l at $k_n = k_A$.
- (ii) Calculate five pairs (l, A_{dB}^*) using (29), (19), and (17) for $l < 1$ and $k_n = k_B$ and determine the interpolating polynomial. Then, repeat the same procedure for

TABLE 1: Bounds for the Monte Carlo simulations for $l \neq 1$ and $\nu = 1$.

	ξ_n	k_A	k_n	l_x
Min	0.05%	0.001	k_A	0.5
Max	1%	0.35	k_B	1.5

$l > 1$. It is now possible to know the value of A_{dB}^* for any value of l at $k_n = k_B$.

- (iii) The value of \widetilde{A}_{dB}^* for a generic value k_n between k_A and k_B and a generic value $l = l_x$ can be computed using (30), where

$$m_l^* = \frac{A_{dB}^*|_{l=l_x, k_n=k_B} - A_{dB}^*|_{l=l_x, k_n=k_A}}{\log_{10} k_B - \log_{10} k_A} \quad (31)$$

$$q_l^* = A_{dB}^*|_{l=l_x, k_n=k_B} - m_l^* \log_{10} k_B.$$

Therefore, it is possible to estimate the attenuation for any value of l and k_n (between k_A and k_B) with only twenty simulations.

The accuracy of this procedure was verified using a Monte Carlo test with more than 10^5 simulations comparing the attenuation values \widetilde{A}_{dB}^* achieved using this procedure and the A_{dB}^* values obtained using (29), (19), and (17). The difference Δ is defined as $\widetilde{A}_{dB}^* - A_{dB}^*$. For each simulation, the values of ξ_n , k_A , k_n , and l_x were extracted from uniform distributions. The bounds of the distributions are presented in Table 1 and were chosen in order to take into account the most part of the practical applications. Table 2 lists the results, hence proving the reliability of the proposed procedure. It should be noted that $k_B = \sqrt{3}k_A$ was used in the simulations. This corresponds to a change of $\gamma\psi_n^2$ within an interval equal to three times the starting value, which is quite a broad interval. If a wider interval of k_n must be considered and the same accuracy is desired, it is possible to analyse the system in two different ranges. For example, if $k_B = 3k_A$, the entire range can be split as follows: $k_A \div k_h$ and $k_h \div k_B$ with $k_h = \sqrt{3}k_A$. This requires using thirty simulations instead of twenty to describe the behaviour of the mistuned shunt system.

4.2. Mistuning on the Electrical Eigenfrequency. Figure 7 illustrates the same information as Figure 5 but for mistuning on ω_p (i.e., $\nu \neq 1$ and $l = 1$). It should be noted that the resulting curves tend to increase their curvature. Nevertheless, the linearity is lost only when A_{dB}^* becomes lower than approximately 4 or 5 dB. However, the curves can be still piecewise approximated as lines with enough accuracy for wide ranges of $\log_{10}(k_n)$. The effect of a nonunitary value of ν is to highly increase the angular coefficient of the lines. Consequently, increasing the value of k_n is even more effective in enhancing the attenuation in the case of mistuning on ω_p than in the case of tuned systems.

The curves of Figure 7 can be expressed as follows:

$$A_{dB}^* \approx q_\nu^*(\nu) + m_\nu^*(\nu) \log_{10}(k_n) = \widetilde{A}_{dB}^*, \quad (32)$$

where \widetilde{A}_{dB}^* is again the estimate of A_{dB}^* and q_ν^* and m_ν^* are the intercept and the angular coefficient of the lines, respectively,

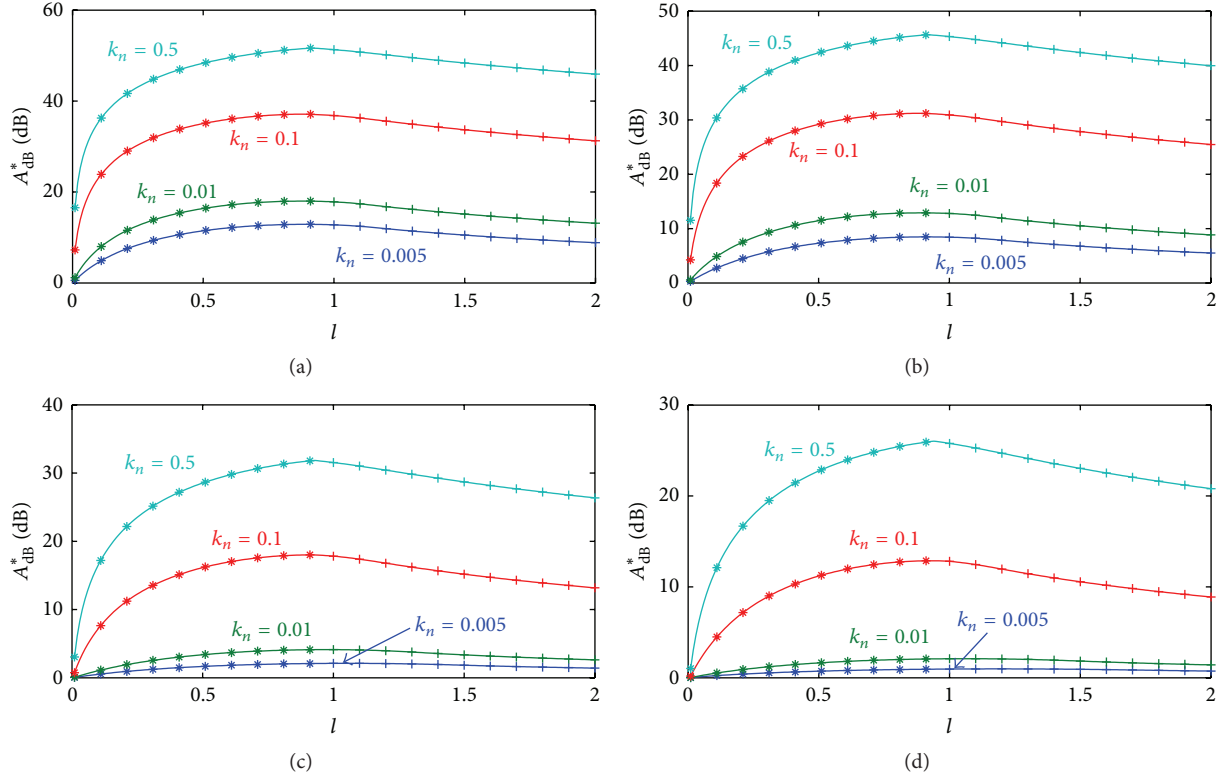


FIGURE 6: Relationship between A_{dB}^* and l for different k_n values and different ξ_n values: 0.05% (a), 0.1% (b), 0.5% (c), and 1% (d). The + are the points related to the case of $l > 1$ calculated using (29), (19), and (17), which are then interpolated by fourth-order polynomials (solid curves). The * are the points related to the case of $l < 1$ calculated using (29), (19), and (17), which are then interpolated by fourth-order polynomials (solid curves).

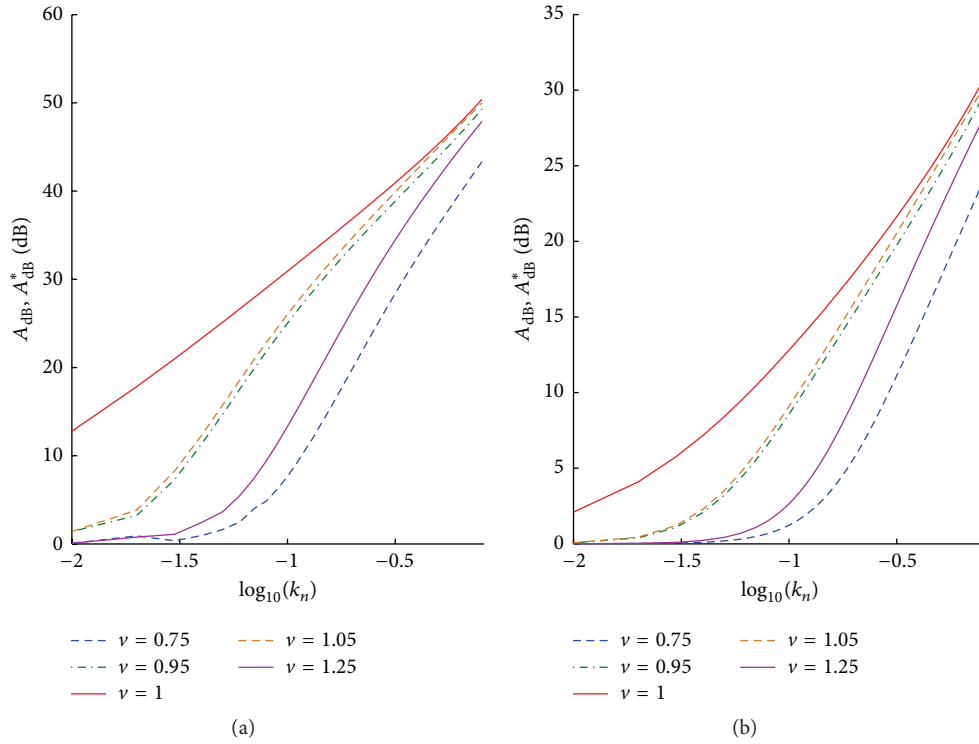


FIGURE 7: Relationship between A_{dB} or A_{dB}^* and $\log_{10}k_n$ for different ξ_n values: 0.1% (a) and 1% (b).

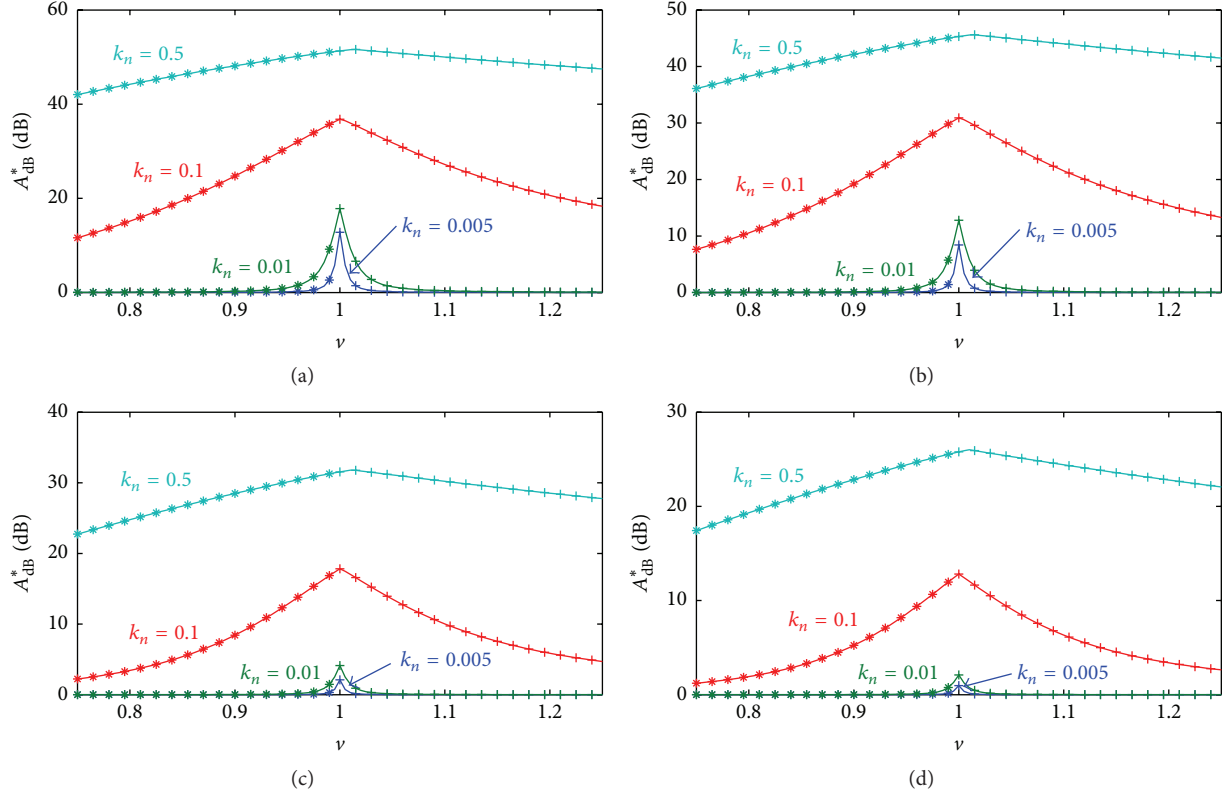


FIGURE 8: Relationship between A_{dB}^* and ν for different k_n values and different ξ_n values: 0.05% (a), 0.1% (b), 0.5% (c), and 1% (d). The + are the points related to the case of $\nu > 1$ calculated using (29), (19), and (17), which are then interpolated by fourth-order polynomials (solid curves). The * are the points related to the case of $\nu < 1$ calculated again using (29), (19), and (17), which are then interpolated by fourth-order polynomials (solid curves).

TABLE 2: Results of the Monte Carlo simulations for the case $l \neq 1$ and $\nu = 1$.

Mean value of Δ [dB]	Standard deviation of Δ [dB]	Minimum value of Δ [dB]	Maximum value of Δ [dB]
-0.05	0.03	-0.21	0.02

TABLE 3: Bounds for the Monte Carlo simulations for $\nu \neq 1$ and $l = 1$.

	ξ_n	k_A	k_n	ν_x
Min	0.05%	0.001	k_A	0.9
Max	1%	0.35	k_B	1.1

which are both functions of ν (see Appendix C for certain clarifications of the symbols used).

If the trend of A_{dB}^* is shown as a function of ν for different values of k_n , a few further interesting facts can be noted (see Figure 8). The same percentage value of mistuning leads to a different decrease in the performance if it is related to an overestimation or underestimation of the optimal value of the electrical eigenfrequency. In fact, values of ν lower than 1 cause higher losses in the attenuation than values greater than 1 (e.g., compare the curves at $\nu = 0.75$ and $\nu = 1.25$).

A further interesting point is that the trend of A_{dB}^* as a function of ν can be modelled as a fourth-order polynomial for both $\nu < 1$ and $\nu > 1$, regardless of the system considered (see Figure 8). Therefore, if the study of the behaviour of a

mistuned shunt system in a range of k_n values between k_A and k_B is considered, the same procedure discussed in Section 4.1 (see the list in Section 4.1) can be applied, and it is possible to estimate the attenuation for any value of ν and k_n (between k_A and k_B) with only twenty simulations. Indeed, it is possible to write

$$m_v^* = \frac{A_{dB}^*|_{\nu=\nu_x, k_n=k_B} - A_{dB}^*|_{\nu=\nu_x, k_n=k_A}}{\log_{10} k_B - \log_{10} k_A} \quad (33)$$

$$q_v^* = A_{dB}^*|_{\nu=\nu_x, k_n=k_B} - m_v^* \log_{10} k_B.$$

Again, a Monte Carlo test was performed with more than 10^5 simulations comparing the attenuation values \tilde{A}_{dB}^* achieved using this procedure and the A_{dB}^* values obtained using (29), (19), and (17). For each simulation, the values of ξ_n , k_A , k_n , and ν_x were extracted from uniform distributions (see Table 3 for the bounds of the distributions, which were chosen in order to take into account the most part of the practical applications), and k_B was fixed to $\sqrt{3}k_A$, as performed in Section 4.1. Table 4 lists the results, thus proving the reliability of the proposed

TABLE 4: Results of the Monte Carlo simulations for $\nu \neq 1$ and $l = 1$.

Mean value of Δ [dB]	Standard deviation of Δ [dB]	Minimum value of Δ [dB]	Maximum value of Δ [dB]
-0.02	0.07	-0.50	0.19

procedure. It should be noted that the range of ν_x is narrower than that used in Section 4.1 for l_x . The reason is that the optimal value of d_i depends on more variables than the optimal value of ω_p , thus leading to more uncertainty (see (15) and (13)).

4.3. Mistuning on Both the Electrical Eigenfrequency and the Damping Ratio. Sections 4.1 and 4.2 have treated cases in which the mistuning is related to either d_i or ω_p . Nevertheless, in actual applications, both of the mistuning effects are expected to appear together.

In these general mistuned situations (i.e., $l \neq 1$ and $\nu \neq 1$), the performance of the shunt system demonstrates a different behaviour for values of l higher or lower than 1. This result can be clearly evidenced using the double-logarithmic representation already utilised in Figures 5 and 7. In fact, Figure 9 depicts the different behaviour for certain systems selected as examples:

- (i) For systems where $l > 1$, the loss of attenuation is essentially due to the mistuning causing the highest loss (see the subplots on the right side).
- (ii) For systems where $l < 1$, the loss of attenuation can be derived as the sum of the losses caused by both the mistuning types (see the subplots on the left side).

Now, for a given system (i.e., fixed values of ξ_n and k_n) and fixed values of l and ν (named l_x and ν_x), the following indexes can be defined:

$$\begin{aligned} y_t &= A_{dB} - A_{dB}^*|_{l=l_x, \nu=\nu_x} \\ y_o &= A_{dB} - A_{dB}^*|_{l=1, \nu=\nu_x} \\ y_d &= A_{dB} - A_{dB}^*|_{l=l_x, \nu=1} \end{aligned} \quad (34)$$

where y_t expresses the loss of attenuation when a mistuning occurs on the values of both ω_p and d_i ; y_o expresses the loss of attenuation when a mistuning occurs only on the value of ω_p ; and y_d expresses the loss of attenuation when a mistuning occurs only on the value of d_i .

Based on the abovementioned considerations related to Figure 9 (see the list above in this section), \tilde{y}_t (the estimate of y_t) can be calculated as follows:

$$\tilde{y}_t = \begin{cases} \max(y_o, y_d), & \forall l_x > 1 \\ y_o + y_d, & \forall l_x < 1. \end{cases} \quad (35)$$

According to (35), \tilde{A}_{dB}^* (i.e., the estimate of A_{dB}^*) can be defined as follows:

$$\begin{aligned} \tilde{A}_{dB}^*|_{l=l_x, \nu=\nu_x} &= \begin{cases} \min(A_{dB}^*|_{l=1, \nu=\nu_x}, A_{dB}^*|_{l=l_x, \nu=1}), & \forall l_x > 1 \\ A_{dB}^*|_{l=1, \nu=\nu_x} + A_{dB}^*|_{l=l_x, \nu=1} - A_{dB}, & \forall l_x < 1. \end{cases} \end{aligned} \quad (36)$$

$A_{dB}^*|_{l=1, \nu=\nu_x}$ and $A_{dB}^*|_{l=l_x, \nu=1}$ can be estimated using (32) and (30), respectively. A_{dB} is given in (22). Hence, (36) allows the attenuation to be estimated for any values of l , ν , and k_n (between k_A and k_B) using only forty-two simulations based on (17), (19), and (29). In fact, (36) allows the behaviour of the mistuned shunt systems to be analysed with a bias on both ω_p and d_i by considering the mistuning on ω_p and d_i separately. Twenty simulations are needed to study the behaviour of the system with $l \neq 1$ and $\nu = 1$ (see Section 4.1), twenty for the case $l = 1$ and $\nu \neq 1$ (see Section 4.2), and two for the case $l = 1$ and $\nu = 1$ (i.e., one with $k_n = k_A$ and the other with $k_n = k_B$); furthermore, the A_{dB} (i.e., the case with $l = 1$ and $\nu = 1$) values for $k_n = k_A$ and $k_n = k_B$ can also be calculated using (22). In the case of N_s (total number of cases to be considered) equal to 10^6 , the amount of time required to perform all the simulations decreases from more than 10 hours (see the end of Section 4) to a few minutes or less (approximately 30 s). Hence, the study of the behaviour of the system in mistuned conditions becomes very fast, thus allowing to quickly analyse the effects of different R values on the attenuation performance and to choose the best one for the given application.

Therefore, by rearranging (36) using (30) and (32), the final form of the approximated model able to describe the behaviour of the mistuned shunt systems can be achieved as follows:

$$\tilde{A}_{dB}^*|_{l=l_x, \nu=\nu_x, k_n} = \begin{cases} \min(q_v^*(\nu_x) + m_v^*(\nu_x) \log_{10}(k_n), q_l^*(l_x) + m_l^*(l_x) \log_{10}(k_n)), & \forall l_x > 1 \\ q_v^*(\nu_x) + m_v^*(\nu_x) \log_{10}(k_n) + q_l^*(l_x) + m_l^*(l_x) \log_{10}(k_n) - A_{dB}|_{k_n}, & \forall l_x < 1, \end{cases} \quad (37)$$

where m_l^* , q_l^* , m_v^* , and q_v^* are defined in (31) and (33).

The accuracy of this model was tested again using a Monte Carlo simulation with more than 10^6 cases, thus comparing

the attenuation values \tilde{A}_{dB}^* achieved using this procedure and the A_{dB}^* values obtained using (29), (19), and (17). For each simulation, the values of ξ_n , k_A , k_n , ν_x , and l_x were extracted

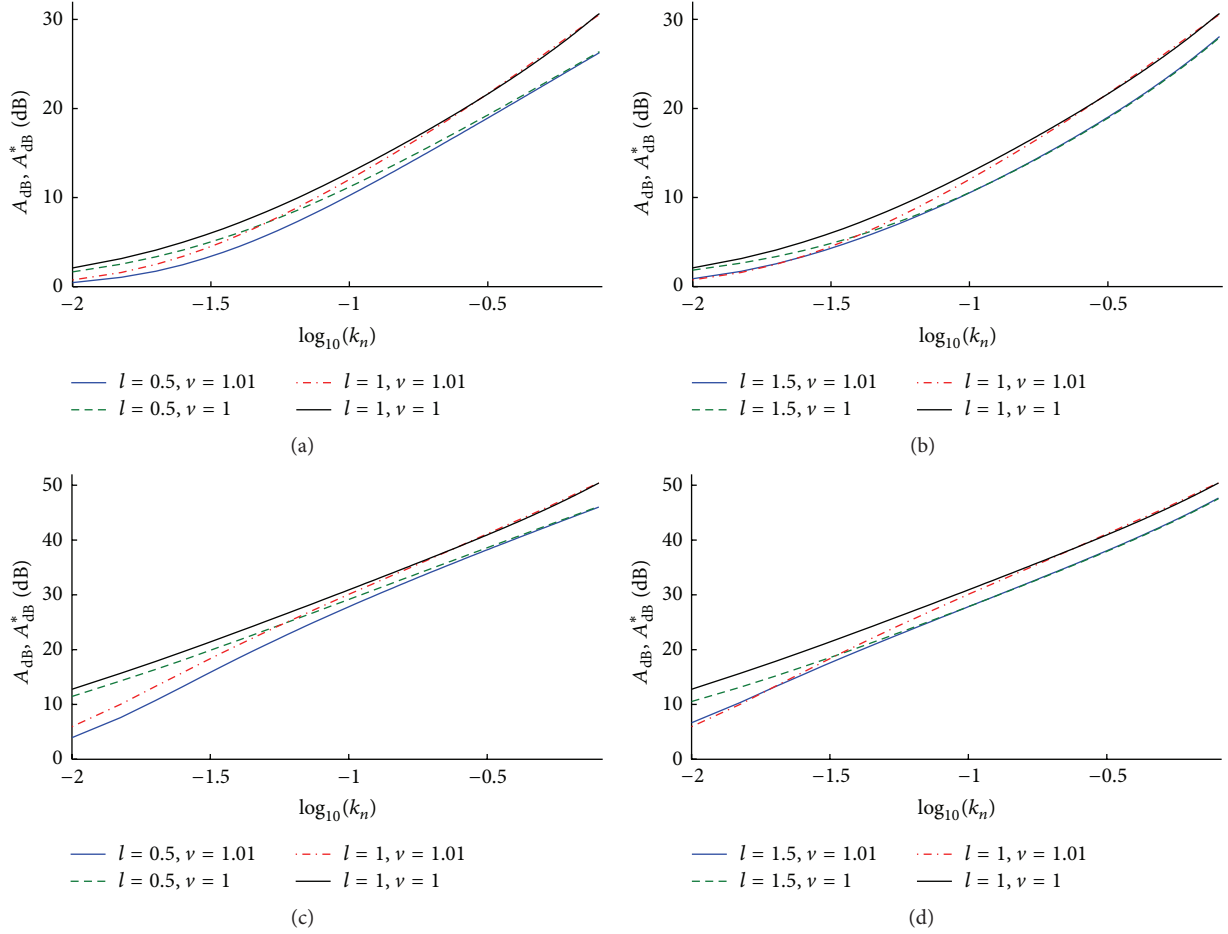


FIGURE 9: Relationship between A_{dB} or A_{dB}^* and $\log_{10}k_n$ for different ξ_n values, l , and v : $\xi_n = 1\%$, $l = 0.5$, and $v = 1.01$ (a), $\xi_n = 1\%$, $l = 1.5$, and $v = 1.01$ (b), $\xi_n = 0.1\%$, $l = 0.5$, and $v = 1.01$ (c), and $\xi_n = 0.1\%$, $l = 1.5$, and $v = 1.01$ (d).

from uniform distributions (see Table 5; $k_B = \sqrt{3}k_A$). Table 6 presents the results (which have a Gaussian distribution), thus proving the reliability of the proposed procedure.

Certain benefits provided by the use of initially overestimated d_i values have already been discussed for the cases of bias just on d_i in Section 4.1. Here, the discussion can be extended to the more general case of mistuning on both d_i and ω_p (which is the typical situation). Also in this case the use of an initially overestimated d_i value allows the loss of attenuation to decrease. In fact, when d_i is overestimated, only one bias has significant effects, whereas the other does not have much influence (see above in this section and Figure 9). Conversely, when the d_i value is lower than its optimal value, the attenuation loss due to mistuning is more severe. Therefore, this property of the mistuned systems along with those already shown in Section 4.1 highlights that the use of initially overestimated d_i values (and thus initially overestimated R values) allows the robustness to increase, thus lowering the loss of attenuation due to mistuning, which is typically experienced starting from the optimal d_i value. Furthermore, this can allow the analysis of the mistuned system to become faster because the study of its behaviour can focus on values of l higher than 1 (because an initially

overestimated d_i value is used on purpose) and possibly slightly lower than 1 (e.g., greater than 0.5). Clearly, these are just guidelines because each practical case could require a different solution. Nevertheless, the points demonstrated thus far clearly indicate how robustness can be typically increased and how the proposed model can help in the tuning process.

The model presented so far has been validated by experimental tests shown in the next section.

5. Experimental Tests

This section describes the experimental tests performed to validate the results shown in the previous sections. Two test structures have been used to investigate different values of the ξ_n and k_n parameters and different values of vibration attenuation. The first structure is an aluminium plate (in free-free condition by suspension) with the shunted piezobender bonded at about its centre (see Figure 10(a)). A bidimensional structure was used because it is a more complex test case when compared to monodimensional structures often used in other studies. The plate length is 600 mm, the width is 400 mm, and the thickness is 8 mm (this set-up is the same

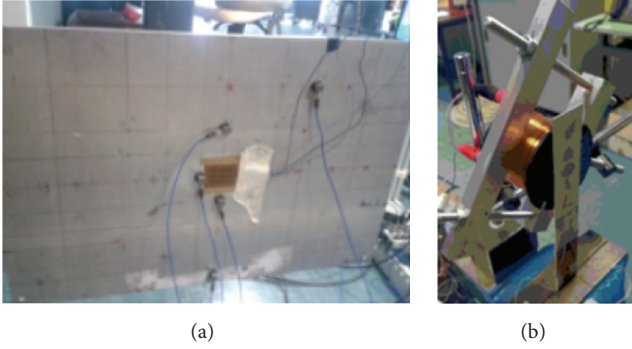


FIGURE 10: Experimental set-ups: plate (a) and beam (b).

TABLE 5: Bounds for the Monte Carlo simulations for $\nu \neq 1$ and $l \neq 1$.

	ξ_n	k_A	k_n	l_x	ν_x
Min	0.05%	0.001	k_A	0.5	0.9
Max	1%	0.35	k_B	1.5	1.1

as that used in the experiments of [19]). The capacitance C_p is $0.02 \mu\text{F}$. Several modes were taken into account in the tests. The one (among others tested) considered here as an example has the following modal parameters (identified by experimental modal analysis [28]): $\omega_n = 530.67 \cdot 2\pi \text{ rad/s}$, $\xi_n = 0.22\%$, $k_n = 0.0081$, and $\gamma\psi_n^2 = 725 \text{ rad}^2/\text{s}^2$. Actually, the value of k_n was estimated by testing the system in both short- and open-circuit conditions (see (12)).

These values of $\gamma\psi_n^2$ and k_n were achieved using a negative capacitance [27], which allowed their initial low values to increase. Furthermore, another value of k_n (i.e., 0.0240) was tested by further boosting the negative capacitance performance. The disturbance to the structure was provided by a dynamometric impact hammer, and the response was measured using a piezoelectric accelerometer.

The second structure is an aluminium cantilever beam (159 mm length, 25 mm width, and 1 mm thickness) with a piezoelectric patch bonded corresponding to the clamped end (see Figure 10(b)). Its capacitance C_p is 31 nF. Again, several modes were considered during the tests; here, the results related to the first mode are presented for the sake of conciseness. It has the following modal parameters, again identified using an experimental modal analysis: $\omega_n = 32.61 \cdot 2\pi \text{ rad/s}$, $\xi_n = 0.40\%$, $k_n = 0.2002$, and $\gamma\psi_n^2 = 944.6 \text{ rad}^2/\text{s}^2$. Furthermore, other tests were performed by increasing the values of k_n up to 0.5108 using a negative capacitance.

Because this second test structure was extremely light, noncontact methods were used to provide excitation and to measure the response. Indeed, an electromagnetic device was used to excite the structure [29], and the response was measured using a laser velocimeter focused on the beam tip. The tests were performed by exciting the beam with a random signal [30] up to 1.6 kHz .

The tests were performed using synthetic impedance based on operational amplifiers [11, 31, 32] to build the inductor. Actually, certain tests on the plate were performed

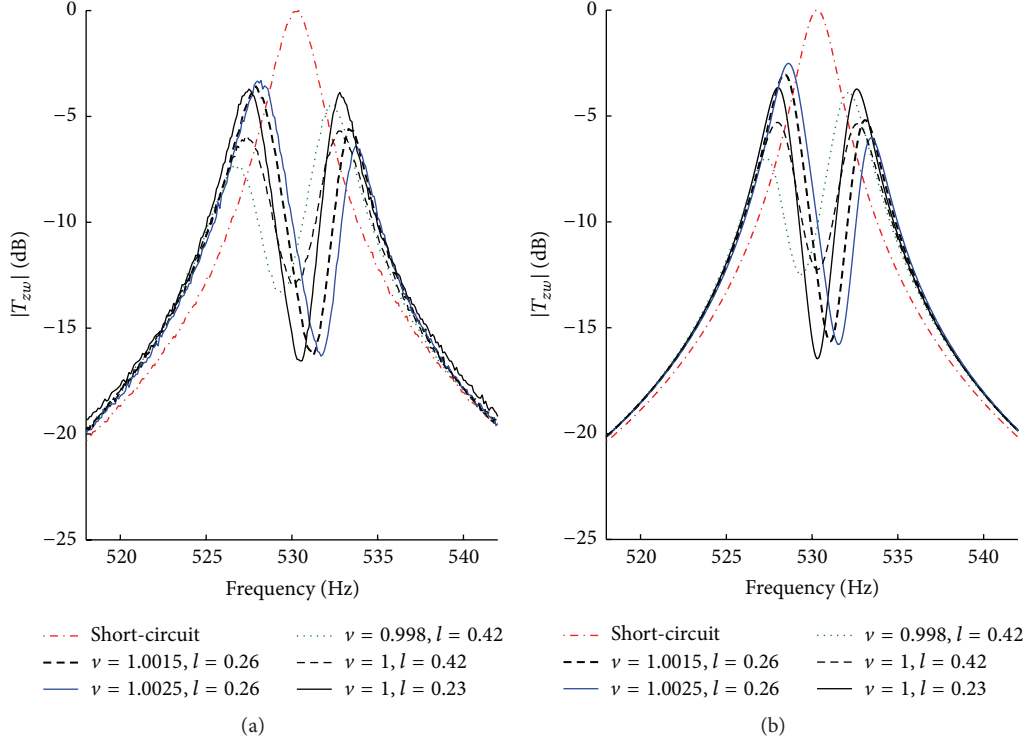
using an additional method: the entire shunt impedance was simulated using a high-speed Field Programmable Gate Array (FPGA) device (in this second case, a colocated piezoelectric patch was used to provide the input voltage to the simulated shunt impedance). The use of the FPGA device allowed for the full control of the parameters of the electric shunt impedance. Nevertheless, the two techniques led to similar results; therefore, those achieved using the synthetic impedance are presented here, since this technique introduces the highest level of uncertainty between the two. Therefore, the authors believed it to be the most representative to demonstrate the model effectiveness.

First, the reliability of the model, represented by (10) and (17), was verified. Figure 11 depicts the FRFs for the mode at approximately 530 Hz of the plate, achieved with different configurations of the shunt (i.e., using different l and ν values). The numerical FRFs match the experimental curves, thus confirming the accuracy of the numerical model. The curves are not plotted on the same graph for the sake of clarity in the figure. Nonetheless, Figure 12 depicts a few of the experimental and numerical FRFs of Figure 11 on the same plot for an easy comparison. Then, the reliability of the proposed approximated model (see (37)) for predicting the attenuation in mistuned conditions was tested. Tables 7 and 8 list the comparisons between experimental attenuations, numerical attenuations calculated using the theoretical model of (17), (19), and (29), and attenuations estimated using the proposed approximated model of (37) for the plate and the beam. To build the approximated model of (37), the values of k_A and k_B must be fixed. Three different situations were tested: one where k_A was close to k_n ($k_n = 1.1k_A$, named case 1), one where k_B was close to k_n ($k_n = 1.63k_A$, named case 2), and a further one where k_n was nearly halfway ($k_n = 1.37k_A$, named case 3). In all of the three cases, k_B was fixed to $\sqrt{3}k_A$. The experimental attenuations are defined in the tables as EA, whereas the numerical ones (see (17), (19), and (29)) are defined as NA for the sake of conciseness. Moreover, the attenuation provided by the model of (37) in cases 1, 2, and 3 is named MA1, MA2, and MA3, respectively. The match among all of the results is good. The results related to the MA1, MA2, and MA3 cases are always close to each other, and the maximum difference if compared to the NA results is on the order of 0.5 dB . Because the EA results differ from the NA results at a maximum of 1.2 dB , the proposed model of (37) is considered to be validated.

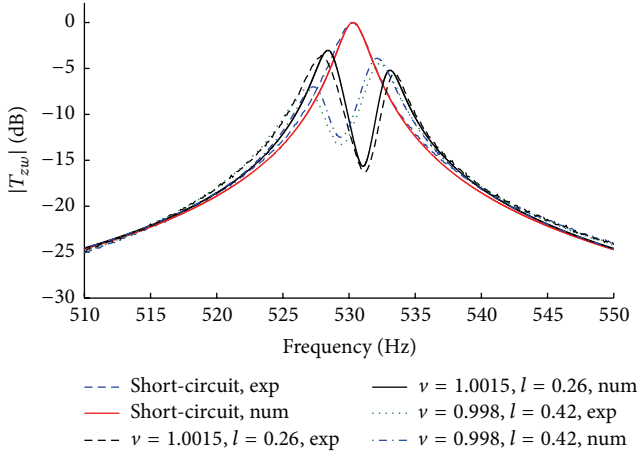
6. Conclusion

This paper addresses monomodal vibration attenuation using piezoelectric transducers shunted to impedances consisting of an inductance and a resistance in series. Although this method works well when the tuning between the mechanical system and the electrical network is properly realised, this control technique is not adaptive, and its performances thus decrease as soon as a mistuning occurs.

The paper analyses the behaviour of mistuned electromechanical systems, demonstrating that a linear relationship between the attenuation and the logarithm of the effective

FIGURE 11: Experimental (a) and numerical (b) FRFs for the plate ($k_n = 0.0081$).TABLE 6: Results of the Monte Carlo simulations for $\nu \neq 1$ and $l \neq 1$.

Mean value of Δ [dB]	Standard deviation of Δ [dB]	Minimum value of Δ [dB]	Maximum value of Δ [dB]
-0.20	0.46	-2.55	2.36

FIGURE 12: Experimental and numerical FRFs for the plate ($k_n = 0.0081$).

coupling coefficient exists when a perfect tuning is reached. The same linear behaviour exists when there is mistuning on either the electrical eigenfrequency or damping. Moreover,

the paper indicates how the loss of attenuation essentially depends on only one bias if the electrical damping is overestimated and describes how the effects of the two bias types (on the electrical eigenfrequency and damping) combine with each other when the damping is underestimated.

This allows an approximated model to be achieved for describing the behaviour of mistuned shunt systems, which was initially validated numerically using Monte Carlo simulations and then experimentally through the use of two test structures. Furthermore, the use of overestimated resistance values is demonstrated to limit the loss of attenuation due to mistuning.

Appendix

A. T_{zw} Normalised Analytical Expression

This appendix provides the mathematical process that allows (17) to be derived from (10).

Based on (10) and passing from the Laplace domain to the frequency domain (i.e., $s = j\omega$), the expression of T_{zw} can be written as follows:

TABLE 7: Attenuations for the mode of the plate.

		$l = 0.6, \nu = 1$	$l = 0.6, \nu = 0.9925$	$l = 0.8, \nu = 1.01$	$l = 1.2, \nu = 0.998$
EA [dB]	$k_n = 0.0081$	6.5	1.7	1.4	5.8
	$k_n = 0.0240$	12.9	9.3	10.0	11.5
NA [dB]	$k_n = 0.0081$	6.2	2.0	1.8	5.4
	$k_n = 0.0240$	12.7	9.6	9.6	12.2
MA1 [dB]	$k_n = 0.0081$	6.3	2.4	2.2	5.5
	$k_n = 0.0240$	12.7	10.1	10.1	12.5
MA2 [dB]	$k_n = 0.0081$	6.3	2.3	2.1	5.5
	$k_n = 0.0240$	12.7	10.1	10.1	12.5
MA3 [dB]	$k_n = 0.0081$	6.4	2.5	2.3	5.6
	$k_n = 0.0240$	12.8	10.1	10.1	12.6

$$T_{zw}(x_M) = \Phi_n(x_M) \Phi_n(x_F) \frac{-\omega^2 + 2j\omega d_i \omega_p + \omega_p^2}{(-\omega^2 + 2j\omega d_i \omega_p + \omega_p^2)(-\omega^2 + 2j\omega \xi_n \omega_n + \omega_n^2) + \gamma \psi_n^2 j\omega(j\omega + 2d_i \omega_p)}. \quad (\text{A.1})$$

Substituting (16) into (A.1) and using (13) and (15), the expression of T_{zw} can be further modified as follows:

$$\begin{aligned} T_{zw}(x_M) &= \Phi_n(x_M) \Phi_n(x_F) \frac{-\omega^2 + 2j\omega l d_i^{\text{opt}} \nu \omega_p^{\text{opt}} + (\nu \omega_p^{\text{opt}})^2}{(-\omega^2 + 2j\omega l d_i^{\text{opt}} \nu \omega_p^{\text{opt}} + (\nu \omega_p^{\text{opt}})^2)(-\omega^2 + 2j\omega \xi_n \omega_n + \omega_n^2) + \gamma \psi_n^2 j\omega(j\omega + 2l d_i^{\text{opt}} \nu \omega_p^{\text{opt}})} \\ &= \frac{\Phi_n(x_M) \Phi_n(x_F) [-\omega^2 + 2j\omega l \nu \sqrt{\gamma \psi_n^2 / 2} + \nu^2 (\omega_n^2 + \gamma \psi_n^2)]}{(-\omega^2 + 2j\omega l \nu \sqrt{\gamma \psi_n^2 / 2} + \nu^2 (\omega_n^2 + \gamma \psi_n^2))(-\omega^2 + 2j\omega \xi_n \omega_n + \omega_n^2) + \gamma \psi_n^2 j\omega(j\omega + 2l \nu \sqrt{\gamma \psi_n^2 / 2})}. \end{aligned} \quad (\text{A.2})$$

By dividing both the numerator and the denominator of (A.2) by a factor ω_n^4 , defining the nondimensional frequency

$\varphi = \omega/\omega_n$, and using (12), the final expression of T_{zw} can be obtained as follows (see (17)):

$$\begin{aligned} T_{zw}(x_M) &= \frac{\omega_n^4}{\omega_n^4} \cdot \frac{\Phi_n(x_M) \Phi_n(x_F) [-\omega^2 + 2j\omega l \nu \sqrt{\gamma \psi_n^2 / 2} + \nu^2 (\omega_n^2 + \gamma \psi_n^2)]}{(-\omega^2 + 2j\omega l \nu \sqrt{\gamma \psi_n^2 / 2} + \nu^2 (\omega_n^2 + \gamma \psi_n^2))(-\omega^2 + 2j\omega \xi_n \omega_n + \omega_n^2) + \gamma \psi_n^2 j\omega(j\omega + 2l \nu \sqrt{\gamma \psi_n^2 / 2})} \\ &= \frac{[\Phi_n(x_M) \Phi_n(x_F) / \omega_n^2] [-\omega^2 / \omega_n^2 + \sqrt{2} j (\omega l \nu \sqrt{\gamma \psi_n^2 / \omega_n^2}) + \nu^2 (\omega_n^2 + \gamma \psi_n^2) / \omega_n^2]}{(-\omega^2 / \omega_n^2 + \sqrt{2} j (\omega l \nu \sqrt{\gamma \psi_n^2 / \omega_n^2}) + \nu^2 (\omega_n^2 + \gamma \psi_n^2) / \omega_n^2)(-\omega^2 + 2j\omega \xi_n \omega_n + \omega_n^2) + (\gamma \psi_n^2 \omega / \omega_n^3) j (j (\omega / \omega_n) + \sqrt{2} (l \nu \sqrt{\gamma \psi_n^2 / \omega_n}))} \\ &= \frac{\Phi_n(x_M) \Phi_n(x_F)}{\omega_n^2} \cdot \frac{-\varphi^2 + \sqrt{2} j \varphi k_n l \nu + \nu^2 (1 + k_n^2)}{(-\varphi^2 + \sqrt{2} j \varphi k_n l \nu + \nu^2 (1 + k_n^2))(-\varphi^2 + 2j \xi_n \varphi + 1) + j \varphi k_n^2 (j \varphi + \sqrt{2} k_n l \nu)}. \end{aligned} \quad (\text{A.3})$$

TABLE 8: Attenuations for the mode of the beam.

		$l = 0.6, \nu = 1.1$	$l = 1.5, \nu = 1$	$l = 0.6, \nu = 0.8$	$l = 1.2, \nu = 0.8$
EA [dB]	$k_n = 0.2002$	19.3	23.1	3.1	13.9
	$k_n = 0.5108$	29.0	29.4	16.4	25.7
NA [dB]	$k_n = 0.2002$	18.6	22.3	3.9	13.5
	$k_n = 0.5108$	29.8	30.8	17.1	26.9
MA1 [dB]	$k_n = 0.2002$	19.8	22.3	4.9	12.9
	$k_n = 0.5108$	30.5	30.9	17.9	26.9
MA2 [dB]	$k_n = 0.2002$	19.8	22.3	4.8	12.9
	$k_n = 0.5108$	30.5	30.8	17.9	26.9
MA3 [dB]	$k_n = 0.2002$	19.8	22.3	5.2	13.0
	$k_n = 0.5108$	30.5	30.9	17.9	26.8

B. attk Analytical Expression

The mathematical process used to express attk (see (21)) is explained here.

The expression of T_{zw} in (17) can be rearranged by separating the real and imaginary parts at the numerator and denominator as follows:

$$T_{zw}(x_M) = \frac{\Phi_n(x_M)\Phi_n(x_F)}{\omega_n^2} \cdot \frac{A_{zw} + jB_{zw}}{C_{zw} + jD_{zw}}, \quad (\text{B.1})$$

where

$$\begin{aligned} A_{zw} &= -\varphi^2 + \nu^2(1 + k_n^2), \\ B_{zw} &= \sqrt{2}\varphi k_n l \nu, \\ C_{zw} &= (-\varphi^2 + \nu^2(1 + k_n^2))(-\varphi^2 + 1) \\ &\quad - 2\sqrt{2}\varphi^2 k_n l \nu \xi_n - \varphi^2 k_n^2, \\ D_{zw} &= \sqrt{2}\varphi k_n l \nu(-\varphi^2 + 1) \\ &\quad + 2\xi_n \varphi(-\varphi^2 + \nu^2(1 + k_n^2)) + \sqrt{2}\varphi k_n^3 l \nu. \end{aligned} \quad (\text{B.2})$$

According to [23], $|T_{zw}|$ can be expressed as follows:

$$\begin{aligned} |T_{zw}(x_M)|^2 &= \left(\frac{\Phi_n(x_M)\Phi_n(x_F)}{\omega_n^2} \right)^2 \\ &\quad \cdot \frac{A_{zw}^2 C_{zw}^2 + B_{zw}^2 D_{zw}^2 + B_{zw}^2 C_{zw}^2 + A_{zw}^2 D_{zw}^2}{(C_{zw}^2 + D_{zw}^2)^2}. \end{aligned} \quad (\text{B.3})$$

The expression of (B.3) can be evaluated in $\omega = \omega_p = \omega_p^{\text{opt}}$ (the case of perfect tuning is considered here), which in turn corresponds to $\varphi = \omega_p^{\text{opt}}/\omega_n = \omega_n^{\text{oc}}/\omega_n = \sqrt{1 + k_n^2}$:

$$|T_{zw}(x_M)|_{\omega_p} = \left| \frac{\Phi_n(x_M)\Phi_n(x_F)}{\omega_n^2} \right| \cdot \frac{\sqrt{2}}{(k_n + 2\sqrt{2}\xi_n)\sqrt{1 + k_n^2}}. \quad (\text{B.4})$$

According to [11], $\max(|G_{zw}|) = |\Phi_n(x_M)\Phi_n(x_F)|/(2\xi_n\omega_n^2\sqrt{1 - \xi_n^2})$. Therefore

$$\text{attk} = \frac{\max(|G_{zw}|)}{|T_{zw}|_{\omega_p}} = (k_n + 2\sqrt{2}\xi_n) \sqrt{\frac{(1 + k_n^2)}{8\xi_n^2(1 - \xi_n^2)}}. \quad (\text{B.5})$$

C. List of the Symbols

This appendix clarifies the meaning of the symbols used.

The symbol $*$ represents a generic mistuned condition.

The symbol \sim represents an estimate of the considered quantity.

A_{dB} expresses the attenuation in decibels achieved in case of perfect tuning (i.e., $l = 1, \nu = 1$).

A_{dB}^* expresses the attenuation in decibels achieved in case of mistuning (this is evidenced by the asterisk).

When A_{dB} and A_{dB}^* are evaluated at specific points (i.e., given values of l, ν , or k_n), the following expressions are used: $A_{\text{dB}}|_{k_n}$ and $A_{\text{dB}}^*|_{l=1, \nu=\nu_x}$, as examples. The former expression indicates that A_{dB} is computed in correspondence with a given value k_n of the effective coupling factor, whereas the latter indicates that A_{dB}^* is computed for $l = 1$ and $\nu = \nu_x$.

$\widetilde{A}_{\text{dB}}^*$ and $\widetilde{A}_{\text{dB}}$ represent the values of A_{dB}^* and A_{dB} , respectively, which are estimated using the model proposed in the paper, that is, by (30), (32), and (37).

As for the angular coefficient m and the intercept q of the linear relations presented in the paper (e.g., (25), (27), (30), and (32)), when they have a subscript 0, they are calculated for a perfectly tuned shunt impedance. Conversely, when they

are calculated for a mistuned system, they have an * as a superscript and a subscript equal to l (for a mistuning on d_i and with ω_p perfectly tuned) or v (for a mistuning on ω_p and with d_i perfectly tuned).

Competing Interests

The authors declare that there are no competing interests regarding the publication of this paper.

References

- [1] A. Preumont, *Vibration Control of Active Structures: An Introduction*, Kluwer Academic, Dordrecht, Netherlands, 2nd edition, 2002.
- [2] A. Preumont, *Mechatronics—Dynamics of Electromechanical and Piezoelectric Systems*, Springer, Dordrecht, The Netherlands, 2006.
- [3] C. Fuller, S. Elliott, and P. Nelson, *Active Control of Vibration*, Academic Press, London, UK, 1997.
- [4] N. W. Hagood and A. von Flotow, "Damping of structural vibrations with piezoelectric materials and passive electrical networks," *Journal of Sound and Vibration*, vol. 146, no. 2, pp. 243–268, 1991.
- [5] D. Guyomar, Y. Jayet, L. Petit et al., "Synchronized switch harvesting applied to selfpowered smart systems: piezoelectric microgenerators for autonomous wireless transmitters," *Sensors and Actuators A: Physical*, vol. 138, no. 1, pp. 151–160, 2007.
- [6] J. Tang and K. W. Wang, "Active-passive hybrid piezoelectric networks for vibration control: comparisons and improvement," *Smart Materials and Structures*, vol. 10, no. 4, pp. 794–806, 2001.
- [7] K. Yamada, H. Matsuhisa, H. Utsuno, and K. Sawada, "Optimum tuning of series and parallel LR circuits for passive vibration suppression using piezoelectric elements," *Journal of Sound and Vibration*, vol. 329, no. 24, pp. 5036–5057, 2010.
- [8] P. Soltani, G. Kerschen, G. Tondreau, and A. Deraemaeker, "Piezoelectric vibration damping using resonant shunt circuits: an exact solution," *Smart Materials and Structures*, vol. 23, no. 12, Article ID 125014, 2014.
- [9] J. Høgsberg and S. Krenk, "Balanced calibration of resonant shunt circuits for piezoelectric vibration control," *Journal of Intelligent Material Systems and Structures*, vol. 23, no. 17, pp. 1937–1948, 2012.
- [10] J. Høgsberg and S. Krenk, "Balanced calibration of resonant piezoelectric RL shunts with quasi-static background flexibility correction," *Journal of Sound and Vibration*, vol. 341, pp. 16–30, 2015.
- [11] O. Thomas, J. Ducarne, and J.-F. Deü, "Performance of piezoelectric shunts for vibration reduction," *Smart Materials and Structures*, vol. 21, no. 1, article 015008, 2012.
- [12] E. Doebelin, *Measurement Systems: Application and Design*, McGraw-Hill, New York, NY, USA, 2003.
- [13] J. J. Hollkamp and T. F. Starchville Jr., "Self-tuning piezoelectric vibration absorber," *Journal of Intelligent Material Systems and Structures*, vol. 5, no. 4, pp. 559–566, 1994.
- [14] B. Zhou, F. Thouverez, and D. Lenoir, "Essentially nonlinear piezoelectric shunt circuits applied to mistuned bladed disks," *Journal of Sound and Vibration*, vol. 333, no. 9, pp. 2520–2542, 2014.
- [15] B. Zhou, F. Thouverez, and D. Lenoir, "Vibration reduction of mistuned bladed disks by passive piezoelectric shunt damping techniques," *AIAA Journal*, vol. 52, no. 6, pp. 1194–1206, 2014.
- [16] S. Behrens, A. J. Fleming, and S. O. R. Moheimani, "A broadband controller for shunt piezoelectric damping of structural vibration," *Smart Materials and Structures*, vol. 18, no. 12, pp. 18–28, 2003.
- [17] D. Niederberger, M. Morari, and S. Pietrzko, "Adaptive resonant shunted piezoelectric devices for vibration suppression," in *Proceedings of the Smart Structures and Materials 2003: Smart Structures and Integrated Systems*, pp. 213–224, San Diego, Calif, USA, March 2003.
- [18] H. Hanselka, "Adaptronik und fragen zur systemzuverl ATP," *Automatisierungstechnische Praxis*, vol. 2, pp. 44–49, 2002.
- [19] M. Berardengo, A. Cigada, S. Manzoni, and M. Vanali, "Vibration control by means of piezoelectric actuators shunted with LR impedances: performance and robustness analysis," *Shock and Vibration*, vol. 2015, Article ID 704265, 30 pages, 2015.
- [20] S. Moheimani and A. Fleming, *Piezoelectric Transducers for Vibration Control and Damping*, Springer, London, UK, 2006.
- [21] S. O. R. Moheimani, A. J. Fleming, and S. Behrens, "On the feedback structure of wideband piezoelectric shunt damping systems," *Smart Materials and Structures*, vol. 12, no. 1, pp. 49–56, 2003.
- [22] B. De Marneffe and A. Preumont, "Vibration damping with negative capacitance shunts: theory and experiment," *Smart Materials and Structures*, vol. 17, no. 3, article 035015, 2008.
- [23] S. Krenk, "Frequency analysis of the tuned mass damper," *Journal of Applied Mechanics*, vol. 72, no. 6, pp. 936–942, 2005.
- [24] D. J. Ewins, *Modal Testing: Theory, Practice and Application*, Research Studies Press, Baldock, UK, 2nd edition, 2000.
- [25] J. Ducarne, O. Thomas, and J.-F. Deü, "Placement and dimension optimization of shunted piezoelectric patches for vibration reduction," *Journal of Sound and Vibration*, vol. 331, no. 14, pp. 3286–3303, 2012.
- [26] O. Thomas, J.-F. Deü, and J. Ducarne, "Vibrations of an elastic structure with shunted piezoelectric patches: efficient finite element formulation and electromechanical coupling coefficients," *International Journal for Numerical Methods in Engineering*, vol. 80, no. 2, pp. 235–268, 2009.
- [27] M. Berardengo, O. Thomas, C. Giraud-Audine, and S. Manzoni, "Improved resistive shunt by means of negative capacitance: new circuit, performances and multi-mode control," *Smart Materials and Structures*, vol. 25, no. 7, Article ID 075033, 2016.
- [28] B. Peeters, H. Van Der Auweraer, P. Guillaume, and J. Leuridan, "The PolyMAX frequency-domain method: a new standard for modal parameter estimation?" *Shock and Vibration*, vol. 11, no. 3–4, pp. 395–409, 2004.
- [29] O. Thomas, C. Touzé, and A. Chaigne, "Asymmetric nonlinear forced vibrations of free-edge circular plates. Part II: experiments," *Journal of Sound and Vibration*, vol. 265, no. 5, pp. 1075–1101, 2003.
- [30] A. Brandt, *Noise and Vibration Analysis—Signal Analysis and Experimental Procedures*, John Wiley & Sons, New York, NY, USA, 2011.
- [31] C. H. Park and D. J. Inman, "Enhanced piezoelectric shunt design," *Shock and Vibration*, vol. 10, no. 2, pp. 127–133, 2003.
- [32] B. Seba, J. Ni, and B. Lohmann, "Vibration attenuation using a piezoelectric shunt circuit based on finite element method analysis," *Smart Materials and Structures*, vol. 15, no. 2, pp. 509–517, 2006.

Research Article

An Updated Analytical Structural Pounding Force Model Based on Viscoelasticity of Materials

Qichao Xue,¹ Chunwei Zhang,² Jian He,¹ Guangping Zou,¹ and Jingcai Zhang¹

¹College of Aerospace and Civil Engineering, Harbin Engineering University, Harbin, China

²Institute for Infrastructure Engineering, Western Sydney University, Sydney, NSW, Australia

Correspondence should be addressed to Chunwei Zhang; chunwei.zhang@westernsydney.edu.au

Received 5 May 2016; Revised 31 July 2016; Accepted 3 August 2016

Academic Editor: Londono Monsalve

Copyright © 2016 Qichao Xue et al. This is an open access article distributed under the Creative Commons Attribution License, which permits unrestricted use, distribution, and reproduction in any medium, provided the original work is properly cited.

Based on the summary of existing pounding force analytical models, an updated pounding force analysis method is proposed by introducing viscoelastic constitutive model and contact mechanics method. Traditional Kelvin viscoelastic pounding force model can be expanded to 3-parameter linear viscoelastic model by separating classic pounding model parameters into geometry parameters and viscoelastic material parameters. Two existing pounding examples, the poundings of steel-to-steel and concrete-to-concrete, are recalculated by utilizing the proposed method. Afterwards, the calculation results are compared with other pounding force models. The results show certain accuracy in proposed model. The relative normalized errors of steel-to-steel and concrete-to-concrete experiments are 19.8% and 12.5%, respectively. Furthermore, a steel-to-polymer pounding example is calculated, and the application of the proposed method in vibration control analysis for pounding tuned mass damper (TMD) is simulated consequently. However, due to insufficient experiment details, the proposed model can only give a rough trend for both single pounding process and vibration control process. Regardless of the cheerful prospect, the study in this paper is only the first step of pounding force calculation. It still needs a more careful assessment of the model performance, especially in the presence of inelastic response.

1. Introduction

Earthquakes may lead to damage and collapse of colliding structures in the case of insufficient gap between adjacent structures. This damage caused by pounding effect has been observed in both adjacent tall buildings and long bridges in all major earthquakes [1–5]. In many cases, these earthquake-induced poundings may cause functionality to be disabled or even more serious results, such as large plastic deformations and splintering and collapse of main structural components of buildings. For bridges girder, dislocations or fallings may occur due to vertical or horizontal poundings [6].

Illustrating the pounding forces between colliding bodies precisely is the basis of simulating pounding process. Numerous literatures have focused on analysing structures of earthquake-induced pounding. Some research [7–11] involves poundings between adjacent buildings. For example, Jankowski [7] analysed the parametric pounding of

two buildings with the same number of stories. Based on Jankowski's nonlinear viscoelastic analytical model, Pratesi et al. [8] developed a special multilink viscoelastic finite element contact model and analysed seismic pounding of a slender reinforced concrete bell tower. Shakya and Wijeyewickrema [9] dealt with the seismic pounding between three typical reinforced concrete moment resisting frame buildings in a row considering the effects of underlying soil on the structural response. Polycarpou and Komodromos [10] investigated the effects of potential pounding incidences on the seismic response of a typical seismically isolated building through numerical simulations. Ye et al. [11] utilized a modified Kelvin impact model to investigate the behavior of the base-isolated building pounding.

More literatures focus on solving the bridges pounding problems. Cui et al. [12] utilized Kelvin model to simulate the pounding between two adjacent highway bridges with expansion joints. Yang and Yin [13] developed a theoretical

approach to investigate the transient behavior of continuous bridges under near-fault vertical ground motions. Dimitrakopoulos [14] proposed a novel nonsmooth rigid body approach so as to analyse the seismic response of pounding skew bridges which involve obliquely frictional multiple-contact phenomena.

At the same time, it has been found that soil-structure interactions in structures are critical in earthquake-pounding problems [15–18]. However, regardless of structures or pounding types, the definition of interactions between two colliding bodies, which is called pounding force models, is necessary and predominant in analysis.

This paper briefly reviews the analytical impact/pounding models firstly. Moreover, an updated pounding force analytical method is proposed by introducing viscoelastic constitutive model and contact mechanics analysis method. Afterwards, two existing pounding examples, the poundings of steel-to-steel and concrete-to-concrete, are recalculated by utilizing the above proposed method and further compared with other pounding force models. The parametric study and feasibility of the proposed model are discussed consequently. Furthermore, this paper calculates a steel-to-polymer pounding example and simulates the application of pounding TMD in vibration control based on the method proposed above. The study here presents only the first step of pounding force calculation. Therefore, it is necessary to carry out more careful assessments of the model performance.

2. Review of Existing Pounding Force Models

Due to the complexity and nonlinearity associated with colliding process, including inelasticity, plasticity, viscoelasticity, frictions, and multiple forms of energy dissipation, many simplified pounding force models have been proposed to calculate, simulate, and represent the force responses between colliding bodies.

Several pounding force models have been proposed to calculate the interaction between pounding structures. All these models are on the basis of stereomechanics which is a classic theory of impact. It is based on the laws of conservation of energy and momentum by neglecting the details of impact process. The energy dissipation during the pounding process is dependent on the differences between approaching and separative velocities of colliding bodies (Figure 1).

Figure 1 is the sketch of classical colliding process, in which m_1 and m_2 are the masses of the two colliding bodies, V_1 and V_2 are velocities before colliding, and V'_1 and V'_2 are velocities after colliding corresponding to m_1 and m_2 . Parameter e is defined as

$$e = \frac{V'_2 - V'_1}{V_1 - V_2}. \quad (1)$$

The velocity of the colliding bodies after collision and energy loss during the colliding process can be illustrated based on parameter e and velocities before collision:

$$V'_1 = V_1 - (1 + e) \frac{m_2 V_1 - m_1 V_2}{m_1 + m_2},$$

$$V'_2 = V_2 - (1 + e) \frac{m_1 V_1 - m_2 V_2}{m_1 + m_2},$$

ΔE

$$= \frac{1}{2} (1 + e) \frac{m_1 m_2}{m_1 + m_2} (V_1 - V_2) (V_1 - V_2 + V'_2 - V'_1), \quad (2)$$

where ΔE is energy dissipation in the pounding process due to the high frequency vibration, heat, and noise. Interactions between two colliding bodies in approaching process and restitution process are ignored under traditional colliding theory. The only parameter to be verified in colliding process is parameter e , which varies from different colliding materials. It can be determined by colliding experiments.

When the transient effects of poundings need to be considered in certain structures under dynamic loads, the time history of pounding forces between two colliding bodies is necessary. A precise pounding force model developed to illustrate pounding process is the key aspect in analysis. Most existing pounding force models are based on classical theory of impact, showing advantages in analysing multiple bodies colliding and structure poundings under seismic loads. The following several types of models are still popular in seismic analysis.

2.1. Linear Spring Model. Linear spring model, which is based on classical theory of impact, considers the interaction between two colliding bodies as a linear spring (Figure 2(a)). It is only effective in rigid and plan-to-plan collision. The force during the collision can be illustrated as follows:

$$F(t) = k_s \delta(t), \quad (3)$$

where k_s is the parameter determined by material elasticity and spring stiffness shown in Figure 2(a); $\delta(t)$ is the relative displacement between two colliding bodies. Ruangrassamee and Kawashima [21] utilized the linear spring model to calculate the pounding of bridge decks with multiple variable dampers. Wang and Shih [6] presented a case study of the sliding for bridge decks and pounding at abutment-backfill by utilizing a linear spring model.

2.2. Nonlinear Spring Model (Hertz Spring Model). Nonlinear spring model, also called Hertz spring model, is based on static contact mechanics. It is initially introduced into analysis for collision process by Goldsmit [22]. This model is extremely effective in elastic poundings and suitable for curved surface contacts with different curvatures. The pounding force can be regarded as a nonlinear spring between colliding bodies (Figure 2(b)) and it can be written as

$$F(t) = k_H \delta(t)^{3/2}, \quad (4)$$

where k_H is the Hertz pounding parameter determined by materials and contact geometries.

Many pounding analyses have utilized this model, which show the effectiveness for elastic poundings. Chau and Wei [23] modelled poundings between two adjacent structures

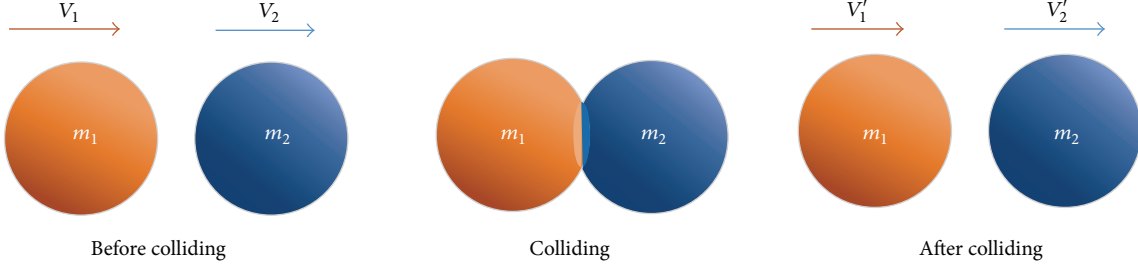


FIGURE 1: Sketch of colliding process.

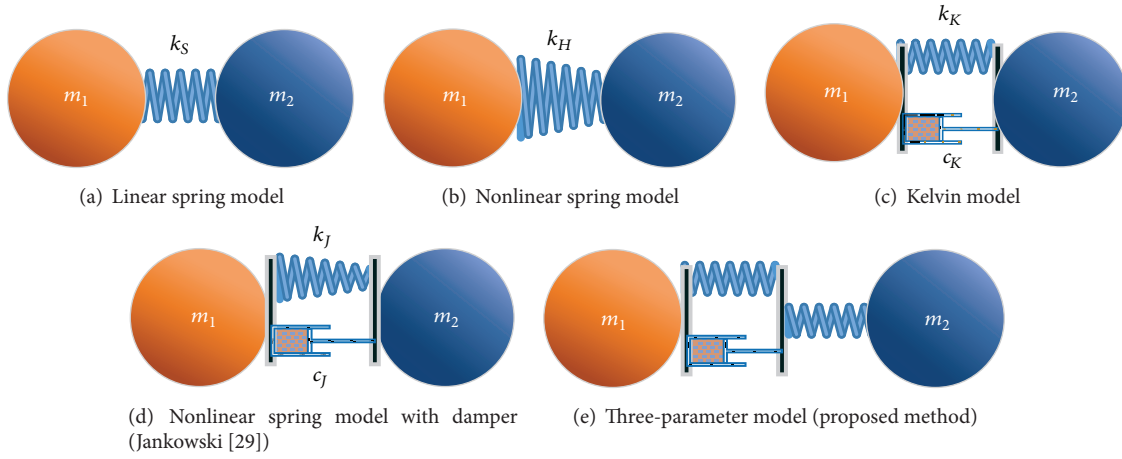


FIGURE 2: Pounding force models.

by utilizing a nonlinear Hertz impact model, in which they simplified the structures as two single-degree-of-freedom oscillators. The results showed that maximum relative impact velocity was not very sensitive to changes in the contact parameters. Pantelides and Ma [24] adopted Hertz pounding model to study the effects of colliding on horizontal pounding of bridges for the first time. Due to lack of precise value of stiffness of impact, Cui et al. [12] calculated the poundings between bridges and deduced parameter k_H .

2.3. Kelvin Model. Kelvin model (Figure 2(c)) is a type of linear viscoelastic model that can deal with energy dissipation during collision deformation. Compared to linear spring model and Hertz nonlinear spring model, it can describe energy dissipation except for tension stress at the end of pounding process. This method was initially proposed and discussed by Anagnostopoulos [25, 26]. Kelvin model can be written as

$$F(t) = k_K \delta(t) + c_K \dot{\delta}(t), \quad (5)$$

where k_K is the stiffness parameter of Kelvin model and c_K is damping factor of damper in Kelvin model. (·) means first-order derivative to the time. According to Anagnostopoulos' work, c_K is not an independent parameter but should be

calculated on the basis of the masses of colliding bodies m_1 and m_2 , stiffness k_K , and parameter e :

$$c_K = 2\xi \sqrt{k_K \left(\frac{m_1 m_2}{m_1 + m_2} \right)} \quad (6)$$

with

$$\xi = -\frac{\ln e}{\sqrt{\pi^2 + (\ln e)^2}}, \quad (7)$$

where k_K is determined by pounding experiment. Many literatures have utilized this model, which showed its effectiveness. Agarwal et al. [27] utilized the Kelvin model and investigated the earthquake-induced upper story pounding response of two buildings in close proximity with different base isolation systems. Shakyia and Wijeyewickrema [9] utilized the Kelvin model to calculate the impact of two multistory buildings. Komodromos et al. [10, 28] utilized the Kelvin model to analyse the pounding between isolated buildings and foundations. Madani et al. [17] also utilized the Kelvin model to analyse the adjacent building poundings considering soil-structure interactions.

2.4. Nonlinear Viscoelastic Model. The nonlinear viscoelastic model (Figure 2(d)) is firstly developed by Jankowski based

on Kelvin model [29, 30]. He constructed a segmental function to avoid the tension stress at the end of restitution period.

$$F(t) = k_J \delta^{3/2}(t) + c_J \dot{\delta}(t) \quad \text{for } \dot{\delta}(t) > 0 \text{ (approaching period)}, \quad (8)$$

$$F(t) = k_J \delta^{3/2}(t) \quad \text{for } \dot{\delta}(t) < 0 \text{ (restitution period)},$$

where k_J is the impact stiffness parameter and c_J is determined by the following formula:

$$c_J = 2\xi_J \sqrt{k_J \sqrt{\delta(t)} \left(\frac{m_1 m_2}{m_1 + m_2} \right)} \quad (9)$$

with

$$\xi_J = \frac{\sqrt{5}}{2\pi} \frac{1 - e^2}{e}. \quad (10)$$

Jankowski utilized this model to calculate the poundings of multistory buildings [7] and isolated elevated bridges [31]. Pratesi et al. [8] proposed a special multiple-link viscoelastic finite element contact model which was deduced from Jankowski's nonlinear viscoelastic model.

2.5. Other Pounding Force Models. Previous literatures have proposed several other pounding models, most of which are revised on the basis of former models. Mahmoud [32] modified Kelvin model which was only activated during the approach period of collision. Khatiwada et al. [33] proposed the Hunt–Crossley model, which changed the power factor of relative displacement in Kelvin model from 3/2 to variable n .

Based on the summarization of existing pounding models, only one dependent parameter in above pounding force models needs to be decided by experiments. This parameter contains much information including the masses of bodies, stiffness, pounding speed, and contact geometries. In engineering practice, the parameter will change with specific situations. Therefore, the parameter obtained from model test will meet limitation of utilization in reality. What is more, the power of penetration displacement will not change for each pounding force model separately: 1 for linear elastic model and 3/2 for nonlinear models. However, as for contact mechanics [34], the power number is determined by the geometry of contacting interface, which varies from 1 to 2. In next section, an updated pounding force model will be developed to overcome the aforementioned disadvantages.

3. Analysis Method

The main idea of the proposed pounding force method in this paper is based on linear viscoelasticity of materials and law of contact mechanics. The author has tried to separate variables from pounding materials and contact geometries. The following assumptions should be observed:

- (1) The transmogrification is small. All deformations during the pounding process are assumed as viscoelastic and tiny, which ignore higher order effects of deformation of pounding responses.

- (2) The inertial effects of deforming part in pounding bodies are ignored. For pounding process of civil engineering structures, strain rate ranges from 10^2 s^{-1} to 10^4 s^{-1} , and it can be classified as low velocity impact. Therefore, the inertial effect of deforming area can be ignored.

- (3) The energy dissipation during pounding process only comes from the viscoelasticity of materials. This means that not only the traditional elastic material, such as steel and concrete, but also the real viscoelastic material, such as polymers, is considered as viscoelastic materials. This assumption is reasonable because the elasticity modulus of most elastic materials has rate-dependent properties. Furthermore, a viscoelastic constitution model can be degenerated to an elastic model in a certain case.

3.1. Viscoelastic Material Constitutive Models. Viscoelasticity of material can be illustrated by linear constitution models, which are composed of springs and dash-pots. The simplest linear constitutive models are Maxwell model and Kelvin model, which are characterized by the fluid properties and solid properties of viscoelastic material (as shown in Figures 3(a) and 3(b)). More complicated model such as 3-parameter solid model (as shown in Figure 3(c)) is more accurate in illustrating the behavior of viscoelasticity.

Kelvin viscoelastic constitution model can be written in a differential type:

$$\sigma = q_0 \varepsilon + q_1 \dot{\varepsilon} \quad \text{with } q_0 = E_1, \quad q_1 = C_1, \quad (11)$$

where σ and ε are stress and strain, respectively; E_1 and C_1 are the spring parameter and dash-pot parameter in constitutive model; q_0 and q_1 are parameters to determine the constitutive model in Figure 3(a).

For 3-parameter solid viscoelastic model (Figure 3(b)), it can be written as

$$\sigma + p_1 \dot{\sigma} = q_0 \varepsilon + q_1 \dot{\varepsilon} \quad \text{with } p_1 = \frac{C_1}{E_1 + E_2}, \quad q_0 = \frac{E_1 E_2}{E_1 + E_2}, \quad q_1 = \frac{C_1 E_2}{E_1 + E_2}, \quad (12)$$

where E_1 , E_2 , and C_1 are the spring parameters and dash-pot parameter in 3-parameter constitutive model; q_0 , q_1 , and q_2 are parameters to determine the constitutive model in Figure 3(b).

Regardless of the complexity of the constitutive models, if they are composed of springs and dash-pots in series or parallel relations (Figure 3(c)), they can be written as following differential equation:

$$p_0 \sigma + p_1 \dot{\sigma} + p_2 \ddot{\sigma} + \dots = q_0 \varepsilon + q_1 \dot{\varepsilon} + q_2 \ddot{\varepsilon} + \dots \quad (13)$$

The equation can be written as

$$P\sigma = Q\varepsilon, \quad (14)$$

where P and Q are differential operators. Laplace transformations are introduced to both sides of the equation, and the expression in Laplace domain can be obtained:

$$\bar{P}(s) \bar{\sigma}(s) = \bar{Q}(s) \bar{\varepsilon}(s), \quad (15)$$

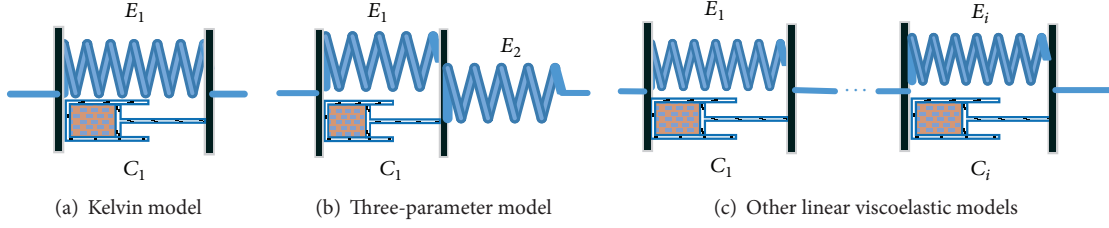


FIGURE 3: Linear viscoelastic constitutive models.

TABLE 1: Expressions and descriptions of parameters.

Contact cases	$D(A, R, l)$	E^*	α	Parameter description
Polyhedral cylinder-to-rigid plane	$\frac{A}{l}$	E	1	A and l are contact area and height of cylinder
Thin plate-to-rigid plane	$\frac{A}{l}$	$\frac{E(1-\nu)}{(1+\nu)(1-2\nu)}$	1	A and l are contact area and thickness of plate
Rigid cylinder-to-elastic plane	$2R$	$\frac{E}{1-\nu^2}$	1	R is the radius of cylinder
Rigid sphere-to-elastic plane	$\frac{4}{3}R^{1/2}$	$\frac{E}{1-\nu^2}$	$\frac{3}{2}$	R is the radius of sphere
Rigid cylinder-to-elastic plane (curvature surface contact)	$\frac{\pi l}{4}$	$\frac{E}{1-\nu^2}$	1	l is the height of cylinder
Rigid cone-to-elastic plane	$\frac{2}{\pi \tan \theta}$	E	2	θ is the angle of cone
Elastic curvature surface-to-elastic curvature surface	$\frac{4}{3} \left(\frac{R_a R_b}{R_a + R_b} \right)^{1/2}$	$\frac{1}{(1-\nu_a^2)/E_a + (1-\nu_b^2)/E_b}$	$\frac{3}{2}$	R_a and R_b are radius of two contact surface
Elastic cylinder-to-elastic cylinder (parallel contact)	$\frac{\pi l}{4}$	$\frac{1}{(1-\nu_a^2)/E_a + (1-\nu_b^2)/E_b}$	1	l is the height of cylinder

where $\bar{P}(s)$ and $\bar{Q}(s)$ are no more differential operators but polynomials of parameter s . $(\bar{\cdot})$ represents the Laplace transformation. Thus, the modulus of elasticity for viscoelastic material in Laplace domain can be defined as

$$\frac{\bar{\sigma}(s)}{\bar{\epsilon}(s)} = \frac{\bar{Q}(s)}{\bar{P}(s)} = \bar{E}(s). \quad (16)$$

3.2. Process of Analysis. Based on the former analysis, all pounding force models can be written in the following form:

$$F_p = D(A, R, l) \cdot E^* \cdot \delta^\alpha, \quad (17)$$

where $D(A, R, l)$ is the function of contact geometry of colliding bodies, which can be represented by contact area A , surface radius R , or the height of contact bodies l . Table 1 shows the illustrative examples of (17) based on contact mechanics. E^* is the parameter related to material properties of contact bodies, which may contain the moduli of elasticity for both bodies, such as E_1 and E_2 as well as Poisson's ratios ν_1 and ν_2 . Parameter δ is the function of penetration displacements. The power number α depends on the shape of contact geometry. In complicated contact pounding cases, such as discontinuous interfaces or noncentral collision, there are no explicit expressions to illustrate the relation between

pounding force and penetration displacements. Even for the simplified pounding model with regular pounding interfaces, the constitutive model of viscoelasticity also has no explicit expressions except for some special simple models, such as Kelvin model and Maxwell model.

The above expressions are constructed by elastic mechanics. In the case that the pounding bodies possess the properties with viscoelasticity, the following expression in Laplace domain can be achieved according to the principle of correspondence:

$$\bar{F}_p = \bar{D}(A, R, l) \cdot \bar{E}(s)^* \cdot \bar{\delta}^\alpha. \quad (18)$$

Since parameter $D(A, R, l)$ is a time-independent function, the inverse Laplace transformation of the above equation can be obtained:

$$F_p(t) = D(A, R, l) \cdot \mathcal{L}^{-1}(E^*(s)) \cdot \delta(s)^\alpha. \quad (19)$$

This represents the relationship between pounding force and contact displacement, which contains the implicit expression of inverse Laplace transformation $\mathcal{L}^{-1}(\cdot)$. In most cases, it cannot be calculated directly except for some specially simplified cases. For material whose properties can be described as a linear viscoelastic constitutive model, there is no need to

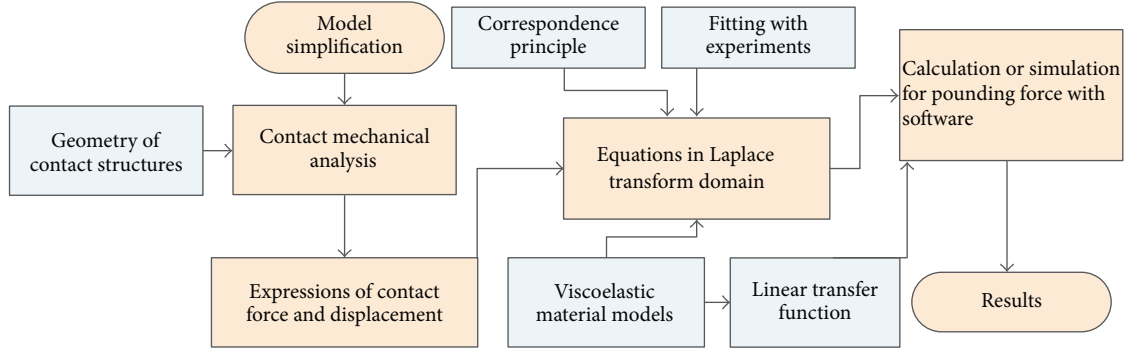


FIGURE 4: Sketch of the proposed pounding force analysis model.

obtain the explicit expression of Laplace inverse transformation, because it can be replaced by transfer function, which is a popular and common instrument in commercial simulation software. Therefore, it could be utilized to represent the pounding force directly in analysis.

According to the above analysis, the whole process in which the pounding force model will be determined is shown in Figure 4. When the pounding force between two colliding bodies is analysed, the first step is to obtain the suitable analysis model (elastic or viscoelastic) through contact geometry simplification. Afterwards, the simple expressions between contact force and displacement can be derived based on contact mechanics. The explicit expressions in Laplace domain can be obtained according to the principle of correspondence in viscoelastic mechanics. By fitting with the experimental curve, the parameters of pounding materials can be determined. Finally, the expressions of pounding force and pounding displacement can be achieved through Laplace inverse transformation. If the expression is implicit, parameter simplification or numerical Laplace inverse transformation can be carried out in simulation or calculation process. In this paper, only a linear 3-parameter solid linear viscoelastic model is utilized to verify the effectiveness of the proposed method.

4. Model Verification

Two classic collision examples are analysed in order to verify the accuracy of the proposed method. In both examples, a 3-parameter viscoelastic model (linear solid) will be utilized to construct pounding force model. The results will be compared with the experiments and the classic models in literature [29, 30]. At same time, parametric study of the 3-parameter model which influences the shape of pounding force-time history will be developed. The difference between the experimental results and the proposed model has been assessed by evaluating the following normalized error:

$$\text{error} = \frac{\|F(t) - \bar{F}(t)\|}{\bar{F}(t)}, \quad (20)$$

where $\bar{F}(t)$ is the collision force obtained by the existing experiments and $F(t)$ is time history response of numerical

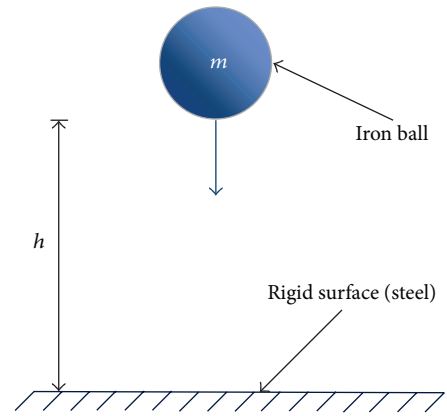


FIGURE 5: Model of a ball falling on a stationary rigid surface [19].

calculation or simulation results. $\|F(t) - \bar{F}(t)\|$ is a Euclidean norm of $F(t) - \bar{F}(t)$, and it can be calculated by a formula in discrete form. A total of 201 points for each curve in equivalent time space will be taken into account to calculate the error:

$$\|F(t) - \bar{F}(t)\| = \sqrt{\sum_{i=1}^n (F(t) - \bar{F}(t))^2}, \quad n = 201, \quad (21)$$

where $n = 201$ means that there are 200 equal intervals along the time axis which begin from time 0 and have the same ending time. According to (21), the values of these 201 discrete points will be calculated to determine the errors of curves. Although more discrete points can generate more precise error results, 201 points corresponding to 200 equal intervals are enough to guarantee the accuracy.

4.1. Steel-to-Steel Impact. The first example was carried out by Goland et al. [19] who dropped an iron ball onto the rigid surface (Figure 5) and measured pounding force changing with time. According to the assumptions above, although steel ball and rigid surface maintain elastic state in the whole pounding process, energy dissipation has occurred. Therefore, 3-parameter solid constitutive model is utilized to calculate the pounding force during collision. This does not

mean that the steel is a typical viscoelastic material. It is aimed at obtaining the energy dissipation during the collision.

According to contact mechanics, the following equations could be obtained to illustrate the pounding force for collision between ball and surface:

$$F_c = \frac{4}{3} R^{1/2} E^* \delta^{3/2}, \quad (22)$$

where R is the radius of the ball and E^* has the same expression as given in Table 1. Since the rigid surface is also made of steel, $E_a = E_b = E_s$ and $\nu_a = \nu_b = \nu_s$ can be obtained according to the expression of “elastic curvature surface-to-elastic curvature surface” in Table 1. The following expression of E^* can be derived:

$$\begin{aligned} E^* &= \frac{1}{(1-\nu_1^2)/E_1 + (1-\nu_2^2)/E_2} = \frac{1}{2((1-\nu_s^2)/E_s)} \\ &= \frac{E_s}{2(1-\nu_s^2)}. \end{aligned} \quad (23)$$

The modulus of elasticity for steel E_s is 2.0×10^{11} Pa, and Poisson's ratio ν_s is 0.23. There are three parameters in 3-parameter viscoelastic model: E_1 , E_2 , and C_1 . Therefore, another two parameters can be defined to illustrate the relationship between them:

$$\begin{aligned} R_1 &= \frac{E_2}{E_1}, \\ R_2 &= \frac{C_1}{E_1}. \end{aligned} \quad (24)$$

In order to constrain the number of parameters, it is assumed that the 3-parameter viscoelastic model can be downgraded to the elastic model when the load is applied to the material in absolute static force. This means that if the existence of dash-pot is ignored, two springs in series (E_1 and E_2) in the model perform the same value with the modules of elasticity in static state E_0 . In this way, three parameters will be reduced to two parameters. This means that, in this static state of this example,

$$E_0 = \frac{E_1 E_2}{E_1 + E_2} = E^* = 1.05 \times 10^{11} \text{ Pa}. \quad (25)$$

The diameter of the ball is 5/32 inches and the height of dropping distance is 2 inches. Since there are at least two parameters to be determined in the pounding force model proposed in this paper, the minimum error will be optimized in the case that the peak value is same with the experimental result. The information of the optimization process is shown as follows:

$$\text{Optimizing variable: } R = [R_1, R_2].$$

$$\begin{aligned} \text{Constrain condition: } \max \quad & (F(t)) = 80.3 \text{ N} \\ \min \quad & \text{error} \end{aligned} \quad (26)$$

From (24) and (25), parameters R_1 and R_2 are independent of one another. According to parametric study

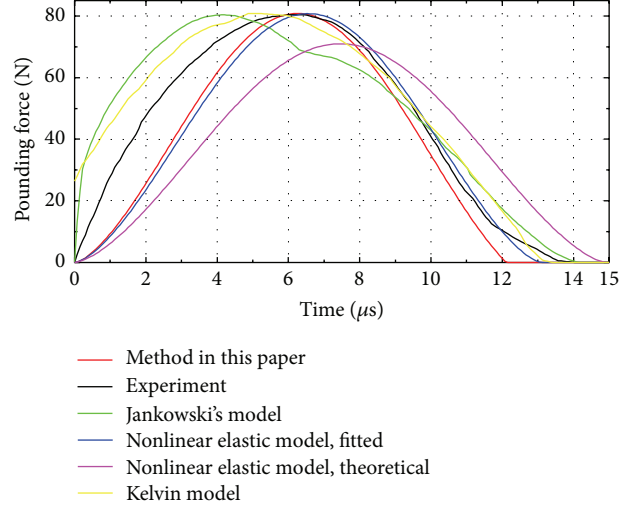


FIGURE 6: Time histories of pounding force of the steel ball dropping onto a rigid surface.

shown later, R_1 is mainly related with the height of the curve without changing areas surrounded by curve, and R_2 only affects the peak value in a limited range. Therefore, the optimization process is relatively easy and can be carried out by manual adjustment. In this way, the parameters of linear viscoelasticity can be determined.

Figure 6 shows the comparison results of impact force-time history among the methods proposed in this paper and other existing pounding models. Based on the comparison, the proposed model, Kelvin model, Jankowski's model [29], and the nonlinear elastic model are fitted by the same peak value with experimental results, in which the curve of the proposed model is obtained by optimizing the error through (23). The pink curve, namely, the nonlinear elastic model, (theoretical) is based on theoretical calculation through (4), where value k_H is determined in Table 1.

The red curve corresponds to the proposed model, where the optimized value of R_1 is 0.46 and R_2 is 0.02. It is found that it shows little difference with the experimental result in the descending part. The time corresponding to the peak value of the pounding force is exactly the same with experimental results, which is at about $6.23 \mu\text{s}$. The nonlinear elastic model result (pink curve, being not fitted with peak value), which is calculated theoretically through (4), has similar shape to the curve of the proposed model except for the peak value of 71.0 N and the time duration. After fitting the nonlinear elastic model with experimental results in the same peak value, the fitted curve (blue curve) is almost coincident with the proposed curve in this paper. This is because the pounding process for dropping iron ball is an elastic colliding process. $R_2 = 0.02$ in the proposed model is so “large” to make the calculating model “rigid” enough to perform as an elastic body. Actually, due to the calculation and parametric study in next section, when parameter R_2 is larger than 2×10^{-4} , parameter R_2 will not influence the curve shape.

The relative error of the proposed model in this paper is 19.8% as compared with nonlinear elastic model which

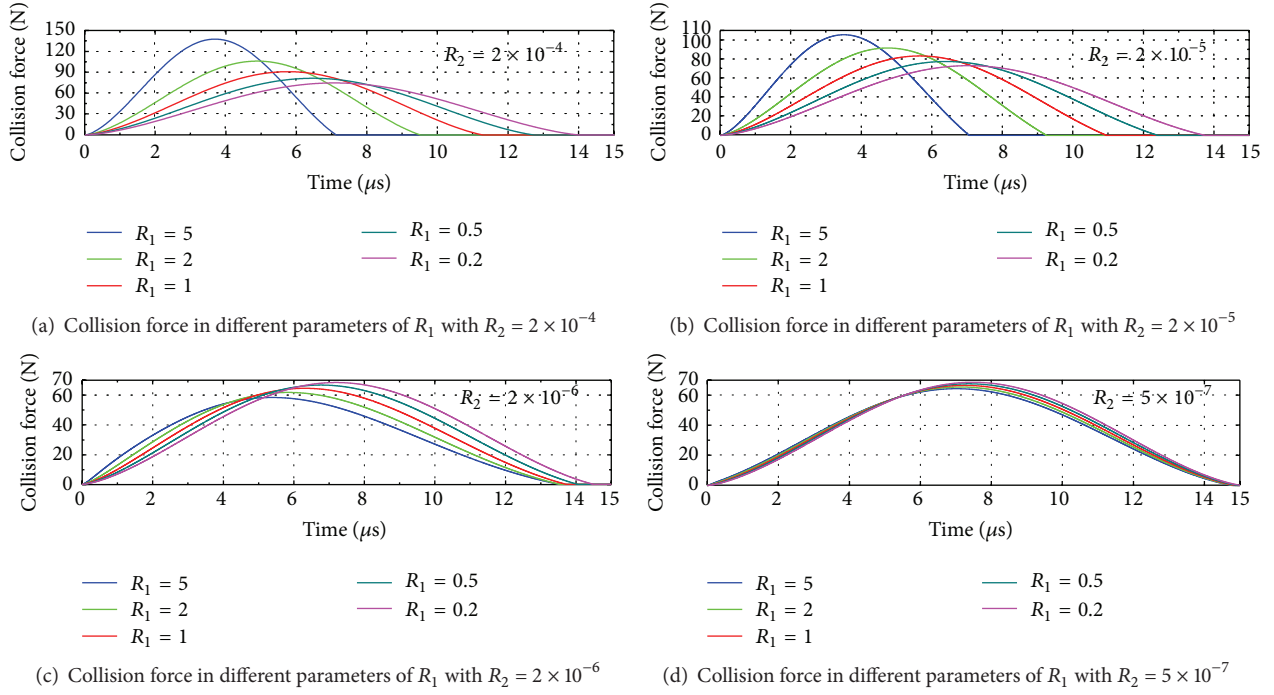


FIGURE 7: Collision force influenced by parameters of R_1 with different R_2 .

is 19.6%. There is only a little gap between them. This means that the nonlinear elastic model (peak value fitted) is precise enough for the case of steel-steel colliding. This is also in accordance with the fact that elasticity is the main property of steel material when the viscoelasticity is ignored. When the elasticity takes the dominant position, the proposed viscoelastic model will be degenerated into elastic model. The relative errors of Jankowski's model, Kelvin model (yellow curve), and nonlinear elastic model (theoretically) are 21.3%, 15.3%, and 35.0%, respectively. The total acting time of the model proposed in this paper is about 12 μs, and the experimental time is 14 μs.

4.2. Parametric Study of the Proposed Model. The proposed model is based on three-parameter viscoelastic constitutive model, but only two parameters are mutually independent according to the assumptions above. In order to study the influences of the two parameters, different curves with different parameters are calculated and plotted as shown in Figure 7.

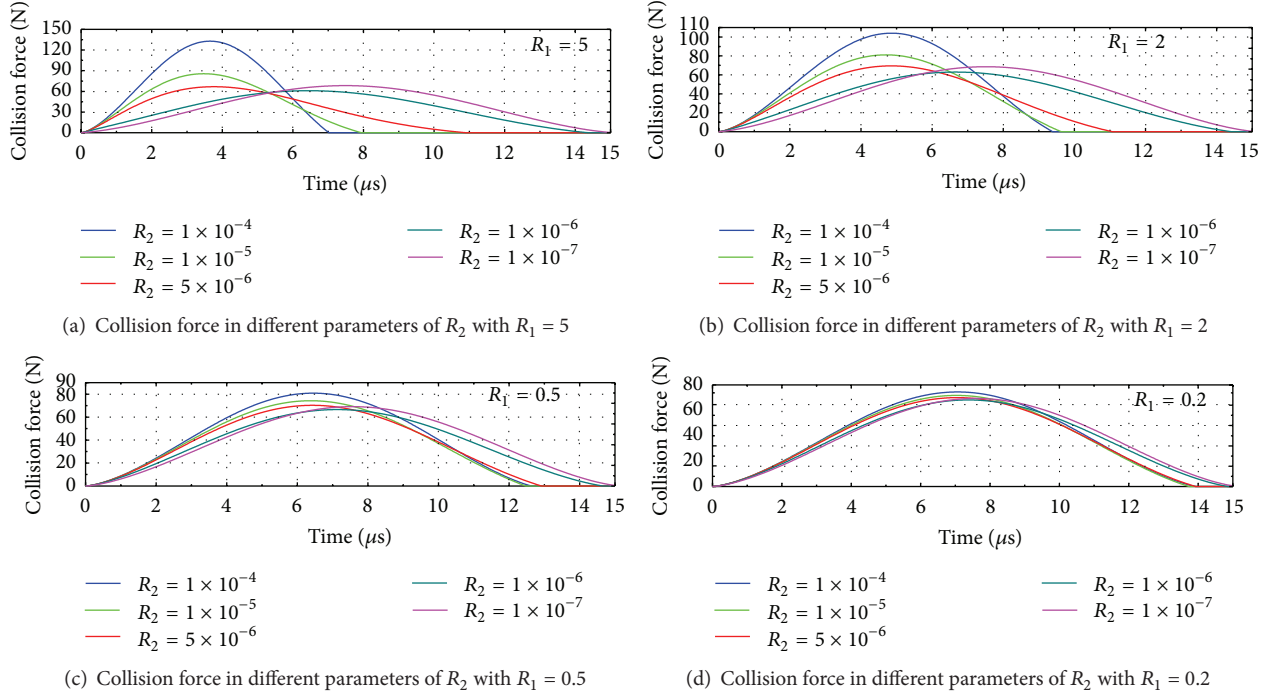
The influences of R_1 are shown in Figure 7, in which R_1 changes as 5, 2, 1, 0.5, and 0.2. R_2 is 2×10^{-4} , 2×10^{-5} , 2×10^{-6} , and 2×10^{-7} , respectively. It can be concluded from Figure 7(a) that when R_1 increases from 0.2 to 5, the peak value of pounding force will increase from 72 N to 142 N. The pounding duration time also rises from 7.5 μs to 14 μs. The shapes of curves are almost symmetric and all of these five curves have almost the same areas in terms of time-force axis represented curve, which means they have the same total impulse.

Figure 7(b) shows the collision forces in the case that $R_2 = 2 \times 10^{-5}$. The curves have similar changing trends and

symmetry curve shapes to curves in Figure 7(a) in which R_1 decreases from 5 to 0.2. When $R_1 = 5$, 2, and 1, the peak value decreases dramatically compared with the results in Figure 7(a). However, for $R_1 = 0.5$ and 0.2, both the peak value and the duration of the curves remain unchanged.

Figure 7(c) is corresponding to the case that $R_2 = 2 \times 10^{-6}$. The curves show a different variation tendency. When R_1 increases from 0.2 to 5, the peak value of pounding force will decrease from 58 N to 69 N. The curve shapes are no longer symmetric and the moment of peak value is not at the middle of the duration but moves forward to the forefront. Figure 7(d) corresponds to the case that $R_2 = 2 \times 10^{-7}$. It can be seen that all the curves are almost coincident with pink curve ($R_1 = 0.2$) in forefront of duration and only small gaps in second half. Also the curves are symmetric and similar to Figure 7(c).

Based on the comparison of these four graphs, it can be discovered that the shape and value of curves almost remain the same with parameter R_2 when R_1 is less than 0.2. The larger R_1 is, the greater the variation amplitude will occur. What is more, it should be noted that when R_2 is large enough (larger than 2×10^{-4} in this case), all curves have almost the same areas in terms of time-force axis, which means that they have the same total impulse. This proves that the pounding process is in almost elastic state, and the effect of dash-pot can be regarded as a rigid body in this pounding case. Spring E_1 which is in parallel with dash-pot in constitutive model is inoperative. Therefore, regardless of the variation of R_1 , momentums of colliding bodies before and after collision remain unchanged. On the other hand, when R_2 is small enough (less than 5×10^{-7} in this case), all curves tend to be coincidental. At this time, the dash-pot in constitutive model

FIGURE 8: Collision force influenced by parameters of R_2 in different R_1 .

can be ignored and only two series of connecting springs are left in the constitutive model.

The influences of R_2 are shown in Figure 8, in which R_1 is 5, 2, 0.5, and 0.2, respectively. The variation values for R_2 is 1×10^{-4} , 1×10^{-5} , 5×10^{-6} , 1×10^{-6} , and 1×10^{-7} . According to Figures 8(a), 8(b), and 8(c), it can be concluded that when the value of R_2 is smaller, the peak value of collision force firstly decreases and then increases. The larger R_1 is, the greater the peak values of the curves will be. As R_1 decreases from 5 to 0.2, all curves tend to be flat except the one corresponding to $R_2 = 1 \times 10^{-7}$ which remains almost unchanged. When R_1 is less than 0.2 (Figure 8(d)), all curves tend to be coincidental with the pink curve (corresponding to $R_2 = 1 \times 10^{-7}$). This reason is similar to previous analysis of Figure 7. From (25), when R_1 is small enough (less than 0.2 in this case), parameter E_1 in the constitutive model will be much bigger than C_1 . The dash-pot can be ignored, and the whole constitutive model changes to the elastic state again.

4.3. Concrete-to-Concrete Impact. The second example is the collision between concrete-to-concrete, which was carried out by van Mier et al. [35] in 1991. He utilized a concrete striker to hit one end of a long concrete pole and obtained a series of force-time curves for different striker masses and velocities. In most cases, the concrete of striker head involves plastic failure, which can be recognized by the step in force-time curve. The curves with obvious peak at lower velocity are selected as an example (57 kg, 1.5 m/s). This example was also calculated by Jankowski [29] in 2005.

The same simplified approach as that in the previous example is utilized to reduce three parameters to two parameters in pounding force model so as to optimize the model

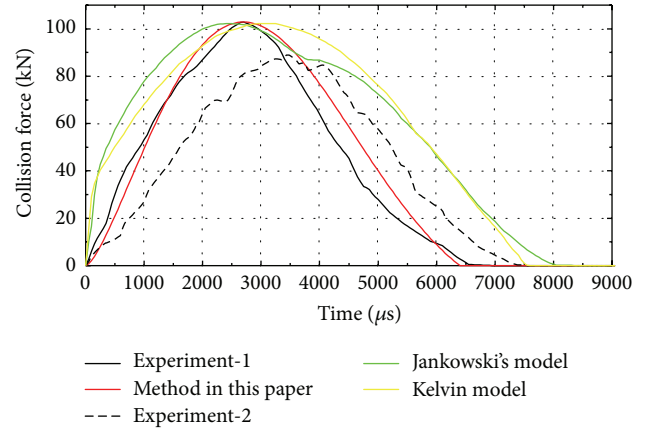


FIGURE 9: Collision force-time histories of concrete-to-concrete (velocity 1.5 m/s).

parameters. However, it is discovered that the fitting curve with the same peak value as the experimental result cannot be obtained by adjusting parameters R_1 and R_2 . This is because that although there is a peak in experimental curves, the plasticity and damage did occur during the pounding process. Therefore, the third parameter E_0 must be considered, which represents the equivalent modulus of elasticity in static state. Afterwards, the curve is fitted with the first experimental result manually, and the fitting results are shown in Figure 9, in which $E_1 = E_2 = 3.2 \times 10^{10}$ Pa, $C_1 = 3.2 \times 10^{10}$ Pa. It can be found that the relative error of the fitting curve is 12.5%, which is smaller than 22.9% of Jankowski's model and 23.8% of the linear viscoelastic model (Kelvin model).

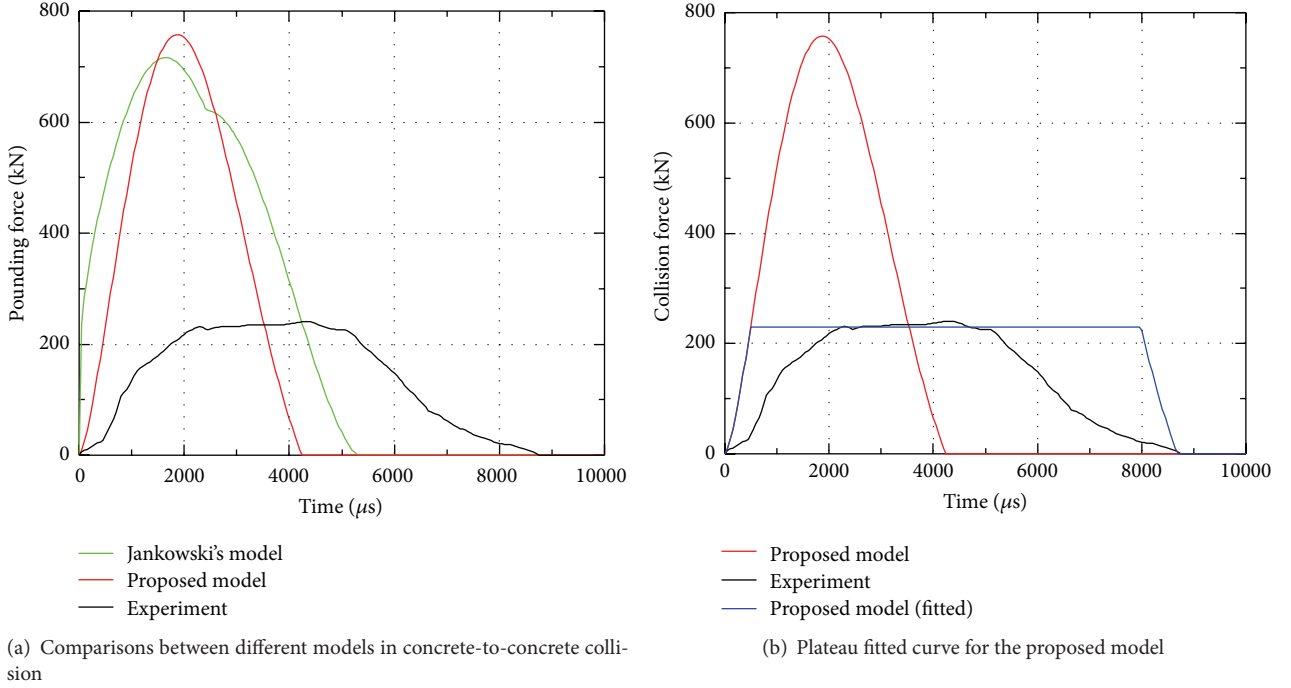


FIGURE 10: Concrete pounding calculation results with initial velocity of 2.5 m/s.

In the previous fitting process of concrete-to-concrete pounding force models, the applicability for these 3 parameters in real practice must be studied. Curves in Figure 10 are the concrete pounding calculation results with the initial velocity of 2.5 m/s.

As shown in Figure 10, it is found that not only the model proposed in this paper but also Jankowski's model has great errors in peak values (Figure 10(a)), which are 227.5% and 209.4%, respectively. Because the plasticity and damage occur during the collision process, the experimental curve has a significant plateau. It is assumed that when the value of the pounding force calculation of the proposed model is the same as that of the plateau, the curve will be flat until the area under the curve is same with the original calculated results. The fitted curve (blue line) is shown in Figure 10(b). It can be discovered that the ending time of the fitted curve and experimental results is basically the same. The surrounding area difference between these two curves is the momentum loss from the pounding process, which comes from the energy absorption induced by plasticity and damage in concrete colliding bodies. According to the analysis, it can be concluded that all of these pounding models, which are based on elastic or viscoelastic analysis, cannot be utilized in the pounding cases with obvious plasticity or damage.

5. Vibration Control Application of Proposed Method

5.1. Pounding Force Model of Pounding TMD. An analysis example is introduced to illustrate the process of constructing a pounding force model. Pounding tuned mass damper (PTMD) is a new type of vibration control device [20,

36, 37] based on traditional tuned mass damper (TMD). An additional pounding constrain device which is covered by polymers is incorporated to dissipate the energy from deformation of polymers in the collision process.

Figure 11 is the sketch of pounding TMD utilized in signal pole vibration control. In order to analyse the vibration characteristics of this device, the pounding force model needs to be constructed.

The following is the process to construct the pounding model by utilizing the above method. The collision between steel beam and polymer ring can be simplified as a cylinder contacting a plane with curvature. According to contact mechanics [34], when the thickness of polymer ring is larger than a certain extent, the equation of elastic pounding force between two contact bodies can be written as follows:

$$F_c = \frac{\pi}{4} E^* l \delta, \quad (27)$$

$$\frac{1}{E^*} = \frac{1 - \nu_p^2}{E_p} + \frac{1 - \nu_s^2}{E_s},$$

where ν_p , ν_s , E_p , and E_s are the Poisson's ratio and modulus of elasticity for polymer and steel, respectively, l is the width of ring, and δ is the penetration displacement.

In the case of polymer contact with steel, the modulus of elasticity of steel is far larger than that of polymer. Therefore, the expression of E^* can be simplified as

$$E^* = \frac{E_p}{1 - \nu_p^2}. \quad (28)$$

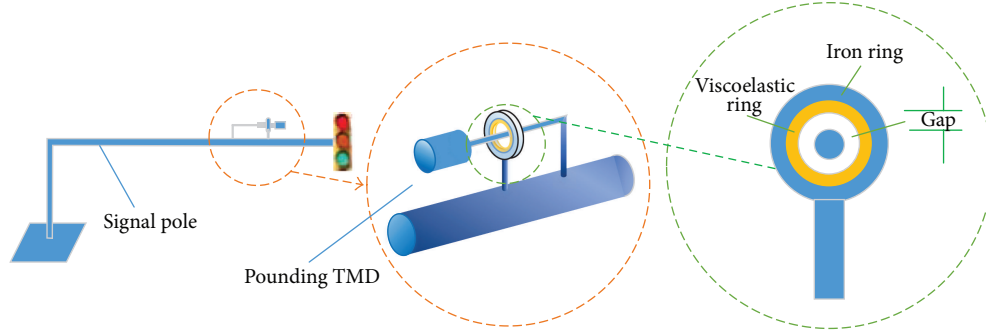


FIGURE 11: Pounding TMD device.

The expression of pounding force is

$$F_c = \frac{\pi}{4} \frac{l}{1 - v_p^2} E_p \delta. \quad (29)$$

For a certain range of strain rate for polymer, Poisson's ratio can be assumed as a constant. When the viscoelasticity of polymer is considered, the same expression in Laplace domain can be achieved according to the Correspondence Principle of Viscoelasticity:

$$\bar{F}(s) = \left(\frac{\pi}{4} \frac{l}{1 - v_p^2} \right) \bar{E}_p(s) \bar{\delta}(s). \quad (30)$$

Based on the above analysis, for viscoelastic properties of polymers,

$$\bar{E}(s) = \frac{\bar{\sigma}(s)}{\bar{\epsilon}(s)} = \frac{\bar{Q}(s)}{\bar{P}(s)}. \quad (31)$$

By inverting Laplace transformation in both sides of (30), expression of pounding force considering viscoelasticity of materials can be achieved:

$$F(t) = \left(\frac{\pi}{4} \frac{l}{1 - v_p^2} \right) \mathcal{L}^{-1} \left(\frac{\bar{Q}(s)}{\bar{P}(s)} \right) \delta(t). \quad (32)$$

For linear viscoelastic materials, $\bar{Q}(s)$ and $\bar{P}(s)$ are polynomial of s and they are governed by the constitutive model shown in (31). For some software, such as MATLAB SIM-LINK, transfer function instrument can replace the inverse Laplace transformation directly. In addition, it is suitable for different linear constitutive models of viscoelastic materials. As for more complicated linear constitutive models, only the sections of polynomials will change.

5.2. Vibration Control Simulation for Pounding TMD. Li et al. [20] carried out a vibration control study on signal pole with pounding TMD. Viscoelastic tapes VHB4936, which made by 3M Company, are made into a ring as pounding damper. The experimental model and fitting curves are shown in Figure 12. The pounding TMD is made up by two steel rods, the diameter of which is 12 mm. The first experiment is to put the lateral rod pounding the constrain device (Figure 12(b)).

In Figure 12(a), the black curve is the pounding experiment result, and the green curve is the fitting curve of Jankowski's model in literature [20], in which fitting criterion is not the same peak value but the minimum error defined by (20)-(21). The red curve is the fitting result in the proposed model, in which $E_0 = 0.6$ MPa, $R_1 = 0.5$, and $R_2 = 0.01$. The errors of Jankowski's model and the proposed model are 23.4% and 16.6%, respectively.

In order to investigate the validity of the proposed method, the pounding TMD is simulated and compared with the experiments based on literature [20]. For the pounding TMD model shown in Figure 13, literature [20] simplifies the model to double-spring-oscillator model, which is shown in Figure 13(b). m_1 , m_2 , k_1 , k_2 , c_1 , and c_2 are masses, rigid toughness, and damping coefficients for experimental traffic pole model and the pounding TMD device, respectively. They can be deduced from the FEM models analysis and resonant vibration tests results in literature [20].

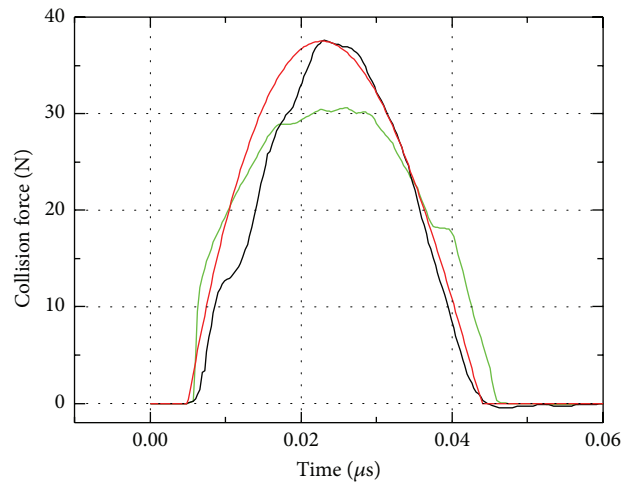
x_1 and x_2 are the displacements of two colliding bodies, and the gap is the distance between L-shaped beam and fixed aluminium ring on traffic pole model with viscoelastic tapes. Therefore, the pounding force $f(t)$ between two oscillators can be illustrated as the following formula:

$$\begin{aligned} f(t) &= F(t) x_2 - x_1 \geq \text{gap}, \\ f(t) &= F(t) x_2 - x_1 \leq -\text{gap}, \\ f(t) &= 0, \quad -\text{gap} \leq x_2 - x_1 \leq \text{gap}. \end{aligned} \quad (33)$$

The vibration equations can be written as follows:

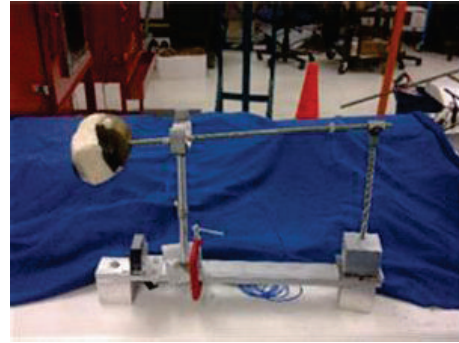
$$\begin{aligned} m_1 \ddot{x}_1 + c_1 \dot{x}_1 + k_1 x_1 - k_2 (x_2 - x_1) - c_2 (\dot{x}_2 - \dot{x}_1) \\ = f(t), \\ m_2 \ddot{x}_2 + c_2 (\dot{x}_2 - \dot{x}_1) + k_2 (x_2 - x_1) + f(t) = 0. \end{aligned} \quad (34)$$

The free vibration simulation for pounding TMD is carried out and compared to the experiment in Figure 14. According to the experimental configuration in literature [20], in which the first-order dominant frequency of the experiment model is 3.03 Hz, damping ratio is 1%, and the mass at the end of pounding TMD is 3.7 lbs. In this simulation, $m_1 = 20$ kg, $m_2 = 1.67$ kg, $k_1 = 7248.9$ N/m, $k_2 = 592.9$ N/m, $c_1 = 7.615$ N·s/m, and $c_2 = 0.6312$ N·s/m.



— Jankowski's model fitting results
 — Experiment results
 — Fitting results with proposed model

(a) Fitting curves in different models

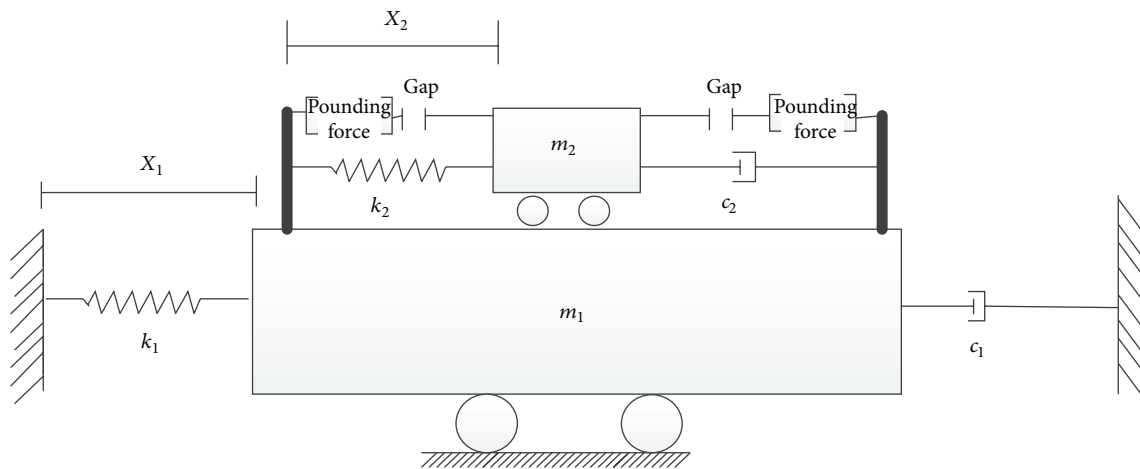


(b) The experiment model of pounding TMD [20]

FIGURE 12: Pounding TMD experimental configuration and fitting curves by different methods.



(a) Traffic pole with pounding TMD [20]



(b) Simplified pounding analysis model

FIGURE 13: Traffic pole device and simplified pounding TMD model.

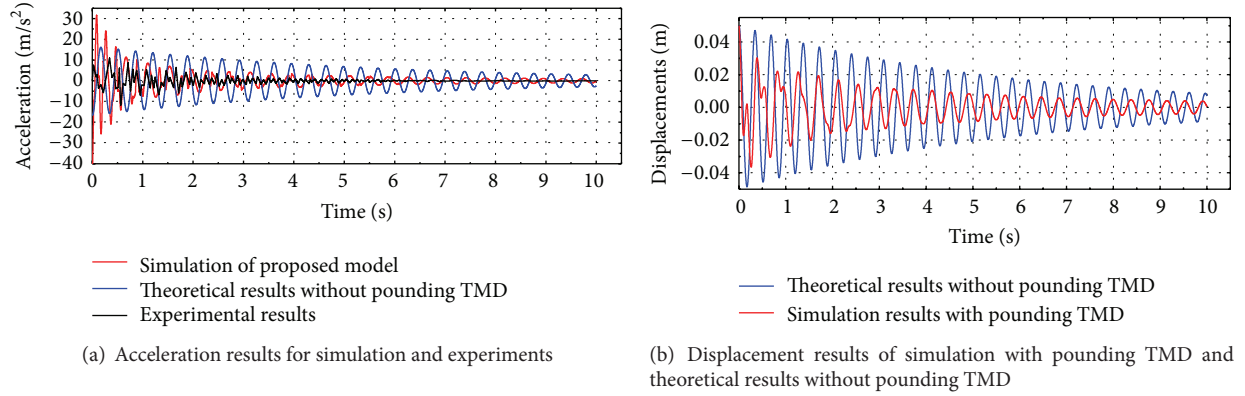


FIGURE 14: Comparisons of acceleration and displacements for simulation and experiments.

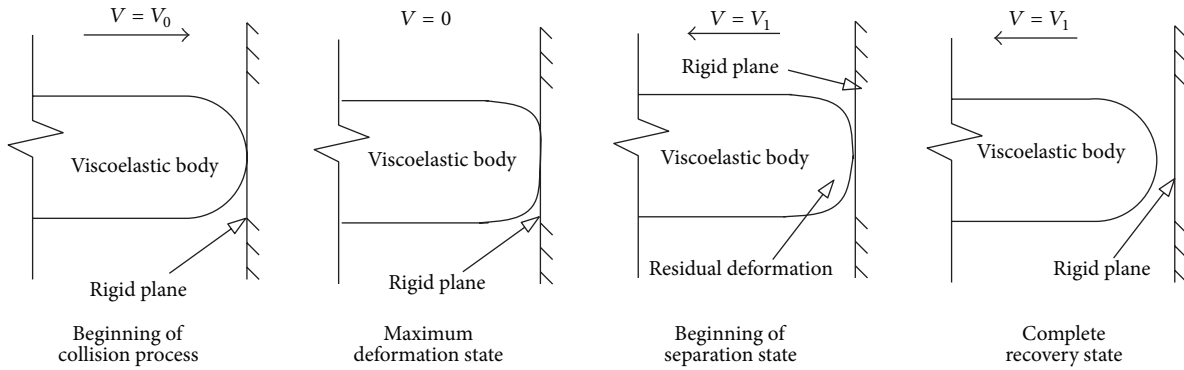


FIGURE 15: Collision process for viscoelastic materials.

The values of gap and widths which are omitted in literature [20] are assumed as 2 cm and 0.3 cm, respectively. The initial displacement applied to the system is 5 cm.

Figure 14(a) is the comparisons of acceleration in simulation and experiments. The blue curve is the theoretical result without pounding TMD. Black curve and red curve are experimental result and simulation result with pounding TMD, respectively. It is found that both the black curve and red curve show the effectiveness of pounding TMD on vibration control, particularly the acceleration suppression. In the initial section, although the value of acceleration in simulation result is much larger than experimental vibration response without pounding TMD, the displacement of the system with pounding TMD (shown in Figure 14(b)) decreases more rapidly than that in the system without pounding device. In the latter section, the red curve is also larger than the experimental value and changes to a sinusoidal wave. This is because when the relative displacement of pounding TMD main model beam is less than the value of the gap, there will be no collision between them and the whole model will vibrate in a way without pounding effect. In Figure 14(b), the response of displacement for simulation model with pounding TMD shows the effectiveness of pounding TMD, and, in the terminal section, the curve changes to sinusoidal wave, which is the same with Figure 14(a). There is a certain error between simulation and experimental results. The reason is that several parameters of experiment details

cannot be precisely determined from insufficient literature details.

Therefore, the proposed model can only illustrate a rough trend in both single pounding process and vibration control process. The study in this paper presents only a first-step assessment, and further numerical and experimental validations are needed in inelastic pounding process.

6. Discussion and Conclusion

6.1. Discussion. In the calculation results of different pounding force models, some of them have traction effect at the end of pounding process, such as linear viscoelastic model, nonlinear viscoelastic model, and 3-parameter model of this paper (the traction has been removed). They all contain damper (dash-pot) in the constitutive model. The existence of damper leads to a delay of material recovery to the original position, which means two colliding bodies begin to separate at the end of restitution process. However, residual deformation still exists and it can bounce back after certain time (Figure 15).

When the pounding force is simulated by utilizing different pounding force models, there is an implicit hypothesis that the full recovery of deformation for colliding bodies occurs concurrently with the separated state. Therefore, for all elastic models, including linear and nonlinear elastic models, the hypothesis is tenable. Nevertheless, as for models with

dash-pot part, separation occurs before the colliding body reaches the complete recovery state, and the traction forces will be deduced at the end of restitution section.

The traction force in the calculation models does not exist in reality, and it has been removed in simulation in the former calculation results. It will affect the calculation results significantly and may cause the divergence in the case of certain set of parameters, especially in the circumstance of extremely little gap values.

6.2. Conclusion. An updated pounding force analysis method based on viscoelasticity of materials is proposed in this paper. Comparisons among proposed pounding force model and other traditional models are analysed. Moreover, the proposed model is applied to simulating the pounding TMD device so as to verify the validity of the model.

The main contribution of the proposed method is that it expands traditional Kelvin viscoelastic model to 3-parameter linear solid viscoelastic model. By utilizing contact mechanics can not only relative parameters be determined but also constitutive model coefficients can be obtained based on the pounding results. For classic elastic collision, the proposed model can also be degenerated or downgraded to represent a linear elastic model to study the pounding process. The feasibility of utilization in different geometric conditions overcomes the shortcoming of classic pounding force models.

Compared with other models, the proposed 3-parameter model for pounding force has shown a certain accuracy in fitting elastic pounding experimental results. However, for plasticity or deformations with damage, such as concrete pounding, it has some limitation in fitting the experiment to a higher precision.

When it is applied in analysis on pounding TMD for vibration control case, there is certain error as compared with the experimental result. However, it has been proved that it can illustrate the changing trend of vibration control process.

The advantage of the method proposed in this paper is that it contains separated parameters of pounding details. What is more, it shows better prospect in calculating polymer materials poundings which have obvious viscoelasticity characteristics. However, it must be noted that the study here is only a first step. Regardless of the cheerful prospect, it still needs a more careful assessment of the model performance, especially in the presence of inelastic response.

Competing Interests

The authors declare that there are no competing interests regarding the publication of this paper.

Acknowledgments

The research is supported by the National Natural Science Foundation of China (Project nos. 51678322 and 51409056), Natural Science Foundation of Heilongjiang Province (E2015047), the Fundamental Research Funds for the Central Universities (HEUCF160202), and the Taishan Scholar Priority Discipline Talent Group program funded by the Shan Dong Province.

References

- [1] N. Chouw and H. Hao, "Pounding damage to buildings and bridges in the 22 february 2011 christchurch earthquake," *International Journal of Protective Structures*, vol. 3, no. 2, pp. 123–140, 2012.
- [2] G. Mondal and D. C. Rai, "Performance of harbour structures in Andaman Islands during 2004 Sumatra earthquake," *Engineering Structures*, vol. 30, no. 1, pp. 174–182, 2008.
- [3] T. C. Shin, K. W. Kuo, W. H. K. Lee, T. L. Teng, and Y. B. Tsai, "A preliminary report on the 1999 Chi-Chi (Taiwan) earthquake," *Seismological Research Letters*, vol. 71, no. 1, pp. 24–30, 2000.
- [4] Y. Wang, "Lessons learned from the '5.12' Wenchuan Earthquake: evaluation of earthquake performance objectives and the importance of seismic conceptual design principles," *Earthquake Engineering and Engineering Vibration*, vol. 7, no. 3, pp. 255–262, 2008.
- [5] J. Wood and P. Jennings, "Damage to freeway structures in the San Fernando earthquake," *Bulletin of the New Zealand Society for Earthquake Engineering*, vol. 4, no. 3, pp. 347–376, 1971.
- [6] C.-J. Wang and M.-H. Shih, "Performance study of a bridge involving sliding decks and pounded abutment during a violent earthquake," *Engineering Structures*, vol. 29, no. 5, pp. 802–812, 2007.
- [7] R. Jankowski, "Earthquake-induced pounding between equal height buildings with substantially different dynamic properties," *Engineering Structures*, vol. 30, no. 10, pp. 2818–2829, 2008.
- [8] F. Pratesi, S. Sorace, and G. Terenzi, "Analysis and mitigation of seismic pounding of a slender R/C bell tower," *Engineering Structures*, vol. 71, pp. 23–34, 2014.
- [9] K. Shakya and A. C. Wijeyewickrema, "Mid-column pounding of multi-story reinforced concrete buildings considering soil effects," *Advances in Structural Engineering*, vol. 12, no. 1, pp. 71–85, 2009.
- [10] P. C. Polycarpou and P. Komodromos, "Earthquake-induced poundings of a seismically isolated building with adjacent structures," *Engineering Structures*, vol. 32, no. 7, pp. 1937–1951, 2010.
- [11] K. Ye, L. Li, and H. Zhu, "A modified Kelvin impact model for pounding simulation of base-isolated building with adjacent structures," *Earthquake Engineering and Engineering Vibration*, vol. 8, no. 3, pp. 433–446, 2009.
- [12] L. L. Cui, A. X. Guo, and H. Li, "Investigation of the parameters of hertz impact model for the pounding analysis of highway bridge," *Procedia Engineering*, vol. 14, pp. 2773–2778, 2011.
- [13] H. Yang and X. Yin, "Transient responses of girder bridges with vertical poundings under near-fault vertical earthquake," *Earthquake Engineering & Structural Dynamics*, vol. 44, no. 15, pp. 2637–2657, 2015.
- [14] E. G. Dimitrakopoulos, "Seismic response analysis of skew bridges with pounding deck-abutment joints," *Engineering Structures*, vol. 33, no. 3, pp. 813–826, 2011.
- [15] B. Shrestha, H. Hao, and K. Bi, "Effectiveness of using rubber bumper and restrainer on mitigating pounding and unseating damage of bridge structures subjected to spatially varying ground motions," *Engineering Structures*, vol. 79, pp. 195–210, 2014.
- [16] J.-H. Won, H.-S. Mha, and S.-H. Kim, "Effects of the earthquake-induced pounding upon pier motions in the multi-span simply supported steel girder bridge," *Engineering Structures*, vol. 93, pp. 1–12, 2015.

- [17] B. Madani, F. Behnamfar, and H. Tajmir Riahi, "Dynamic response of structures subjected to pounding and structure-soil-structure interaction," *Soil Dynamics and Earthquake Engineering*, vol. 78, pp. 46–60, 2015.
- [18] K. Bi and H. Hao, "Numerical simulation of pounding damage to bridge structures under spatially varying ground motions," *Engineering Structures*, vol. 46, pp. 62–76, 2013.
- [19] M. Goland, P. Wickersham, and M. Dengler, "Propagation of elastic impact in beams in bending," *Journal of Applied Mechanics*, vol. 22, pp. 1–7, 1955.
- [20] L. Li, G. Song, M. Singla, and Y.-L. Mo, "Vibration control of a traffic signal pole using a pounding tuned mass damper with viscoelastic materials (II): experimental verification," *Journal of Vibration and Control*, vol. 21, no. 4, pp. 670–675, 2015.
- [21] A. Ruangrassamee and K. Kawashima, "Control of nonlinear bridge response with pounding effect by variable dampers," *Engineering Structures*, vol. 25, no. 5, pp. 593–606, 2003.
- [22] W. Goldsmit, *The Theory and Physical Behavior of Colliding Solids*, Arnold, London, UK, 1960.
- [23] K. T. Chau and X. X. Wei, "Pounding of structures modelled as non-linear impacts of two oscillators," *Earthquake Engineering & Structural Dynamics*, vol. 30, no. 5, pp. 633–651, 2001.
- [24] C. P. Pantelides and X. Ma, "Linear and nonlinear pounding of structural systems," *Computers & Structures*, vol. 66, no. 1, pp. 79–92, 1998.
- [25] S. A. Anagnostopoulos, "Pounding of buildings in series during earthquakes," *Earthquake Engineering & Structural Dynamics*, vol. 16, no. 3, pp. 443–456, 1988.
- [26] S. A. Anagnostopoulos, "Equivalent viscous damping for modeling inelastic impacts in earthquake pounding problems," *Earthquake Engineering and Structural Dynamics*, vol. 33, no. 8, pp. 897–902, 2004.
- [27] V. K. Agarwal, J. M. Niedzwecki, and J. W. van de Lindt, "Earthquake induced pounding in friction varying base isolated buildings," *Engineering Structures*, vol. 29, no. 11, pp. 2825–2832, 2007.
- [28] P. Komodromos, "Simulation of the earthquake-induced pounding of seismically isolated buildings," *Computers & Structures*, vol. 86, no. 7-8, pp. 618–626, 2008.
- [29] R. Jankowski, "Non-linear viscoelastic modelling of earthquake-induced structural pounding," *Earthquake Engineering and Structural Dynamics*, vol. 34, no. 6, pp. 595–611, 2005.
- [30] R. Jankowski, "Analytical expression between the impact damping ratio and the coefficient of restitution in the non-linear viscoelastic model of structural pounding," *Earthquake Engineering & Structural Dynamics*, vol. 35, no. 4, pp. 517–524, 2006.
- [31] R. Jankowski, K. Wilde, and Y. Fujino, "Pounding of superstructure segments in isolated elevated bridge during earthquakes," *Earthquake Engineering & Structural Dynamics*, vol. 27, no. 5, pp. 487–502, 1998.
- [32] S. Mahmoud, "Modified linear viscoelastic model for elimination of the tension force in the linear viscoelastic," in *Proceedings of the 14th World Conference on Earthquake Engineering*, 2008.
- [33] S. Khatiwada, N. Chouw, and J. W. Butterworth, "A generic structural pounding model using numerically exact displacement proportional damping," *Engineering Structures*, vol. 62-63, pp. 33–41, 2014.
- [34] V. Popov, *Contact Mechanics and Friction: Physical Principles and Applications*, Springer Science & Business Media, Berlin, Germany, 2010.
- [35] J. G. M. van Mier, A. F. Pruijssers, H. W. Reinhardt, and T. Monnier, "Load-time response of colliding concrete bodies," *Journal of Structural Engineering*, vol. 117, no. 2, pp. 354–374, 1991.
- [36] G. B. Song, P. Zhang, L. Y. Li et al., "Vibration control of a pipeline structure using pounding tuned mass damper," *Journal of Engineering Mechanics*, vol. 142, no. 6, Article ID 04016031, 2016.
- [37] C.-C. Lin, J.-F. Wang, and J.-M. Ueng, "Vibration control identification of seismically excited mdof structure-PTMD systems," *Journal of Sound and Vibration*, vol. 240, no. 1, pp. 87–115, 2001.

Research Article

Analysis of Free Pendulum Vibration Absorber Using Flexible Multi-Body Dynamics

Emrah Gumus and Atila Ertas

Mechanical Engineering Department, Texas Tech University, Lubbock, TX 79409, USA

Correspondence should be addressed to Atila Ertas; aertas@coe.ttu.edu

Received 9 February 2016; Revised 3 July 2016; Accepted 11 July 2016

Academic Editor: Londono Monsalve

Copyright © 2016 E. Gumus and A. Ertas. This is an open access article distributed under the Creative Commons Attribution License, which permits unrestricted use, distribution, and reproduction in any medium, provided the original work is properly cited.

Structures which are commonly used in our infrastructures are becoming lighter with progress in material science. These structures due to their light weight and low stiffness have shown potential problem of wind-induced vibrations, a direct outcome of which is fatigue failure. In particular, if the structure is long and flexible, failure by fatigue will be inevitable if not designed properly. The main objective of this paper is to perform theoretical analysis for a novel free pendulum device as a passive vibration absorber. In this paper, the beam-tip mass-free pendulum structure is treated as a flexible multibody dynamic system and the ANCF formulation is used to demonstrate the coupled nonlinear dynamics of a large deflection of a beam with an appendage consisting of a mass-ball system. It is also aimed at showing the complete energy transfer between two modes occurring when the beam frequency is twice the ball frequency, which is known as autoparametric vibration absorption. Results are discussed and compared with findings of MSC ADAMS. This novel free pendulum device is practical and feasible passive vibration absorber in the mitigation of large amplitude wind-induced vibrations in traffic signal structures.

1. Introduction

Many mechanical systems can be modeled as a beam with a lumped mass, such as a wing of an airplane with a mounted engine, a robot arm carrying a welding tool, or a traffic light. Understanding the dynamics of those systems having flexible and slender beams is of great importance in vibration analyses to prevent catastrophic failures of the structures. Therefore, there is an extensive amount of experimental and numerical work on the responses of beams in the nonlinear dynamics and vibration field.

There is widespread interest in pendulum modeling and the use of the pendulum as a vibration absorber. This interest ranges from the dynamics of Josephson's Junction in solid state physics [1] to the rolling motion of ships [2, 3] and the rocking motion of buildings and structures under earthquakes [4].

Autoparametric vibration absorber is a device designed to absorb the energy from the primary mass (main mass)

at conditions of combined internal and external resonance. Autoparametric resonance is a special case of parametric vibration and is said to exist if the conditions at the internal resonance and external resonance are met simultaneously due to external force [5–7]. Autoparametric vibration absorber has received considerable attention since mid-1980s and researchers published many interesting papers [8–19]. There are many practical examples of designing vibration absorber published using the concept of autoparametric resonance [20–26].

The first studies in multibody systems were on the dynamics of the rigid bodies which were related to gyro dynamics, the mechanism theory, and biomechanics. A good review of this topic is given by Schiehlen [27]. One of the first formalisms is given by Hooker and Margulies [28] in which they analyzed the satellites interconnected with spherical joints. Another formulation was published in 1967 by Roberson and Wittenburg [29]. Wittenburg [30] wrote the first textbook on multibody dynamics in which he

explained rigid body kinematics and dynamics as well as general multibody systems. In 1988, Nikravesh [31] provided information about the computer-aided analysis of multibody systems in his textbook. Haug [32] provided basic methods of the computer-aided kinematics and dynamics for spatial and planar systems. Many more authors provided textbooks in the field of kinematic and dynamic simulations of multibody systems such as Roberson and Schwertassek [33], Huston [34], and García de Jalón and Bayo [35].

Until now, we discussed papers and textbooks that were related to the multibody systems consisting of rigid bodies. However, in many applications, bodies undergo large deformations, which necessitate the modeling of the flexible bodies. Flexible multibody systems have attracted many researchers and several flexible multibody formulations have been established such as the floating frame of reference method, incremental finite element corotational method, and the large rotation vector method. Agrawal and Shabana [36] proposed the component mode synthesis method in which each elastic component is identified by three sets of modes: rigid body, reference modes, and normal modes. Rigid body modes are used to describe the rigid body translation and large rotations of a body reference, reference modes are used to define a unique displacement field, and the normal modes are used to define the deformation relative to the body reference. An alternative formulation was proposed by Yoo and Haug [37] in which a lumped mass finite element structural analysis formulation is used to generate deformation modes. In the floating reference frame formulation, a mixed set of absolute and local deformation coordinates are used to define the configuration of the deformable body [38–40]. This method became the most widely used approach due to its straightforward nature. However, the mass matrix, centrifugal, and Coriolis forces appear to be highly nonlinear. The incremental finite element approach uses rotation angles as nodal variables, which lead to linearized kinematic equations. Therefore, models obtained by using incremental finite elements cannot describe the exact rigid body displacements [41]. In order to solve this problem in the incremental finite element approach, a different approach called the large rotation vector formulation has been proposed. In this method, finite rotations are employed instead of infinitesimal rotations, which results in an exact modeling of the rigid body displacements [42].

Most of the methods explained above suffer from highly nonlinear terms inside the mass matrix, centrifugal, and Coriolis forces. Therefore, a new approach called the absolute nodal coordinate formulation (ANCF) was proposed for the solution of large deformation problems [40, 43–50]. In this formulation, instead of the angle of rotations, absolute slopes are used as nodal variables.

In this paper, the beam-tip mass-ball structure is treated as a flexible multibody dynamic system and the ANCF formulation is used to demonstrate the coupled nonlinear dynamics of a large deflection of a beam with an appendage consisting of a mass-free pendulum system. This novel free pendulum device is practical and feasible passive vibration absorber in the mitigation of large amplitude wind-induced vibrations in traffic signal structures.

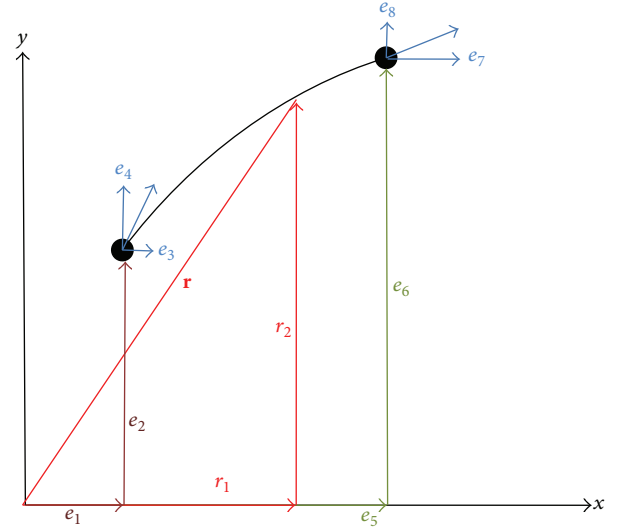


FIGURE 1: Planar beam element.

2. Formulation of Equations of Motions for Flexible Multibody Dynamics

2.1. Displacement Field. In this paper, a planar beam element is used to model flexible beam under investigation. Referring to Figure 1, the global position vector \mathbf{r} of an arbitrary point P on the element is defined in terms of the nodal coordinates and the element shape function as [44]

$$\mathbf{r} = \begin{pmatrix} r_1 \\ r_2 \end{pmatrix} = \mathbf{S}\mathbf{e}, \quad (1)$$

where \mathbf{S} is the global shape function and \mathbf{e} is the vector of element nodal coordinates defined as

$$\mathbf{e} = [e_1 \ e_2 \ e_3 \ e_4 \ e_5 \ e_6 \ e_7 \ e_8]^T. \quad (2)$$

The elements of the vector of nodal coordinates are defined as [44]

$$\begin{aligned} e_1 &= r_1(x=0), \\ e_2 &= r_2(x=0), \\ e_3 &= \frac{\partial r_1(x=0)}{\partial x}, \\ e_4 &= \frac{\partial r_2(x=0)}{\partial x}, \\ e_5 &= r_1(x=l), \\ e_6 &= r_2(x=l), \\ e_7 &= \frac{\partial r_1(x=l)}{\partial x}, \\ e_8 &= \frac{\partial r_2(x=l)}{\partial x}, \end{aligned} \quad (3)$$

where l is the beam element length and x is the axial coordinate that defines the position of an arbitrary point on

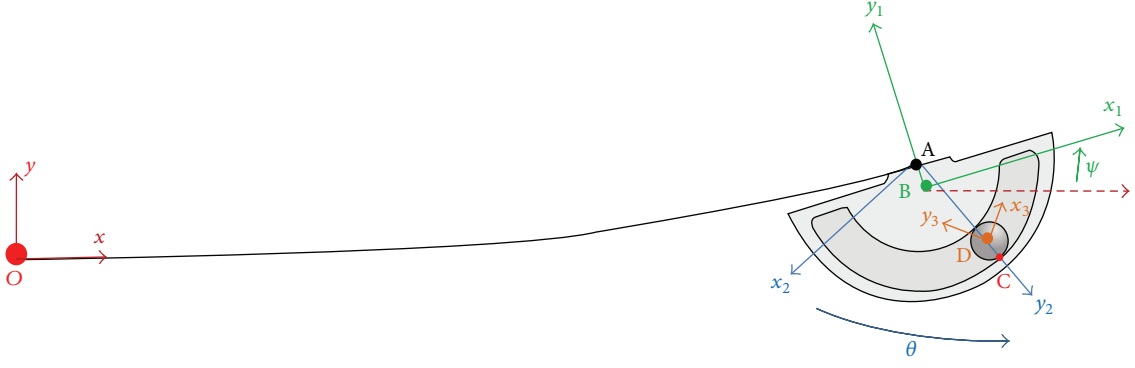


FIGURE 2: Beam coordinate system.

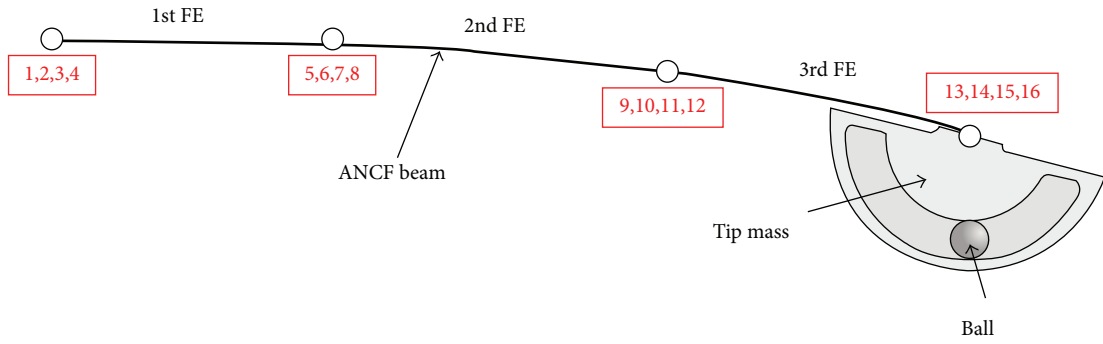


FIGURE 3: Global nodes.

the element in the undeformed state. e_1, e_2, e_5 , and e_6 are the absolute displacement coordinates and e_3, e_4, e_7 , and e_8 are the global slopes of the nodes.

The element shape function can be defined as [43]

$$\mathbf{S} = \begin{bmatrix} s_1 & 0 & s_2 & 0 & s_3 & 0 & s_4 & 0 \\ 0 & s_1 & 0 & s_2 & 0 & s_3 & 0 & s_4 \end{bmatrix}, \quad (4)$$

where

$$\begin{aligned} s_1 &= 1 - 3\xi^2 + 2\xi^3, \\ s_2 &= l(\xi - 2\xi^2 + \xi^3), \\ s_3 &= 3\xi^2 - 2\xi^3, \\ s_4 &= l(\xi^3 - \xi^2), \\ \xi &= \frac{x}{l}. \end{aligned} \quad (5)$$

2.2. Mass Matrix. Kinetic energy of the finite element can be written as

$$T = \frac{1}{2} \int \rho \dot{\mathbf{r}}^T \dot{\mathbf{r}} dV. \quad (6)$$

Substituting (1) into (6) yields

$$T = \frac{1}{2} \dot{\mathbf{e}}^T \left(\int \rho \mathbf{S}^T \mathbf{S} dV \right) \dot{\mathbf{e}} = \frac{1}{2} \dot{\mathbf{e}}^T \mathbf{M}_a \dot{\mathbf{e}}, \quad (7)$$

where V is the element volume, ρ is the mass density of the beam element material, and \mathbf{M}_a is the mass matrix of the element. Using (7), the mass matrix of the element can be calculated as

$$\mathbf{M}_a = \int \rho \mathbf{S}^T \mathbf{S} dV. \quad (8)$$

2.3. Generalized Elastic Forces. In order to develop the equations of motion of the beam element, generalized elastic forces, \mathbf{Q}_k , corresponding to the beam element have to be defined. If the strain energy of the element is U , then the vector of elastic forces is defined as

$$\mathbf{Q}_k = \left(\frac{\partial U}{\partial \mathbf{e}} \right)^T. \quad (9)$$

In this paper, continuum mechanics approach is used to derive the strain energy of the element in the absolute nodal coordinate formulation. This approach uses arc length to define the element deformation instead of using the local coordinate system. The strain energy of the element can be written as

$$U = U_l + U_t = \frac{1}{2} \int_0^l E a \varepsilon_l^2 dx + \frac{1}{2} \int_0^l E I \kappa^2 dx, \quad (10)$$

where U_l is the strain energy due to the longitudinal deformation and U_t is the strain energy due to the bending.

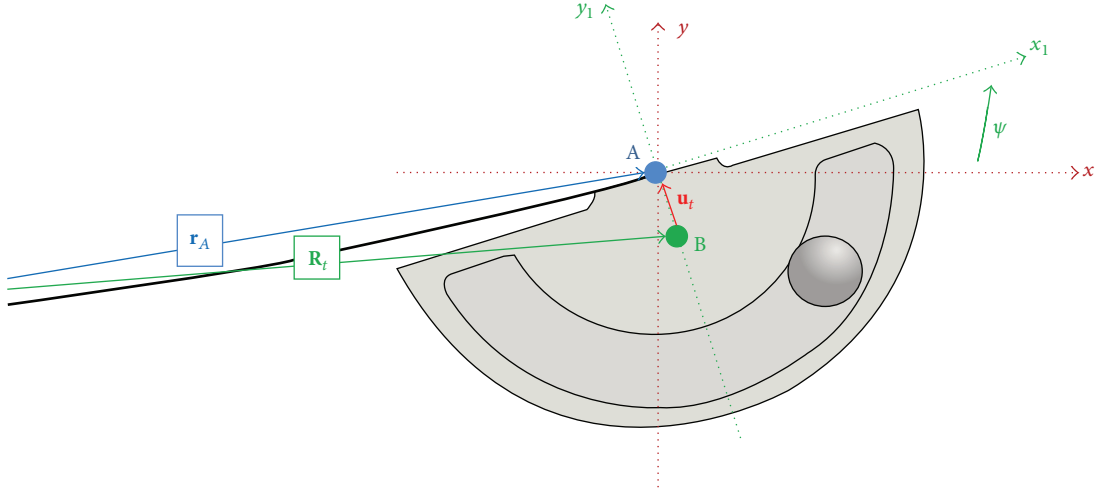


FIGURE 4: Tip mass displacement vectors.

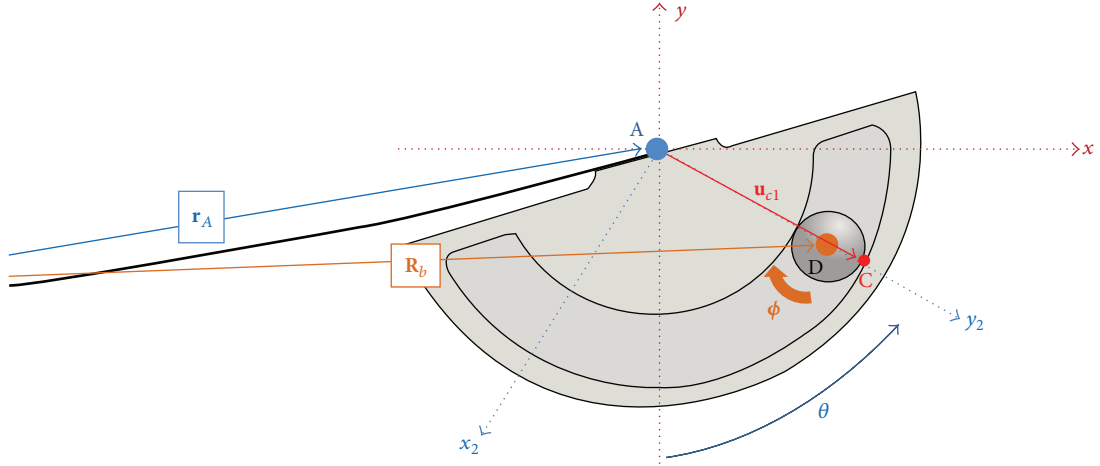


FIGURE 5: Ball displacement vectors.

The longitudinal strain, ε_l , and the bending curvature, κ , can be defined as [51]

$$\begin{aligned}\varepsilon_l &= \frac{1}{2} \left(\mathbf{r}'^T \mathbf{r}' - 1 \right), \\ \kappa &= \left| \frac{d^2 \mathbf{r}}{dx^2} \right|.\end{aligned}\quad (11)$$

Using (1), (9), (10), and (11), one can find the vector of elastic forces as

$$\mathbf{Q}_k = \mathbf{K}_l \mathbf{e} + \mathbf{K}_t \mathbf{e}, \quad (12)$$

where stiffness matrices \mathbf{K}_l and \mathbf{K}_t are defined as [51]

$$\begin{aligned}\mathbf{K}_l &= Eal \int_0^l \varepsilon_l \mathbf{S}_l d\xi, \\ \mathbf{K}_t &= \int_0^l EIS''^T \mathbf{S}'' dx.\end{aligned}\quad (13)$$

More detailed derivation for the elastic forces is well explained in [51].

2.4. Generalized Gravity Forces. Let F be the distributed gravity force applied on an arbitrary point on the element. Then, the virtual work done due to this external force can be defined as

$$\delta W_f = F^T \delta \mathbf{r}, \quad (14)$$

where $\delta \mathbf{r}$ is the virtual change in the position vector of the point of application of the force. Using (1), one can write the virtual work term as

$$\delta W_f = \mathbf{Q}_f^T \delta \mathbf{e}, \quad (15)$$

where $\mathbf{Q}_f = \mathbf{S}^T F$ is the vector of generalized forces associated with the element nodal coordinates.

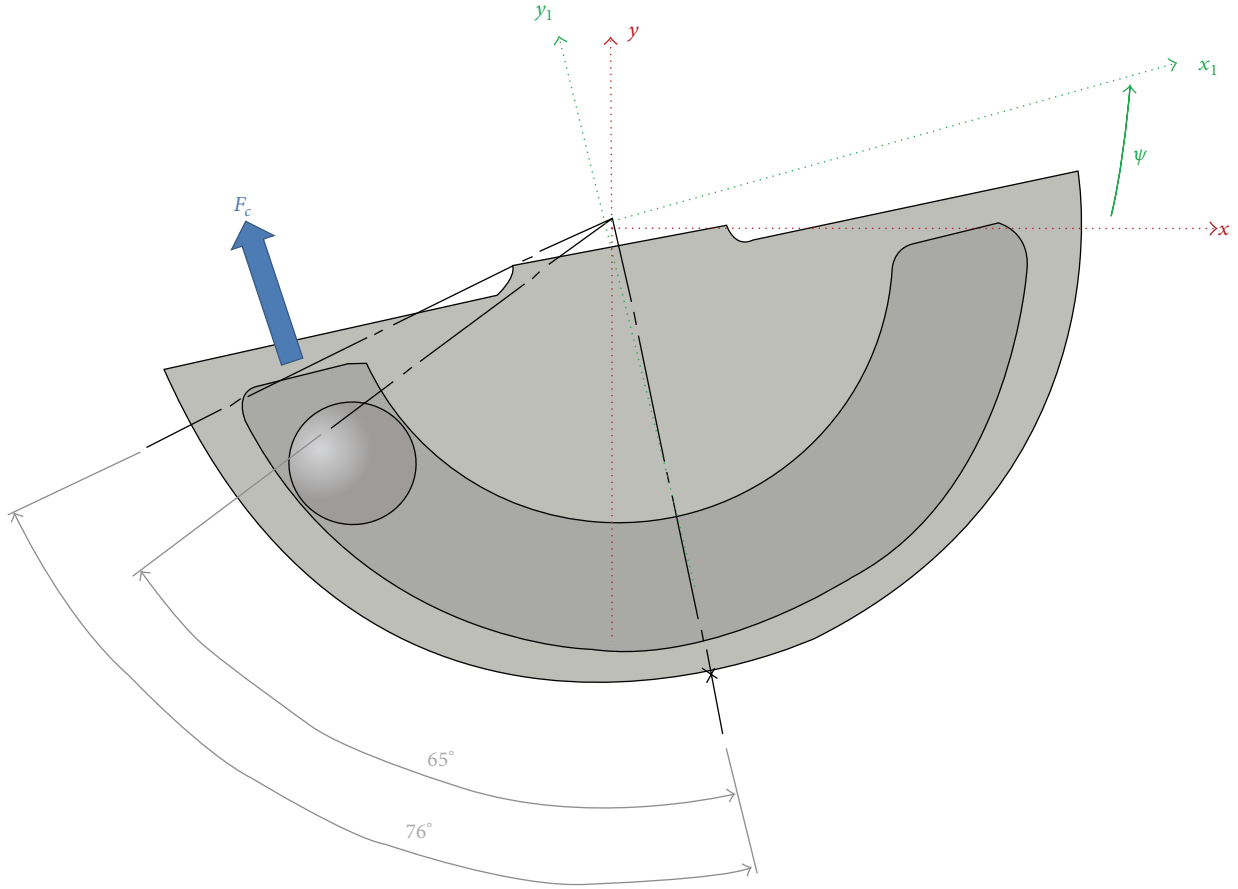


FIGURE 6: Impact condition.

Using (15), virtual work due to the distributed gravity force of the beam element for the planar case can be written as

$$\begin{aligned} & \int [0 \quad -\rho g] \mathbf{S} \delta \mathbf{e} dV \\ & = mg \left[0 \quad -\frac{1}{2} \quad 0 \quad -\frac{l}{12} \quad 0 \quad -\frac{1}{2} \quad 0 \quad \frac{l}{12} \right] \delta \mathbf{e}. \end{aligned} \quad (16)$$

Therefore, using (16), the vector of generalized distributed gravity forces can be written as

$$\mathbf{Q}_f = mg \left[0 \quad -\frac{1}{2} \quad 0 \quad -\frac{l}{12} \quad 0 \quad -\frac{1}{2} \quad 0 \quad \frac{l}{12} \right]^T. \quad (17)$$

2.5. Generalized Constraint Forces. Let $\mathbf{q} = [q_1 \ q_2 \ q_3 \ \dots \ q_n]^T$ be the set of generalized coordinates of the flexible body, where n is the number of coordinates. If n_h is the number of the constraints, where $n_h \leq n$, then the vector of constraint equations can be written in the form of

$$\begin{aligned} \mathbf{C}(q_1, q_2, \dots, q_n, t) &= \mathbf{C}(\mathbf{q}, t) \\ &= [C_1(\mathbf{q}, t) \ C_2(\mathbf{q}, t) \ \dots \ C_{n_h}(\mathbf{q}, t)]^T = 0 \end{aligned} \quad (18)$$

and the Jacobian of the constraint equations can be defined as

$$\mathbf{C}_q(\mathbf{q}, t) = \begin{bmatrix} \frac{\partial C_1(\mathbf{q}, t)}{\partial \mathbf{q}} \\ \frac{\partial C_2(\mathbf{q}, t)}{\partial \mathbf{q}} \\ \vdots \\ \frac{\partial C_{n_h}(\mathbf{q}, t)}{\partial \mathbf{q}} \end{bmatrix} = 0. \quad (19)$$

Using the vector of Lagrange Multipliers, λ , one can write generalized constraint forces, \mathbf{Q}_c , as [40]

$$\mathbf{Q}_c = -\mathbf{C}_q(\mathbf{q}, t)^T \lambda, \quad (20)$$

where $\mathbf{C}_q(\mathbf{q}, t)$ is given by (19) and λ is defined as

$$\lambda = \begin{bmatrix} \lambda_1 \\ \lambda_2 \\ \vdots \\ \lambda_{n_h} \end{bmatrix}. \quad (21)$$

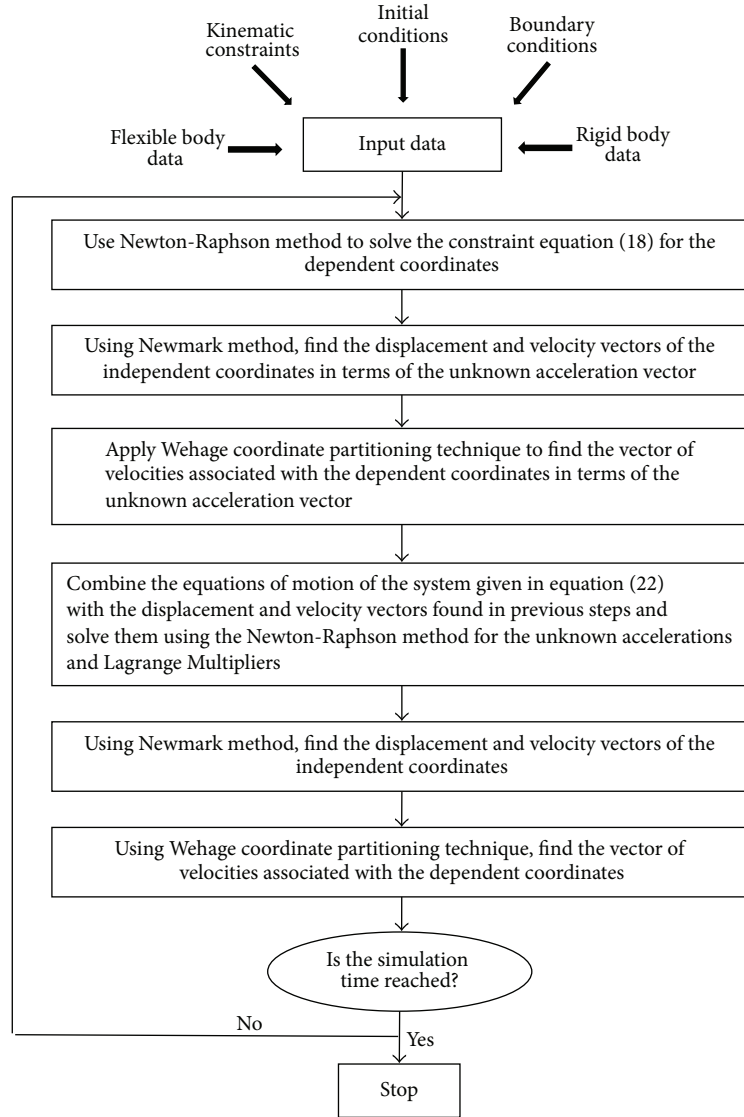


FIGURE 7: Computational algorithm for dynamic analysis.

2.6. Equations of Motion. Using the principles of virtual work in dynamics and the expression of the kinetic and strain energies given in (6) and (10), the system equations of motion in augmented form can be written as [40]

$$\begin{bmatrix} \mathbf{M} & \mathbf{C}_q^T \\ \mathbf{C}_q & 0 \end{bmatrix} \begin{bmatrix} \ddot{\mathbf{q}} \\ \boldsymbol{\lambda} \end{bmatrix} = \begin{bmatrix} \mathbf{Q}_e - \mathbf{Q}_k \\ \mathbf{Q}_d \end{bmatrix}, \quad (22)$$

where \mathbf{M} is the constant symmetric mass matrix, $\boldsymbol{\lambda}$ is the vector of Lagrange Multipliers, \mathbf{Q}_k is the vector of body elastic forces, \mathbf{Q}_e is the vector of the externally applied body forces such as gravity, magnetic, and other forces, and the vector \mathbf{Q}_d is given by [40]

$$\mathbf{Q}_d = -\mathbf{C}_{tt} - (\mathbf{C}_q \dot{\mathbf{q}})_q \dot{\mathbf{q}} - 2\mathbf{C}_{qt} \dot{\mathbf{q}}, \quad (23)$$

where subscript t denotes partial differentiation with respect to time.

3. Modeling Beam-Tip Mass-Free Pendulum System

3.1. Coordinate Systems. Referring to Figure 2, the following coordinate systems can be defined for the beam-tip mass-free pendulum system:

- (i) x - y : inertial coordinate system
- (ii) x_1 - y_1 : body coordinate system of the tip mass, where origin is rigidly attached to the center of mass of the tip mass
- (iii) x_2 - y_2 : ball coordinate system, where origin attached to the end of the beam and the coordinate system rotates with the motion of the ball
- (iv) x_3 - y_3 : body coordinate system of the ball, where origin is rigidly attached to the center of mass of the ball.

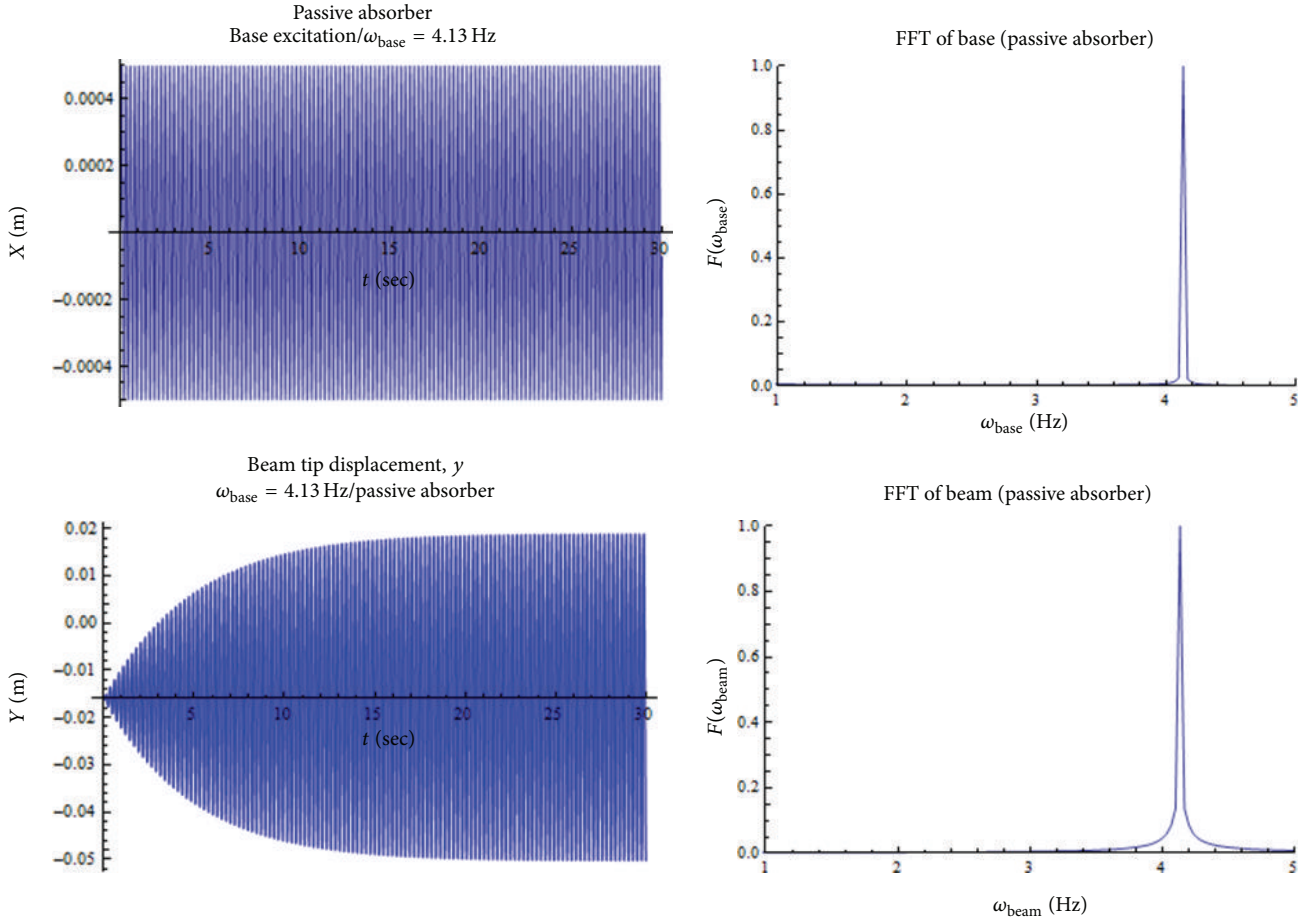


FIGURE 8: Ball locked/detailed dynamics of the beam for the forcing frequency of 4.13 Hz.

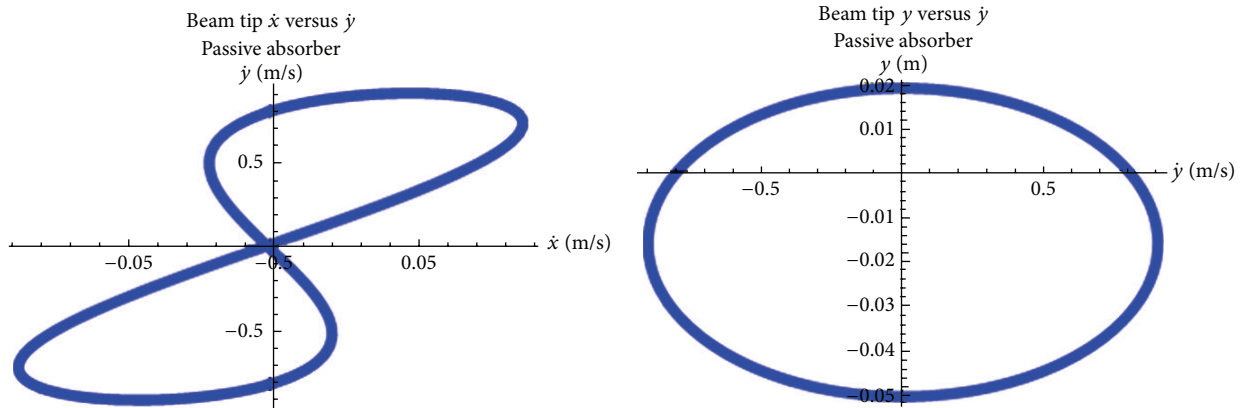


FIGURE 9: Ball locked/phase plane curves for the forcing frequency of 4.13 Hz at steady state.

3.2. Generalized Coordinates. The beam-tip mass-free pendulum system consists of three bodies, among which the beam is assumed to be flexible, and the tip mass and ball are assumed to be rigid. The ANCF beam is modeled using three finite elements. Referring to Figure 3, the ANCF beam element has four nodes; each node has four degrees of freedom. Therefore, the total degree of freedom of the beam

is 16. The vector of system generalized coordinates can be defined as

$$\mathbf{q}_{\text{sys}} = [e_1 \ e_2 \ \cdots \ e_{15} \ e_{16} \ \phi \ R_{b_1} \ R_{b_2} \ R_{t_1} \ R_{t_2} \ \psi]^T, \quad (24)$$

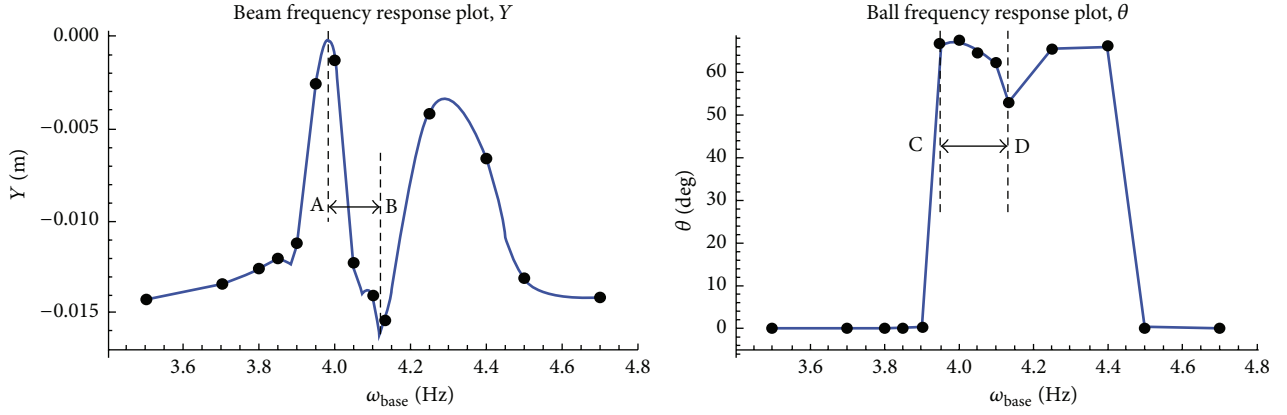


FIGURE 10: Frequency response curves for an excitation amplitude of 1 mm peak-to-peak.

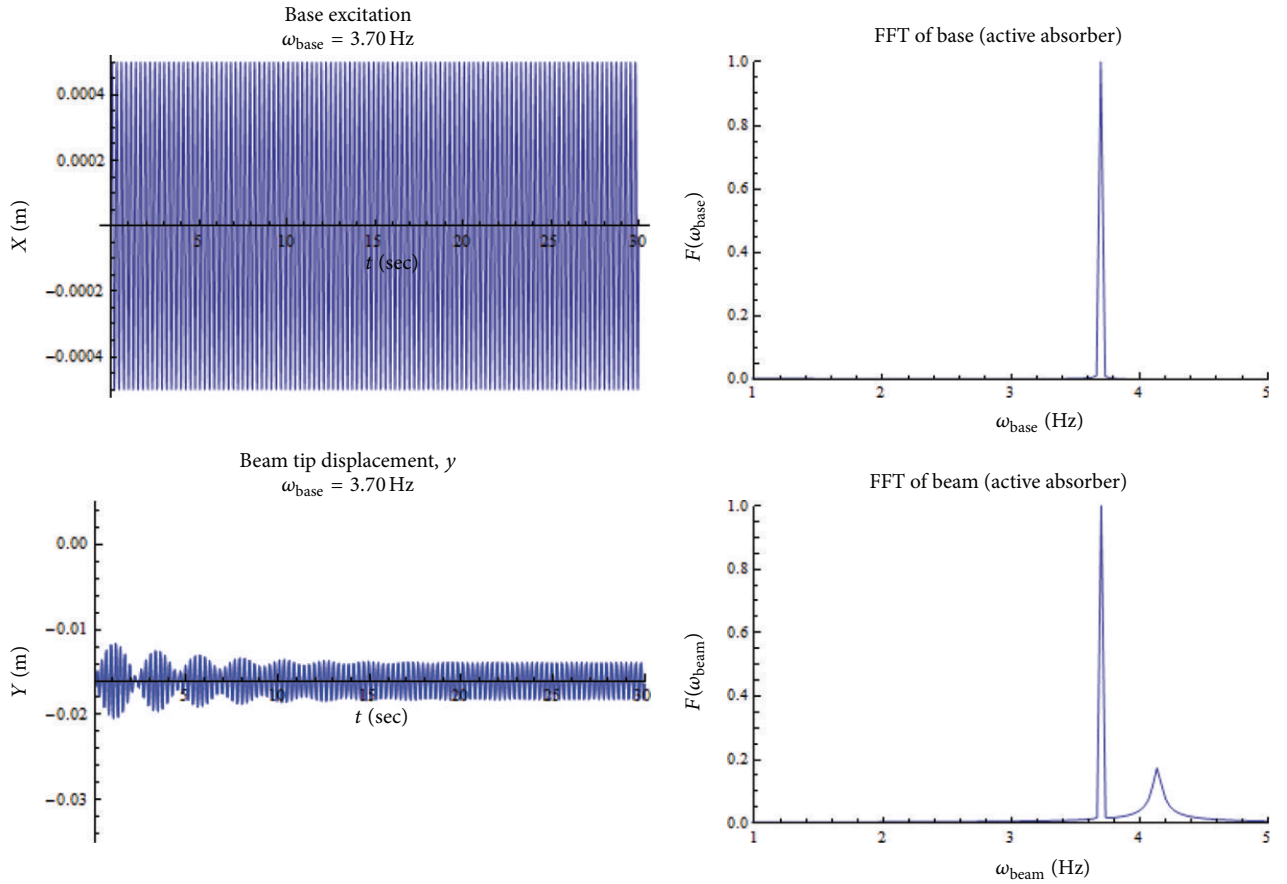


FIGURE 11: Detailed dynamics of the system for the forcing frequency of 3.70 Hz.

where $[e_1 \ e_2 \ \cdots \ e_{15} \ e_{16}]^T$ are beam absolute nodal coordinates, $[\phi \ R_{b_1} \ R_{b_2}]^T$ are ball (free pendulum) rotational and translational coordinates, and $[R_{t_1} \ R_{t_2} \ \psi]^T$ are tip mass translational and rotational coordinates, respectively.

3.3. Kinematic Constraints. The connection between the free end of the beam and the tip mass is modeled using a

fixed joint. Referring to Figure 4, the following constraint equations for the fixed joint between the two bodies can be written:

$$\begin{aligned} \mathbf{r}_A &= \mathbf{R}_t + \mathbf{A}_t \mathbf{u}_t, \\ \psi - \text{Arctan} \left[\frac{e_{16}}{e_{15}} \right] &= 0, \end{aligned} \quad (25)$$

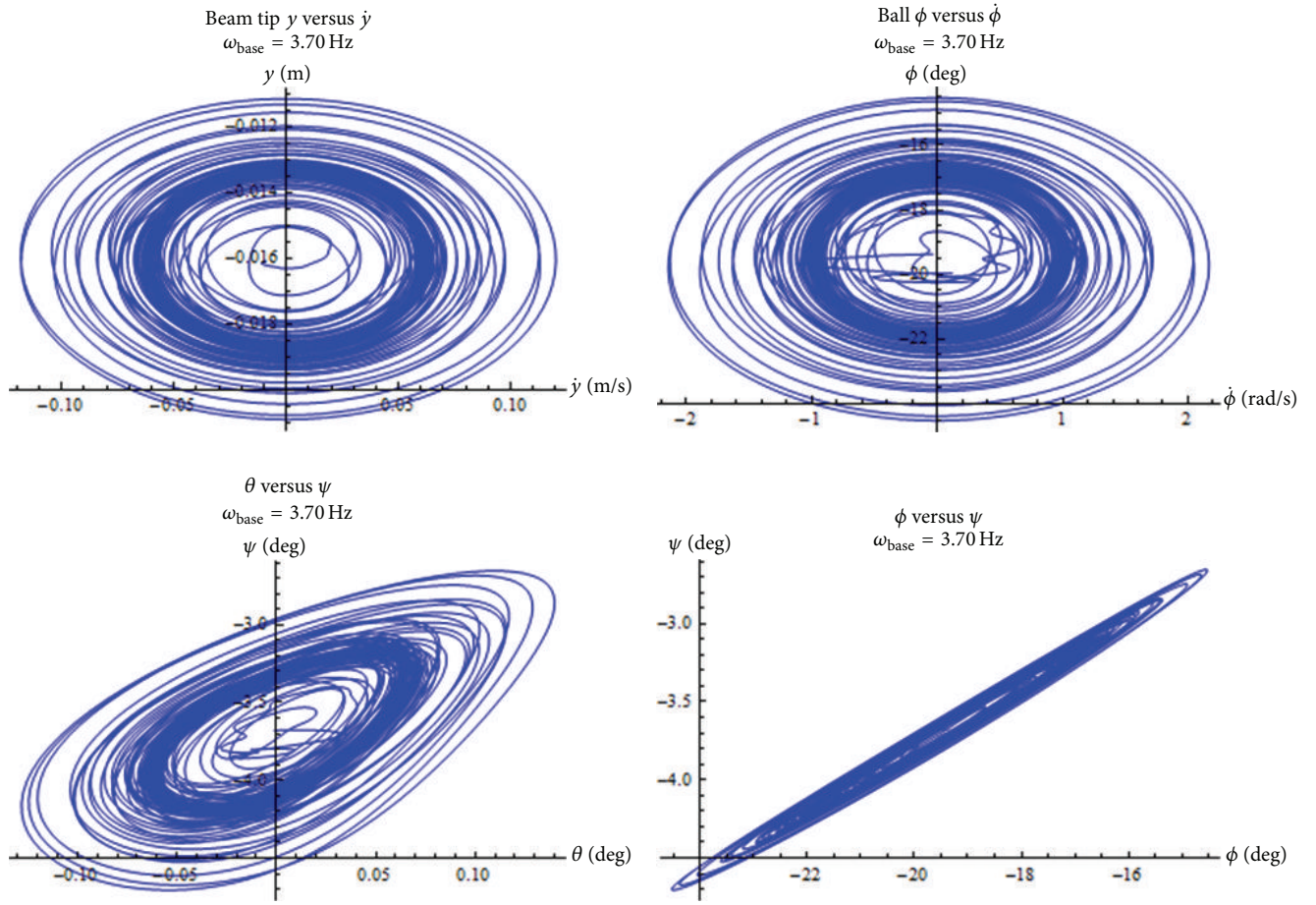


FIGURE 12: Phase plane curves for the forcing frequency of 3.70 Hz.

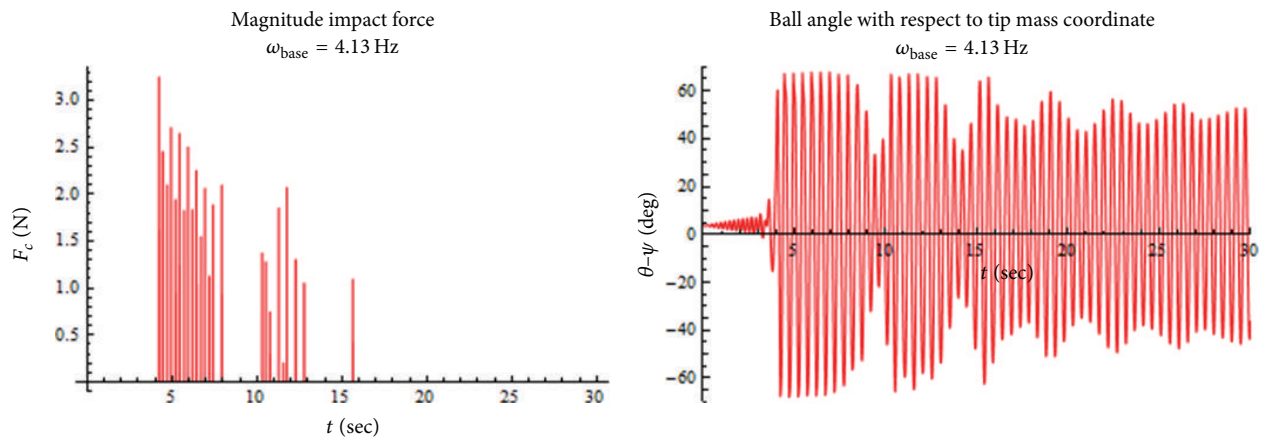


FIGURE 13: Impact details for the forcing frequency of 4.13 Hz.

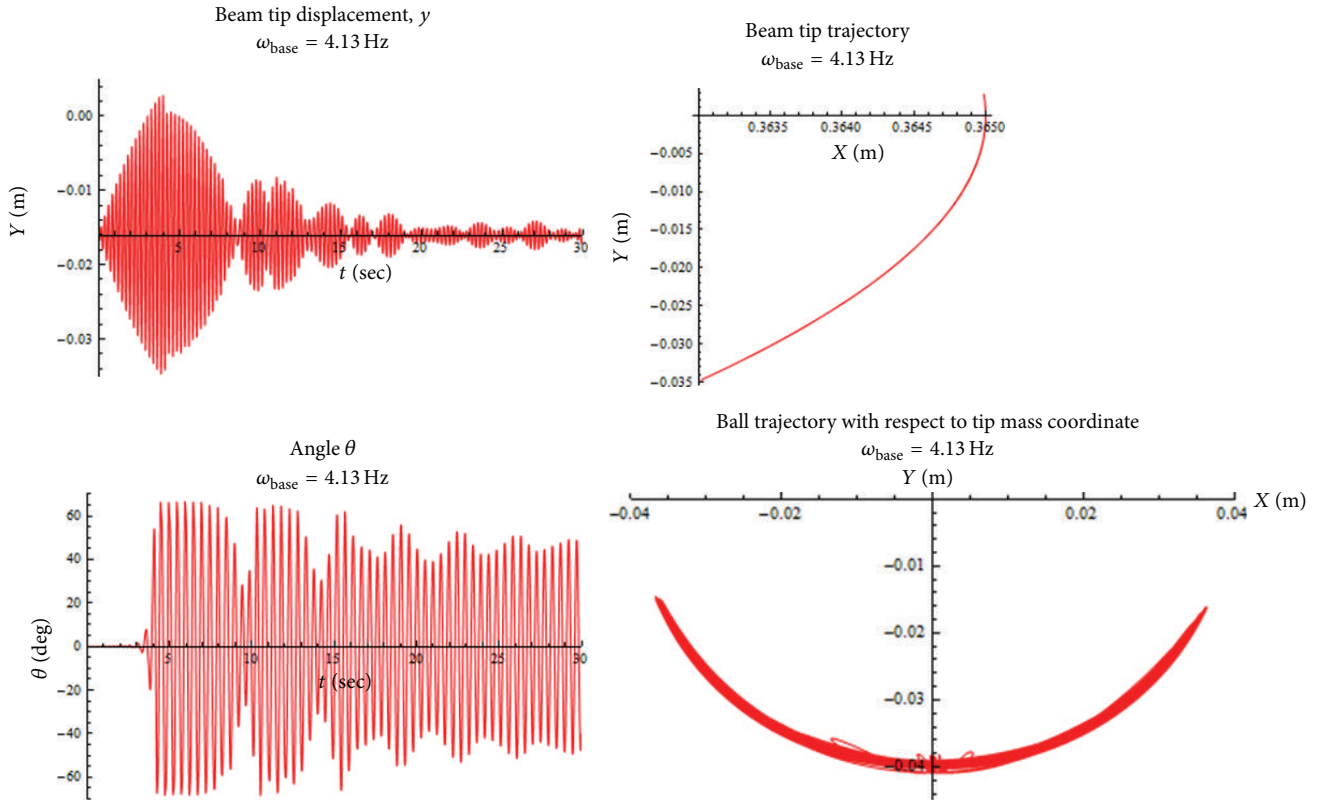


FIGURE 14: System trajectories for the forcing frequency of 4.13 Hz.

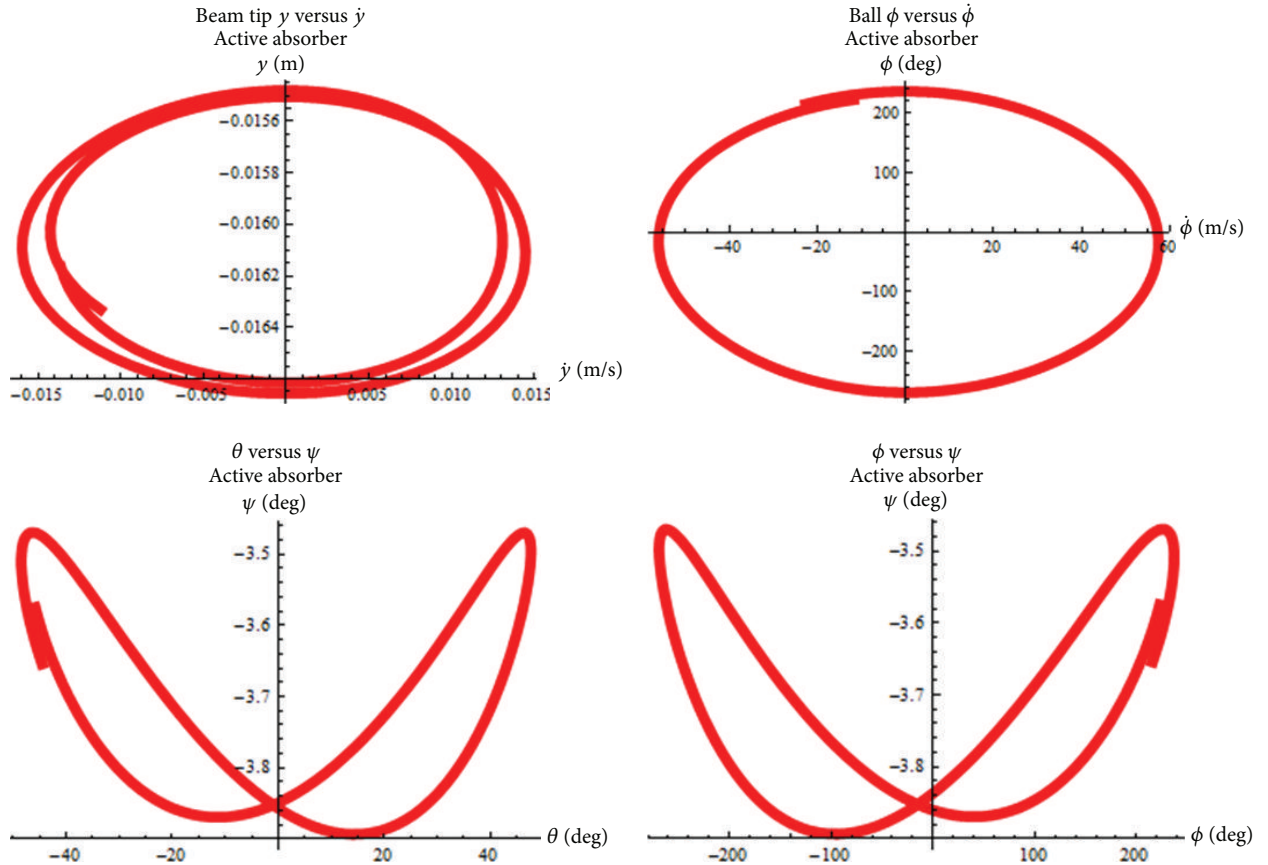


FIGURE 15: Phase plane curves for the forcing frequency of 4.13 Hz at steady state.

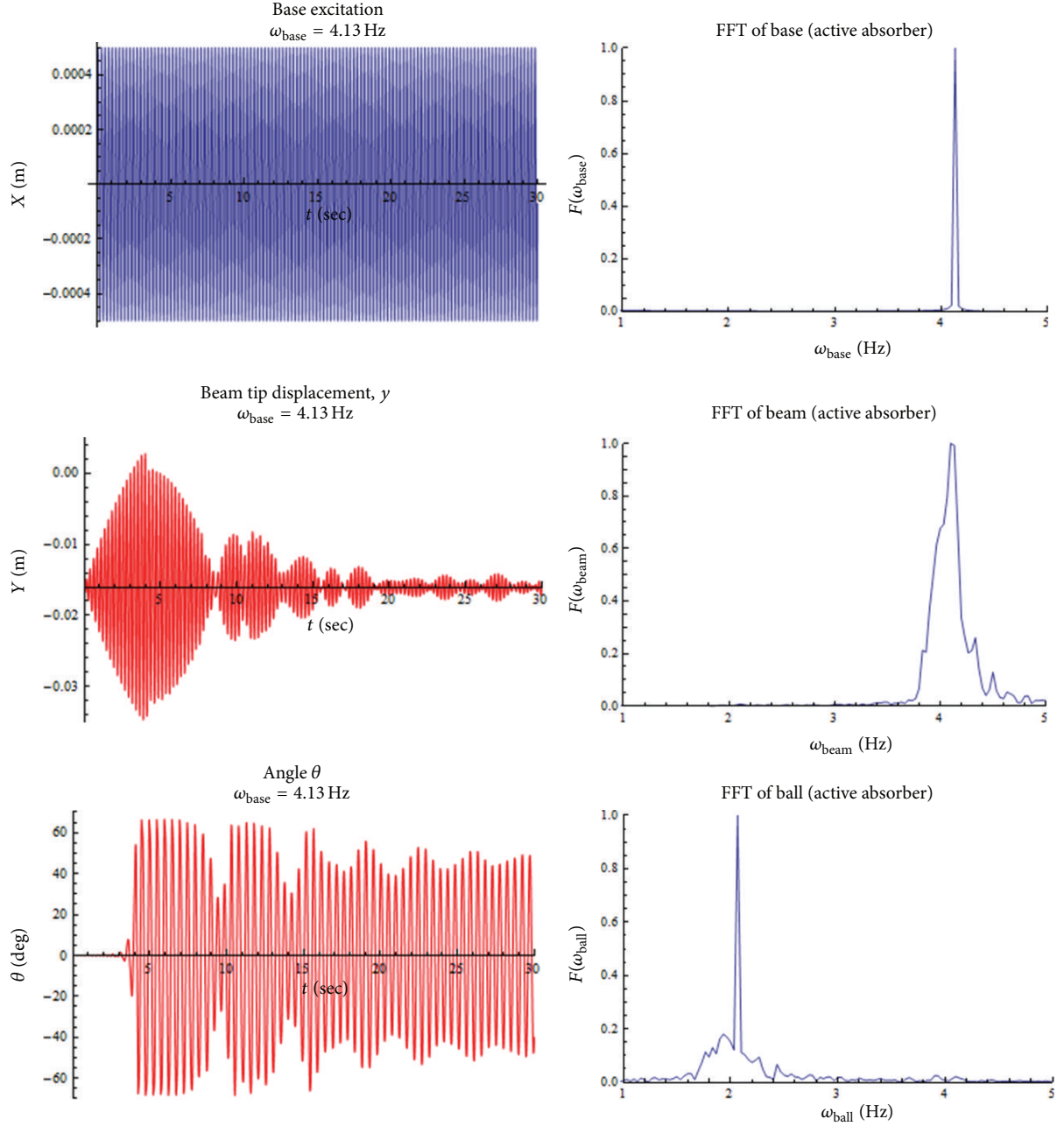


FIGURE 16: FFT of the system for the forcing frequency of 4.13 Hz.

where \mathbf{R}_t is the absolute displacement vector of the center of mass of the tip appendage, \mathbf{r}_A is the absolute displacement vector of the beam free end, \mathbf{A}_t is the transformation matrix between the coordinates x - y and x_1 - y_1 , and \mathbf{u}_t is the displacement vector of point A relative to point B in x_1 - y_1 coordinate system.

Constraint equations between the ball and the tip mass can be defined such that the velocity of the contact point C on the ball has to be equal to the velocity of the contact point C on the tip mass. Therefore, referring to Figure 5, one can write the following equations:

$$\dot{\mathbf{r}}_{C_b} = \dot{\mathbf{r}}_{C_t} \quad (26)$$

or

$$\begin{aligned} \dot{\mathbf{r}}_{C_t} &= \dot{\mathbf{r}}_A + \dot{\mathbf{A}}_{b1} \mathbf{u}_{c1}, \\ \dot{\mathbf{r}}_{C_b} &= \dot{\mathbf{R}}_b + \dot{\mathbf{A}}_{b2} \mathbf{u}_{c2}, \end{aligned} \quad (27)$$

where $\dot{\mathbf{r}}_A$ is the absolute velocity vector of the beam free end A, $\dot{\mathbf{R}}_b$ is the absolute velocity vector of the center of mass of the ball, \mathbf{u}_{c1} is the displacement vector of point C relative to point A in x_2 - y_2 coordinate system, \mathbf{u}_{c2} is the displacement vector of point C relative to point D in x_3 - y_3 coordinate system, $\dot{\mathbf{A}}_{b1}$ is the time derivative of the transformation matrix \mathbf{A}_{b1} between the coordinates x - y and x_2 - y_2 , and $\dot{\mathbf{A}}_{b2}$ is the time

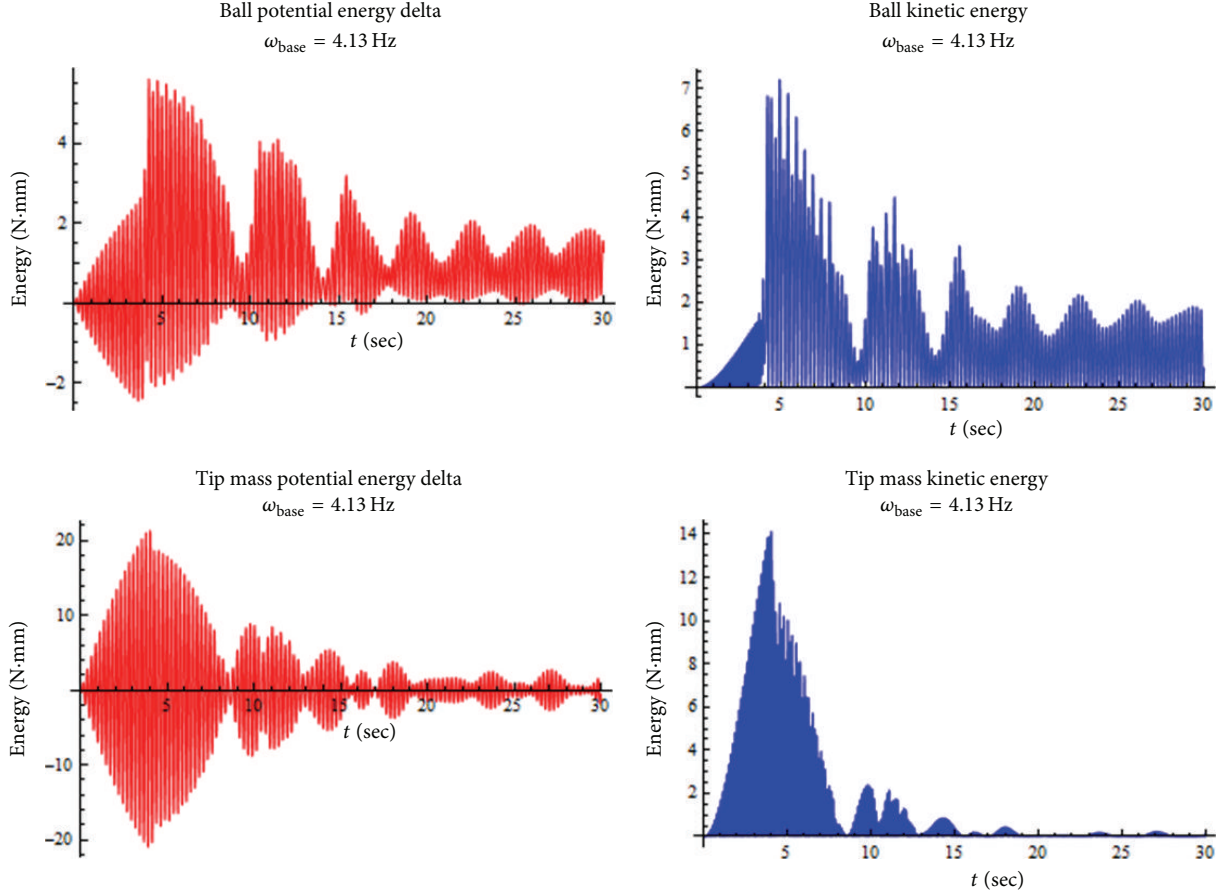


FIGURE 17: Energy curves of the ball and the tip mass for the forcing frequency of 4.13 Hz.

derivative of the transformation matrix \mathbf{A}_{b2} between the coordinates x - y and x_3 - y_3 .

3.4. Identifying Dependent and Independent Coordinates. The system has five dependent coordinates and seventeen independent coordinates. For the numerical analysis, the vectors of independent and dependent coordinates are selected as

$$\begin{aligned} \mathbf{q}_i &= [e_1 \ e_2 \ \cdots \ e_{15} \ e_{16} \ \phi]^T, \\ \mathbf{q}_d &= [R_{b_1} \ R_{b_2} \ R_{t_1} \ R_{t_2} \ \psi]^T. \end{aligned} \quad (28)$$

3.5. Impact Force. Referring to Figure 6, if $|\theta - \psi| \geq 65^\circ$, the system will have impact between the tip mass and the ball. The average contact force, $F_{c_{av}}$, between the bodies during the collision can be defined as

$$F_{c_{av}} = \frac{\Delta P}{\Delta t}, \quad (29)$$

where Δt is the contact time and ΔP is the change in momentum of one of the colliding bodies which can be calculated using the conservation of momentum law and the concept of coefficient of restitution.

3.6. System Parameters. Numerical integration parameters, rigid body parameters, and flexible body parameters are given in Table 1.

4. Numerical Solution

The equations of motion of a multibody system consisting of interconnected rigid and deformable bodies are a combined set of ordinary differential and algebraic equations. These kinds of equation sets are called differential algebraic equations (DAEs) in literature. The solutions to DAEs are not as straightforward as ordinary differential equations. Specialized numerical techniques have been developed for the solution of DAEs. In this paper, the direct integration approach based on the Wehage coordinate partitioning technique [52] and the Newmark [53] and the Newton-Raphson methods is used for the solution of DAEs of the multibody system under investigation. The computational algorithm for the dynamic analysis of the multibody system is given in Figure 7.

5. Results

5.1. ANCF Results. System parameters given in Table 1 are used for the numerical solution, and detailed system

TABLE 1: System parameters.

Numerical integration parameters		Rigid body data		Flexible beam data
Newmark parameters	Newton-Raphson parameters	Tip mass	Ball	Flexible beam
$\gamma = 0.7$ $\beta = 0.36$ $h = 0.003$ sec	$\varepsilon = 10^{-5}$ $n_m = 100$	$J_t = 1.871 \times 10^{-5}$ kg·m ² $m_t = 0.1154$ kg $u_{t2} = 0.0204$ m	$J_b = 3.15 \times 10^{-7}$ kg·m ² $m_b = 0.014$ kg $r_b = 0.0075$ m $R = 0.0395$ m	$l = 0.365/3$ m $m = 0.116/3$ kg $a = 4.06 \times 10^{-5}$ m ² $E = 200$ GPa $I = 8.47 \times 10^{-12}$ m ⁴

n_m = maximum number of iterations.

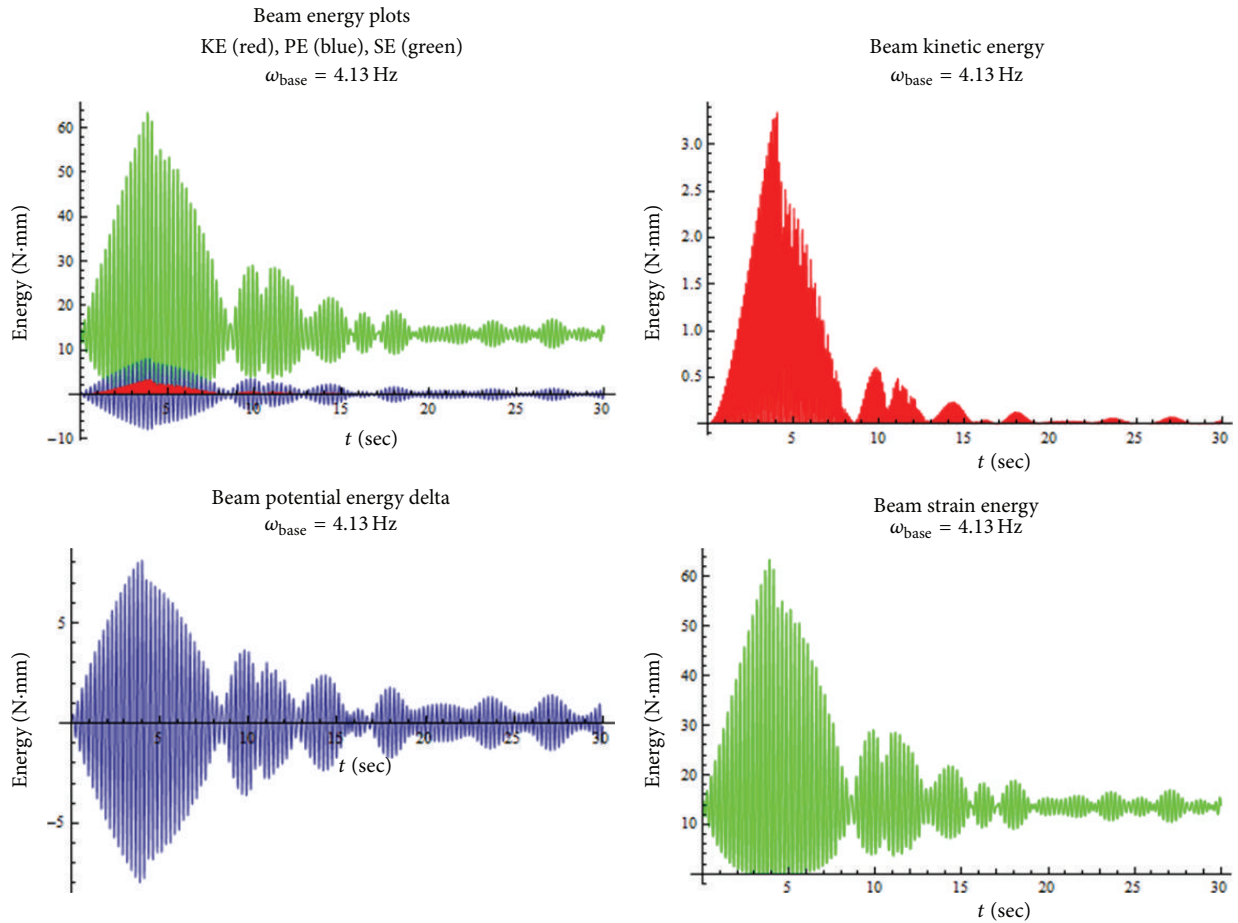


FIGURE 18: Beam energy curves for the forcing frequency of 4.13 Hz.

dynamics, including frequency response curves, time history curves, FFT curves, phase plane curves, and energy curves, are plotted for various base excitation frequencies. For each of the numerical analyses, the frequency of the beam-tip mass system is set to 4.13 Hz, and in order to maintain the condition of autoparametric interaction the frequency of the ball is tuned to one half of the beam-tip mass system frequency (i.e., it is set to 2.065 Hz).

Before having detailed discussions on the unlocked ball cases, one can refer to Figure 8, which shows the system dynamics when the ball is locked. For the passive absorber

case, the ball is locked inside the housing track and the system is excited at its natural frequency. Figure 9 shows the phase plane curve of the system, where a periodic response can be observed.

Figure 10 shows the frequency response (Y in meters) curves of the beam and the ball (θ in degrees) for the forcing amplitude of 1 mm peak-to-peak. To create this figure, numerical analyses with the base excitation frequencies (ω_{base} in Hz) 3.50 Hz, 3.70 Hz, 3.80 Hz, 3.85 Hz, 3.90 Hz, 3.95 Hz, 4.00 Hz, 4.05 Hz, 4.10 Hz, 4.13 Hz, 4.25 Hz, 4.40 Hz, 4.50 Hz, and 4.70 Hz were performed. Steady-state response

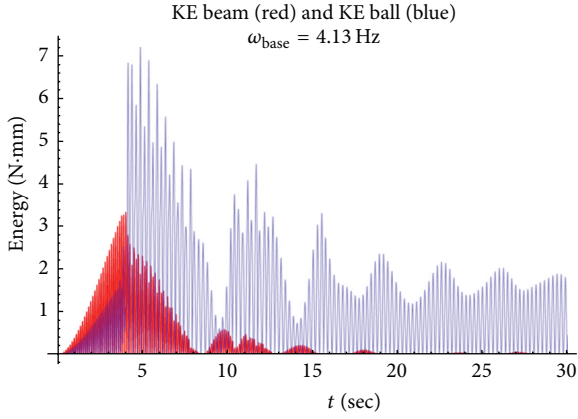


FIGURE 19: Comparison of the beam kinetic energy and the ball kinetic energy for the forcing frequency of 4.13 Hz.

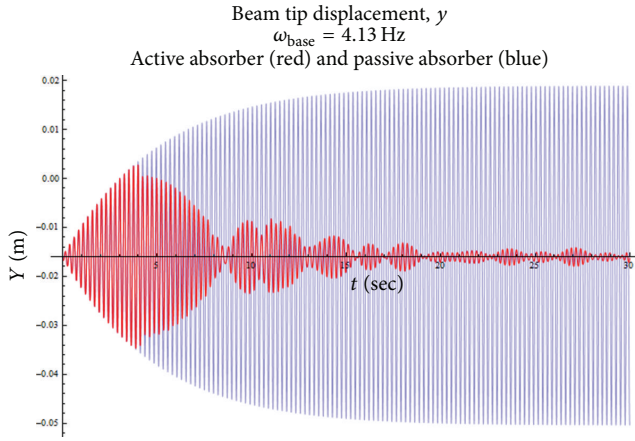


FIGURE 20: Comparison of the beam tip displacement, y , in active (ball unlocked) and passive (ball locked) cases.

amplitudes were used to create frequency response curves. A detailed investigation of Figure 10 reveals a strong autoparametric interaction between the beam and the free pendulum when the forcing frequency reaches 3.95 Hz and the first jump phenomenon is observed.

As shown in Figure 10, point A on the beam response curve and point C on the ball response curve are starting points of the autoparametric region. The oscillation of the ball and the decrease in the beam response continue until points B and D, where the frequency of the beam is 4.13 Hz. Points A-B on the beam response curve and points C-D on the ball response curve are important as they define the complete energy exchange region. From Figure 10, it is evident that the amplitude of the beam is decreased and the energy is transferred to the ball when the primary resonance case is reached. Moreover, the second peak observed in the beam response is due to the beating phenomena and will be explained later in this paper. In this paper, the detailed system dynamics for the following important frequency values are given: 3.70 Hz is the frequency before the autoparametric

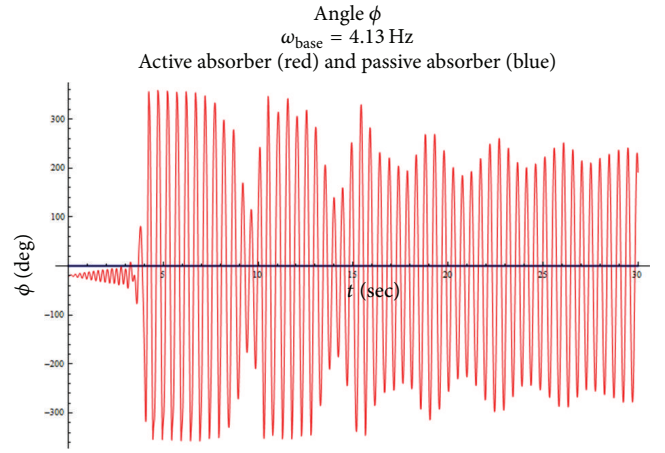


FIGURE 21: Comparison of ball rotation angle in active (ball unlocked) and passive (ball locked) cases.

region, 4.13 Hz is the frequency at which complete energy transfer occurs, and 4.25 Hz is the frequency where beating phenomena is observed.

Figures 11 and 12 show system (ball is free to move) dynamics for the forcing frequency of 3.70 Hz. The time history curves of the beam and the ball, shown in Figure 11, are examined, in which the beam has oscillation, whereas the ball does not have any significance. The phase plane curves shown in Figure 12 are obtained for the full simulation time. Therefore, curves start from the static equilibrium position. After passing the transient response region, they go to steady state, where darker circular patterns on the curves are obtained. Beam y versus \dot{y} and ball ϕ versus $\dot{\phi}$ curves prove that the responses are periodic. The noninteractive motion between the beam and the ball can be verified by examining θ versus ψ and ϕ versus ψ curves in Figure 12. From these curves, it is clear that both the beam and the ball frequency ratios are one. Investigating the FFT curves in Figure 11 reveals that the dominant frequency information is due to the base excitation. In this figure, two peaks are observed, in which one of them is the base excitation frequency, which is dominant, and the other is the beam-mass frequency. Since the ball is not oscillating, its frequency information cannot be observed.

Among the numerical analysis performed for the system, the most important results are given in Figures 13–19 for the forcing frequency of 4.13 Hz, where complete energy transfer from the beam to the ball takes place. From Figure 16, one can see that the beam frequency (4.13 Hz) is twice the ball frequency (2.065 Hz) and the forcing frequency is equal to the beam frequency (4.13 Hz), which is the condition for the complete autoparametric interaction. Coupling between the modes of the beam and the ball can also be verified by looking to the phase plane curves of the system at steady state as shown in Figure 15. The loop shown in this figure is the evidence for one to two frequency relationships between the beam and the ball. For further proof of the energy transfer, one can refer to Figure 19, which shows the kinetic energies

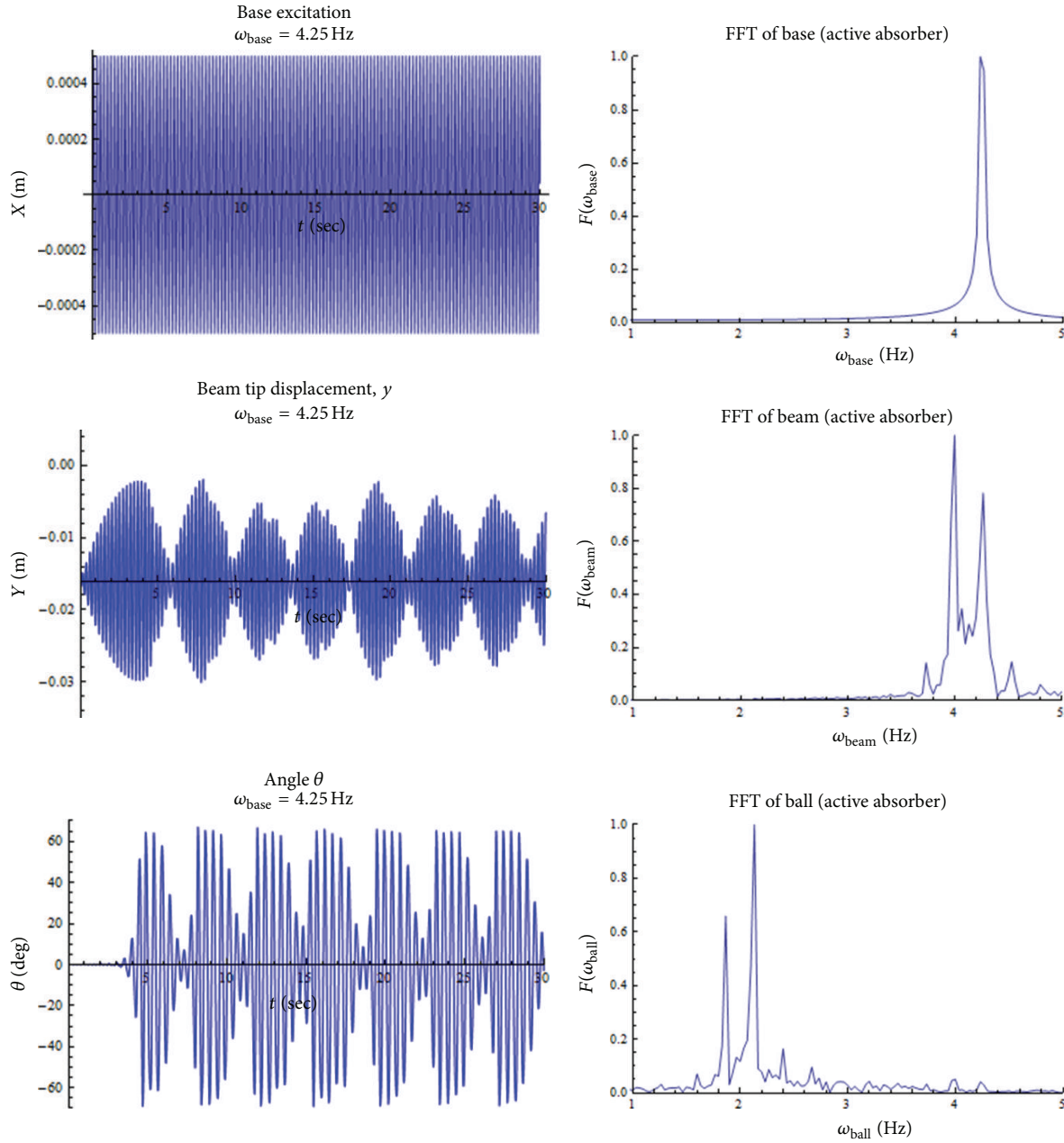


FIGURE 22: FFT of the system for the forcing frequency of 4.25 Hz.

of the beam and the ball during the full simulation time. From this figure, one can see that the beam kinetic energy diminishes as time passes; however, the ball kinetic energy still exists. Detailed system energy curves given in Figures 17 and 18 will be compared with ADAMS results found in Section 5.2 in order to validate the ANCF results.

Referring to Figure 20, which compares the transverse displacement of the beam tip for active (ball unlocked) and passive (ball locked) cases, and Figure 21, which compares the rotational angle of the ball for unlocked and locked cases, one can claim the free pendulum as a suitable autoparametric vibration absorber under periodic excitation.

Referring to Figure 22, time history curves of the beam and the ball for the forcing frequency of 4.25 Hz show an interesting phenomenon called beating in vibration literature. Beating can be expressed as a special case in which the amplitude of the vibrations periodically varies when the forcing frequency is very close to the frequency of the free vibrations of the system. Beating is undesirable in absorber systems because energy can be transferred from the secondary system (ball) back to the primary system (beam-tip mass). As it can be seen from the FFT of the ball in Figure 22, besides the peak value at 2.065 Hz that corresponds to the ball frequency, peaks with values around 1.9 Hz and

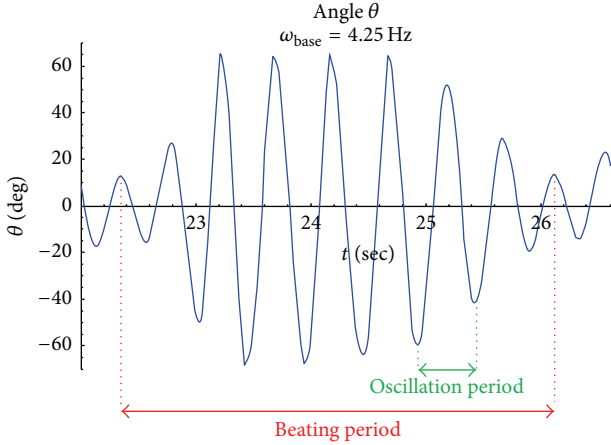


FIGURE 23: Beating cycle (ball response curve).

2.2 Hz have been observed which are different from the excitation frequency (4.25 Hz) and the beam frequency (4.13 Hz). The source of this peak can be attributed to the beating phenomenon. Therefore, a beating computation analysis will be performed to figure out and confirm this conclusion.

Figure 23 shows the time history curve of the ball during a complete beating cycle. Referring to this figure, the beating period can be computed using the start and end time of the cycle as follows:

$$\text{beating period} = 26.1 - 22.2 = 3.9 \text{ sec.} \quad (30)$$

Similarly, the oscillation period can be computed as

$$\text{oscillation period} = \frac{\text{beating period}}{8} = 0.4875 \text{ sec,} \quad (31)$$

where 8 is the number of oscillations during one complete beating cycle.

Moreover, equations for the beating period and the oscillation period in terms of the beating frequencies ω_1 and ω_2 can be written as [54]

$$\begin{aligned} \text{beating period} &= \frac{2\pi}{\omega_1 - \omega_2}, \\ \text{oscillation period} &= \frac{4\pi}{\omega_1 + \omega_2}. \end{aligned} \quad (32)$$

Combining (30), (31), and (32) and solving for the unknown frequencies, one can obtain

$$\begin{aligned} \omega_1 &= 13.82 \text{ rad/s} = 2.2 \text{ Hz,} \\ \omega_2 &= 11.94 \text{ rad/s} = 1.9 \text{ Hz.} \end{aligned} \quad (33)$$

Therefore, it is confirmed that the additional peaks seen around 1.9 Hz and 2.2 Hz in the ball FFT are due to beating. Similarly, investigating the beam FFT curve in Figure 23, one can see two major peaks corresponding to the excitation frequency (4.25 Hz) and the beam natural frequency (4.13 Hz) and two minor peaks corresponding to integer multiples ($\times 2$) of the beating frequencies ω_1 and ω_2 . Figure 24 shows impact details of the system at the beating.

5.2. ADAMS Results. Since the system has complete energy transfer at the forcing frequency of 4.13 Hz, ADAMS simulation is performed at this frequency, and the results are given in Figures 25–30.

Comparing the transverse displacement curves of the beam shown in Figures 16 and 27, one can see that both curves start from the static equilibrium position -0.016 m and have their maximum value approximately around 0.003 m before 5 seconds. After reaching the maximum value, they decrease gradually, and toward the end of the simulation they have small fluctuations around the static equilibrium position.

Figures 26, 27, and 28 show details of the beam kinetic, potential, and strain energies, respectively. Comparing Figure 28 with the beam strain energy curve given in Figure 18, maximum strain energy is observed before 5 seconds and its value is around 60 N-mm. Similarly, for potential energy and kinetic energy curves, maximum values are approximately 6 N-mm and 3.25 N-mm, respectively. In addition to the numerical matches, similarities can be seen between the decreasing and increasing trends of the strain energy, kinetic energy, and potential energy curves of the two models. Similar observations can be seen between the kinetic energy and the potential energy curves of the ball and the tip mass.

In conclusion, the results obtained from ADAMS and ANCF are observed to be in good quantitative and qualitative agreement even though two methods used different solution approaches.

6. Conclusion

This paper is concerned with the dynamics of a flexible beam with a tip mass-ball arrangement. The system is treated as a flexible multibody system interconnected with joints. The tip mass and the ball are assumed to be rigid, and the beam is treated as a flexible body. Connection between the tip mass and the free end of the beam is modeled using a fixed joint, and the contact between the ball and the tip mass is modeled using the geometry of the bodies.

The absolute nodal coordinate formulation (ANCF) is used to determine the mass matrix, stiffness matrix, and generalized forces of the system. Generalized elastic forces for the flexible beam are found using the continuum mechanics approach. Nonlinear equations of motion of the system are found using the Lagrangian Formulation, in which constraints are treated explicitly as extra equations by using Lagrange Multipliers. The resulting differential algebraic equations are solved using a two-loop sparse matrix numerical integration method, in which the kinematic constraint equations are satisfied at the position, velocity, and acceleration levels.

The detailed system dynamics including frequency response curves, time history curves, FFT curves, phase plane curves, and energy curves are plotted for various base excitation frequencies. Numerical results are compared with the results of previously studied similar systems and a good qualitative agreement is observed. Moreover, the same system with the same parameters is modeled using the mechanical analysis software, ADAMS, and the results are observed to be in good quantitative agreement, although the two

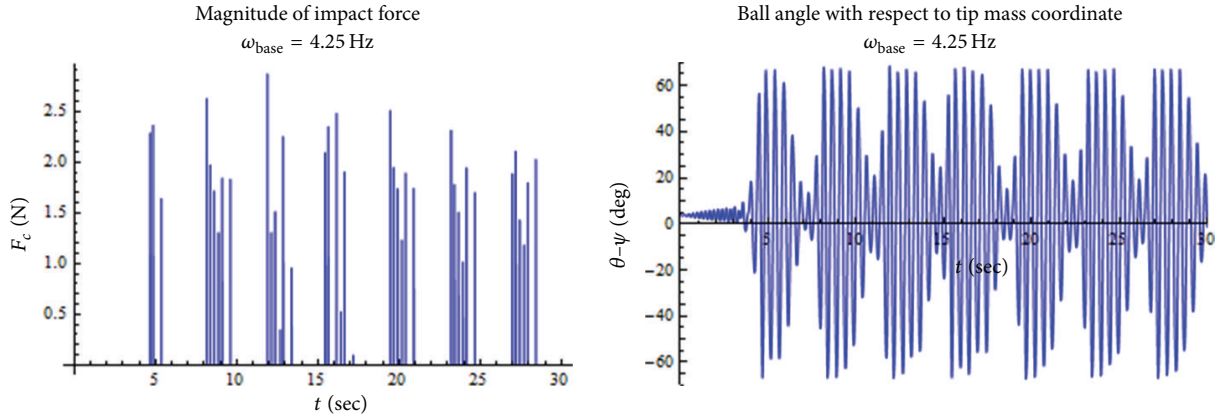


FIGURE 24: Impact details for the forcing frequency of 4.25 Hz.

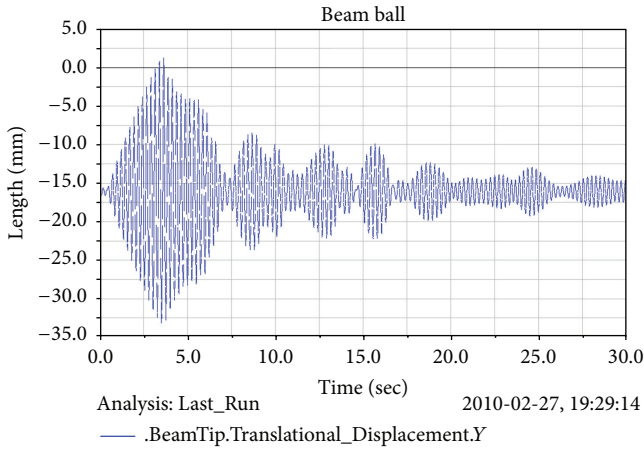
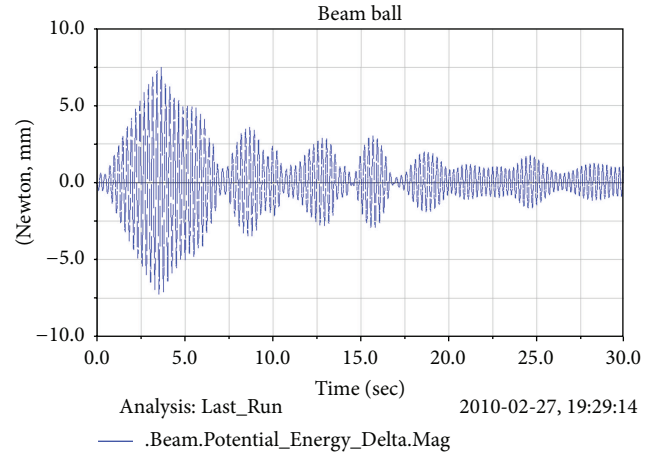
FIGURE 25: Beam tip displacement, y , for the forcing frequency of 4.13 Hz.

FIGURE 27: Beam potential energy delta curve for the forcing frequency of 4.13 Hz.

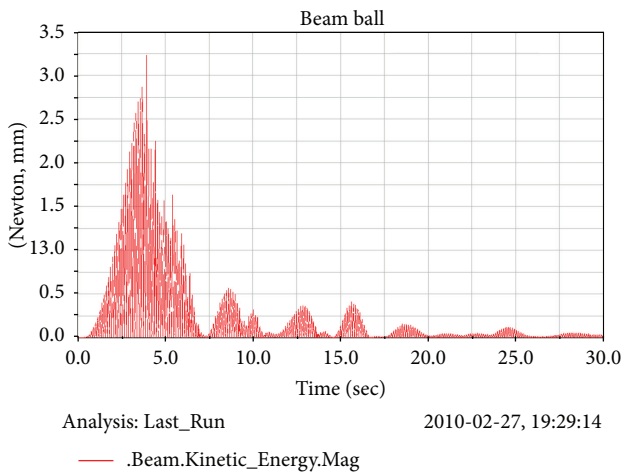


FIGURE 26: Beam kinetic energy curve for the forcing frequency of 4.13 Hz.

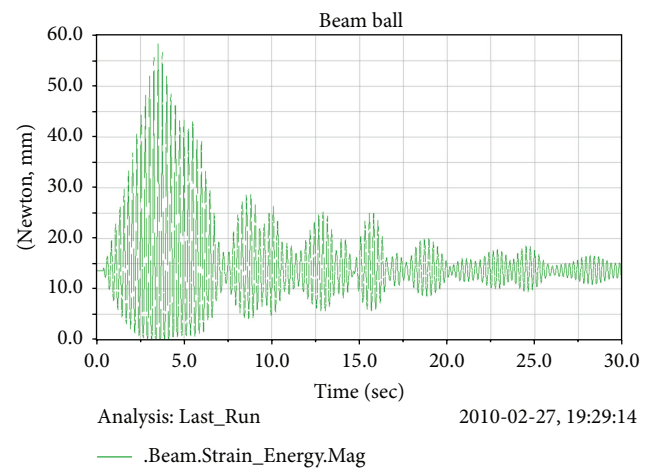


FIGURE 28: Beam strain energy curve for the forcing frequency of 4.13 Hz.

methods use different formulations. Therefore, in view of the numerical results, it is found that the free pendulum can

be considered a suitable autoparametric vibration absorber under periodic excitation.

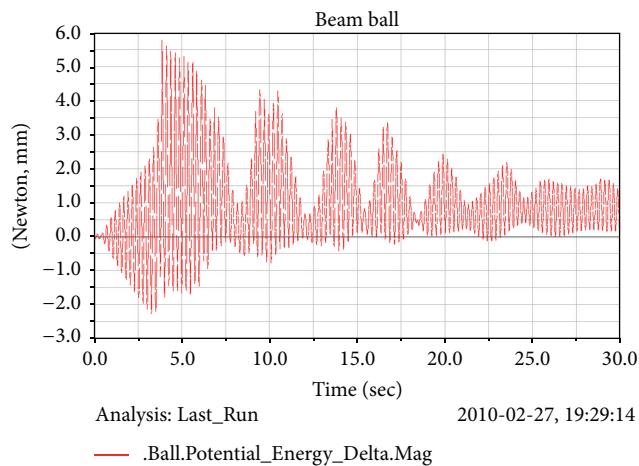


FIGURE 29: Ball potential energy delta curve for the forcing frequency of 4.13 Hz.

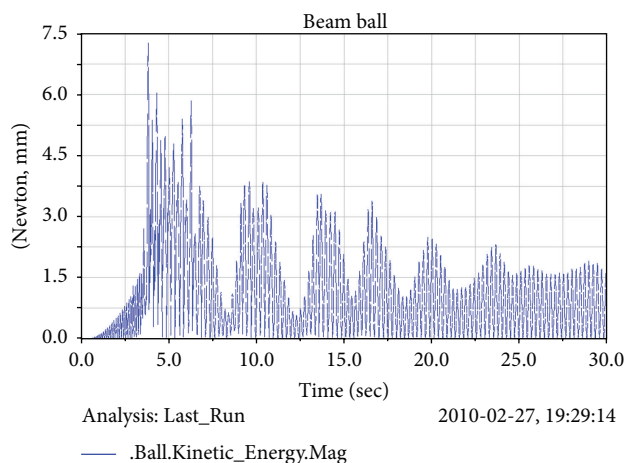


FIGURE 30: Ball kinetic energy curve for the forcing frequency of 4.13 Hz.

Futuristic structures will be made of materials like fiber reinforced polymers which are much lighter than steel and hence the vibration problem will be more acute. For example, traffic signal light structures, highway signs, and luminaires are observed to vibrate regularly at steady winds of 10 to 30 mph. The amplitude of vibration depends upon the characteristics of the wind like mean speed, mean direction, and gustiness; dynamic characteristics of the structures; and shape and size of the structure. Vortex shedding and buffeting are the two predominant wind-structure interaction phenomena which could cause vibrations in this class of structures, consisting mainly of a vertical pole and horizontal arm and lights or signs attached to the arm.

This study will provide useful information for designing passive vibration control devices and systems in an exposed environment. Also it will provide important information for the design-iteration process leading to an optimum passive vibration absorber for use in the real world. Results obtained from this study will generate knowledge to develop (a) better understanding of the working principles of control

systems, (b) design guidelines and standards, and (c) practical approaches for design, fabrication, and field installations.

Competing Interests

The authors declare that they have no competing interests.

References

- [1] F. Salam and S. Sastry, "Dynamics of the forced Josephson junction: the regions of chaos," *IEEE Transactions on Circuits and Systems*, vol. 32, no. 8, pp. 784–796, 1985.
- [2] W. Lee, *A global analysis of a forced spring pendulum system [Ph.D. thesis]*, University of California, Berkeley, Calif, USA, 1988.
- [3] A. H. Nayfeh, D. T. Mook, and L. R. Marshall, "Nonlinear coupling of pitch and roll modes in ship motions," *Journal of Hydrodynamics*, vol. 7, no. 4, pp. 145–152, 1973.
- [4] G. Mustafa, *Three-dimensional rocking and topping of block-like structures on rigid foundation [M.S. thesis]*, Texas Tech University, Lubbock, Tex, USA, 1987.
- [5] R. A. Ibrahim, *Parametric Random Vibration*, John Wiley & Sons, New York, NY, USA, 1985.
- [6] A. H. Nayfeh and B. Balachandran, "Modal interactions in dynamical and structural systems," *Applied Mechanics Reviews*, vol. 42, supplement 11, pp. S175–S201, 1989.
- [7] A. H. Nayfeh, *Nonlinear Interactions*, Wiley, New York, NY, USA, 2000.
- [8] E. Sevin, "On the parametric excitation of pendulum-type vibration absorber," *Journal of Applied Mechanics*, vol. 28, no. 3, pp. 330–334, 1961.
- [9] J.-C. Nissen, K. Popp, and B. Schmalhorst, "Optimization of a non-linear dynamic vibration absorber," *Journal of Sound and Vibration*, vol. 99, no. 1, pp. 149–154, 1985.
- [10] A. Ertas and G. Mustafa, "Real-time response of the simple pendulum: an experimental technique," *Experimental Techniques*, vol. 16, no. 4, pp. 33–35, 1992.
- [11] G. Mustafa and A. Ertas, "Dynamics and bifurcations of a coupled column-pendulum oscillator," *Journal of Sound and Vibration*, vol. 182, no. 3, pp. 393–413, 1995.
- [12] G. Mustafa and A. Ertas, "Experimental evidence of quasiperiodicity and its breakdown in the column-pendulum oscillator," *Journal of Dynamic Systems, Measurement and Control*, vol. 117, no. 2, pp. 218–225, 1995.
- [13] O. Cuvalci and A. Ertas, "Pendulum as vibration absorber for flexible structures: experiments and theory," *ASME Journal of Vibration and Acoustics*, vol. 118, no. 4, pp. 558–566, 1996.
- [14] W. Lacarbonara, R. R. Soper, A. H. Nayfeh, and D. T. Mook, "Nonclassical vibration absorber for pendulation reduction," *Journal of Vibration and Control*, vol. 7, no. 3, pp. 365–393, 2001.
- [15] I. Cicek and A. Ertas, "Experimental investigation of beam-tip mass and pendulum system under random excitation," *Mechanical Systems and Signal Processing*, vol. 16, no. 6, pp. 1059–1072, 2002.
- [16] K. E. Rifai, G. Haller, and A. K. Bajaj, "Global dynamics of an autoparametric spring-mass-pendulum system," *Nonlinear Dynamics*, vol. 49, no. 1-2, pp. 105–116, 2007.
- [17] B. Vazquez-Gonzalez and G. Silva-Navarro, "Evaluation of the autoparametric pendulum vibration absorber for a Duffing system," *Shock and Vibration*, vol. 15, no. 3-4, pp. 355–368, 2008.

- [18] N. Jiří and F. Cyril, "Auto-parametric semi-trivial and post-critical response of a spherical pendulum damper," *Computers & Structures*, vol. 87, no. 19–20, pp. 1204–1215, 2009.
- [19] R. Vigié and G. Kerschen, "Nonlinear vibration absorber coupled to a nonlinear primary system: a tuning methodology," *Journal of Sound and Vibration*, vol. 326, no. 3–5, pp. 780–793, 2009.
- [20] A. Vyas and A. K. Bajaj, "Dynamics of autoparametric vibration absorbers using multiple pendulums," *Journal of Sound and Vibration*, vol. 246, no. 1, pp. 115–135, 2001.
- [21] R. S. Haxton and A. D. S. Barr, "The autoparametric vibration absorber," *Journal of Engineering for Industry*, vol. 94, no. 1, pp. 119–225, 1972.
- [22] H. Hatwal, A. K. Mallik, and A. Ghosh, "Forced nonlinear oscillations of an autoparametric system—part 1: periodic responses," *Journal of Applied Mechanics*, vol. 50, no. 3, pp. 657–662, 1983.
- [23] S. S. Oueini, A. H. Nayfeh, and J. R. Pratt, "A nonlinear vibration absorber for flexible structures," *Nonlinear Dynamics*, vol. 15, no. 3, pp. 259–282, 1998.
- [24] O. N. Ashour and A. H. Nayfeh, "Adaptive control of flexible structures using a nonlinear vibration absorber," *Nonlinear Dynamics*, vol. 28, no. 3–4, pp. 309–322, 2002.
- [25] S. S. Oueini and A. H. Nayfeh, "Analysis and application of a nonlinear vibration absorber," *Journal of Vibration and Control*, vol. 6, no. 7, pp. 999–1016, 2000.
- [26] E. Matta, A. De Stefano, and B. F. Spencer Jr., "A new passive rolling-pendulum vibration absorber using a non-axial-symmetrical guide to achieve bidirectional tuning," *Earthquake Engineering & Structural Dynamics*, vol. 38, no. 15, pp. 1729–1750, 2009.
- [27] W. Schiehlen, "Multibody system dynamics: roots and perspectives," *Multibody System Dynamics*, vol. 1, no. 2, pp. 149–188, 1997.
- [28] W. W. Hooker and G. Margulies, "The dynamical attitude equations for n-body satellite," *Journal of the Astronautical Sciences*, vol. 12, pp. 123–128, 1965.
- [29] R. E. Roberson and J. Wittenburg, "A dynamical formalism for an arbitrary number of interconnected rigid bodies with reference to the problem of satellite attitude control," in *Proceedings of the 3rd Congress International Federation of Automatic Control*, Warsaw, Poland, 1967.
- [30] J. Wittenburg, *Dynamics of Systems of Rigid Bodies*, Teubner, Stuttgart, Germany, 1977.
- [31] P. E. Nikravesh, *Computer Aided Analysis of Mechanical Systems*, Prentice-Hall, Upper Saddle River, NJ, USA, 1988.
- [32] E. J. Haug, *Computer Aided Kinematics and Dynamics of Mechanical Systems*, Allyn and Bacon, Boston, Mass, USA, 1989.
- [33] R. E. Roberson and R. Schwertassek, *Dynamics of Multibody Systems*, Springer, Berlin, Germany, 1988.
- [34] R. L. Huston, *Multibody Dynamics*, Butterworth-Heinemann, Boston, Mass, USA, 1990.
- [35] J. García de Jalón and E. Bayo, *Kinematic and Dynamic Simulation of Multibody Systems*, Mechanical Engineering Series, Springer, Berlin, Germany, 1994.
- [36] O. P. Agrawal and A. A. Shabana, "Dynamic analysis of multibody systems using component modes," *Computers & Structures*, vol. 21, no. 6, pp. 1303–1312, 1985.
- [37] W. S. Yoo and E. J. Haug, "Dynamics of articulated structures: part I. Theory," *Journal of Structural Mechanics*, vol. 14, no. 1, pp. 105–126, 1986.
- [38] J. O. Song and E. J. Haug, "Dynamic analysis of planar flexible mechanisms," *Computer Methods in Applied Mechanics and Engineering*, vol. 24, no. 3, pp. 359–381, 1980.
- [39] A. A. Shabana, "Finite element incremental approach and exact rigid body inertia," *ASME Journal of Mechanical Design*, vol. 118, no. 2, pp. 171–178, 1996.
- [40] A. A. Shabana, *Dynamics of Multibody Systems*, Cambridge University Press, New York, NY, USA, 2005.
- [41] C. C. Rankin and F. A. Brogan, "An element independent corotational procedure for the treatment of large rotations," *Journal of Pressure Vessel Technology*, vol. 108, no. 2, pp. 165–174, 1986.
- [42] J. C. Simo and L. Vu-Quoc, "On the dynamics of flexible beams under large overall motions—the plane case: part I," *Journal of Applied Mechanics*, vol. 53, no. 4, pp. 849–854, 1986.
- [43] J. L. Escalona, H. A. Hussien, and A. A. Shabana, "Application of the absolute nodal coordinate formulation to multibody system dynamics," Tech. Rep., University of Illinois at Chicago, Chicago, Ill, USA, 1997.
- [44] J. L. Escalona, H. A. Hussien, and A. A. Shabana, "Application of the absolute nodal co-ordinate formulation to multibody system dynamics," *Journal of Sound and Vibration*, vol. 214, no. 5, pp. 833–851, 1998.
- [45] J. T. Sopanen and A. M. Mikkola, "Description of elastic forces in absolute nodal coordinate formulation," *Nonlinear Dynamics*, vol. 34, no. 1–2, pp. 53–74, 2003.
- [46] R. Iwai and N. Kobayashi, "A new flexible multibody beam element based on the absolute nodal coordinate formulation using the global shape function and the analytical mode shape function," *Nonlinear Dynamics*, vol. 34, no. 1–2, pp. 207–232, 2003.
- [47] O. Wallrapp and S. Wiedemann, "Comparison of results in flexible multibody dynamics using various approaches," *Nonlinear Dynamics*, vol. 34, no. 1–2, pp. 189–206, 2003.
- [48] A. A. Shabana, "Computer implementation of the absolute nodal coordinate formulation for flexible multibody dynamics," *Nonlinear Dynamics*, vol. 16, no. 3, pp. 293–306, 1998.
- [49] W.-S. Yoo, J.-H. Lee, S.-J. Park, J.-H. Sohn, O. Dmitrochenko, and D. Pogorelov, "Large oscillations of a thin cantilever beam: physical experiments and simulation using the absolute nodal coordinate formulation," *Nonlinear Dynamics*, vol. 34, no. 1–2, pp. 3–29, 2003.
- [50] W.-S. Yoo, J.-H. Lee, S.-J. Park, J.-H. Sohn, D. Pogorelov, and O. Dmitrochenko, "Large deflection analysis of a thin plate: computer simulations and experiments," *Multibody System Dynamics*, vol. 11, no. 2, pp. 185–208, 2004.
- [51] M. Berzeri and A. A. Shabana, "Development of simple models for the elastic forces in the absolute nodal co-ordinate formulation," *Journal of Sound and Vibration*, vol. 235, no. 4, pp. 539–565, 2000.
- [52] R. A. Wehage and E. J. Haug, "Generalized coordinate partitioning for dimension reduction in analysis of constrained dynamic systems," *Journal of Mechanical Design*, vol. 104, no. 1, pp. 247–255, 1982.
- [53] N. M. Newmark, "A method of computation for structural dynamics," *Journal of the Engineering Mechanics Division*, vol. 85, no. 3, pp. 67–94, 1959.
- [54] F. N. Mayoof, "Beating phenomenon of multi-harmonics defect frequencies in a rolling element bearing: case study from water pumping station," *World Academy of Science, Engineering and Technology*, vol. 57, pp. 327–331, 2009.

Research Article

Performance Analysis of a Magnetorheological Damper with Energy Harvesting Ability

Guoliang Hu,^{1,2} Yun Lu,² Shuaishuai Sun,² and Weihua Li²

¹Key Laboratory of Conveyance and Equipment, The Ministry of Education, East China Jiaotong University, Nanchang, Jiangxi 330013, China

²School of Mechanical, Materials and Mechatronics Engineering, University of Wollongong, Wollongong, NSW 2522, Australia

Correspondence should be addressed to Guoliang Hu; glhu2006@163.com and Weihua Li; weihuali@uow.edu.au

Received 18 May 2016; Accepted 11 July 2016

Academic Editor: Londono Monsalve

Copyright © 2016 Guoliang Hu et al. This is an open access article distributed under the Creative Commons Attribution License, which permits unrestricted use, distribution, and reproduction in any medium, provided the original work is properly cited.

A magnetorheological (MR) damper with energy harvesting ability was proposed based on electromagnetic induction (EMI) principle. The energy harvesting part was composed of a permanent magnet array and inducing coils which move vertically. This device could act as a linear power generator when the external excitation was applied, and the kinetic energy could be converted into electrical energy due to the relative linear motion between the magnets array and the inducing coils. Finite element models of both the MR damper part and the linear power generator part were built up separately to address the magnetic flux distributions, the magnetic flux densities, and the power generating efficiency using ANSYS software. The experimental tests were carried out to evaluate the damping performance and power generating efficiency. The results show that the proposed MR damper can produce approximately 750 N damping forces at the current of 0.6 A, and the energy harvesting device can generate about 1.0 V DC voltage at $0.06 \text{ m}\cdot\text{s}^{-1}$ excitation.

1. Introduction

Over the past couple of decades, magnetorheological (MR) fluid has undergone significant development due to its unique rheological properties under exerted magnetic fields [1]. These features have led to the development of many MRF-based devices such as the MR damper, MR valve, MR brake, and MR clutch. The most popular MRF-based devices are MR dampers due to their long range controllable damping force, fast adjustable response, and low energy consumption [2].

Till now, the MR dampers have wide applications in automotive industry including off-road vehicles [3, 4], and they are also used in naval gun controlling [5], field of landing gear [6], prosthetic knees [7], washing machines [8], high speed train suspension [9, 10], seismic vibration control of different civil structures [11, 12], and so forth. However, a significant drawback of traditional MR damper is witnessed; that is, the kinetic energy from the vibration is wasted in heating rather than harvested as a reusable power resource due to lack of energy harvesting device.

Recently, energy harvesting MR dampers have received a great deal of attention due to their capability of recovering kinetic energy that normally dissipated by traditional MR dampers. Many researchers explored different principles and designs of energy harvesting MR dampers, which can be classified into two main categories. The first category is to convert the linear damper vibration into oscillatory rotation and use rotational permanent magnetic DC or AC generators to harvest kinetic energy. These mechanical mechanisms include rack and pinion, ball screw, and hydraulic transmission. Avadhany et al. [13] patented one type of rotary regenerative shock absorber based on hydraulic transmission. Choi et al. [14] proposed an electrorheological (ER) shock absorber integrated with a generator by employing a rack and pinion gear mechanism, which converted a linear motion of the piston to a rotary motion, thus activating a generator to produce electrical energy to self-power the excitation coil in the piston head. Li and Zuo [15, 16] proposed an energy harvesting shock absorber with a mechanical motion rectifier (MMR), the roller clutches were embedded in two bevel

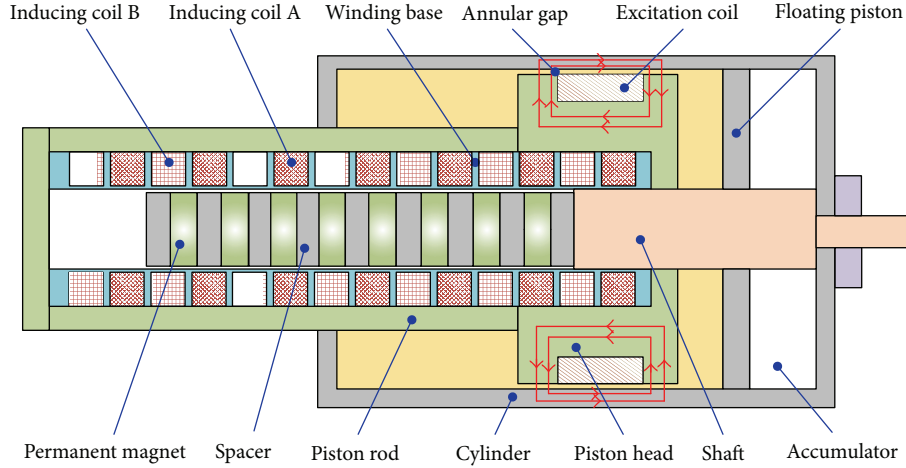


FIGURE 1: Schematic diagram of the proposed MR damper with energy harvesting ability.

gears, and the function of “motion rectifier” was achieved with three bevel gears in the MMR. Yu et al. [17] proposed a new type of energy harvesting device system for the wireless sensing of inner-state conditions in the operation of MR dampers, where an impeller mechanism was used as the amplitude convert device, and an AC generator was applied as the energy converting part to convert the linear shock into electrical energy. Zhang et al. [18] developed and prototyped a regenerative shock absorber based on a ball screw mechanism and validated it with full vehicle experiments in the lab. Guan et al. [19] proposed a novel MR damper with a self-powered capability; the vibration energy harvesting mechanisms were adopted based on ball screw mechanisms and a rotary permanent magnet DC generator, which converted the external vibration energy into electrical energy to power the MR damping unit.

In addition to the energy harvesting with mechanical transmission mechanism in the MR damper, the second category is based on the design of an electromagnetic induction (EMI) device, which generates power from the relative linear motion between magnets and coils. Cho et al. [20] proposed a special structure of an EMI device to be used with an MR damper. Choi et al. [21] investigated experimentally a smart passive control system comprising an MR damper and an EMI device to generate electrical power. Choi and Wereley [22] studied the feasibility and effectiveness of a self-powered MR damper using a spring-mass EMI device. Sapiński established a permanent magnet power generator for MR damper, the designed vibration generator consisted of a special arrangement and a foil wound coil, and the numerical analysis and experiment were carried out to investigate the magnetic field distribution and efficiency of the generator [23, 24]. Then, Sapiński proposed a multipole magnetic generator, the design of permanent magnets array was optimized, and both numerical method and finite element simulation were carried out to investigate the performance of the whole energy harvesting MR damper [25]. However, the large cogging force generated in the interaction between ferromagnetic components and

permanent magnets array led to a negative impact on the control of MR damper. Chen and Liao also proposed a self-sensing MR damper with power generation; the design of the power generator significantly minimized the cogging force and improved the dynamic damping performance [26]. The guild layer and shield layer were adopted to minimize magnetic interaction effect between permanent generator and MR damper. However, the extra shield and guild layer increased the complex of the whole structure while the component itself provided litter contribution to the dynamic control or improvement of generating effect.

In this paper, a new MR damper with energy harvesting ability was proposed based on the EMI principle. The sharing component between the damper part and the linear power generator part could minimize the magnetic field interference without extra guild layer and shell layer; also the component itself provided necessary function in both generating process and damping capability. This new design is expected to simplify the structure of linear power generator and also provided a low cogging force. The inducing coils in the linear power generator had two representative electric circuits. In this study, finite element method was utilized to address the magnetic field distribution and magnetic flux density for the damper part and linear power generator part, respectively, and cogging force conducted from linear power generator was also identified. The properties of proposed MR damper were experimentally investigated, and power regenerative characteristics were also discussed.

2. Principle and Structure of the Proposed MR Damper with Energy Harvesting Ability

Figure 1 shows the schematic diagram of the proposed MR damper with energy harvesting ability. The MR damper consists of a damping part and a linear power generator part. In the damping part, there are two chambers in the cylinder, and the chamber is separated by a floating piston. The chamber with piston is filled with MR fluid, and the other chamber is used as an accumulator to compensate the

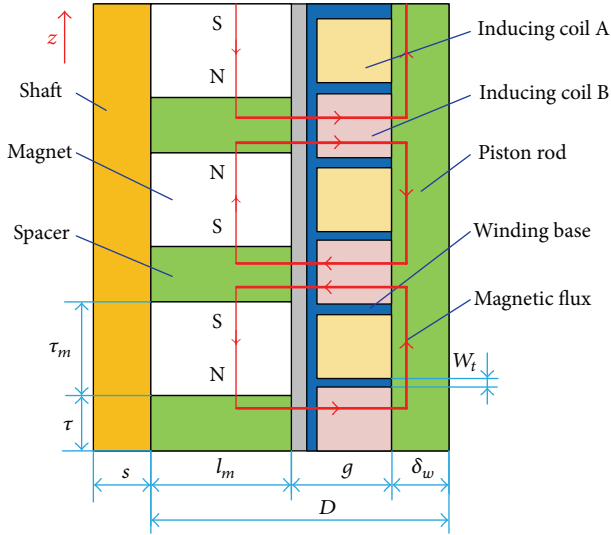


FIGURE 2: Magnetic circuit of the linear power generator.

volume change when the piston rod moves vertically along the vibration direction. A compression spring is stalled in the accumulator to support the movement of floating piston. When the piston rod moves, the MR fluid in the cylinder flows through the annular gap between piston head and cylinder. The excitation coil wound around the piston head is electrically insulated. When a direct current was applied on the excitation coil, a magnetic field is generated around the excitation coil and piston head. Then the annular gap would become an activated area and the viscosity of MR fluid in the gap would be changed. Finally, the changeable damping force is achieved.

The linear power generator is radially arranged inside the MR damper. Each two permanent magnets are separated by a spacer; also a magnet and a spacer are grouped to a pole pair. There are totally eight pairs of magnet-spacer assembling together, and they are screwed on the shaft. The inducing coil was arranged on the winding base. The phase of the generated voltage depends on the magnetic field distribution, the phase angle is 90° between each nearby coil, and each two different phases of coil are connected together to increase power generating efficiency. In this design, the 0° and 180° phase coils are connected together, which is called coil A; also the 90° and 270° are connected together, which is called coil B. Thus, the 14 phase coils are wound in the winding base and combined into two inducing coils, that is, coil A and coil B. When the interaction between permanent magnets and inducing coils occurred, the vibration energy would be converted into electric into coil A and coil B.

The magnetic circuit of the linear power generator is shown in Figure 2. The rotor of the linear power generator consists of a winding base and two inducing coils A and B, and the stator is assembled by a shaft, permanent magnets, and spacers. Each pole pair includes a permanent magnet and a pole spacer, and 8 pairs of magnet arrays are installed on the shaft; and the shaft is fixed by the cylinder through the screw, and this structure is also called multipole. As shown

in Figure 2, the magnetic flux radially passes through the half-length of the spacer and then through air gap and the inducing coil, reaching the piston rod, and then returns to the winding base, air gap, and half-length of spacer, finally reaching the opposite of permanent magnet.

3. Finite Element Analysis of the Proposed MR Damper with Energy Harvesting Ability

In order to address the magnetic field distribution and magnetic flux density on the piston head and the generating property of the linear power generator, the finite element models were built up using ANSYS software, and the issues of cogging force and magnetic interference were also discussed in this section.

3.1. Modelling of the MR Damper Part. As shown in Figure 1, the damper piston is radially outside of the linear power generator. The benefit of this structure is that the piston rod is utilized both as the shield and outer core of the linear power generator. This design can minimize the magnetic interaction between the linear power generator and the MR damper part while not adding extra structure in the damper. As the producer of electromagnetic field, the excitation coil is considered as electromagnet. By varying the driving current through the excitation coil, the magnetic flux density can be varied too. The DC current is supplied to the excitation coil, and the current density J_s is given by

$$J_s = \frac{NI}{A}, \quad (1)$$

where N is the number of turns of the excitation coil, I is the DC current, and A is the cross-sectional area of the coil.

In this simulation analysis, the physics environment is set as magnetic nodal option from preferences of ANSYS. The two-dimensional axisymmetric entity model of the MR damper part is built up as shown in Figure 3(a). The entity model includes the piston rod, the piston head, the excitation coil, the cylinder, and the resistance gap filled with MR fluid. Figure 3(b) presents the finite element model of the damper part. The element type is chosen as PLANE 13, and the 4-node quadrilateral meshing is used for the finite element model. This model is divided into 1237 elements and 3850 nodes. The leakage of magnetic flux is considered to acquire the reliable magnetic field distribution for the piston head.

Figure 4 illustrates the finite element model and static electromagnetic field simulation of the MR damper part. Figure 4(a) shows the magnetic flux of the MR damper part; it can be seen that the magnetic flux vertically passes through the annular gap, which means the high efficiency of magnetic field. Figure 4(b) illustrates the magnetic flux density of the main area for the MR damper part; the magnetic flux density within the annular gap ranged from 0.55 T to 0.74 T when the excitation current was set as 1 A, which leads to generating a large damping force.

Figure 5 shows the magnetic flux density of the annular resistance gap under the different applied current. As shown in the figure, the magnetic flux density is increased with

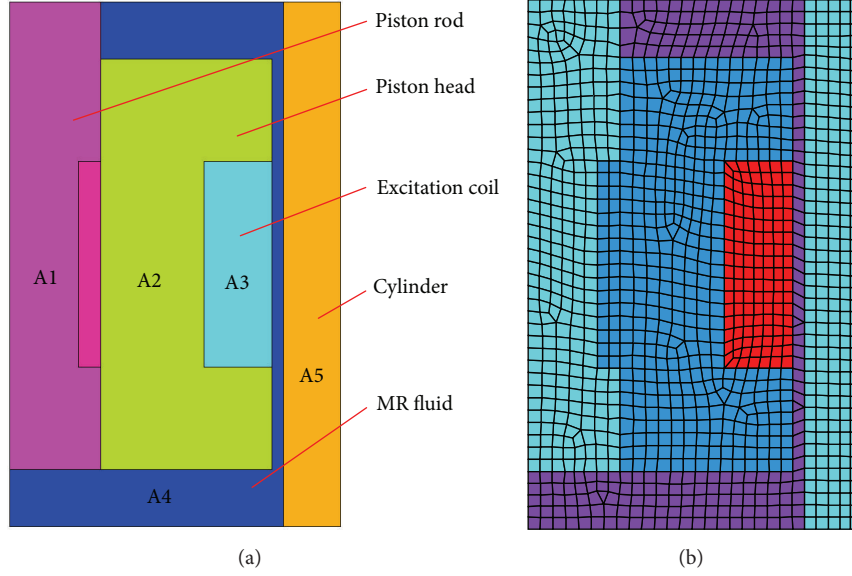


FIGURE 3: Modelling of the MR damper part: (a) entity model and (b) finite element model.

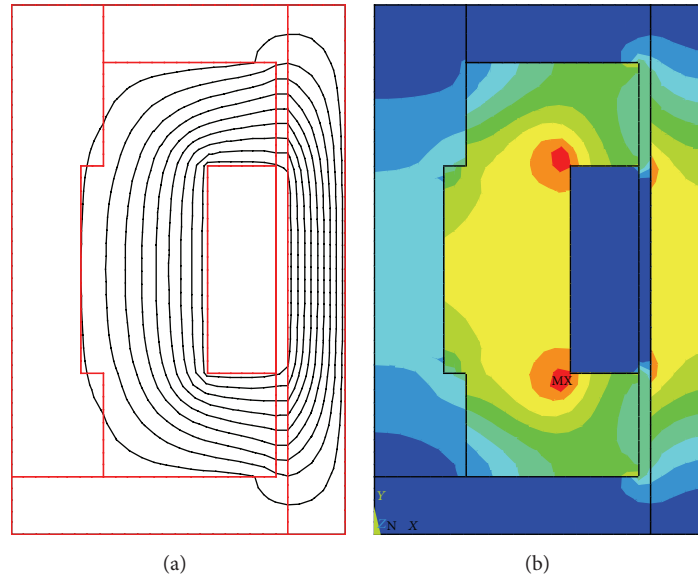


FIGURE 4: Finite element analysis of MR damper part: (a) magnetic flux distribution and (b) magnetic flux density.

the increment of the applied current. The most efficient energy utilization point occurred at the current of 0.6 A, and the magnetic saturation point occurred at the point of 1 A excitation.

Figure 6 shows the relation between damping force and displacement under different applied current. The amplitude is set as 5 mm and the frequency is 1 Hz. Observing the figure, the damping force increased as the increasing of the excitation, and the change of damping force agreed well with the simulation result for the magnetic field.

3.2. Modelling of the Linear Power Generator Part. The numerical analysis was carried out to address the magnetic

property for only one pole pair. It can be assumed that the reluctance values of the pole spacer are neglected for their high magnetic permeability; thus the magnetic flux is given as [27]

$$\phi_g = \frac{B_{rem} \tau_m \mu_0 H_c A_c}{2g B_{rem} + \tau_m \mu_0 H_c A_c (A_g / A_m)}, \quad (2)$$

where ϕ_g is the magnetic flux of air gap without considering the leakage, μ_0 is the relative magnetic permeability and equals $4\pi \times 10e^{-7}$ (N/A²), H_c is the magnetic field intensity of magnet, B_{rem} is the flux density of the magnet, A_g is

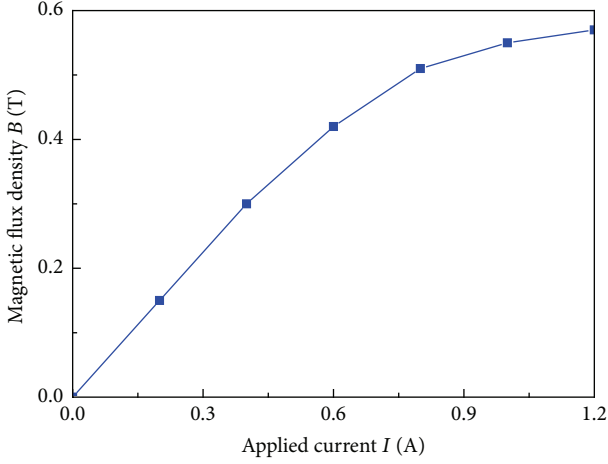


FIGURE 5: Magnetic flux density under different applied current.

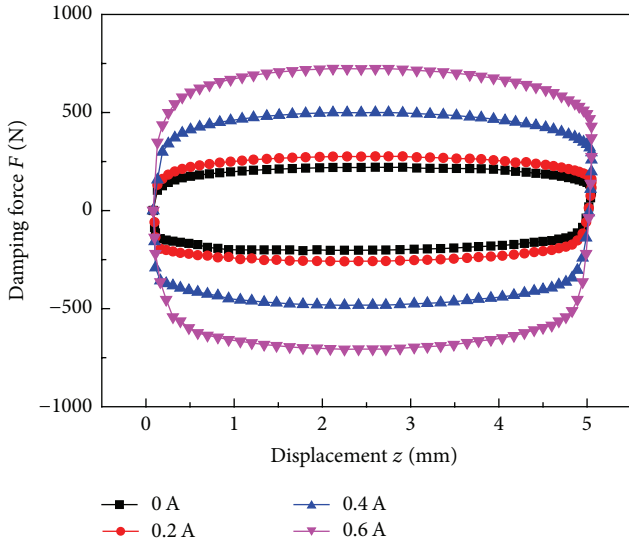


FIGURE 6: Damping force versus displacement at the different applied current.

the surface area of cylindrical air gap, A_m is the cross-section area of magnet, and A_g and A_m can be obtained by

$$\begin{aligned} A_g &= \pi \left(s + l_m + \frac{g}{2} \right) \tau_m, \\ A_m &= \pi \left[(s + l_m)^2 - s^2 \right], \end{aligned} \quad (3)$$

where s is the diameter of shaft, l_m is the thickness of the permanent magnet, g is the length of air gap between piston rod and permanent magnet array, and τ_m is the magnet thickness.

The induced voltage E in the inducing coil is defined as

$$E = -N \phi_g \frac{\pi}{\tau + \tau_m} \sin \left(\frac{\pi}{\tau + \tau_m} z + \theta \right) \frac{dz}{dt}, \quad (4)$$

where N is number of turns of the inducing coil, τ is spacer thickness, z is the displacement, dz/dt is the velocity, and θ is the initial phase angle of inducing coil.

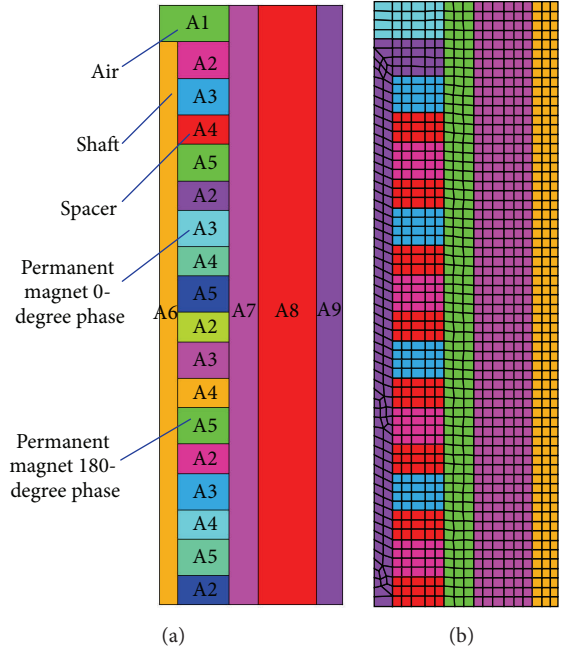


FIGURE 7: Modelling of the linear power generator: (a) entity model and (b) finite element model.

The number of turns of N is defined as

$$N = \frac{2A_c}{\sqrt{3}d^2}, \quad (5)$$

where A_c is the cross-sectional area of electrical wire and d is the diameter of the wire.

Figure 7 shows the modelling of the linear power regenerator. As shown in Figure 7(a), the main components of the linear power generator include the air chamber (A1), the permanent magnet arrays (A2, A3, A4, and A5), the shaft (A6), the winding base and inducing coils (A7), the piston rod (A8), and the zone filled with MR fluid (A9). There are two arrangements for the permanent magnets: 0° phase and 180° phase. Each two opposite arranged magnets are represented by a spacer. Figure 7(b) shows the finite element model of the linear power generator. The element type is chosen as PLANE 13, and the finite element model consists of 1217 elements and 3816 nodes. The winding base is made of ABS material, which is a nonmagnetic material; the electrical wire is made of brass material. As a result, the permeability of the two materials in the air gap is identical. The shaft is made of aluminum. The spacer and piston rod are made of steel 1020 which provide a high permeability.

Figure 8 illustrates the finite element analysis of the linear power regenerator. Figure 8(a) shows the magnetic flux distribution; the magnetic flux passes through the gap between the magnet arrays and the piston rod. As a result, the inducing coils installed in the winding base can generate induced voltage when the relative linear motion between the magnet arrays and inducing coil occurred. Figure 8(b) presents the static electromagnetic field distribution. The maximum magnetic flux density in the pole spacer is 0.9 T,

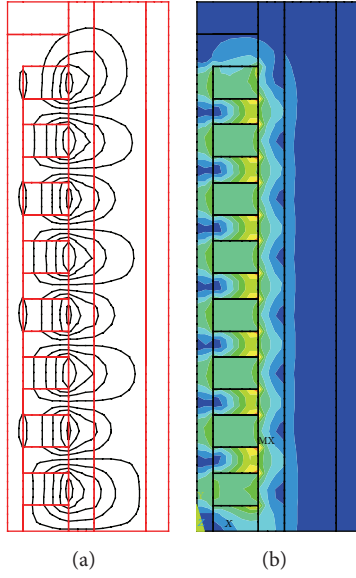


FIGURE 8: Finite element analysis of the linear power generator: (a) magnetic flux distribution and (b) magnetic flux density.

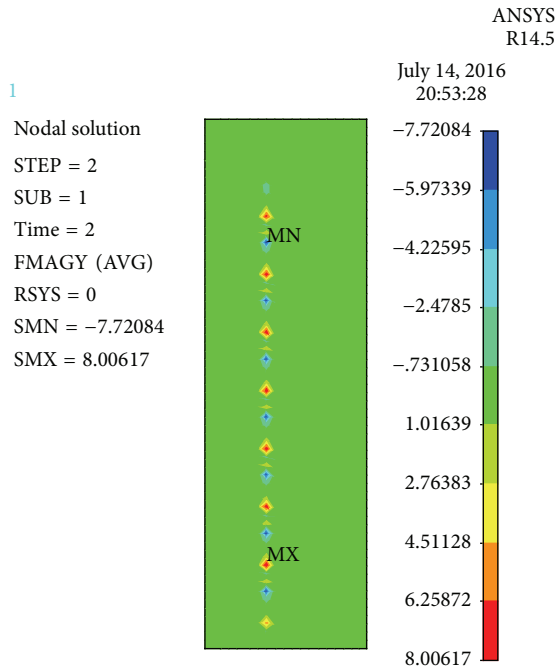


FIGURE 9: Magnet force distribution of the linear power generator.

while the flux density in the spacer is 0.3 T on average. The winding base is made of ABS material, which is a nonmagnetic material; also the electrical wire is made of brass material. As a result, the magnetic flux density within the inducing coils and the flux leakage coefficient is small.

Figure 9 shows the cogging force distribution of the linear power generator. As shown in the figure, a low cogging force is obtained due to the compact structural design, and the total cogging force is about 1 N.

TABLE 1: Specifications of the proposed MR damper.

Parameter	Value
Diameter of piston R	79 mm
Diameter of coil space R_c	50 mm
Thickness of cylinder R_h	5 mm
Gaps of MR fluid h	1 mm
Length of piston L	28 mm
Height of gallery W_c	9 mm
Length of gallery L_1, L_2	9 mm
Number of turns N	250
Weight of coil space L_c	18 mm
Diameter of excitation coil wire	0.5 mm
Resistance of excitation coil	4 Ω
Diameter of generator structure D	17 mm
Magnet thickness τ_m	5 mm
Magnet height l_m	5 mm
Magnet number	8
Diameter of rod s	2.5 mm
Spacer thickness τ	4 mm
Length of teeth W_t	2 mm
Thickness of piston rod δ_w	5 mm
Length of air gap g	4.5 mm
Coil maximum current	1.5 A
Coil wire turns	256
Diameter of inducing coil wire	0.5 mm
Resistance per inducing coil	4 Ω

4. Experiment Analysis of the Proposed MR Damper with Energy Harvesting Ability

4.1. Prototyping of the Proposed MR Damper. Figure 10 shows the main components and assembly of the manufactured MR damper, and the parameters of the MR damper are shown in Table 1. The cylinder and the piston rod are made of high magnetic material steel 1020, the shaft of the linear power generator is made of aluminum which is a nonmagnetic material, and the material used in spacers is steel 1020. The permanent magnets that are used in the design are NdFeB magnets grade N52. The magnets are stacked in pairs as shown in Figure 1; the magnetic flux passes through the spacers under the driving of opposite magnetomotive forces.

4.2. Damping Performance of the MR Damper Part. Figure 11 shows the damping properties under different coil currents, in the test, the frequency is set as 1 Hz and the amplitude is 5 mm, and the direct current is selected as 0 A, 0.2 A, 0.4 A, and 0.6 A, respectively. It can be seen that the damping force is about 200 N without the applied current; the reason is that the damping force at 0 A is generally from the stiffness of the accumulator and the MR fluid in the damper that works under Newtonian fluid model. The damping force increases from 200 N to about 750 N when 0.6 A current is applied. In this situation, the power consuming of the proposed damper is about 1.4 W. It can be seen that the damping force depends on the applied current, and the damping force will be changed

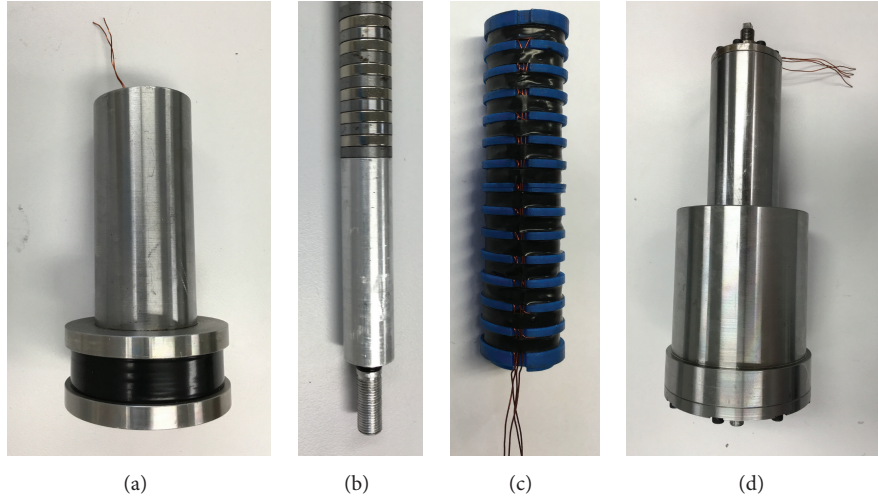


FIGURE 10: The proposed MR damper: (a) piston head, (b) permanent magnets array and shaft, (c) winding base and inducing coils of generator, and (d) the assembly.

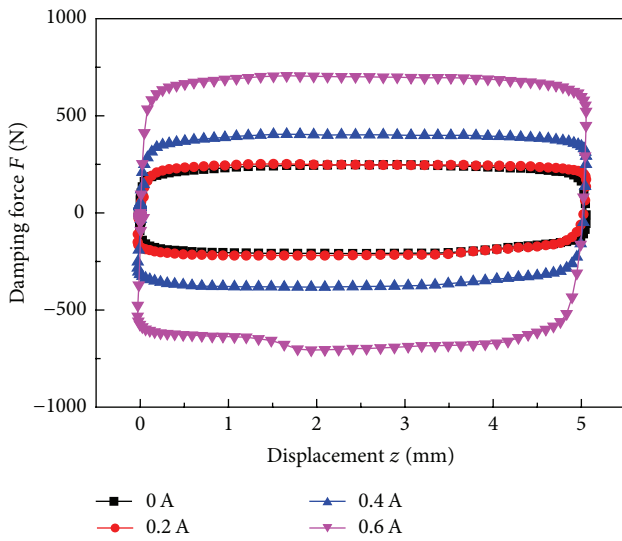


FIGURE 11: Damping force and displacement relation of the MR damper.

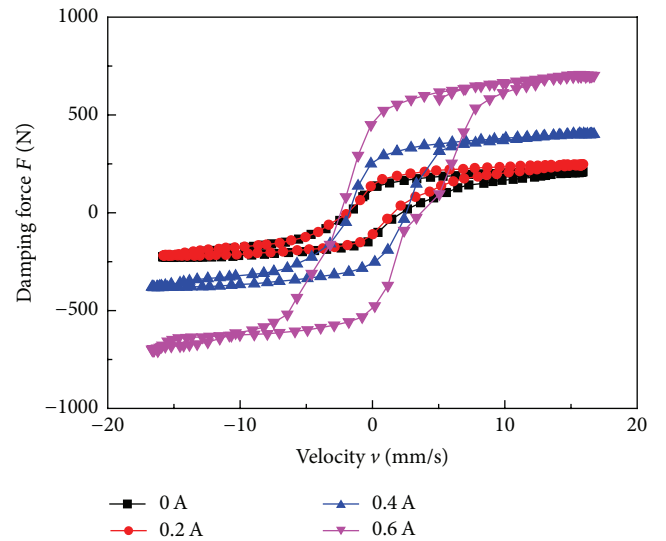


FIGURE 12: Damping force and velocity relation of the MR damper.

by changing the current input. Thus, the proposed damper could generate large controllable damping force output, while under relatively low power consumption.

Figure 12 illustrates the damping force and velocity response under different applied currents, and in the test, the frequency is set as 1 Hz and the amplitude is 5 mm. The maximum velocity is 17 mm/s when the MR damper operates under 0.6 A excitation.

Figure 13 shows the comparison of damping force between the theoretical result and experimental result. The excitation current is set at 0.6 A. As shown in Figures 13(a) and 13(b), the theoretical results agree well with the experimental ones. It can be summarized that the feasibility of proposed analysis had been proved.

4.3. Energy Harvesting Capability of the Linear Power Generator without AC-DC Rectifier. In this experiment, the measured inducing voltage from the two inducing coils A and B illustrated the properties of the linear power regenerator. The calculation data was obtained by the numerical analysis mentioned in Section 3.2. The comparison of inducing voltage between numerical analysis and experiment measurement is shown in Figure 14. Observing Figures 14(a) and 14(b), the experiment data from coil A and coil B agreed well with the numerical results, and the measured peak inducing voltage is 1.22 V. However, the wave of the inducing voltage is not the typical sinusoidal wave when the amplitude increases; the reason is the effect of frequency multiplication [26].

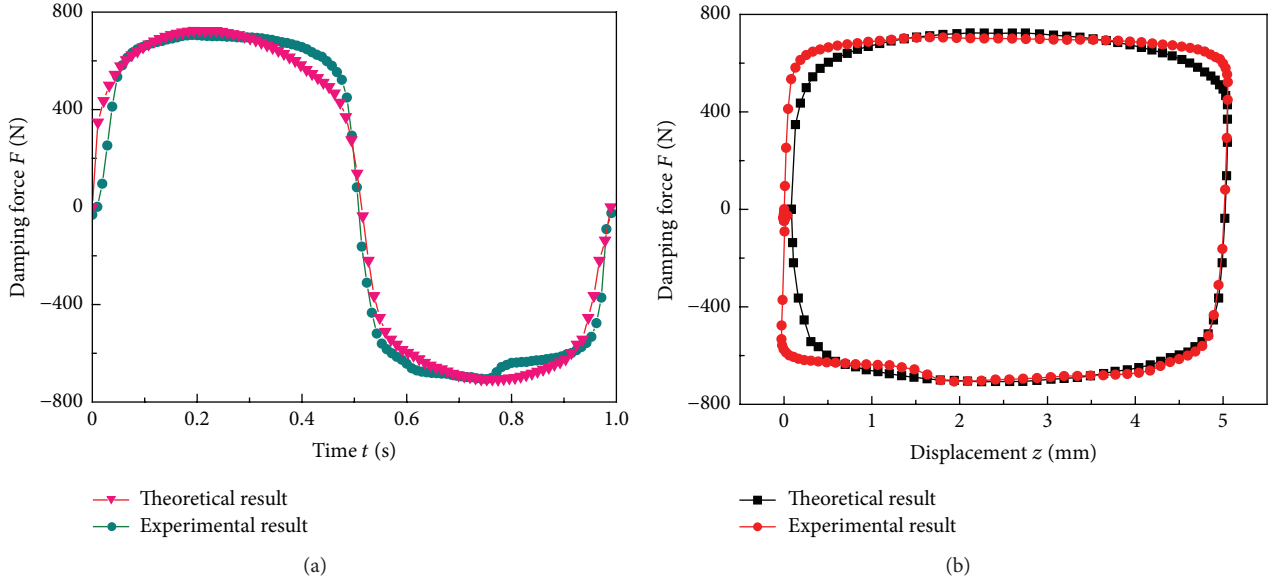


FIGURE 13: Comparison between theoretical result and experimental data: (a) damping force versus time and (b) damping force versus displacement.

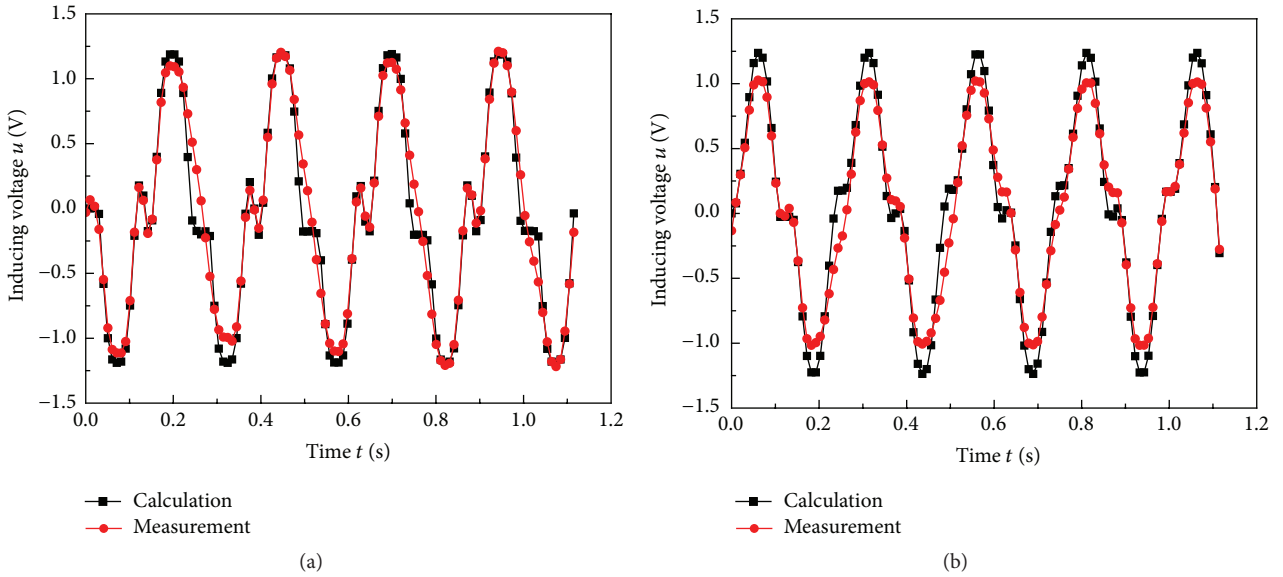


FIGURE 14: Comparison between numerical analysis result and experimental test of inducing voltage: (a) coil A and (b) coil B.

4.4. Energy Harvesting Capability of the Linear Power Generator with AC-DC Rectifier. Because the inducing coils installed in the piston are equivalent as an electrical inductance, the value of generated DC voltage is better to evaluate the performance effect of proposed linear power generator compared with AC voltage. Thus, a bridge rectifier is developed, and the relevant experiment was carried out to evaluate performance of the linear power generator. The principle of the bridge rectifier is shown in Figure 15, two inducing coils A and B were applied in the linear power generator, and six diodes and one capacitor were needed in the bridge rectifier. In the experiment, the vibration excitation was constant,

and the output of the proposed rectifier was connected to DAQ board. The MR damper was installed in the MTS which provided the amplitude and frequency excitation. The inducing coils from the generator were connected with the rectifier which adhered with the outer cylinder of the MR damper. In order to prevent the noise signal from DC power source, the DC power source state was set as off. However, there are still large numbers of noises in the experimental data.

Figure 16 shows the inducing voltage of the linear power generator after the rectifier processing. The rectified DC voltage from the two inducing coils is approximately 1.0 V

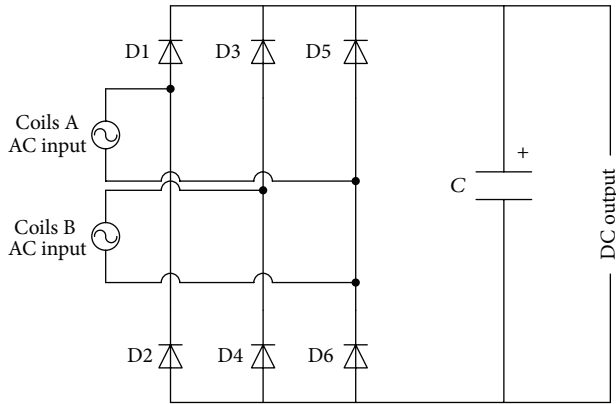


FIGURE 15: Schematic of the AC-DC rectifier.

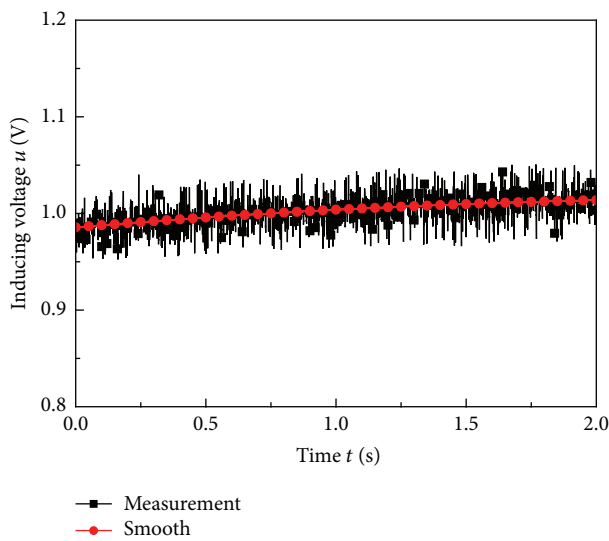


FIGURE 16: Inducing voltage of linear power generator with AC-DC rectifier.

at $0.06 \text{ m}\cdot\text{s}^{-1}$ excitation. However, there are still some noises existing in the initial data denoted as black line due to lack of filtering. There are two ways to minimize the signal noises: the first is a commercial rectifier or DAQ board should be adopted as the signal processing unit to minimize the noises from electro circuit. The second is a shield or a filter should be applied to isolate the interference from environment.

5. Conclusions

In this study, an MR damper with energy harvesting ability was designed, fabricated, and tested. The proposed MR damper used the piston rod as the sharing component between the linear power regenerator and the MR damper part, and this shared component could isolate the magnetic field between two function areas. As a result, the magnetic field interference was minimized without extra designed shield and guild layer.

The finite element method was developed to address the magnetic field and magnetic flux distribution of the MR

damper part. The simulation result proved the efficiency and feasibility of the proposed MR damper. Then the numerical method was utilized to evaluate the generating performance of the linear power generator, and the finite element model was utilized to investigate the magnetic field distribution. The issue of cogging force and minimization of the magnetic interaction had been solved.

Experimental tests were carried out to address the performances of the proposed MR damper. The results show that the damping force ranges from 200 N at the current of 0 A to 750 N at the current of 0.6 A. The dynamic range equals about 3.75. The AC-DC rectifier was applied on the power generating, and the results show that 1.0 V DC voltage output was harvested after the AC-DC processing.

Competing Interests

The authors declare that there are no competing interests regarding the publication of this paper.

Acknowledgments

This research was financially supported by the National Natural Science Foundation of China (nos. 51475165 and 11462004), the Natural Science Foundation and the Educational Commission Project of Jiangxi Province of China (nos. 20151BAB206035 and GJJ150525), and the Australian Research Council Discovery Project (no. 1501002636).

References

- [1] W. H. Li, H. Du, G. Chen, S. H. Yeo, and N. Guo, "Nonlinear viscoelastic properties of MR fluids under large-amplitude-oscillatory-shear," *Rheologica Acta*, vol. 42, no. 3, pp. 280–286, 2003.
- [2] X. Zhu, X. Jing, and L. Cheng, "Magnetorheological fluid dampers: a review on structure design and analysis," *Journal of Intelligent Material Systems and Structures*, vol. 23, no. 8, pp. 839–873, 2012.
- [3] K. El Majdoub, D. Ghani, F. Giri, and F. Z. Chaoui, "Adaptive semi-active suspension of quarter-vehicle with magnetorheological damper," *Journal of Dynamic Systems, Measurement and Control*, vol. 137, no. 2, Article ID 021010, 2015.
- [4] Y. J. Shin, W. H. You, H. M. Hur et al., "Improvement of ride quality of railway vehicle by semiactive secondary suspension system on roller rig using magnetorheological damper," *Advances in Mechanical Engineering*, vol. 6, Article ID 298382, 2014.
- [5] H. J. Singh and N. M. Wereley, "Optimal control of gun recoil in direct fire using magnetorheological absorbers," *Smart Materials and Structures*, vol. 23, no. 5, Article ID 055009, 2014.
- [6] L. A. Powell, W. Hu, and N. M. Wereley, "Magnetorheological fluid composites synthesized for helicopter landing gear applications," *Journal of Intelligent Material Systems and Structures*, vol. 24, no. 9, pp. 1043–1048, 2013.
- [7] K. H. Gudmundsson, F. Jonsdottir, F. Thorsteinsson, and O. Gutfleisch, "An experimental investigation of unimodal and bimodal magnetorheological fluids with an application in prosthetic devices," *Journal of Intelligent Material Systems and Structures*, vol. 22, no. 6, pp. 539–549, 2011.

- [8] Q. H. Nguyen, S.-B. Choi, and J. K. Woo, "Optimal design of magnetorheological fluid-based dampers for front-loaded washing machines," *Proceedings of the Institution of Mechanical Engineers, Part C: Journal of Mechanical Engineering Science*, vol. 228, no. 2, pp. 294–306, 2014.
- [9] Z. Li, Y.-Q. Ni, H. Dai, and S. Ye, "Viscoelastic plastic continuous physical model of a magnetorheological damper applied in the high speed train," *Science China Technological Sciences*, vol. 56, no. 10, pp. 2433–2446, 2013.
- [10] S. Sun, H. Deng, W. Li et al., "Improving the critical speeds of high-speed trains using magnetorheological technology," *Smart Materials and Structures*, vol. 22, no. 11, Article ID 115012, 2013.
- [11] G. Yang, B. F. Spencer Jr., H.-J. Jung, and J. D. Carlson, "Dynamic modeling of large-scale magnetorheological damper systems for civil engineering applications," *Journal of Engineering Mechanics*, vol. 130, no. 9, pp. 1107–1114, 2004.
- [12] F. Amini and P. Ghaderi, "Optimal locations for MR dampers in civil structures using improved ant colony algorithm," *Optimal Control Applications & Methods*, vol. 33, no. 2, pp. 232–248, 2012.
- [13] S. Avadhany, P. Abel, V. Tarasov et al., "Regenerative shock absorber," U.S. Patent No. 8,376,100, February 2013.
- [14] S.-B. Choi, M.-S. Seong, and K.-S. Kim, "Vibration control of an electrorheological fluid-based suspension system with an energy regenerative mechanism," *Proceedings of the Institution of Mechanical Engineers, Part D: Journal of Automobile Engineering*, vol. 223, no. 4, pp. 459–469, 2009.
- [15] Z. Li, L. Zuo, G. Luhrs, L. Lin, and Y.-X. Qin, "Electromagnetic energy-harvesting shock absorbers: design, modeling, and road tests," *IEEE Transactions on Vehicular Technology*, vol. 62, no. 3, pp. 1065–1074, 2013.
- [16] Z. Li, L. Zuo, J. Kuang, and G. Luhrs, "Energy-harvesting shock absorber with a mechanical motion rectifier," *Smart Materials and Structures*, vol. 22, no. 2, Article ID 025008, 2013.
- [17] M. Yu, Y. Peng, S. Wang, J. Fu, and S. B. Choi, "A new energy-harvesting device system for wireless sensors, adaptable to on-site monitoring of MR damper motion," *Smart Materials and Structures*, vol. 23, no. 7, Article ID 077002, 2014.
- [18] Y. Zhang, K. Huang, F. Yu, Y. Gu, and D. Li, "Experimental verification of energy-regenerative feasibility for an automotive electrical suspension system," in *Proceedings of the IEEE International Conference on Vehicular Electronics and Safety (ICVES '07)*, pp. 1–5, Beijing, China, December 2007.
- [19] X. C. Guan, Y. H. Huang, Y. Ru, H. Li, and J. P. Ou, "A novel self-powered MR damper: theoretical and experimental analysis," *Smart Materials and Structures*, vol. 24, no. 10, Article ID 105033, 2015.
- [20] S.-W. Cho, H.-J. Jung, and I.-W. Lee, "Smart passive system based on magnetorheological damper," *Smart Materials and Structures*, vol. 14, no. 4, pp. 707–714, 2005.
- [21] K.-M. Choi, H.-J. Jung, H.-J. Lee, and S.-W. Cho, "Feasibility study of an MR damper-based smart passive control system employing an electromagnetic induction device," *Smart Materials and Structures*, vol. 16, no. 6, pp. 2323–2329, 2007.
- [22] Y.-T. Choi and N. M. Wereley, "Self-powered magnetorheological dampers," *Journal of Vibration and Acoustics, Transactions of the ASME*, vol. 131, no. 4, pp. 0445011–0445015, 2009.
- [23] B. Sapiński, "Vibration power generator for a linear MR damper," *Smart Materials and Structures*, vol. 19, no. 10, Article ID 105012, 2010.
- [24] B. Sapiński and M. Wegrzynowski, "Experimental setup for testing rotary MR dampers with energy harvesting capability," *Acta Mechanica et Automatica*, vol. 7, no. 4, pp. 241–244, 2013.
- [25] B. Sapiński, "Energy-harvesting linear MR damper: prototyping and testing," *Smart Materials and Structures*, vol. 23, no. 3, Article ID 035021, 2014.
- [26] C. Chen and W.-H. Liao, "A self-sensing magnetorheological damper with power generation," *Smart Materials and Structures*, vol. 21, no. 2, Article ID 025014, 2012.
- [27] B. Ebrahimi, M. B. Khamesee, and M. F. Golnaraghi, "Feasibility study of an electromagnetic shock absorber with position sensing capability," in *Proceedings of the 34th Annual Conference of the IEEE Industrial Electronics Society (IECON '08)*, pp. 2988–2991, Orlando, Fla, USA, November 2008.

Research Article

Seismic Proofing Capability of the Accumulated Semiactive Hydraulic Damper as an Active Interaction Control Device with Predictive Control

Ming-Hsiang Shih¹ and Wen-Pei Sung²

¹Department of Civil Engineering, National Chi-Nan University, Puli, Nantou 545, Taiwan

²Department of Landscape Architecture, Integrated Research Center for Green Living Technologies, National Chin-Yi University of Technology, Taichung 41170, Taiwan

Correspondence should be addressed to Wen-Pei Sung; wps@ncut.edu.tw

Received 4 March 2016; Revised 22 May 2016; Accepted 26 May 2016

Academic Editor: Nicola Caterino

Copyright © 2016 M.-H. Shih and W.-P. Sung. This is an open access article distributed under the Creative Commons Attribution License, which permits unrestricted use, distribution, and reproduction in any medium, provided the original work is properly cited.

The intensity of natural disasters has increased recently, causing buildings' damages which need to be reinforced to prevent their destruction. To improve the seismic proofing capability of Accumulated Semiactive Hydraulic Damper, it is converted to an Active Interaction Control device and synchronous control and predictive control methods are proposed. The full-scale shaking table test is used to test and verify the seismic proofing capability of the proposed AIC with these control methods. This study examines the shock absorption of test structure under excitation by external forces, influences of prediction time, stiffness of the auxiliary structure, synchronous switching, and asynchronous switching on the control effects, and the influence of control locations of test structure on the control effects of the proposed AIC. Test results show that, for the proposed AIC with synchronous control and predictive control of 0.10~0.13 seconds, the displacement reduction ratios are greater than 71%, the average acceleration reduction ratios are, respectively, 36.2% and 36.9%, at the 1st and 2nd floors, and the average base shear reduction ratio is 29.6%. The proposed AIC with suitable stiffeners for the auxiliary structure at each floor with synchronous control and predictive control provide high reliability and practicability for seismic proofing of buildings.

1. Introduction

Recently, strong earthquakes have caused great damage and loss of life. The Indian Ocean earthquake of 2004 caused widespread damage. In Sumatra Indonesia, the earthquake had a magnitude of 9.0 on the Richter scale (M 9.0), and the resulting South Asian tsunami killed more than 200,000 people. In 2008, the Wenchuan earthquake (M 8.0) struck along the Longmenshan Fault, a thrust structure along the border of the Indo-Australian Plate and Eurasian Plate. In 2011, an earthquake of the shore of Japan (M 9.0) caused a 10-meter-high tsunami that carried water into coastal areas, washing away buildings and leaving more than twenty thousand people dead or missing. In 2013, a strong earthquake in Pakistan (M 7.7) left 825 people dead and more than 700

injured. In 2015, an earthquake in Nepal (M 7.8) killed more than 7,600 people. An aftershock in May 2015 (M 7.3) caused numerous casualties. In January 2016, an earthquake with a Richter magnitude of 6.8 caused widespread damage in India and surrounding countries.

Taiwan, which is located on the Ring of Fire at the junction of the Eurasian Plate and the Philippine Sea Plate, has numerous earthquakes every year. In 1999, an earthquake with a Richter magnitude of 7.3 occurred in the vicinity of the Chelungpu Fault, which stretches for hundreds of kilometers under buildings and bridges. In February 2016, the Meinong earthquake (M 6.5) collapsed multiple buildings in southern Taiwan. In 2015, the "Seismic Hazard Potential Map of the Taiwan Area" was released by the Ministry of Science and

Technology (MOST), Taiwan. According to the MOST, the probability of a strong earthquake of magnitude 6.5 occurring in southern Taiwan within the next thirty years is 64%, and the probability of a strong earthquake of magnitude 7.0 occurring in Eastern Taiwan is 20%. In Taiwan, the threat of earthquakes is not negligible.

The present structural design concept is based on economic considerations. The premise is not life-threatening as long as the structural design meets the principle of suffering no damage in a small earthquake, being repairable after a moderate earthquake, and not collapsing in a large earthquake. Some damage to buildings is inevitable. However, damaged buildings need to be reinforced as quickly as possible, for aftershocks can cause further damage or total collapse before the designated life span of the buildings. To mend this kind of building, many researchers have developed active [1–4] or semiactive [5–10] bracings. For example, Chung et al. [1] carried out an experimental study on a building structure with active control subjected to base motion. Soong et al. [2, 3] designed and installed an active bracing system for a full-scale test structure under actual ground excitation to observe its seismic resistance. Dyke et al. [4] developed an acceleration feedback control method of active control for buildings. Symans and Constantinou [5] installed semiactive dampers in the lateral bracing of multiple degree of freedom (MDOF) test structures to test and verify the seismic control performance. Hiemenz et al. [6] presented a three-story building with semiactive magnetorheological (MR) braces under external excitation, which performed well under control efficiency. Gattulli et al. [7] proposed a prototype of a semiactive protection system for Chevron braces with embedded MR dampers. Caterino et al. [8] highlighted the several problems of structures equipped with semiactive control systems. Pourzeynali and Joeei [9] proposed a particular type of semiactive control device, the Variable Stiffness Device (VSD), and applied a Semiactive Fuzzy Logic Controller (SFLC) to this system to optimize the seismic reduction of the building responses under earthquake excitations. Hiramoto et al. [10] proposed a structural model for a semiactive control design and a model-based semiactive control law to improve the performance of the semiactive control system.

In addition, Iwan [11, 12] proposed Active Interaction Control (AIC), a semiactive control method, in 1996. The experimental and numerical analysis results [13–15] showed that the key to this AIC for dissipating the energy of external forces was the interface elements (IE), which reversed internal forces from the subordinate structures. Shih and Sung [16] installed an accumulator into a Displacement Semiactive Hydraulic Damper (DSHD) by converting it to AIC (Active Interaction Control) device. Tests indicated that the deformation of the main structure could be minimized by mutual interaction between the subordinate structure and the main structure. In this study, the Accumulated Semiactive Hydraulic Damper (ASHD) proposed by Shih and Sung [17, 18] was converted to Active Interaction Control (AIC). Nevertheless, “time delay” phenomena occur in research achievements [16]. In order to improve this kind of problem, the predictive control method proposed by Shih and Sung

[19, 20] was applied to improve the seismic proofing capability of the proposed AIC. In this study, a theoretical analysis model is derived for ASHD and converted to AIC based on the concept of AIC. The predictive control method for AIC is briefly discussed in the Methodology. Then, a full-scale two-story single-bay steel frame with ASHD converted to AIC is tested on a shaking table under the excitation of the El Centro (1940) and Kobe earthquake records to test and verify the seismic proofing capability of this proposed device under various control conditions. In this paper, the shock absorption effects of the test structure under excitation by external forces, influence of predictive time, stiffness of the auxiliary structure, and synchronous switching and asynchronous switching on the control effect of the proposed AIC, and the influence of the control positions of the test structure on the control effects of the proposed AIC are discussed to determine the optimal control conditions for the proposed AIC.

2. Methodology

2.1. Composition of Accumulated Semiactive Hydraulic Damper. The Accumulated Semiactive Hydraulic Damper (ASHD) is converted to an Active Interaction Control device in this study. An ASHD is a kind of controllable energy-dissipating element of a passive control system, and it is also treated as a semiactive control device. The main design concept is based on the energy-dissipating component; the damping force can be generated by the flow of fluid through the orifice so as to conduct control. An ASHD is composed of a hydraulic jack, a directional valve, a check valve, a relief valve, and an accumulator, as shown in Figure 1. The energy-dissipating characteristics of the ASHD are controlled by the flow of oil in the hydraulic jack. In this study, this ASHD is proposed as the major component of the Hydraulic Interaction Element, IE.

2.2. Theoretical Derivation of the ASHD as AIC. Assuming that two auxiliary structures (AS) are installed in the two degrees of freedom of the primary structure (PS), the organizational structure of this control system with an added mechanical sensor-switching assembly device developed from an Accumulated Semiactive Hydraulic Damper (ASHD) is shown in Figure 2. In that figure, $m_1, c_1, k_1, m_2, c_2, k_2; m_{a1}, c_{a1}, k_{a1}$; and m_{a2}, c_{a2}, k_{a2} represent the mass, damping coefficient, and stiffness of the primary structure at the 1st and 2nd floors and of the auxiliary structures at the 1st and 2nd floors, respectively. x_1 and x_2 represent the structural displacement of the 1st and 2nd floors, with the ground as the reference frame. x_{a1} and x_{a2} represent substructural displacement of the 1st and 2nd floors, with the ground as the reference frame. \ddot{x}_g is the acceleration of ground motion. f_{IE1} and f_{IE2} denote the internal forces of the interface elements of the 1st and 2nd substructures, respectively. In this study, it is assumed that tension is positive. Therefore, the dynamic equilibrium equation of motion for these four mass blocks under excitation of earthquake forces and the internal force

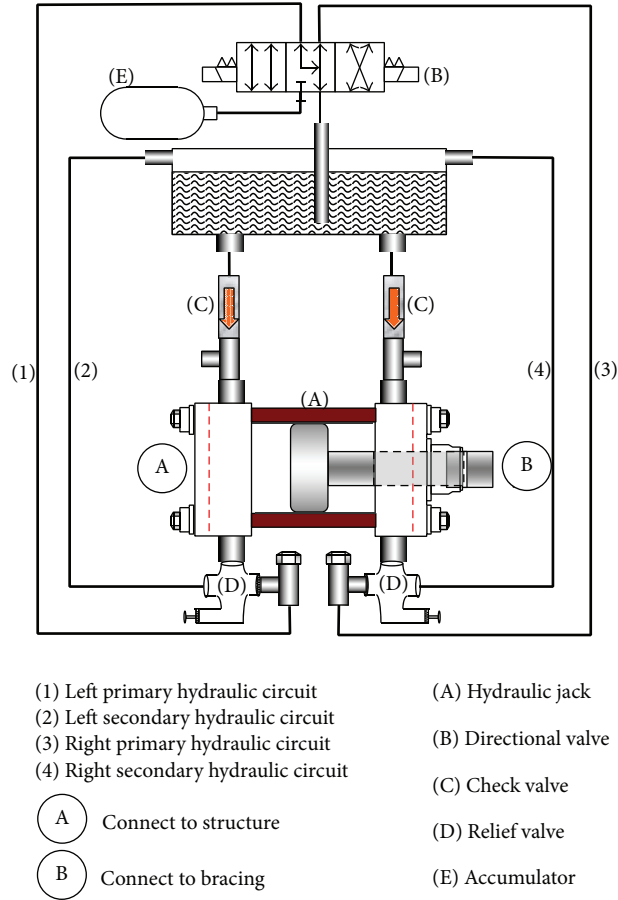


FIGURE 1: Framework of Accumulated Semiactive Hydraulic Device [17].

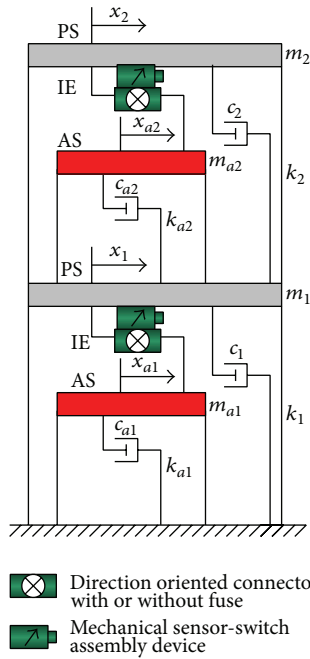


FIGURE 2: The systematic organization of ASHD as AIC [16].

of the interface elements of the 1st and 2nd substructures are listed as follows:

$$\begin{aligned}
 & \begin{bmatrix} m_1 & 0 & 0 & 0 \\ 0 & m_2 & 0 & 0 \\ 0 & 0 & m_{a1} & 0 \\ 0 & 0 & 0 & m_{a2} \end{bmatrix} \begin{Bmatrix} \ddot{x}_1 \\ \ddot{x}_2 \\ \ddot{x}_{a1} \\ \ddot{x}_{a2} \end{Bmatrix} \\
 & + \begin{bmatrix} c_1 + c_2 + c_{a2} & -c_2 & 0 & -c_{a2} \\ -c_2 & c_2 & 0 & 0 \\ 0 & 0 & c_{a1} & 0 \\ -c_{a2} & 0 & 0 & c_{a2} \end{bmatrix} \begin{Bmatrix} \dot{x}_1 \\ \dot{x}_2 \\ \dot{x}_{a1} \\ \dot{x}_{a2} \end{Bmatrix} \\
 & + \begin{bmatrix} k_1 + k_2 + k_{a2} & -k_2 & 0 & -k_{a2} \\ -k_2 & k_2 & 0 & 0 \\ 0 & 0 & k_{a1} & 0 \\ -k_{a2} & 0 & 0 & k_{a2} \end{bmatrix} \begin{Bmatrix} x_1 \\ x_2 \\ x_{a1} \\ x_{a2} \end{Bmatrix} \\
 & = - \begin{bmatrix} m_1 \\ m_2 \\ m_{a1} \\ m_{a2} \end{bmatrix} \ddot{x}_g + \begin{bmatrix} f_{IE1} \\ f_{IE2} \\ -f_{IE1} \\ -f_{IE2} \end{bmatrix}.
 \end{aligned} \tag{1}$$

The first item on the right-hand side of (1) is uncontrollable external force or external ground acceleration; the only controllable item is the second part—the controllable vector on the right-hand side of the equation. This controllable vector converts part of the controllability of the interaction interface element via switching IE. Each status of the control force vector of the interaction interface element is discussed as follows:

- (1) Unlocked status of interaction IE: the control force of IE is zero. Auxiliary structures may freely vibrate. In this study, the auxiliary structure is considered as an independent oscillator. The equation of motion of each auxiliary structure can be expressed as follows:

$$\begin{aligned} m_{a,i} \ddot{x}_{a,i}(t) + c_{a,i} \dot{x}_{a,i}(t) + k_{a,i} x_{a,i}(t) \\ = -m_{a,i} \ddot{x}_g(t) + c_{a,i} \dot{x}_{i-1}(t) + k_{a,i} x_{i-1}(t) - u_i(t), \end{aligned} \quad (2)$$

where suffix a, i represents systematic parameter of the i th floor of the auxiliary structure and $u_i(t)$ is the i th element force of the interaction IE.

- (2) Locked status of interaction IE: there is an interaction acting force. The relative displacement of mass between the primary and auxiliary structures is incapable of change. Therefore, the relative displacement before the unlocked status is equal to that of just the locked status. That is,

$$x_i(t) - x_{a,i}(t) = x_i(t_0) - x_{a,i}(t_0), \quad t_0 \leq t \leq t_1, \quad (3)$$

where t_0 and t_1 represent the time points at the beginnings of the locked and unlocked statuses, respectively. Suffix i means the i th element of IE. Equation (3) is only suitable for the time between t_0 and t_1 . Therefore, the constraint condition is inferred to represent the relations of the displacement response of the auxiliary structures and primary structures, as follows:

$$x_{a,i}(t) = x_i(t) - x_i(t_0) + x_{a,i}(t_0). \quad (4)$$

Thus, the interaction force of the i th IE is as follows:

$$\begin{aligned} f_{EL,i} = -m_{ai}(\ddot{x}_i - \ddot{x}_{i-1}) - c_{ai}(\dot{x}_i - \dot{x}_{i-1}) \\ - k_{ai}(x_i - x_{i-1} - x_{i,t_0} + x_{a,i,t_0}). \end{aligned} \quad (5)$$

2.3. Predictive Control for AIC. According to previous research [16] on applying the Semiactive Hydraulic Damper as an Active Interaction Control device, the hysteretic loops of a single floor test structure under excitation by external earthquake records show a “time delay” phenomenon. In order to improve the seismic proofing capability of this proposed ASHD as AIC, a predictive control method for a Semiactive Hydraulic Damper is applied to reduce the time delay [19, 20]. This predictive method was proposed by Shih and Sung [19, 20] to diminish the time delay and improve the seismic proofing capability of an ASHD. The structural

TABLE 1: Natural frequency, damping ratio, and mass of test structure.

Original/FL	Stiffness (N/m)	Mass (kg)
1st FL	327680	4402
2nd FL	327680	4329
Dynamic parameters		
Parameters	Mode 1	Mode 2
Frequency	0.85 Hz	2.256 Hz
Damping ratio	0.0028	0.0033
Mode vector	0.608	-1.241
	1.000	1

responses of a test building under external excitation, namely, displacement, velocity, and acceleration, in a previous step are used to establish the signals for the next step. To ensure that the ASHD of AIC is activated on time, the request signal can be started before the optimal reverse point in order to compensate for the time delay.

The equation of the optimal displacement is shown as follows:

$$\hat{x}_i = \{F_i\} \cdot \{x\}, \quad (6)$$

where $\{F_i\}$ is the coefficient regression system and $\{x\}$ is the structural displacement.

The velocity can be obtained by differentiating the displacement equation with respect to time as

$$\dot{\hat{x}}_i = \frac{d}{dt} \hat{x}(t), \quad t = i \cdot \Delta t. \quad (7)$$

Details of the derivation of this predictive control method are provided in Appendix A.

3. Experimental Setup

Multiple degrees of freedom (MDOF) shaking table test is used to investigate the control performance of the proposed AIC with different control conditions: passive control, synchronous control with prediction time control, synchronous control, asynchronous control with prediction time control, and predictive control at different floors. The auxiliary structure (AS) with various stiffeners added at different floors is also tested. In this study, the El Centro (1940) and Kobe earthquake records are used as excitation inputs to the shaking table. All of the tests are full-scale shaking table tests, and all are used to test and verify the seismic proofing capability of the proposed AIC with various control conditions. The dimensions of the shaking table are 3.0 m × 3.0 m. The maximum acceleration of the shaking table is $\pm 9.8 \text{ m/s}^2$ ($\pm 1.0 \text{ g}$) with hydraulic actuator loads of up to 15 tons. A two-story single-bay steel frame is used as the test structure, as shown in Figure 3. In order to acquire the obvious elastic deformation, all four columns of this test structure are made of 100 mm × 32 mm solid steel. The mechanical characteristics of the test structure are listed in Table 1.



FIGURE 3: The shaking table test for ASHD as AIC with various control conditions.

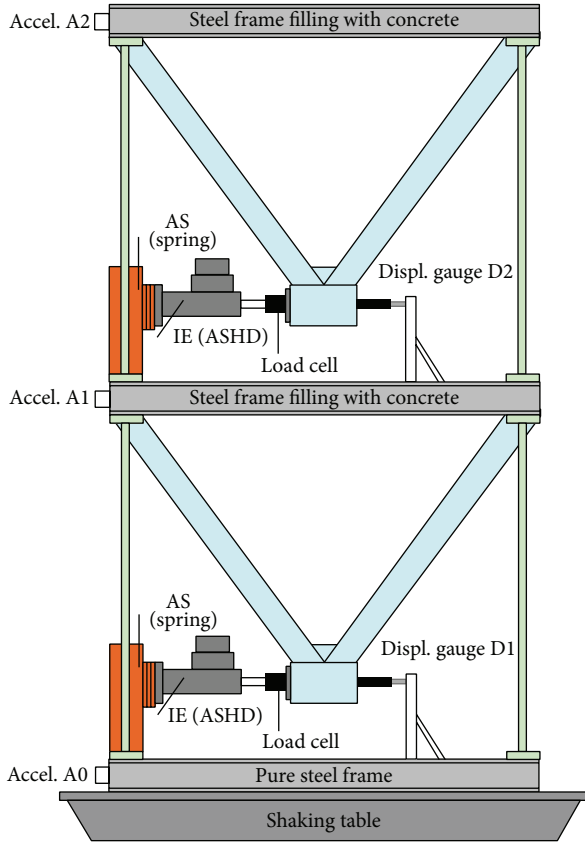


FIGURE 4: The full-scale shaking test structure added with IE, stiffeners, and sensors.

Three accelerometers, two displacement gauges, and two load cells are installed in the test model to measure the absolute acceleration, story drift, and output force of the damper. Figure 4 shows the added accelerometers, displacement gauge, and load cell on the auxiliary structures. All structural responses of this test structure are recorded with

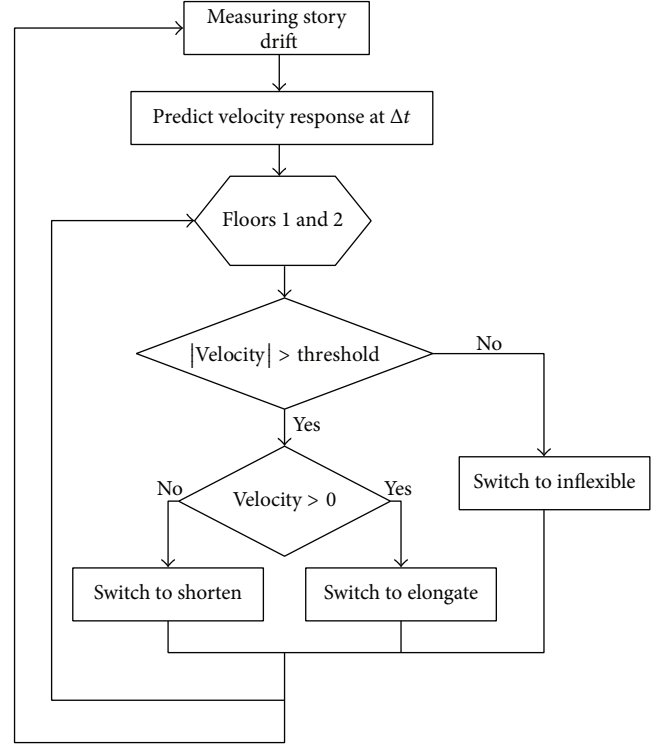


FIGURE 5: The signal process flowchart of this full-scale shaking table test.

the signal processing flowchart of the control computer, as shown in Figure 5.

4. Test Results and Discussion

4.1. The Maximum Shock Absorption Effects of Structure with Various Control Conditions under Excitation of the El Centro and Kobe Earthquake Record. To compare the seismic proofing capability of the proposed AIC under various control conditions, a two-story single-bay steel frame without control is excited with various earthquake records to obtain the time history of the structural responses of story drift, absolute acceleration, and base shear and thereby to determine the maximum structural responses. This test structure is tested under multiple control conditions: (1) passive control (i) with 2 stiffeners added at the 1st and 2nd floors and (ii) with 4 stiffeners added at the 1st floor and 3 stiffeners at the 2nd floor and (2) Active Interaction Control with (i) 2 stiffeners at the 1st and 2nd floors combined with synchronous control and predictive control of 0.13, 0.10, and 0.07 seconds, (ii) synchronous control with no predictive control, and (iii) asynchronous control with predictive control of 0.10 seconds. Then, testing conditions for location of control are 2 stiffeners added at the 1st and 2nd floors and (i) control at the 1st floor with predictive control of 0.10 seconds and (ii) control at the 2nd floor with predictive control of 0.10 seconds. Finally, a test structure with 4 stiffeners at the 1st floor and 3 stiffeners at the 2nd floor is tested with synchronous predictive control of 0.10 seconds. All test structures with

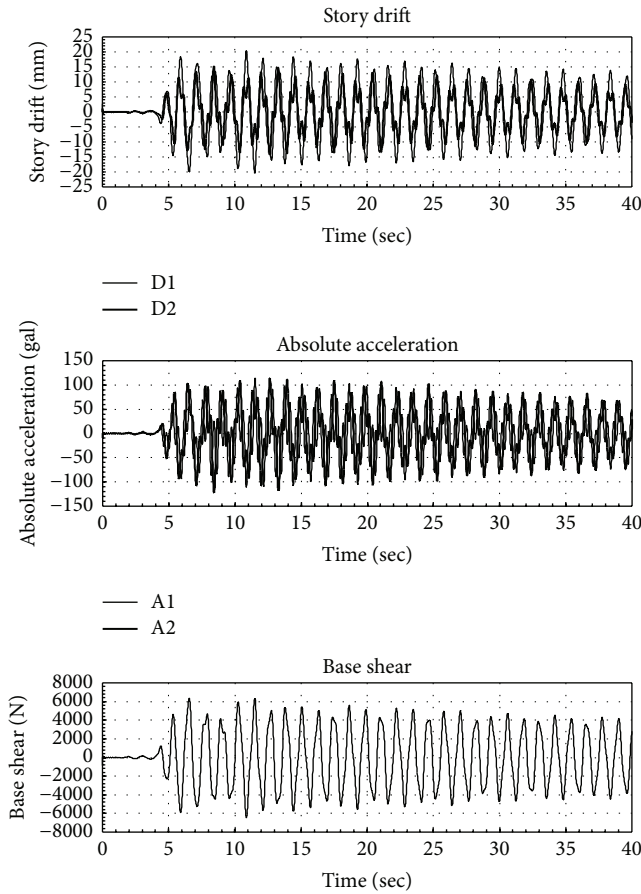


FIGURE 6: Time history of story drift, absolute acceleration, and base shear responses of bare structure under excitation of Kobe earthquake record with $\text{PGA} = 0.50 \text{ m/sec}^2$ (50 gal).

various control conditions and added various stiffeners are under excitation with the El Centro and Kobe earthquake records, with various peak ground acceleration rates. All test results are analyzed to determine the maximum responses and ratios of the maximum shock absorption; those results are listed in Tables 2–5. The typical time history of story drift, absolute acceleration, and base shear response of the bare test structure under excitation of the Kobe earthquake are shown in Figure 6. The typical time history of story drift, absolute acceleration, and base shear response of the test structure with two stiffeners and synchronous predictive control of 0.13 seconds under excitation of the Kobe earthquake are shown in Figure 7. The maximum response of base shear; acceleration records at the base, 1st floor, and 2nd floor; and displacement records at the 1st and 2nd floors of the test structure under excitation of the El Centro and Kobe earthquake records with various peak ground acceleration rates are listed in Tables 2 and 3, respectively, located in Appendix B. Ratios of the maximum shock absorption of the test structure under excitation of the El Centro and Kobe earthquake records with various peak ground acceleration rates are listed in Tables 4 and 5, respectively.

All of the control methods provide shock absorption of displacement. However, the displacement shock absorption of the test structure is less under excitation of the Kobe earthquake record than under excitation of the El Centro earthquake record. Although the structural response of displacement can be reduced by a passive stiffened structure, the decrement rate is not proportional to the stiffness ratio. Notably, adding more stiffeners increases the structural responses to acceleration and base shear. Actually, dynamic responses are relative to structural frequencies. The test and analysis results of Tables 4 and 5 are discussed as follows.

(1) *Synchronous Control with and without Predictive Control.* The results in Tables 4 and 5 show that the structural responses to displacement, acceleration, and base shear of the test structure are effectively reduced by the proposed AIC with synchronous control with and without predictive control under excitation of the El Centro and Kobe earthquake records with various peak ground acceleration rates. For the proposed AIC with synchronous control and predictive control of 0.10~0.13 seconds, the shock absorption ratios of displacement are greater than 71%, the average acceleration reduction ratios are 36.2% and 36.9% at the 1st and 2nd floors, respectively, and the average base shear reduction ratio is 29.6% for the test structure. For the proposed AIC with synchronous control and predictive control of 0.07 seconds, the shock absorption reduction ratios of displacement are greater than 55%, the average acceleration control reduction ratios are 19% and 7.7% at the 1st and 2nd floors, respectively, and the average base shear reduction ratio is 6% for the test structure. For synchronous control without predictive control, the shock absorption ratios of displacement are greater than 54%, the average acceleration reduction ratios are 31% and 14% at the 1st and 2nd floors, respectively, and the average base shear reduction ratio is 11%. The test results in Table 5 reveal that, for the proposed AIC with synchronous control and predictive control of 0.10~0.13 seconds, the shock absorption reduction ratios of displacement are greater than 54%, the average acceleration reduction ratios are 34% and 3.13% at the 1st and 2nd floors, respectively, and the average base shear reduction ratio is increased slightly. For synchronous control with predictive control of 0.07 seconds, the shock absorption ratios of displacement are greater than 28% and the acceleration response of the 1st floor is reduced. However, the acceleration response increased slightly at the 2nd floor and base shear increased by 76.1%. For synchronous control without predictive control, the average shock absorption ratios of displacement are 26% and 41% at the 1st and 2nd floors, respectively, but the average acceleration increased by 3% at the 1st floor and 42.5% at the 2nd floor; in addition, the base shear increased by 95.6%. All of the control effects of the proposed AIC with synchronous control with and without predictive control are superior to those of passive control.

(2) *Asynchronous Control with Predictive Control.* The test results in Table 4 show that the shock absorption ratio of displacement of the test structure under asynchronous control with predictive control of 0.07 seconds is greater than 52%, superior to that of the test structure under passive control.

TABLE 2: The maximum structural response of test structure under excitation of El Centro earthquake record with various control conditions and different peak ground acceleration.

Number of stiffeners at 1st floor	Number of stiffeners at 2nd floor	Control conditions	A0 m/sec ²	D1 mm	D2 mm	A1 m/sec ²	A2 m/sec ²	Base shear kN
0	0	NC	0.445	25.8	16.8	1.057	1.353	8.2
2	2	Passive	0.423	17.5	9.9	1.393	1.701	12.4
2	2	Passive	0.908	33.4	18.1	3.149	3.121	25.4
4	3	Passive	0.439	14.0	10.7	1.616	2.408	15.8
4	3	Passive	0.795	25.7	18.8	3.000	4.178	29.7
2	2	Synchronic and 0.13-second predictive control	2.159	29.7	23.0	2.941	3.967	24.5
2	2	Synchronic and 0.13-second predictive control	1.758	23.7	17.7	2.632	3.349	24.1
2	2	Synchronic and 0.13-second predictive control	1.335	17.6	12.7	1.791	2.401	15.3
2	2	Synchronic and 0.13-second predictive control	0.957	12.0	8.1	1.807	1.708	13.6
2	2	Synchronic and 0.13-second predictive control	0.474	7.4	5.3	1.228	1.045	8.6
2	2	Synchronic and 0.10-second predictive control	2.189	31.0	24.1	3.095	4.413	25.7
2	2	Synchronic and 0.10-second predictive control	2.119	23.5	17.8	2.180	3.336	21.3
2	2	Synchronic and 0.10-second predictive control	1.503	17.3	12.7	1.669	2.512	14.5
2	2	Synchronic and 0.10-second predictive control	0.870	11.4	8.1	1.063	1.801	9.9
2	2	Synchronic and 0.10-second predictive control	0.476	7.5	5.2	0.806	1.098	8.3
2	2	Synchronic and 0.07-second predictive control	1.222	24.4	19.2	2.249	3.485	20.5
2	2	Synchronic and 0.07-second predictive control	0.881	18.1	14.0	1.515	2.364	14.3
2	2	Synchronic and 0.07-second predictive control	0.422	10.1	7.2	0.927	1.221	7.9
2	2	Synchronic control	1.406	25.9	20.5	2.301	3.677	21.0
2	2	Synchronic control	0.928	18.5	14.1	1.505	2.392	14.2
2	2	Synchronic control	0.423	11.0	7.3	0.903	1.267	8.1
2	2	Asynchronic and 0.10-second predictive control	1.646	31.4	26.7	6.112	4.653	28.7
2	2	Asynchronic and 0.10-second predictive control	1.473	21.4	19.6	4.199	3.445	19.1
2	2	Asynchronic and 0.10-second predictive control	0.855	17.8	14.2	2.749	2.629	11.5
2	2	Asynchronic and 0.10-second predictive control	0.456	9.0	8.3	1.663	1.443	7.0
2	2	0.10-second predictive control at 1st floor	1.642	30.0	30.7	6.782	5.908	29.0
2	2	0.10-second predictive control at 1st floor	1.259	22.1	22.8	4.928	4.238	20.9
2	2	0.10-second predictive control at 1st floor	0.971	16.4	15.7	3.250	2.767	13.1
2	2	0.10-second predictive control at 1st floor	0.437	8.8	8.4	1.774	1.547	7.7

TABLE 2: Continued.

Number of stiffeners at 1st floor	Number of stiffeners at 2nd floor	Control conditions	A0 m/sec ²	D1 mm	D2 mm	A1 m/sec ²	A2 m/sec ²	Base shear kN
2	2	0.10-second predictive control at 2nd floor	0.851	24.2	20.9	3.727	3.798	20.9
2	2	0.10-second predictive control at 2nd floor	0.465	12.8	11.2	1.759	1.902	11.1
4	3	Synchronic and 0.10-second predictive control	2.607	26.6	23.3	4.674	6.536	37.1
4	3	Synchronic and 0.10-second predictive control	2.374	21.9	20.3	4.116	5.336	35.3
4	3	Synchronic and 0.10-second predictive control	1.934	18.5	17.3	3.619	4.853	26.1
4	3	Synchronic and 0.10-second predictive control	1.295	14.8	13.5	2.913	3.406	22.3
4	3	Synchronic and 0.10-second predictive control	0.914	10.1	10.0	1.788	2.378	14.7
4	3	Synchronic and 0.10-second predictive control	0.435	6.5	4.1	0.883	1.379	9.4

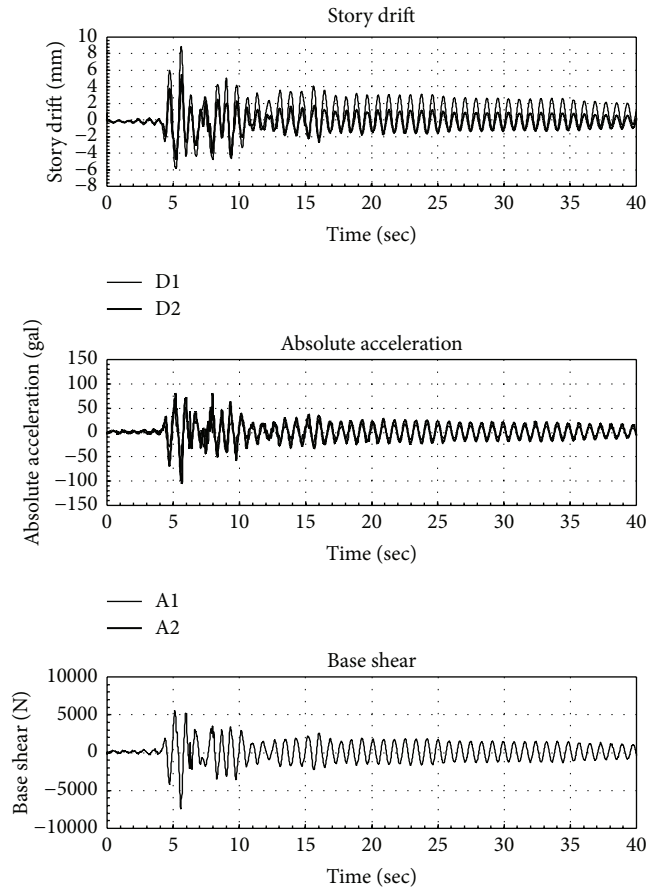


FIGURE 7: Time history of story drift, absolute acceleration, and base shear responses of test structure added with two stiffeners and with synchronic and 0.13-second predictive control under excitation of Kobe earthquake record with PGA = 0.50 m/sec² (50 gal).

TABLE 3: The maximum structural response of test structure under excitation of Kobe earthquake record with various control conditions and different peak ground acceleration.

Number of stiffeners at 1st floor	Number of stiffeners at 2nd floor	Control conditions	A0 m/sec ²	D1 mm	D2 mm	A1 m/sec ²	A2 m/sec ²	Base shear kN
0	0	NC	0.693	28.8	21.7	1.637	1.751	9.0
2	2	Passive	0.940	33.2	20.5	3.217	3.549	26.0
4	3	Passive	0.534	16.1	12.8	1.863	2.854	18.4
4	3	Passive	0.938	30.0	22.2	3.618	4.982	34.9
2	2	Synchronic and 0.13-second predictive control	2.053	32.0	25.4	3.292	4.657	29.5
2	2	Synchronic and 0.13-second predictive control	1.396	24.8	18.5	2.056	3.546	22.4
2	2	Synchronic and 0.13-second predictive control	1.082	16.9	11.6	1.380	2.247	15.6
2	2	Synchronic and 0.13-second predictive control	0.458	8.9	5.5	0.809	1.051	7.5
2	2	Synchronic and 0.10-second predictive control	1.973	32.2	25.4	3.310	5.298	31.7
2	2	Synchronic and 0.10-second predictive control	1.378	23.9	17.8	2.233	3.548	23.3
2	2	Synchronic and 0.10-second predictive control	0.946	16.3	11.0	1.362	2.441	14.5
2	2	Synchronic and 0.10-second predictive control	0.503	8.7	5.5	0.817	1.282	7.9
2	2	Synchronic and 0.07-second predictive control	0.919	26.1	15.9	2.160	3.081	21.8
2	2	Synchronic and 0.07-second predictive control	0.485	14.6	9.1	1.032	1.560	11.1
2	2	Synchronic control	0.862	26.6	15.9	2.164	3.041	21.6
2	2	Synchronic control	0.436	14.7	9.1	1.026	1.598	11.3
2	2	Asynchronic and 0.10-second predictive control	1.099	26.5	15.7	3.141	3.173	19.7
2	2	Asynchronic and 0.10-second predictive control	0.477	9.0	8.6	1.505	1.428	8.2
2	2	0.10-second predictive control at 1st floor	1.337	29.9	26.9	4.914	4.652	25.6
2	2	0.10-second predictive control at 1st floor	1.160	18.4	17.8	3.067	3.254	16.6
2	2	0.10-second predictive control at 1st floor	0.482	8.8	8.3	1.561	1.509	8.0
2	2	0.10-second predictive control at 2nd floor	0.917	29.1	20.8	4.347	3.920	26.3
2	2	0.10-second predictive control at 2nd floor	0.489	15.0	11.0	2.051	2.155	12.2
4	3	Synchronic and 0.10-second predictive control	2.375	26.3	19.3	3.167	4.549	31.6
4	3	Synchronic and 0.10-second predictive control	1.752	20.8	15.5	2.443	3.691	26.2
4	3	Synchronic and 0.10-second predictive control	1.355	15.3	12.3	1.771	2.851	19.9
4	3	Synchronic and 0.10-second predictive control	0.925	9.1	8.0	1.236	1.823	12.2
4	3	Synchronic and 0.10-second predictive control	0.515	5.6	4.4	0.710	1.577	5.8

TABLE 4: The ratios of maximum shock absorption of test structure under excitation of El Centro earthquake record with various control conditions and different peak ground acceleration.

Number of stiffeners at 1st floor	Number of stiffeners at 2nd floor	Control conditions	A0	D1	D2	A1	A2	Base shear
0	0	NC	44.5	0%	0%	0%	0%	0%
2	2	Passive	42.3	29%	38%	-39%	-32%	-60%
2	2	Passive	90.8	36%	47%	-46%	-13%	-52%
4	3	Passive	43.9	45%	35%	-55%	-81%	-97%
4	3	Passive	79.5	44%	37%	-59%	-73%	-104%
2	2	Synchronic and 0.13-second predictive control	215.9	76%	72%	43%	40%	38%
2	2	Synchronic and 0.13-second predictive control	175.8	77%	73%	37%	37%	25%
2	2	Synchronic and 0.13-second predictive control	133.5	77%	75%	43%	41%	38%
2	2	Synchronic and 0.13-second predictive control	95.7	78%	78%	20%	41%	23%
2	2	Synchronic and 0.13-second predictive control	47.4	73%	71%	-9%	27%	1%
2	2	Synchronic and 0.10-second predictive control	218.9	76%	71%	40%	34%	36%
2	2	Synchronic and 0.10-second predictive control	211.9	81%	78%	57%	48%	45%
2	2	Synchronic and 0.10-second predictive control	150.3	80%	78%	53%	45%	47%
2	2	Synchronic and 0.10-second predictive control	87.0	77%	75%	49%	32%	38%
2	2	Synchronic and 0.10-second predictive control	47.6	73%	71%	29%	24%	5%
2	2	Synchronic and 0.07-second predictive control	122.2	65%	58%	22%	6%	9%
2	2	Synchronic and 0.07-second predictive control	88.1	64%	58%	28%	12%	12%
2	2	Synchronic and 0.07-second predictive control	42.2	59%	55%	7%	5%	-3%
2	2	Synchronic control	140.6	68%	61%	31%	14%	18%
2	2	Synchronic control	92.8	66%	60%	32%	15%	17%
2	2	Synchronic control	42.3	55%	54%	10%	1%	-4%
2	2	Asynchronic and 0.10-second predictive control	164.6	67%	57%	-56%	7%	5%
2	2	Asynchronic and 0.10-second predictive control	147.3	75%	65%	-20%	23%	29%
2	2	Asynchronic and 0.10-second predictive control	85.5	64%	56%	-35%	-1%	26%
2	2	Asynchronic and 0.10-second predictive control	45.6	66%	52%	-54%	-4%	16%
2	2	0.10-second predictive control at 1st floor	164.2	68%	50%	-74%	-18%	3%
2	2	0.10-second predictive control at 1st floor	125.9	70%	52%	-65%	-11%	9%
2	2	0.10-second predictive control at 1st floor	97.1	71%	57%	-41%	6%	26%

TABLE 4: Continued.

Number of stiffeners at 1st floor	Number of stiffeners at 2nd floor	Control conditions	A0	D1	D2	A1	A2	Base shear
2	2	0.10-second predictive control at 1st floor	43.7	65%	49%	−71%	−16%	4%
2	2	0.10-second predictive control at 2nd floor	85.1	51%	35%	−84%	−47%	−34%
2	2	0.10-second predictive control at 2nd floor	46.5	53%	36%	−59%	−35%	−31%
4	3	Synchronic and 0.10-second predictive control	260.7	82%	76%	25%	17%	22%
4	3	Synchronic and 0.10-second predictive control	237.4	84%	77%	27%	26%	19%
4	3	Synchronic and 0.10-second predictive control	193.4	83%	76%	21%	17%	26%
4	3	Synchronic and 0.10-second predictive control	129.5	80%	72%	5%	13%	6%
4	3	Synchronic and 0.10-second predictive control	91.4	81%	71%	18%	14%	12%
4	3	Synchronic and 0.10-second predictive control	43.5	74%	75%	14%	−4%	−18%

Although the acceleration response of the test structure at the 1st floor increased to almost equal those of passive control, the acceleration control at the 2nd floor and base shear control are superior to those of passive control. The test results in Table 5 show that the shock absorption ratios of displacement of the test structure under asynchronous control with predictive control of 0.07 seconds are greater than 42%, superior to those under passive control. Although the acceleration response of the test structure at the 1st and 2nd floors and the base shear responses of the test structure increased, the control effects are superior to those of passive control.

(3) *Synchronous Switching at Different Floors.* Table 4 reveals that the shock absorption ratios of displacement of the test structure under synchronous control with predictive control of 0.10 seconds at the 1st floor are greater than 50%. Although the base shear responses of the test structure are effectively controlled under this condition, the acceleration responses at the 1st floor increased. The shock absorption ratios of displacement of the test structure under synchronous control with predictive control of 0.10 seconds at the 2nd floor are greater than 35%. However, the acceleration responses at the 1st and 2nd floors and the base shear responses of the test structure under this control condition increased; these results are worse than those of passive control. The test results in Table 5 show that, for synchronous control with predictive control of 0.10 seconds at the 1st floor, the average shock absorption ratios of displacement of the test structure are 54.67% at the 1st floor and 44% at the 2nd floor. Nevertheless, the acceleration responses increased at the 1st and 2nd floors, as did base shear, and the results are superior to those of passive control. For synchronous control with predictive control of 0.10 seconds at the 2nd floor, the shock absorption ratios of displacement of the test structure are greater than

24%. However, the acceleration responses at the 1st and 2nd floors and the base shear responses of the test structure under this control condition increased, and these results are worse than those of passive control.

When the structural control capability is insufficient to control the dynamic response of the test structure, the following phenomena occurred. (1) Shock absorption ratios are reduced by about 10 to 20% when only the 1st floor is under control. The shock absorption effect is smaller at the 2nd floor than that at the 1st floor. (2) If the 2nd floor is under control, the shock absorption effect is still smaller at the 2nd floor than at the 1st floor. Thus, if only one control set is to be used, it should be installed on a lower floor to provide better seismic proofing.

From the above descriptions, it is clear that the displacement control, acceleration control, and base shear control of the three active control methods—(1) synchronous control with predictive control of 0.13, 0.10, and 0.07 seconds, (2) synchronous control without predictive control, and (3) asynchronous control with predictive control of 0.10 seconds—are superior to those of passive control. The best control effects are achieved with synchronous control with predictive control of 0.13 and 0.10 seconds.

(4) *Control Effects of Various Stiffeners with Synchronous Control and Predictive Control.* The control effects of 2 stiffeners (stiffening ratio = 1.193) added at the 1st and 2nd floors and those of 4 stiffeners (stiffening ratio = 2.338) added at the 1st floor and 3 stiffeners (stiffening ratio = 1.790) added at the 2nd floor with synchronous control and predictive control of 0.10 seconds under excitation of El Centro earthquake records with various peak ground acceleration rates are compared, and the displacement control effects are found to be almost the same. The acceleration control and base

TABLE 5: The ratios of maximum shock absorption of test structure under excitation of Kobe earthquake record with various control conditions and different peak ground acceleration.

Number of stiffeners at 1st floor	Number of stiffeners at 2nd floor	Control conditions	A0	D1	D2	A1	A2	Base shear
0	0	NC	69.3	0%	0%	0%	0%	0.0%
2	2	Passive	94.0	15%	30%	-45%	-49%	-112.0%
4	3	Passive	53.4	27%	23%	-48%	-112%	-164.0%
4	3	Passive	93.8	23%	24%	-63%	-110%	-185.5%
2	2	Synchronic and 0.13-second predictive control	205.3	62%	60%	32%	10%	-10.2%
2	2	Synchronic and 0.13-second predictive control	139.6	57%	57%	38%	-1%	-23.1%
2	2	Synchronic and 0.13-second predictive control	108.2	62%	66%	46%	18%	-10.2%
2	2	Synchronic and 0.13-second predictive control	45.8	54%	62%	25%	9%	-24.7%
2	2	Synchronic and 0.10-second predictive control	197.3	61%	59%	29%	-6%	-23.1%
2	2	Synchronic and 0.10-second predictive control	137.8	58%	59%	31%	-2%	-29.3%
2	2	Synchronic and 0.10-second predictive control	94.6	59%	63%	39%	-2%	-17.2%
2	2	Synchronic and 0.10-second predictive control	50.3	58%	65%	31%	-1%	-19.9%
2	2	Synchronic and 0.07-second predictive control	91.9	32%	45%	0%	-33%	-82.1%
2	2	Synchronic and 0.07-second predictive control	48.5	28%	40%	10%	-28%	-76.1%
2	2	Synchronic control	86.2	26%	41%	-6%	-40%	-92.4%
2	2	Synchronic control	43.6	19%	33%	0%	-45%	-98.7%
2	2	Asynchronic and 0.10-second predictive control	109.9	42%	54%	-21%	-14%	-37.4%
2	2	Asynchronic and 0.10-second predictive control	47.7	55%	43%	-34%	-19%	-31.7%
2	2	0.10-second predictive control at 1st floor	133.7	46%	36%	-56%	-38%	-46.6%
2	2	0.10-second predictive control at 1st floor	116.0	62%	51%	-12%	-11%	-10.0%
2	2	0.10-second predictive control at 1st floor	48.2	56%	45%	-37%	-24%	-26.9%
2	2	0.10-second predictive control at 2nd floor	91.7	24%	28%	-101%	-69%	-120.2%
2	2	0.10-second predictive control at 2nd floor	48.9	26%	28%	-78%	-74%	-90.9%
4	3	Synchronic and 0.10-second predictive control	237.5	73%	74%	44%	24%	-2.1%
4	3	Synchronic and 0.10-second predictive control	175.2	71%	72%	41%	17%	-14.7%
4	3	Synchronic and 0.10-second predictive control	135.5	73%	71%	45%	17%	-12.5%
4	3	Synchronic and 0.10-second predictive control	92.5	76%	72%	43%	22%	-1.2%
4	3	Synchronic and 0.10-second predictive control	51.5	74%	73%	42%	-21%	14.2%

shear control are lower with higher stiffening ratios than with lower stiffening ratios. However, the control effects of these two control methods achieve an acceptable seismic proofing capability. In contrast, the control effects of these two control methods with synchronous control and predictive control of 0.10 seconds under excitation of the Kobe earthquake records with various peak ground acceleration rates show that the displacement control and acceleration control effects are higher with higher stiffening ratios than with lower stiffening ratios. Furthermore, the displacement control effects are less with asynchronous control than with synchronous control. It is clear that the asynchronous switching caused an interaction phenomenon. Regarding the structural response to acceleration, large discrepancies are found in the shock absorption effects of the various structural control methods. The structural responses to acceleration are increased by the passive control method, with acceleration increasing by up to 80%. The structural responses to acceleration increased under the bad control conditions of the test structure, as can be seen from Table 4. Base shear is increased by passive stiffening of the structure but not by the proposed control method. These results indicate that the proposed control method is suitable for strengthening existing structures under excitation of far field earthquakes. The test results in Table 5 show that the structural control effects of displacement for near fault effects were similar to those of far field effects. Nevertheless, most of the acceleration and base shear responses of the test structure under excitation of the Kobe earthquake increased, in some cases by up to 100%. These results reveal that the parameters of structural control of this proposed method should be designed carefully to avoid countereffects.

4.2. Influence of Prediction Time on Control Effect of the Proposed AIC. The predictive time control method is intended to predict a transient time for the time delay problem of the proposed AIC. If the device has no predictive reaction, the AIC device response for velocity is too slow to switch at the optimal time, and the control effect of this device will be degraded. In contrast, if the prediction time is too long, the device will become unstable. In order to investigate the influence of prediction time on the control effect of the proposed AIC, a series of AIC under passive control and active control without prediction time and with prediction times of 0.07, 0.10, and 0.13 seconds and an AIC device with synchronous switching are tested to determine the seismic proofing capability of the AIC device proposed in this study. The average shock absorption ratios of the test structure with various control conditions under excitation of the El Centro and Kobe earthquake records are shown in Figures 8 and 9, respectively.

The test results for the influence of prediction time on the control effect of the proposed AIC are discussed as follows.

(1) *Without Predictive Control.* When the test structure is under excitation of the El Centro earthquake without predictive control, the average shock absorption ratios of displacement at the 1st and 2nd floors are 67% and 60%, respectively. When two steel stiffeners (stiffening ratio = 1.193) are added at the 1st and 2nd floors, the average shock

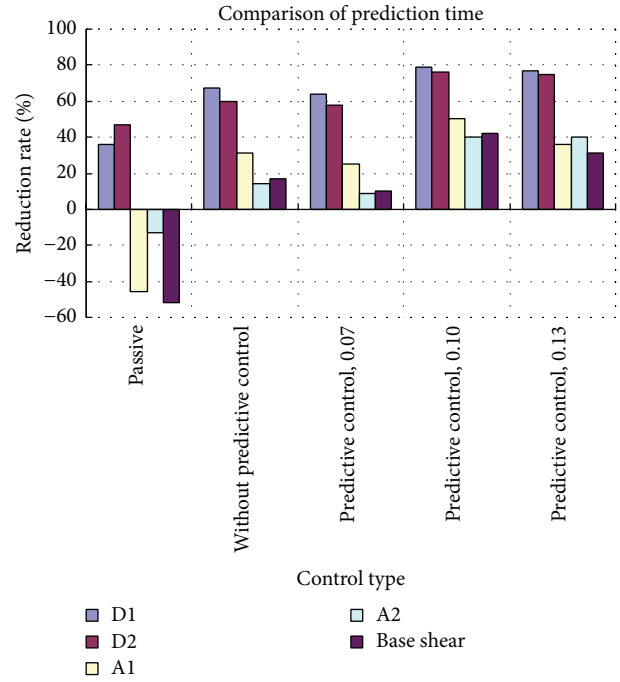


FIGURE 8: The average shock absorption ratios of the test structure with various control conditions under excitation of the El Centro earthquake.

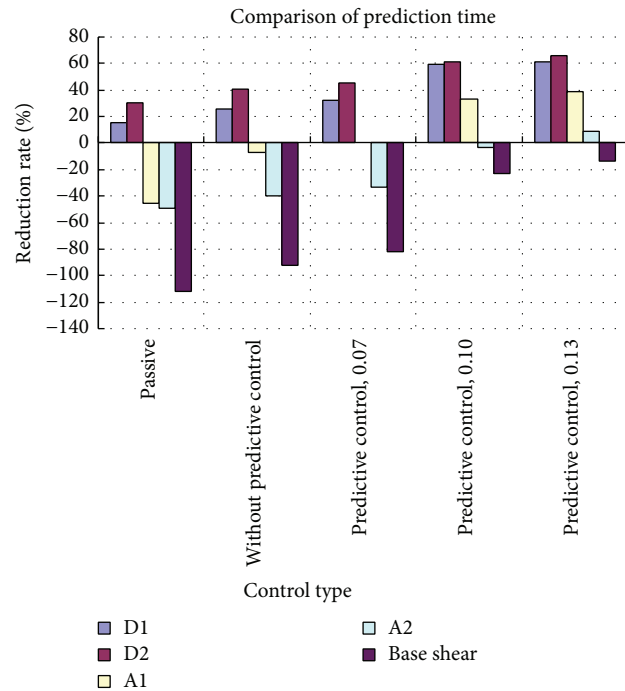


FIGURE 9: The average shock absorption ratios of the test structure with various control conditions under excitation of the Kobe earthquake.

absorption ratios of acceleration at these floors are 31% and 14%, respectively. Nevertheless, the shock absorption

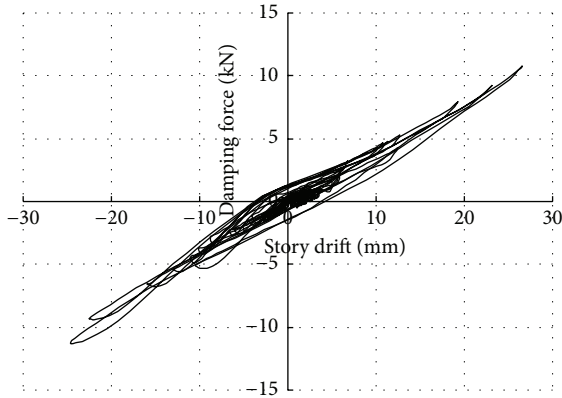


FIGURE 10: Hysteretic loop of interaction force of the test structure at the 1st floor under excitation of scaled-down Kobe earthquake with $\text{PGA} = 0.862 \text{ m/sec}^2$ (86.2 gal).

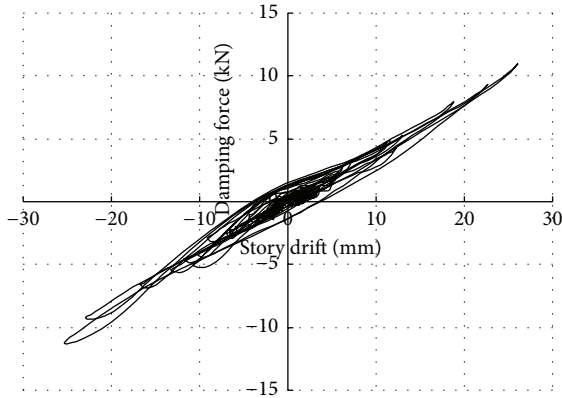


FIGURE 11: Hysteretic loop of interaction force of the test structure at the 1st floor with predictive control of 0.07 seconds under excitation of the Kobe earthquake with $\text{PGA} = 0.912 \text{ m/sec}^2$ (91.2 gal).

performance of the test structure without predictive control is undesirable under excitation of the Kobe earthquake. The average shock absorption ratios of displacement are only 26% and 41% at the 1st and 2nd floors, respectively. These ratios are almost the same as those of passive added stiffeners. However, the shock absorption of acceleration is undesirable. The acceleration responses of the test structure increased by about 6% and 40% for the 1st and 2nd floors, respectively, and the base shear of the test structure is amplified to 85%. The reasons for these phenomena can be explained by the interaction force of the curve of force-displacement, shown in Figure 10, which presents the hysteretic loop of the interaction force at the 1st floor of the test structure under excitation of the Kobe earthquake with peak ground acceleration of 0.862 m/sec^2 (86.2 gal). Figure 10 shows that the area of seismic proofing is not produced significantly by the interaction force, so the seismic proofing performance is not acceptable.

(2) *With a Predictive Control Time of 0.07 Seconds.* The average shock absorption ratios of the test structure with this predictive control time are similar to those of the test

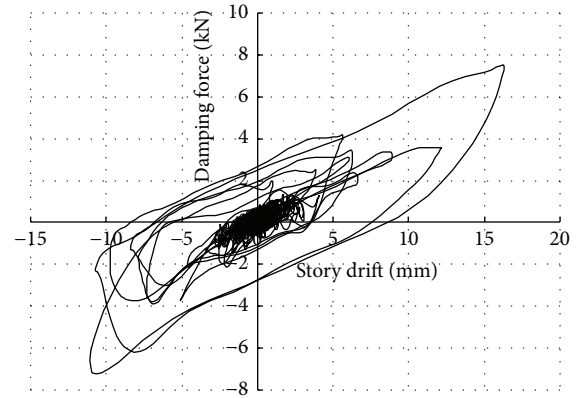


FIGURE 12: Hysteretic loop of interaction force of the test structure at the 1st floor with predictive control of 0.10 seconds under excitation of the Kobe earthquake with $\text{PGA} = 0.946 \text{ m/sec}^2$ (94.6 gal).

structure without predictive control, as shown in Figure 8. In Figure 9, it can be seen that the average shock absorption ratios of the test structure under excitation of the Kobe earthquake are slightly better with predictive control than without predictive control. These results reveal that the shock absorption performance of the test structure with this prediction time is insufficient for seismic proofing of this AIC control. However, the performance with this predictive control is superior to that of passive stiffening of the structure. Figure 11 is a hysteretic loop of the interaction force at the 1st floor of the test structure with predictive control of 0.07 seconds under excitation of the Kobe earthquake with peak ground acceleration 0.912 m/sec^2 (91.2 gal). The area of seismic proofing is still limited by the interaction force.

(3) *With a Predictive Control Time of 0.10 Seconds.* The average shock absorption ratios for displacement and acceleration with a predictive control time of 0.10 seconds are greater than those without predictive control, as shown in Figure 9. In addition, the control effects of base shear suggested acceptable seismic proofing. Figure 12 is a hysteretic loop of the interaction force at the 1st floor of the test structure under excitation of the Kobe earthquake with peak ground acceleration of 0.946 m/sec^2 (94.6 gal). The area of shock absorption is increased by the interaction force. Therefore, the predictive control method reduced the time delay and improved the seismic proofing capability of the proposed AIC, as shown in Figure 12.

(4) *With a Predictive Control Time of 0.13 Seconds.* The control effects of this predictive control time are almost the same as those of the predictive control time of 0.10 seconds. The results show that the optimal predictive control time for this control method is between 0.10 seconds and 0.13 seconds.

4.3. *Influence of Stiffness of the Auxiliary Structure on the Control Effect of the Proposed AIC.* The control forces of the interaction system are induced earlier on the primary structure when stiffness of the auxiliary structure is greater to reduce the time delay problem. But greater stiffness

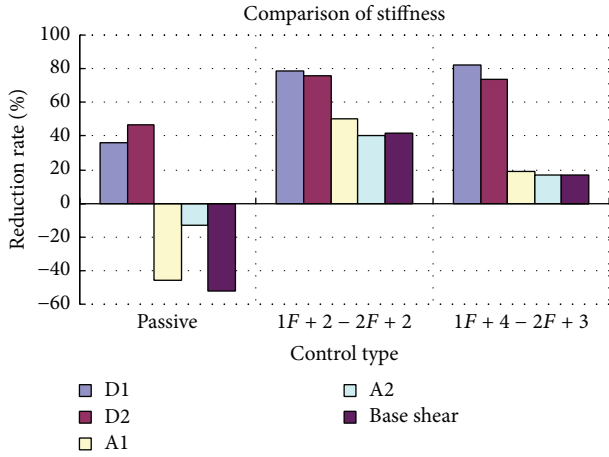


FIGURE 13: Comparison of the shock absorption ratios of the test structure under excitation of the El Centro earthquake with different control types.

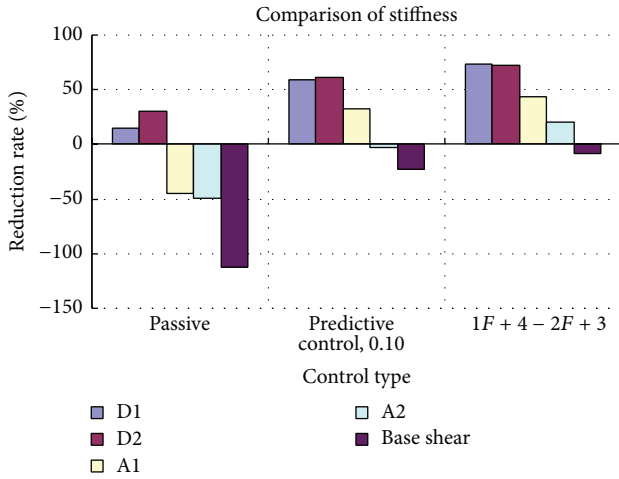


FIGURE 14: Comparison of shock absorption ratios of the test structure under excitation of the Kobe earthquake with different control types.

increased the impact force, amplified acceleration responses, and increased the base shear forces of the structure. In order to investigate the influence of the stiffness of the auxiliary structure on the control effect, two sets of shaking table tests are conducted under synchronous control with a prediction time of 0.10-second condition to test and verify the control effects: (1) with two steel stiffeners (stiffening ratio = 1.193) added at the 1st and 2nd floors and (2) with four steel stiffeners (stiffening ratio = 2.396) at the 1st floor and three steel stiffeners (stiffening ratio = 1.790) at the 2nd floor. The comparisons of the shock absorption ratios of the test structure under excitation of various earthquake records are shown in Figures 13 and 14. Figure 13 shows that adding more stiffeners to the auxiliary structure does not increase the displacement control effects, but it does reduce the effects on acceleration. However, the test results in Figure 14 reveal that adding more stiffeners increased the control effects on

displacement. The differences in the shock absorption ratios of displacement and acceleration with more and less stiffeners are 10 to 15% and 10 to 23%, respectively. These results indicate that the stiffened structure had the characteristics of a stabilized structure under excitation of a near fault earthquake with velocity impulse action.

4.4. Influence of Synchronous Switching and Asynchronous Switching on the Control Effects of the Proposed AIC. The switching of the connection status of the auxiliary structure for each floor is dependent on the story velocity. According to the contributions of multiple modal shapes, it is difficult to reach simultaneously the switching requirements of the connection status for each floor such that there is little difference in switching between each floor. If the upper floor reaches the switching requirement, the auxiliary structure will switch first to produce the extra control force to the lower level and cause greater acceleration responses. Figure 15 presents these reactions.

If the upper level switches first, the acceleration responses of the lower level will increase suddenly, as shown in Figure 15(b). Although this situation signifies the release of internal force, it will not affect the base shear immediately. However, this phenomenon affects the follow-up signal process, causing instability of the control effects. Figure 15(c) shows that when the lower level switches first, the upper level will be affected, but when the upper level switches first, the lower level will not be affected. Nevertheless, the acceleration of the lower level will switch suddenly to cause the mass of the 1st floor to move in the right direction. The control signal is in a state of chaos and cannot deduce the control effect. In order to prevent the abovementioned phenomenon, a rule for a synchronous control method is proposed in this study. The sum of the story velocity of each floor is the total velocity of the test building for judging the direction of the interaction force, which should be opposite to the direction of the total velocity. This test is intended to investigate the high frequency responses of the test structure under the control of the synchronous control method. The test results are listed in Tables 2–5. The average shock absorption ratios of the test structure under the control of the synchronous and asynchronous control methods are presented in Figures 16 and 17, respectively.

Figures 16 and 17 show that the structural response to displacement of the test structure is controlled well by asynchronous control. The average shock absorption ratios of displacement are about 50–60%. However, the average shock absorption ratios of the displacement differences between these two control methods are 10 to 20%. This result reveals clearly that the control effects of the synchronous control method are superior to those of the asynchronous control method. With regard to acceleration control, the structural responses to acceleration are amplified by the asynchronous control method and reduced by the synchronous control method. The variations in acceleration of these results are the same as those in Figures 13 and 14. Therefore, since the synchronous control method does not amplify the structural responses to acceleration, no high frequency responses of the test structure are induced under the control of the synchronous control method.

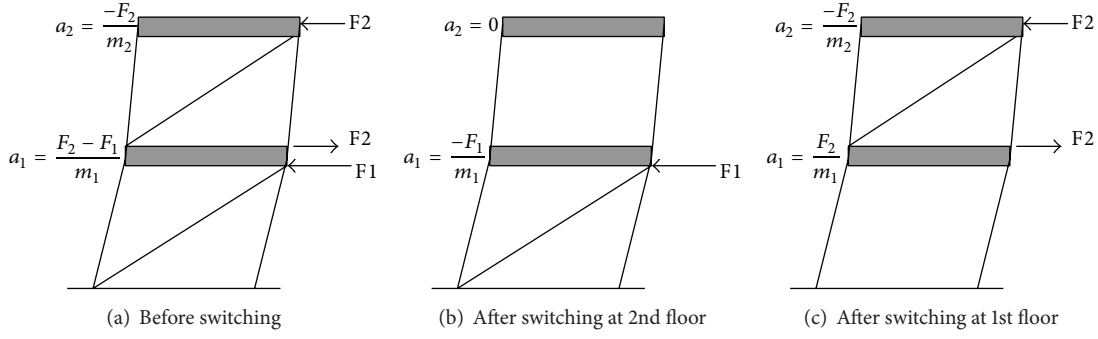


FIGURE 15: The reasons for inducing extra acceleration response of test structure with asynchronous switch.

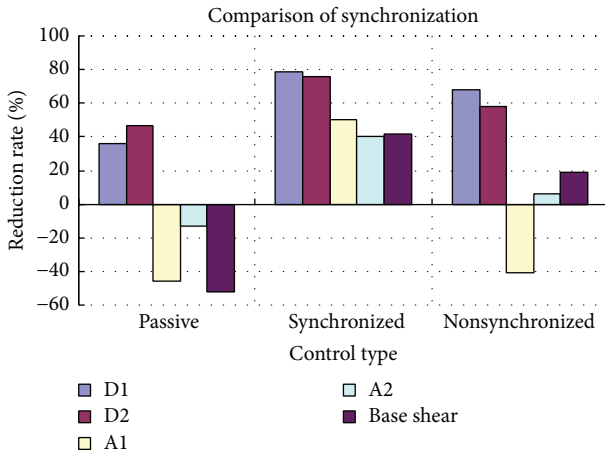


FIGURE 16: Comparison of shock absorption ratios of the test structure with synchronous and asynchronous control under excitation of the El Centro earthquake.

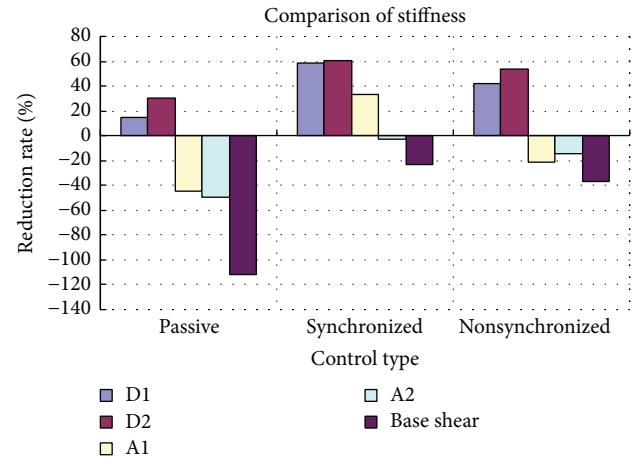


FIGURE 17: Comparison of shock absorption ratios of the test structure with synchronous and asynchronous control under excitation of the Kobe earthquake.

4.5. Influence of Control Locations of the Test Structure on the Control Effects of the Proposed AIC. In order to find the optimal place and right quantity to install this kind of device, a series of tests are planned. In this study, the shock absorption ratios of passive control, full control, control at the 1st floor, and control at the 2nd floor are investigated with a structure having a stiffening ratio of 1.193, synchronous control, and predictive control of 0.10 seconds. The test results for the average shock absorption ratios of the test structure under various control conditions are shown in Figures 18 and 19.

Figures 18 and 19 show that the control effects of the test structure with critically inadequate devices are greatly reduced. Comparison of the average shock absorption ratios of the displacement responses of the test structure with full control and that with control with fixed type stiffeners at the 1st and 2nd floors revealed decreases of about 10 to 20% and 35 to 45%, respectively. The shock absorption ratios of displacement with full control and with control with fixed type stiffeners at the 1st floor are superior to those of passive control. Although the structural responses of displacement at the 1st floor are diminished by the control with fixed type stiffeners at the 2nd floor, they are still superior to

those of passive control, but the shock absorption ratios of displacement at the 2nd floor are lower than those of passive control. Furthermore, the story drift at the 1st floor is comparable to that at the 2nd floor, and the average shock absorption ratios at the 1st floor are twice as large as those of passive control. However, the average shock absorption ratios at the 2nd floor are less than those at the 1st floor. Regarding acceleration control, the structural responses to acceleration are amplified at the 1st floor such that they are even larger than those of passive control. According to the master control motion responses of the high frequency mode, although the displacement responses are reduced by this control type, the acceleration responses increased. The displacement responses with control at the 2nd floor and fixed stiffeners at the 1st floor are nonshowable characters of control effects, which are almost the same as those of passive control. Nevertheless, with control at the 2nd floor, the structural responses to acceleration and base shear are greater than those of passive control; these phenomena could be harmful to the structure. Therefore, the best control condition for the structure is full control and the second best is control at the first floor.

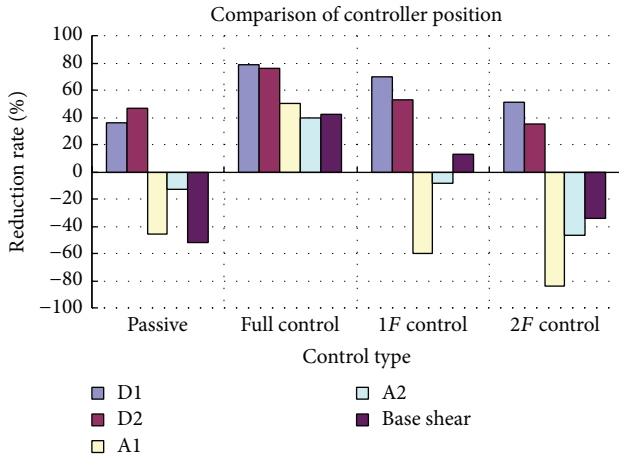


FIGURE 18: Comparison of shock absorption ratios of the test structure with different control types under excitation of the El Centro earthquake.

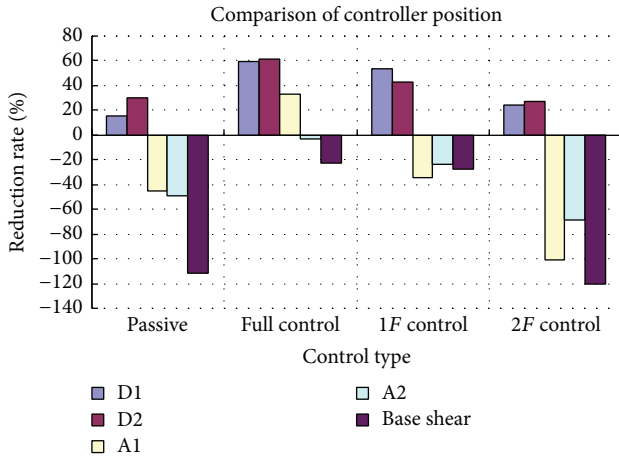


FIGURE 19: Comparison of shock absorption ratios of the test structure with different control types under excitation of the Kobe earthquake.

5. Conclusions

An Active Interaction Control (AIC) system was proposed by Iwan [10–15]. In this study, the Accumulated Semiactive Hydraulic Damper (ASHD) proposed by Shih et al. [16–18] is converted to a Hydraulic Interaction Element (IE) based on the energy-dissipating function of the ASHD. Then the dynamic equilibrium equation of motion for the systematic organization of the ASHD as the AIC is derived from the unlocked status and the locked status of the interactive IE. In order to improve the seismic proofing capability of this proposed new AIC, a predictive control method [19, 20] is applied to improve the energy-dissipating defects of the ASHD. Then, to test and verify the seismic proofing capability of the proposed AIC with and without predictive control, a full-scale two-story one-bay steel structure is tested on a shaking table in multiple forms, namely, the bare structure and the structure with various stiffeners added at different

floors and with passive control, synchronous control, and asynchronous control and also with or without predictive control, under excitation of the El Centro and Kobe earthquake records with various peak ground acceleration rates. The maximum shock absorption effects of the test structure under excitation of various earthquake records and the influences on the control effects of the prediction time, stiffness of the auxiliary structure, synchronous and asynchronous switching, and control positions of the proposed AIC are discussed. The conclusions from a series of laboratory test results are summarized as follows:

- (1) All of the control methods, applied in this research, provide shock absorption effects of displacement. The shock absorption effects of displacement for the test structure under the control of synchronous switching with predictive control greatly reduce the displacement of the structure. Nevertheless, the structural responses to acceleration and base shear are increased by this device under passive control. However, these structural responses are not increased by the proposed AIC device with synchronous control and a suitable prediction time.
- (2) The control effects of the test structure with the proposed AIC under active control without prediction time are poor because the response to structural velocity does not provide sufficient time for the AIC device to switch at the optimal time. The area of the hysteretic loop increased when the AIC is under active control and had proper prediction time. Therefore, the seismic proofing capability of displacement and acceleration control of the test structure with this AIC under active control with proper prediction time could be increased. Test results show that, for the test structure under the control of the proposed AIC with synchronous control and predictive control of 0.10~0.13 seconds, the shock absorption ratios of displacement are greater than 71%, the average acceleration reduction ratios are 36.2% and 36.9% at the 1st and 2nd floors, respectively, and the average base shear reduction ratio is 29.6%.
- (3) The time delay defects of the AIC control forces, induced from the interaction element to the primary structure, are reduced by the stiffness of the auxiliary structure. The test results show that adding more stiffeners to the auxiliary structure could provide the characteristics of a stabilized structure under excitation of a near fault earthquake with velocity impulse action.
- (4) The connection statuses of the auxiliary structures for each floor with simultaneous switching are hard to attain because they are dependent on the velocity of each floor. To prevent these phenomena, a rule for the synchronous control method is proposed. The test results reveal that the structural responses of displacement and acceleration control are controlled well by this proposed control method, which does not amplify the structural responses to acceleration.

- (5) The test results for the influence of the control positions of the AIC in the structure show that full control of the structure provides the best shock absorption effects, and control at the first floor is the second best option.

In this study, the ASHD is converted to AIC and predictive control methods with synchronous control are proposed to improve the seismic proofing capability of the proposed AIC. A full-scale two-story single-bay steel frame is tested on a shaking table to verify the energy-dissipating capability of this proposed device. All of the test results show that the proposed AIC with suitable stiffeners for the auxiliary structure at each floor and synchronous control and predictive control provide high reliability and practicability for improving the seismic proofing capability of a building under excitation by external forces.

Appendix

A. The Detailed Derivation of This Predictive Control Method

A.1. Noise Estimation [19, 20]. If the function of displacement corresponding to time has $M - 1$ terms in variety of polynomials, it can be written as

$$\hat{x}(t) = \sum_{j=0}^{M-1} a_j t^j, \quad (\text{A.1})$$

where $\hat{x}(t)$ is defined as the regression displacement, by taking a dynamic sample of a fixed frequency from relative displacements of N structures, the sampling data is x_i , $i = 0 \rightarrow N - 1$, where x_i represents the displacement backward to i steps from current time step, x_0 is current displacement, and a_j is the coefficient of the j th term.

According to the least square regression, the optimal estimation of polynomial coefficient in (A.1) is

$$\{a\} = [E^{-1}] \{y\}, \quad (\text{A.2})$$

where $\{a\}$ is a coefficient vector in M dimension, $[E^{-1}]$ represents M by M system matrix, and $\{y\}$ determines the M dimensional vector of sampling data:

$$[E] = \begin{bmatrix} N & \sum_{i=0}^{N-1} i & \sum_{i=0}^{N-1} i^2 & \cdots & \sum_{i=0}^{N-1} i^{M-1} \\ \sum_{i=0}^{N-1} i^2 & \sum_{i=0}^{N-1} i^3 & \cdots & \sum_{i=0}^{N-1} i^M \\ \sum_{i=0}^{N-1} i^4 & \cdots & \sum_{i=0}^{N-1} i^{M+1} \\ \text{symm.} & \ddots & \vdots \\ \sum_{i=0}^{N-1} i^{2M-2} \end{bmatrix}, \quad (\text{A.3})$$

$$\{y\} = \begin{bmatrix} \sum_{i=0}^{N-1} x_i \\ \sum_{i=0}^{N-1} i \cdot x_i \\ \sum_{i=0}^{N-1} i^2 \cdot x_i \\ \vdots \\ \sum_{i=0}^{N-1} i^{M-1} \cdot x_i \end{bmatrix}. \quad (\text{A.4})$$

Practically, the data queue of displacement signals is stored in the signal creator as first-in-first-out (FIFO) information for executing semiactive control with the same frequency, which in general is greater than 100 Hz. Therefore, the real-time optimal polynomial coefficient can be derived by modifying (A.4) as

$$\{y\} = [B]_{M \times N} \{x\}_N, \quad (\text{A.5})$$

where $\{x\}$ is the vector of structure displacement:

$$[B] = \begin{bmatrix} 1 & 1 & 1 & \cdots & 1 \\ 0 & 1 & 2 & \cdots & N-1 \\ 0 & 1^2 & 2^2 & \cdots & (N-1)^2 \\ \vdots & \vdots & \vdots & \ddots & \vdots \\ 0 & 1^{M-1} & 2^{M-1} & \cdots & (N-1)^{M-1} \end{bmatrix}. \quad (\text{A.6})$$

Substituting (A.5) into (A.2), the optimal coefficient matrix is expressed as

$$\{a\} = [E^{-1}] [B] \{x\}. \quad (\text{A.7})$$

Consequently, a new matrix of coefficient regression system $[F]$ is a constant matrix depending on the number of sampling points and regression ranks but independent of time or vector of data queue:

$$\begin{aligned} [F]_{M \times N} &= [E^{-1}]_{M \times M} [B]_{M \times N} \\ &= [E^{-1}]_{M \times M} [B]_{M \times N} \{x\} = [F]_{M \times N} \{x\} \\ &= [F] \{x\}. \end{aligned} \quad (\text{A.8})$$

Furthermore, (A.8) can be substituted into (A.7) to obtain the regression value of displacement in matrix form as

$$\hat{x}_i = [1 \ i \ i^2 \ \cdots \ i^{M-1}] [F] \{x\}. \quad (\text{A.9})$$

An optimal coefficient vector $\{F_i\}$, stored in computer memory, estimated for the displacement at previous i steps for carrying out real-time computations can be defined as

$$[F_i^T] = [1 \ i \ i^2 \ \cdots \ i^{M-1}] [F]. \quad (\text{A.10})$$

Then, the optimal displacement $\hat{x}_i = \{F_i\} \cdot \{x\}$ can be estimated based on this equation.

A.2. *Velocity Estimation* [19, 20]. The optimal displacements can be easily predicted using $\hat{x}_i = \{F_i\} \cdot \{x\}$. Meanwhile, the velocity can be obtained by differentiating the displacement equation with respect to time as

$$\dot{\hat{x}}_i = \frac{d}{dt} \hat{x}(t), \quad t = i \cdot \Delta t. \quad (\text{A.11})$$

Therefore, (A.11) can be rewritten as

$$\dot{\hat{x}}_i = \frac{((d/dt) \{F_i\} \cdot \{x\})}{\Delta t}. \quad (\text{A.12})$$

Substituting (A.10) into (A.12), this equation can be expressed as

$$\dot{\hat{x}}_i = \{G_i\} \cdot \{x\}, \quad (\text{A.13})$$

where $\{G_i\}$ is the optimal vector of estimation velocity.

And

$$[G^T] = [0 \quad 1 \quad 2i \quad 3i^2 \quad \dots \quad (M-1)i^{M-2}] [F]. \quad (\text{A.14})$$

$\{G_i\}$ can be stored in computer memory for predicting the real-time velocity or regressing velocity at any arbitrary time step; that is, the optimal velocity for previous i time steps from the current time can be estimated by multiplying $\{G_i\}$ with the derivative of the displacement vector shown as (A.12).

B. Test Results of Test Structure under Excitation of Various Earthquake Records with Various Control Conditions

See Tables 2 and 3.

Competing Interests

The authors declare that there is no conflict of interests regarding the publication of this paper.

Acknowledgments

The authors would like to acknowledge the support of Taiwan Ministry of Science and Technology through Grant nos. MOST-103-2625-M-260-001 and MOST-103-2625-M-167-001.

References

- [1] L. L. Chung, R. C. Lin, T. T. Soong, and A. M. Reinhorn, "Experimental study of active control for MDOF seismic structures," *Journal of Engineering Mechanics*, vol. 115, no. 8, pp. 1609–1627, 1989.
- [2] T. T. Soong, A. M. Reinhorn, Y. P. Wang, and R. C. Lin, "Full-scale implementation of active control I: design and simulation," *Journal of Structural Engineering*, vol. 117, no. 11, pp. 3516–3536, 1991.
- [3] A. M. Reinhorn, T. T. Soong, M. A. Riley, R. C. Lin, S. Aizawa, and M. Higashino, "Full-scale implementation of active control. II: installation and performance," *Journal of Structural Engineering*, vol. 119, no. 6, pp. 1935–1960, 1993.
- [4] S. J. Dyke, B. F. Spencer Jr., P. Quast, M. K. Sain, D. C. Kaspari Jr., and T. T. Soong, "Acceleration feedback control of MDOF structures," *Journal of Engineering Mechanics*, vol. 122, no. 9, pp. 907–918, 1996.
- [5] M. D. Symans and M. C. Constantinou, "Seismic testing of a building structure with a semi-active fluid damper control system," *Earthquake Engineering and Structural Dynamics*, vol. 26, no. 7, pp. 759–777, 1997.
- [6] G. J. Hiemenz, Y. T. Choi, and N. M. Wereley, "Seismic control of civil structures utilizing semi-active MR braces," *Computer-Aided Civil and Infrastructure Engineering*, vol. 18, no. 1, pp. 31–44, 2003.
- [7] V. Gattulli, M. Lepidi, and F. Potenza, "Seismic protection of frame structures via semi-active control: modeling and implementation issues," *Earthquake Engineering and Engineering Vibration*, vol. 8, no. 4, pp. 627–645, 2010.
- [8] N. Caterino, M. Spizzuoco, J. M. Londoño, and A. Occhiuzzi, "Experimental issues in testing a semiactive technique to control earthquake induced vibration," *Modelling and Simulation in Engineering*, vol. 2014, Article ID 535434, 11 pages, 2014.
- [9] S. Pourzeynali and P. Jooei, "Semi-active control of building structures using variable stiffness device and fuzzy logic," *International Journal of Engineering, Transactions A: Basics*, vol. 26, no. 10, pp. 1169–1182, 2013.
- [10] K. Hiramoto, T. Matsuoka, and K. Sunakoda, "Simultaneous optimal design of the structural model for the semi-active control design and the model-based semi-active control," *Structural Control and Health Monitoring*, vol. 21, no. 4, pp. 522–541, 2014.
- [11] W. D. Iwan and L. J. Wang, "New developments in active interaction control," in *Proceedings of the 2nd International Workshop on Structural Control*, Hong Kong, 1996.
- [12] L. J. Wang, "Active interaction control for civil structures," Tech. Rep. CaltechEERL:1997.EERL-97-04, California Institute of Technology, 1997.
- [13] Y. Zhang and W. D. Iwan, "Active interaction control of tall buildings subjected to near-field ground motions," *Journal of Structural Engineering*, vol. 128, no. 1, pp. 69–79, 2002.
- [14] Y. Zhang and W. D. Iwan, "Active interaction control of civil structures—part I: SDOF systems," *Earthquake Engineering and Structural Dynamics*, vol. 31, no. 1, pp. 161–178, 2002.
- [15] Y. Zhang and W. D. Iwan, "Active interaction control of civil structures. Part 2: MDOF systems," *Earthquake Engineering & Structural Dynamics*, vol. 31, no. 1, pp. 179–194, 2002.
- [16] M.-H. Shih and W.-P. Sung, "Development of semi-active hydraulic damper as active interaction control device to withstand external excitation," *Sadhana*, vol. 39, no. 1, pp. 123–138, 2014.
- [17] M.-H. Shih, W.-P. Sung, and C. G. Go, "Development of accumulated semi-active hydraulic damper," *Experimental Techniques*, vol. 26, no. 5, pp. 29–32, 2002.
- [18] M.-H. Shih, C.-I. Lin, and W.-P. Sung, "Numerical analysis for shock absorption performance of accumulated semi-active hydraulic damper," *Journal of Dynamical Systems & Geometric Theories*, vol. 4, no. 1, pp. 29–45, 2006.
- [19] M.-H. Shih, W.-P. Sung, and C.-J. Wang, "A model for signal processing and predictive control of semi-active structural control system," *Sadhana—Academy Proceedings in Engineering Sciences*, vol. 34, part 3, pp. 421–437, 2009.
- [20] M.-H. Shih and W.-P. Sung, "Predictive control and signal on noise reduction for semi-active hydraulic damper," *International Journal of Structural Stability and Dynamics*, vol. 7, no. 1, pp. 129–149, 2007.

Research Article

Mechanism Analysis and Parameter Optimization of Mega-Sub-Isolation System

Xiangxiu Li,¹ Ping Tan,² Xiaojun Li,¹ and Aiwen Liu¹

¹*Institute of Geophysics, China Earthquake Administration, Beijing 100081, China*

²*Earthquake Engineering Research & Test Center, Guangzhou University, Guangzhou 510405, China*

Correspondence should be addressed to Ping Tan; ptan@gzhu.edu.cn

Received 8 April 2016; Accepted 24 May 2016

Academic Editor: Nicola Caterino

Copyright © 2016 Xiangxiu Li et al. This is an open access article distributed under the Creative Commons Attribution License, which permits unrestricted use, distribution, and reproduction in any medium, provided the original work is properly cited.

The equation of motion of mega-sub-isolation system is established. The working mechanism of the mega-sub-isolation system is obtained by systematically investigating its dynamic characteristics corresponding to various structural parameters. Considering the number and location of the isolated substructures, a procedure to optimally design the isolator parameters of the mega-sub-isolation system is put forward based on the genetic algorithm with base shear as the optimization objective. The influence of the number and locations of isolated substructures on the control performance of mega-sub-isolation system has also been investigated from the perspective of energy. Results show that, with increase in substructure mass, the working mechanism of the mega-sub-isolation system is changed from tuned vibration absorber and energy dissipation to seismic isolation. The locations of the isolated substructures have little influence on the optimal frequency ratio but have great influence on the optimal damping ratio, while the number of isolated substructures shows great impact on both the optimal frequency ratio and damping ratio. When the number of the isolated substructures is determined, the higher the isolated substructures, the more the energy that will be consumed by the isolation devices, and with the increase of the number of isolated substructures, the better control performance can be achieved.

1. Introduction

With the development of economics and the advancement of science and technology, more and more tall buildings and super tall buildings have been built in recent years. The most significant engineering concerns in construction of tall and super tall buildings are the safety of the building structures and the comfort of occupants under external forces such as winds and earthquakes. Isolation technology is known as an effective way to improve the structural seismic response. The objective of seismic isolation is to decouple the structure from the ground motion, preventing the structure from absorbing the earthquake energy. Recently some significant research has been done on the isolation structures. Khoshnoudian and Mehrparvar [1] proposed a new control algorithm to protect nonlinear base-isolated structures against earthquakes. Intensity measures for the seismic response prediction of base-isolated buildings were investigated by Mollaioli et al. [2]. Leopa et al. [3] have done some research studies on

damage identification in passive vibroisolation devices, which dealt with the theoretical aspects combined with experimental analysis regarding early damage identification in passive vibroisolation devices. Briman and Ribakov [4] have developed a method for building retrofits, that is, replacing weak conventional columns with low static and dynamic load-carrying capacities by seismic isolation columns. The effectiveness of various control strategies in hybrid base isolation systems including isolators and semiactive variable friction dampers has been investigated by Ribakov [5]. The disorder and damage of base-isolated medical facilities when subjected to near-fault and long-period ground motions have been investigated by Shi et al. [6]. Yan and Chen [7] have studied the seismic performance of midstory isolated structures under near-field pulse-like ground motion, in which a mechanical model has been put forward for this protective system based on the Kelvin pounding model, and a new method has been proposed that synthesizes artificial near-field pulse-like ground motion by combining

the real near-field nonpulse ground motion with simple equivalent pulses. Ozdemir and Akyuz [8] have analyzed the dynamic responses of isolated structures under bidirectional excitations of near-field ground motions, in which nonlinear response history analyses of a 3-story isolated reinforced concrete building have been carried out under both uni- and bidirectional earthquake excitations of near-field records. A comparative analytical study of several control strategies for semiactive devices installed in base-isolated buildings aiming at reducing earthquake induced vibrations is presented by Oliveira et al. [9]. Castaldo et al. [10] have studied the seismic reliability of a base-isolated structure with friction pendulum isolators considering both isolator properties and earthquake main characteristics as random variables.

For buildings of modest height, implementation of passive control devices offers a potential improvement in structural safety and human comfort. But the structural characteristics common to most tall and super tall buildings, such as high shear rigidity, tend to prevent the application of the traditional control devices. It is still a serious challenge for structural engineers to effectively reduce the structural responses of tall and super tall buildings to further improve the structural safety. A new method for controlling the response of tall and super tall buildings under severe external loads was first introduced by Feng and Mita [11]. Feng and Mita first proposed releasing the connections between the megastructure and the substructures in a mega-sub-structure, but without installing dampers between the megastructure and the substructures. Chai and Feng [12] subsequently improved this configuration and presented a mega-sub-controlled system based on a conventional mega-sub-frame and undertook a study of its dynamic response to random wind load excitations. Recently, some studies on the optimal parameters between the substructure and megastructure have been done in order to achieve the best performance by Tian [13]. Lan et al. proposed a multifunction mega-sub-controlled structure; this structure has the function of the mass dampers and base isolation as well as damping energy dissipation. However, there is a lack of theoretical certification [14]. A new connection form between the substructures and megastructure was put forward by Pei and Wang [15], in which the top substructure was connected with the megastructure by dampers. And the studies showed that this new connection form can achieve better damping effect and also can prevent collisions between the top substructures and the megastructure. Qin et al. [16, 17] proposed a new control method, which employs active control and passive dampers together to form a huge control system based on the particular conformation characteristic of mega-sub-controlled system, and also presented a new kind of structural configuration, named mega-sub-controlled structure, which was constructed by applying the structural control principle to structural configuration itself, to form a new structure with obvious response self-control ability, instead of employing the conventional method. Xun'an et al. [18, 19] have investigated the control performances of the mega-sub-controlled structure with different control strategies. Lian et al. [20, 21] have analyzed the seismic responses of the mega-sub-controlled frame with friction damper, in

which friction damped structure is first designed as the substructure in the mega-sub-controlled frame to further reduce structural dynamical responses. A more reasonable and realistic scaled model has been designed to investigate the dynamical characteristics and controlling performances of the mega-sub-controlled system when subjected to strong earthquake motion by Limazie et al. [22], and the control parameters of the structure system, such as the modulated substructures disposition, the damping coefficient ratio, the stiffness ratio, and the mass ratio of the mega-structure and substructure, have been investigated. A parametric study of the relative stiffness ratio and relative mass ratio between the mega-frame and the substructures, as well as the additional column stiffness ratio that influences the response control effectiveness of the mega-sub-controlled structure, was discussed in the literature [23], but the number and locations of the isolated substructures were not considered.

The research of the control mechanism and parameter optimization of the mega-sub-isolation system are insufficient in the past few years. In this paper, the working mechanism of the mega-sub-isolation system is investigated by systematically studying its dynamic characteristics corresponding to various structural parameters. By considering the number and locations of the isolated substructures, the parameter optimization of mega-sub-isolation system has been studied based on the genetic algorithm theory where base shear was used as the optimization objective function. The influence of the number and locations of isolated substructures on the control performance of mega-sub-isolation system has also been investigated from the perspective of energy.

2. Control Mechanism Study of Mega-Sub-Isolation System

2.1. Equations of Motion of Mega-Sub-Isolation System. In a mega-sub-isolation system, substructures are connected with the megastructure by isolation devices. For the analysis purposes, the isolation devices are simulated with Kelvin model, and the megastructure is simplified as a series of pointed models, while each substructure is simplified as a lumped mass. Figure 1 shows the simplified analysis model of the mega-sub-isolation system.

According to the D'Alembert principle, motion equation of the analysis model shown in Figure 1 can be established as follows.

For substructure

$$m_i \ddot{x}_i + c_i (\dot{x}_i - \dot{y}_i) + k_i (x_i - y_i) = -m_i \ddot{x}_g, \quad (1)$$

where m_i is the equivalent mass of each substructure; c_i and k_i are the equivalent damping and horizontal stiffness of the isolation device, respectively; $\{\ddot{x}_i\}$, $\{\dot{x}_i\}$, and $\{x_i\}$ are the acceleration, velocity, and displacement of the substructure relative to the ground; $\{\ddot{y}_i\}$, $\{\dot{y}_i\}$, and $\{y_i\}$ are the acceleration,

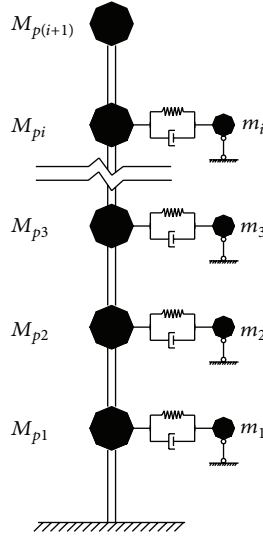


FIGURE 1: Analysis model of mega-sub-isolation system.

velocity, and displacement of the megastructure relative to the ground; \ddot{x}_g is the ground motion acceleration.

For megastructure

$$\begin{aligned} [M_p] \{\ddot{y}\} + [C_p] \{\dot{y}\} + [K_p] \{y\} \\ = -[M_p] \{I\} \ddot{x}_g + \{f_s\} \end{aligned} \quad (2)$$

in which $\{I\}$ represents the unit vector; $\{f_s\}$ is the force vector (substructures apply to the megastructures); $[M_p]$, $[C_p]$, and $[K_p]$ are the equivalent mass, equivalent damping, and equivalent stiffness of each megastructure, respectively. There is no substructure installed at the first floor of the megastructure because the bottom story of substructure is supported on the ground, and its movement will not directly influence the structural responses. So the number of the substructures is fewer than that of the megastructures by one. The mass matrix, stiffness matrix of the megastructure, and the force vector can be expressed as follows, and the damping matrix of the megastructure is determined by the Rayleigh damping:

$$\begin{aligned} [M_p] &= \text{diag} [M_{p1}, M_{p2}, \dots, M_{pi+1}], \\ [K_p] &= \text{diag} [K_{p1}, K_{p2}, \dots, K_{pi+1}], \\ \{f_s\} &= [f_1, f_2, \dots, f_i]^T, \\ f_i &= c_i (\dot{x}_i - \dot{y}_i) + k_i (x_i - y_i). \end{aligned} \quad (3)$$

According to (1) and (2), the motion equation of the analysis model shown in Figure 1 is given as

$$[M] \{\ddot{z}\} + [C] \{\dot{z}\} + [K] \{z\} = -[M] \{I\} \ddot{x}_g, \quad (4)$$

where $\{z\} = [\{x\}^T \{y\}^T]^T$, and the mass matrix, stiffness matrix, and damping matrix of the mega-sub-isolation system can be obtained as follows:

$$\begin{aligned} [M] &= \text{diag} ([m_i], [M_{p(i+1)}]), \\ [K] &= \begin{bmatrix} [k_i] & -[k_i] \\ -[k_i] & [K_{pi}] + [k_i] & -K_{pi} \\ & -K_{pi} & K_{p(i+1)} \end{bmatrix}, \\ [C] &= \begin{bmatrix} [c_i] & -[c_i] \\ -[c_i] & [C_{pi}] + [c_i] & -C_{pi} \\ & -C_{pi} & C_{p(i+1)} \end{bmatrix}. \end{aligned} \quad (5)$$

2.2. Control Mechanism Analysis of Mega-Sub-Isolation System. A typical project is selected as an example [14], which is composed of five mega-stories and the substructures are attached to megastructure from the second floor to the fifth floor. The mass and shear stiffness of each megastructure are 9×10^5 kg and 9×10^7 N/m, respectively, and the mass of top megastructure is 4.5×10^5 kg. The mass of each substructure is determined by the mass ratio u , the frequency ratio f is defined as the ratio of the substructure's frequency to the first-order frequency of the megastructure, and each substructure has the same parameter values. When the megastructure is simplified as a series of particle-based models, its first period is 2 s, and the fundamental period of the structure is 2.8 s when the substructures are rigidly connected with the megastructures.

The modal analysis results of the structure when the mass ratio $u = 1$ and frequency ratio $f = 0.8$ are shown in Table 1 and Figure 2. It can be observed from Table 1 that the first mode and the fifth mode are the main vibration modes of the structure, and these two vibration modes are the global motion of the structure, while the others are local modes of the substructure or megastructure, which can also be seen from Figure 2. Therefore we believe that the control mechanism of the mega-sub-isolation system is related to these two vibration modes.

Figure 3 shows the relationship between the modal mass participation factors and mass ratio and the relationship between the modal mass participation factors and frequency ratio. From Figure 3, it can be confirmed that the first vibration mode and the fifth vibration mode are the main modes of the structure and it is found that when the frequency ratio increases, the modal mass participation factor of the first vibration mode will increase, while that of the fifth vibration mode will decrease.

In order to study the control mechanism of the mega-sub-isolation system, a 2-DOF equivalent model is adopted based on the modal analysis results. The mass of the bottom-structure in the equivalent model is the total mass of the megastructures, the first-order equivalent stiffness of the megastructure is adopted as the stiffness of the bottom-structure, and the mass of the superstructure is determined by the mass ratio u . The connection between the superstructure and bottom-structure is simulated by a Kelvin model.

TABLE 1: Modal analysis results of mega-sub-isolation system.

Modes	Period (s)	Modal mass participation factors	Cumulative mass participation factors
1	4.7173	0.7828	0.7828
2	2.8245	0.0450	0.8278
3	2.6443	0.0098	0.8376
4	2.5993	0.0018	0.8394
5	1.0868	0.1067	0.9461
6	0.6168	0.0395	0.9856
7	0.4230	0.0112	0.9968
8	0.3417	0.003	0.9998
9	0.3099	0.0003	1.0000

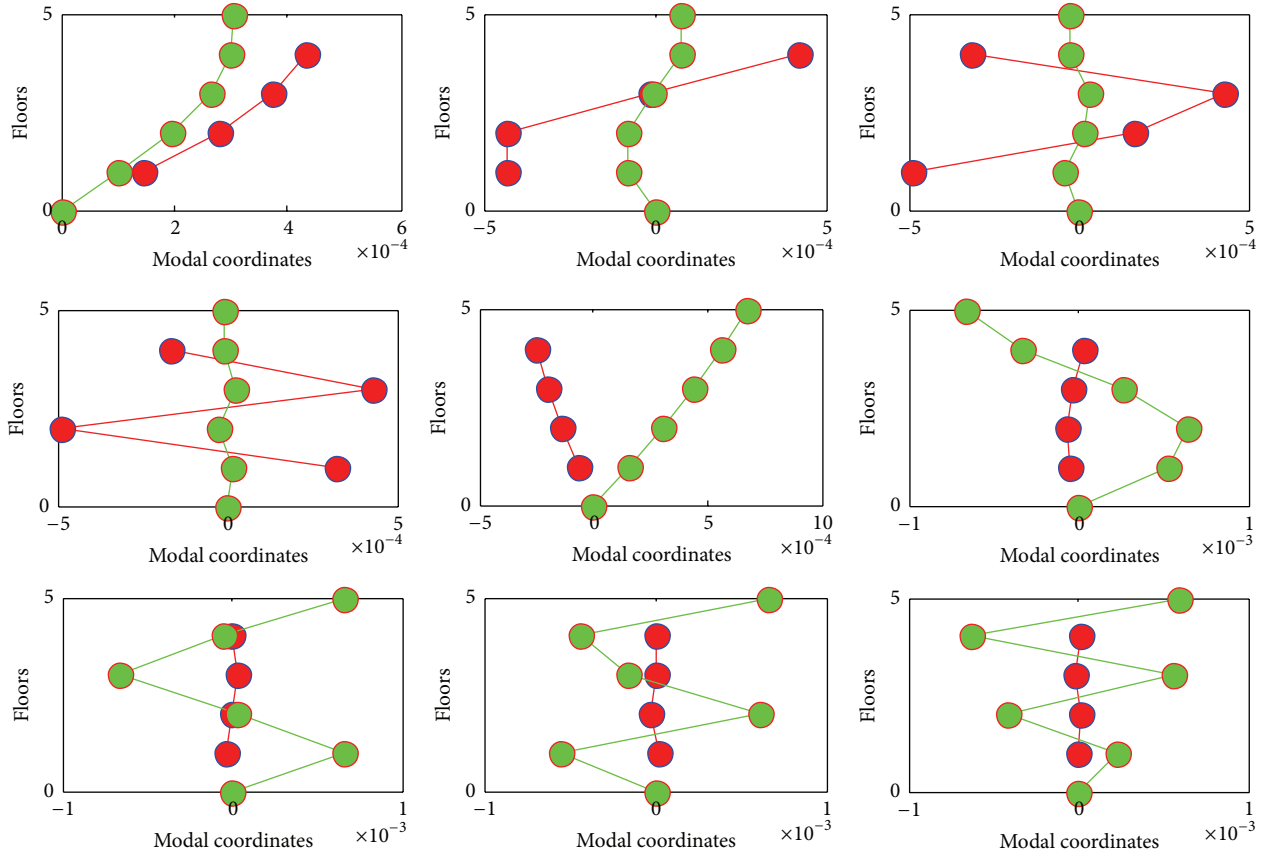


FIGURE 2: Mode shapes of mega-sub-isolation system.

From Figure 4, it can be seen that the relationship between the modal mass participation factors and frequency ratio of the mega-sub-isolation system is consistent with that of the 2-DOF equivalent model when the mass ratio is taken as $u = 0.5$, $u = 2$, and $u = 4$. Then, the 2-DOF equivalent model can be used to explain the control mechanism of the mega-sub-isolation system; that is, the working mechanism of the mega-sub-isolation system is changed from tuned vibration absorber and energy dissipation to seismic isolation with increase in substructure mass, according to the literature [24],

in which the working mechanism of the 2-DOF equivalent model has been systematically investigated.

3. Parameters Optimization

Base shear is very important in earthquake resistant design of building structures. As for isolation system, changing the stiffness and damping of isolators will shift the dynamic characteristic of the system and the distribution of the story shear in the system. In this paper, a procedure to optimally

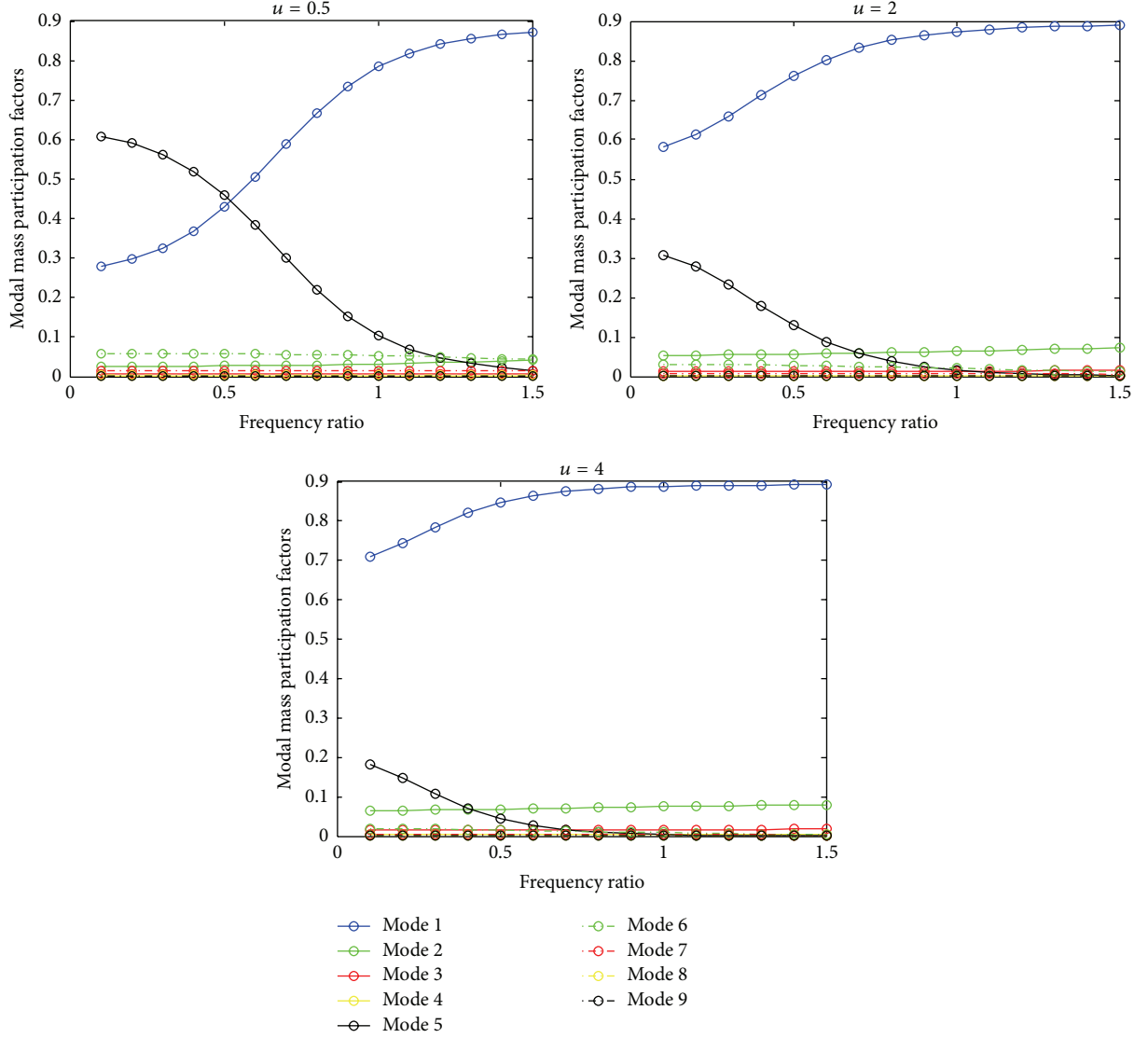


FIGURE 3: Mass participation factors of mega-sub-isolation system.

design the isolator parameters of the mega-sub-isolation system is put forward using the genetic algorithm based on the minimum base shear variance criterion.

The base shear of the mega-sub-isolation system is given by

$$F_v = C_1 \dot{x}_1 + K_1 x_1, \quad (6)$$

where C_1 and K_1 are the damping and stiffness of the bottom megastructure, respectively. Assuming earthquake excitation to be a stationary stochastic process with zero mean, the responses \dot{x}_1, x_1 can also be considered as two statistically stationary processes with zero mean. According to superposition principle of a stationary stochastic process, the following formulas can be achieved:

$$\begin{aligned} \bar{F}_v &= C_1 \bar{\dot{x}}_1 + K_1 \bar{x}_1, \\ \bar{F}_v^2 &= C_1^2 \bar{\dot{x}}_1^2 + K_1^2 \bar{x}_1^2 + \text{Re} \left(2K_1 C_1 \bar{\dot{x}}_1 \bar{x}_1 \right), \end{aligned} \quad (7)$$

where “ $\bar{\cdot}$ ” represents a mean value of a variable and $\text{Re}(\cdot)$ means taking the real part of complex number. Let $S_{\ddot{x}_g}(\omega)$ represent the power spectral density function of seismic excitation and let $H_{\bar{x}_1}(\omega), H_{\dot{x}_1}(\omega)$ represent the transfer functions of the displacement response and velocity response of the bottom megastructure, respectively, which can be obtained by complex modal analysis methods [25]. The mean square value of the velocity response, the displacement response and the mean value of product $\bar{\dot{x}}_1 \bar{x}_1$ can be evaluated as follows by stochastic vibration method:

$$\bar{\dot{x}}_1^2 = \int_{-\infty}^{+\infty} S_{\dot{x}_1}(\omega) d\omega = \int_{-\infty}^{+\infty} S_{\ddot{x}_g}(\omega) |H_{\dot{x}_1}(\omega)|^2 d\omega, \quad (8)$$

$$\bar{x}_1^2 = \int_{-\infty}^{+\infty} S_{x_1}(\omega) d\omega = \int_{-\infty}^{+\infty} S_{\ddot{x}_g}(\omega) |H_{x_1}(\omega)|^2 d\omega, \quad (9)$$

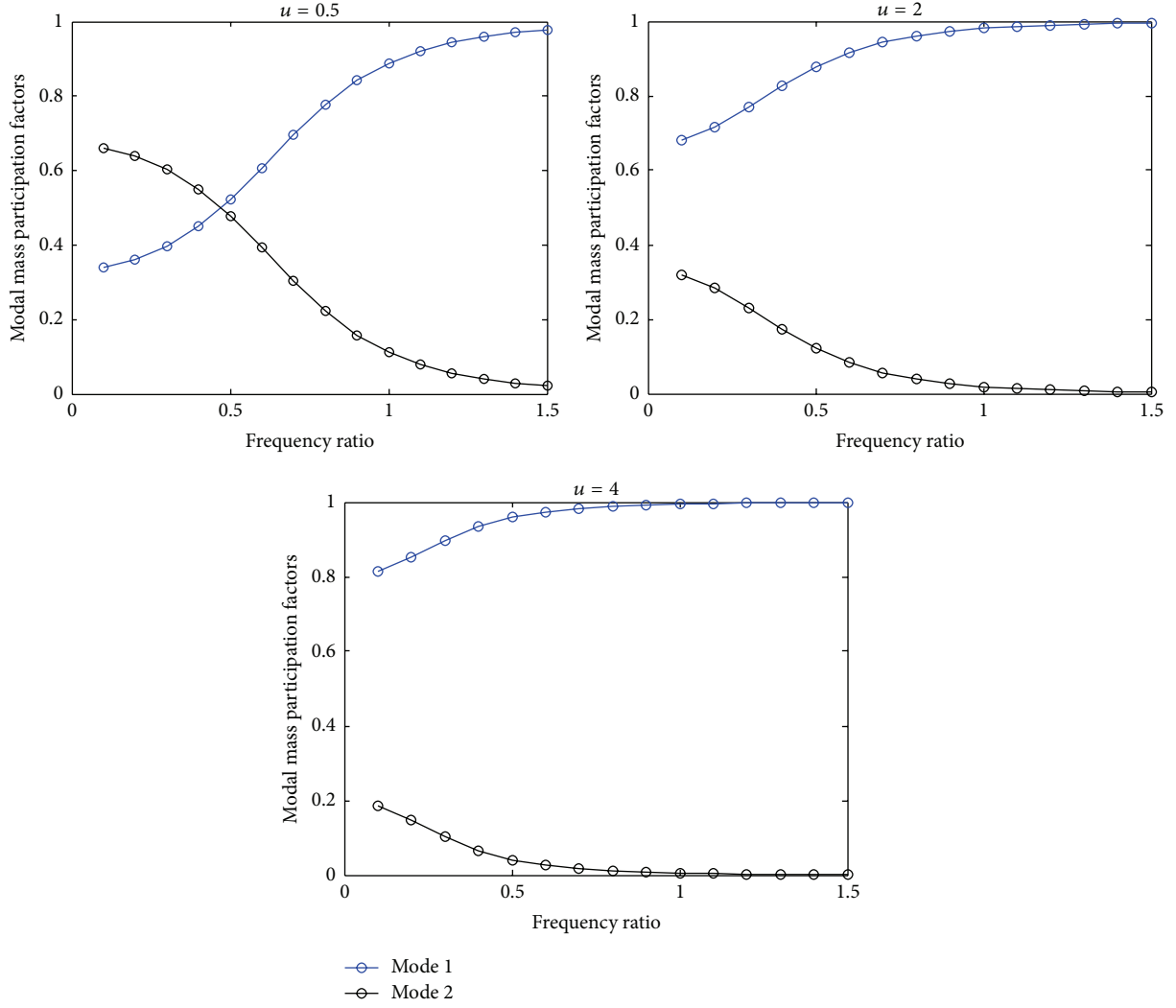


FIGURE 4: Mass participation factors of 2-DOF equivalent model.

$$\begin{aligned} \bar{\dot{x}}_1 \bar{\dot{x}}_1 &= \int_{-\infty}^{+\infty} S_{\bar{\dot{x}}_1 \bar{\dot{x}}_1}(\omega) d\omega \\ &= \int_{-\infty}^{+\infty} |H_{\bar{\dot{x}}_1}(\omega)| S_{\dot{x}_g}(\omega) |H_{\bar{\dot{x}}_1}(\omega)|^* d\omega. \end{aligned} \quad (10)$$

Noting that $S_{\bar{\dot{x}}_1 \bar{\dot{x}}_1}(\omega)$ is the complex conjugate function, then only the real part of $S_{\bar{\dot{x}}_1 \bar{\dot{x}}_1}(\omega)$ contributes to the integration in (10). The power spectral function of the base shear of the mega-sub-isolation system can be obtained by the formula $S_{F_v}(\omega) = \bar{F}_v^2$. The base shear variance is given by

$$\sigma_{F_v}^2 = \int_{-\infty}^{\infty} S_{F_v}(\omega) d\omega. \quad (11)$$

In order to minimize the base shear of the mega-sub-isolation system, the optimal isolator parameters such as frequency

ratio f and isolator damping ratio ξ can be solved by a nonlinear mathematical programming method:

$$\begin{aligned} \min_{f, \xi} \quad & \sigma_{F_v}^2(f, \xi) \\ \text{s.t.} \quad & \xi_{\min} \leq \xi \leq \xi_{\max} \\ & f_{\min} \leq f \leq f_{\max}, \end{aligned} \quad (12)$$

where f_{\min} and f_{\max} represent the lower and upper limit of the frequency ratio which are taken as 0.01 and 1.2, respectively, and ξ_{\min} , ξ_{\max} represent the lower and upper limit of the damping ratio which are taken as 0.01 and 0.3, respectively. The damping ratio of the megastructure is supposed as 0.05. A modified Kanai-Tajimi model suggested by Hu Yuxian is employed as the stochastic ground motion model, and the parameters of S_0 , w_g , ξ_g , and w_c are taken as $15.74 \text{ cm}^2/(\text{rad} \cdot \text{s}^3)$, 19.07 rad/s , 0.784 , and 2.015 rad/s , respectively. Figure 5 shows the optimization process by genetic

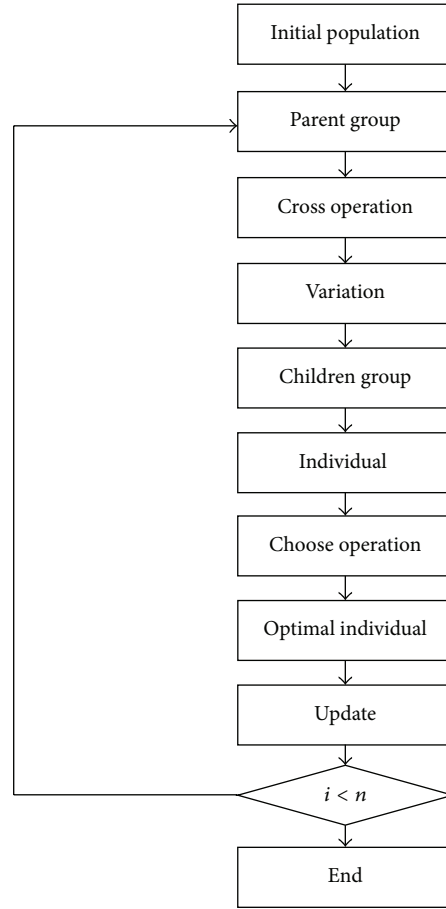
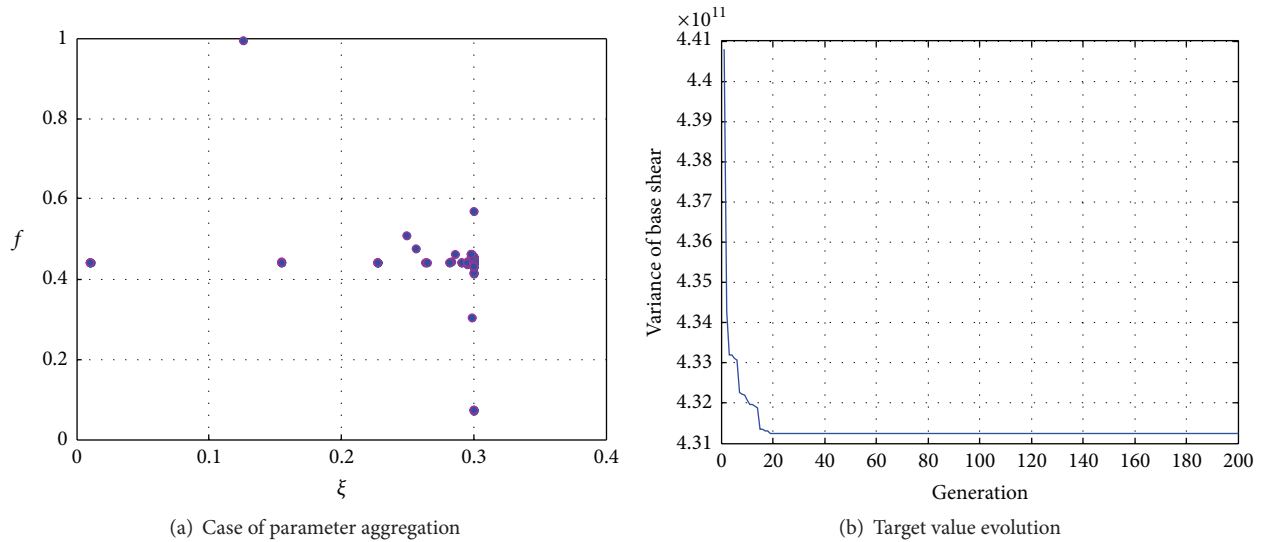


FIGURE 5: Optimization process by genetic algorithm method.

FIGURE 6: Optimization results of $u = 1$.

algorithm method and Figure 6 shows the optimization results when the mass ratio u is taken as 1.

As can be seen from Figure 6(b), the convergence rate of the genetic algorithm is fast, and an optimal design can

be obtained in less than 50 generations. From Figure 6(a), it can be seen that the optimal values of the frequency ratio and damping ratio are 0.44 and 0.3, respectively, when the mass ratio u is taken as 1.

TABLE 2: Optimal damping ratio and optimal frequency ratio of substructures.

Programs		5	4	3	2	4, 5	3, 5	2, 5	3, 4, 5	2, 4, 5	2, 3, 4, 5
$\mu = 0.5$	f_{opt}	0.8037	0.8143	0.8216	0.8409	0.7121	0.7236	0.7564	0.6451	0.6644	0.61
	ξ_{opt}	0.1490	0.1438	0.1111	0.0778	0.1881	0.1747	0.1623	0.2040	0.1933	0.2700
$\mu = 1$	f_{opt}	0.7617	0.7750	0.7890	0.8215	0.6344	0.6505	0.6986	0.5417	0.5687	0.4400
	ξ_{opt}	0.1792	0.1443	0.1293	0.0900	0.2181	0.2013	0.1879	0.2313	0.2183	0.300
$\mu = 2$	f_{opt}	0.7239	0.7430	0.7620	0.7955	0.5608	0.5832	0.6456	0.4410	0.4792	0.2900
	ξ_{opt}	0.1959	0.1472	0.1423	0.1009	0.2387	0.2191	0.2056	0.2460	0.2308	0.300

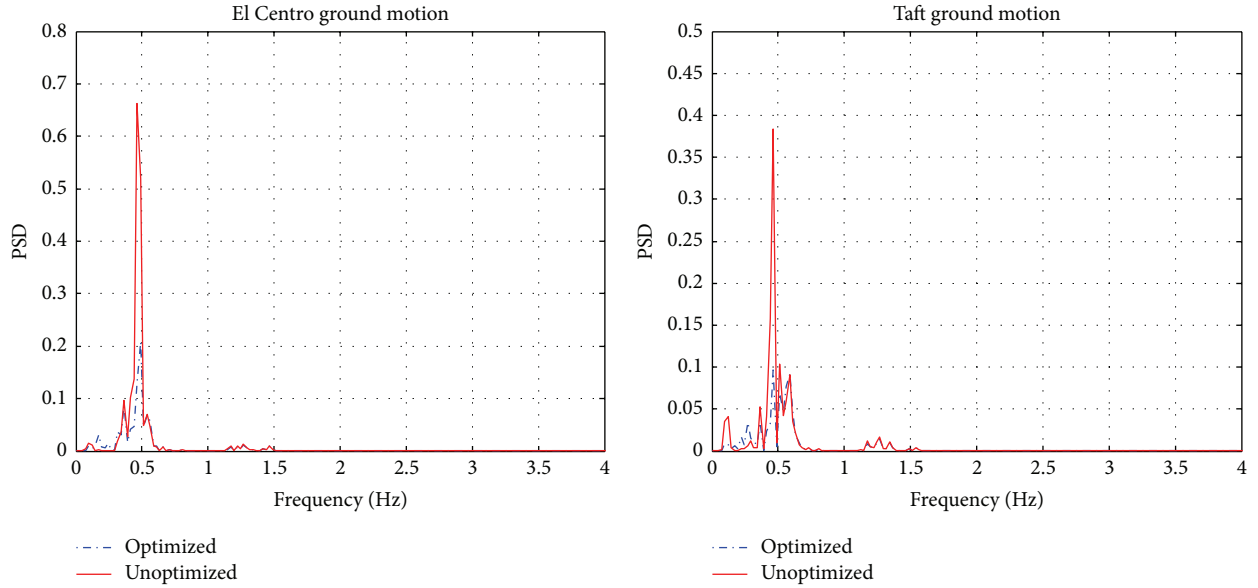


FIGURE 7: Power spectral density for displacement of top megastructure.

The optimal results with the changes of the number and location of the isolated substructures can also be obtained by this method, which are shown in Table 2.

The numbers shown in Table 2 represent the isolated floors of the substructures; for example, number 2 indicates that the second floor of the substructure is connected with the megastructure by isolation device, and the other substructures are rigidly connected with the megastructures; numbers 4 and 5 indicate that the fourth and the fifth floors of the substructures are connected with the megastructure by isolation device, while the other substructures are rigidly connected with the megastructures. From Table 2, it can be seen that the locations of isolated substructures have little influence on the optimal frequency ratio but have great influence on the optimal damping ratio; when the location of the isolated substructures is lower, the optimal damping ratio shows a trend of decreasing, while the number of isolated substructures shows great impact on both the optimal frequency ratio and damping ratio. With the increasing number of the isolated substructures, the optimal frequency ratio decreases, and the optimal damping ratio increases.

Meanwhile, the mass ratio shows great impact on both the optimal frequency ratio and optimal damping ratio; for the same arrangement scheme of the isolated substructures,

the optimal frequency ratio decreases, and the optimal damping ratio increases with the increase of mass ratio.

After the parameters optimization, the power spectral density for displacement of top megastructure and the power spectral density for acceleration of top substructure are compared to those before optimization, as shown in Figures 7 and 8. From Figures 7 and 8, it can be seen that the structural responses after parameter optimization can be reduced obviously compared with that before parameter optimization, so these optimization results can give useful information to designers.

4. Energy Equation

In accordance with the energy balance principle, the energy of each part of structure can be obtained by taking integration for the relative displacement z of (4) on both sides at the same time as follows:

$$E_K + E_D + E_P + E_T = E_I \quad (13)$$

in which the total kinetic energy of the structure is defined by $E_K = (1/2)\dot{z}^T M \dot{z}$, the damping energy is $E_D = \int \dot{z}^T C \dot{z} dt$, and the elastic strain energy of the structure is defined by

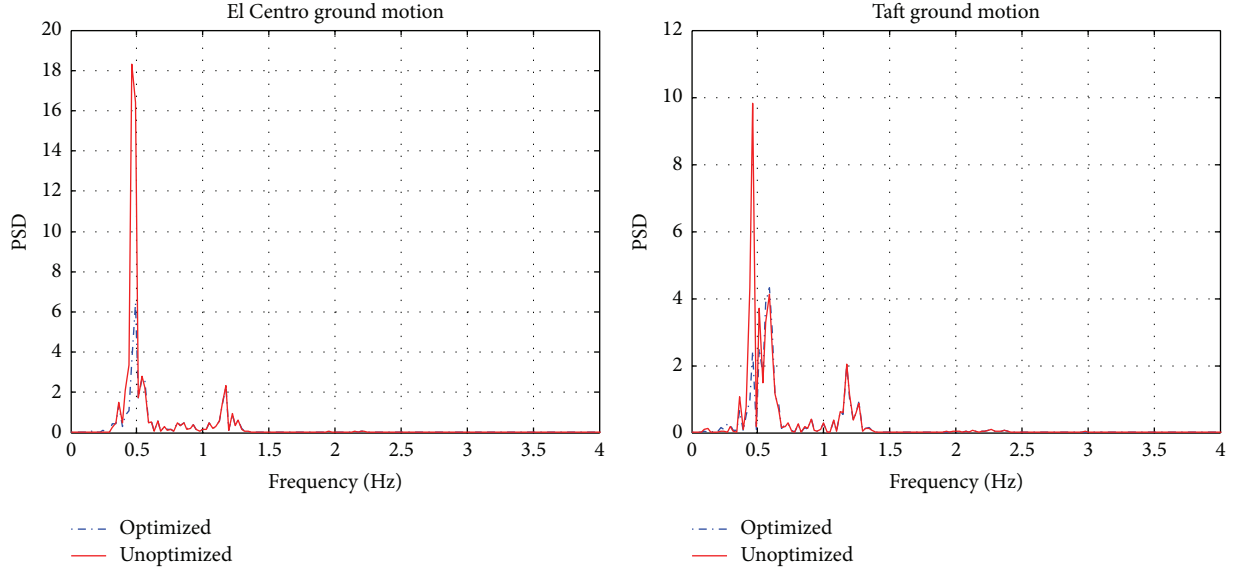


FIGURE 8: Power spectral density for acceleration of top substructure.

TABLE 3: Influence of the number and locations of isolated substructures on control performance under El Centro ground motion.

Programs	Maximum displacement of top main structure (m)	Maximum acceleration of top substructure (m/s^2)	Total input energy $\times 10^6$ (J)	Transfer energy $\times 10^6$ (J)	Ratio (%)
5	0.2485	4.6909	4.0509	2.6134	64.51
4	0.2583	—	4.6270	2.6066	56.33
3	0.2683	—	4.0293	1.7367	43.10
2	0.2792	—	4.0063	1.4347	35.81
4, 5	0.1905	4.7294	3.0926	2.4105	77.94
3, 5	0.1938	4.8097	3.1616	2.3381	73.95
2, 5	0.2299	5.3732	3.2344	2.0418	63.13
3, 4, 5	0.1565	3.4037	3.0567	2.7649	90.45
2, 4, 5	0.1812	3.3913	2.8621	2.2933	80.13
2, 3, 4, 5	0.1207	0.7740	2.3153	2.2736	98.20

$E_p = \int z^T K dz$; at the same time, $E_I = - \int \ddot{x}_g^T M dz$ is defined as the total input energy, and $E_T = \int [c_1(\dot{x}_1 - \dot{y}_1) + k_1(x_1 - y_1)]dy_1 + \dots + \int [c_i(\dot{x}_i - \dot{y}_i) + k_i(x_i - y_i)]dy_i$ is defined as the transfer energy.

5. Influence of the Number and Locations of Isolated Substructures on Control Performance

The number and locations of isolated substructures are important factors influencing the damping effect of the mega-sub-isolation system. Ten layout programs of the isolated substructures are adopted in this paper and, based on the optimization results obtained from Section 2, the maximum displacement of top megastructure, the maximum acceleration of top substructure, the total input energy of the system, and the transfer energy of the substructure have been calculated when the mass ratio u is taken as 1, which are shown in Tables 3 and 4. Both the El Centro ground motion and Taft ground motion are employed for the seismic excitation and the PGA of them are taken as 0.4 g.

It can be seen from Tables 3 and 4 that when the number of the isolated substructures is given, locations of isolated substructures have little effect on the maximum displacement of the top megastructure, the maximum acceleration of the top substructure, and the total input energy, but they do have great impact on the transfer energy of substructure, and the transfer energy of substructure is larger when the substructures are located in the upper part of the system. The larger transfer energy of substructure indicates that the more energy consumed by the isolators, the less energy consumed by the megastructure itself when the amount of the total input energy is determined, and thus the safety of the megastructure can be enhanced.

The number of the isolated substructures shows great impact on the control performance of the mega-sub-isolation system. With the increase of the number of isolated substructures, the maximum displacement of the top megastructure, the maximum acceleration of the top substructure, and the total input energy decrease, while the transfer energy increases. Figure 9 shows the average values of maximum displacement of top megastructure, maximum acceleration of top substructure, the total input energy of the system, and

TABLE 4: Influence of the number and locations of isolated substructures on control performance under Taft ground motion.

Programs	Maximum displacement of top main structure (m)	Maximum acceleration of top substructure (m/s^2)	Total input energy $\times 10^6$ (J)	Transfer energy $\times 10^6$ (J)	Ratio (%)
5	0.2145	3.4452	2.6300	1.8100	68.65
4	0.2150	—	2.6512	1.6200	61.13
3	0.2230	—	2.7239	1.5271	56.10
2	0.2310	—	2.9320	1.3658	46.58
4, 5	0.2073	4.5531	2.2600	1.4202	62.76
3, 5	0.2152	4.7848	2.4763	1.3413	54.16
2, 5	0.2214	4.8455	2.5872	1.4460	55.80
3, 4, 5	0.1742	3.0521	2.3292	1.9363	83.13
2, 4, 5	0.1816	3.0168	2.2393	1.6692	74.53
2, 3, 4, 5	0.1200	0.73	2.1208	1.8520	86.12

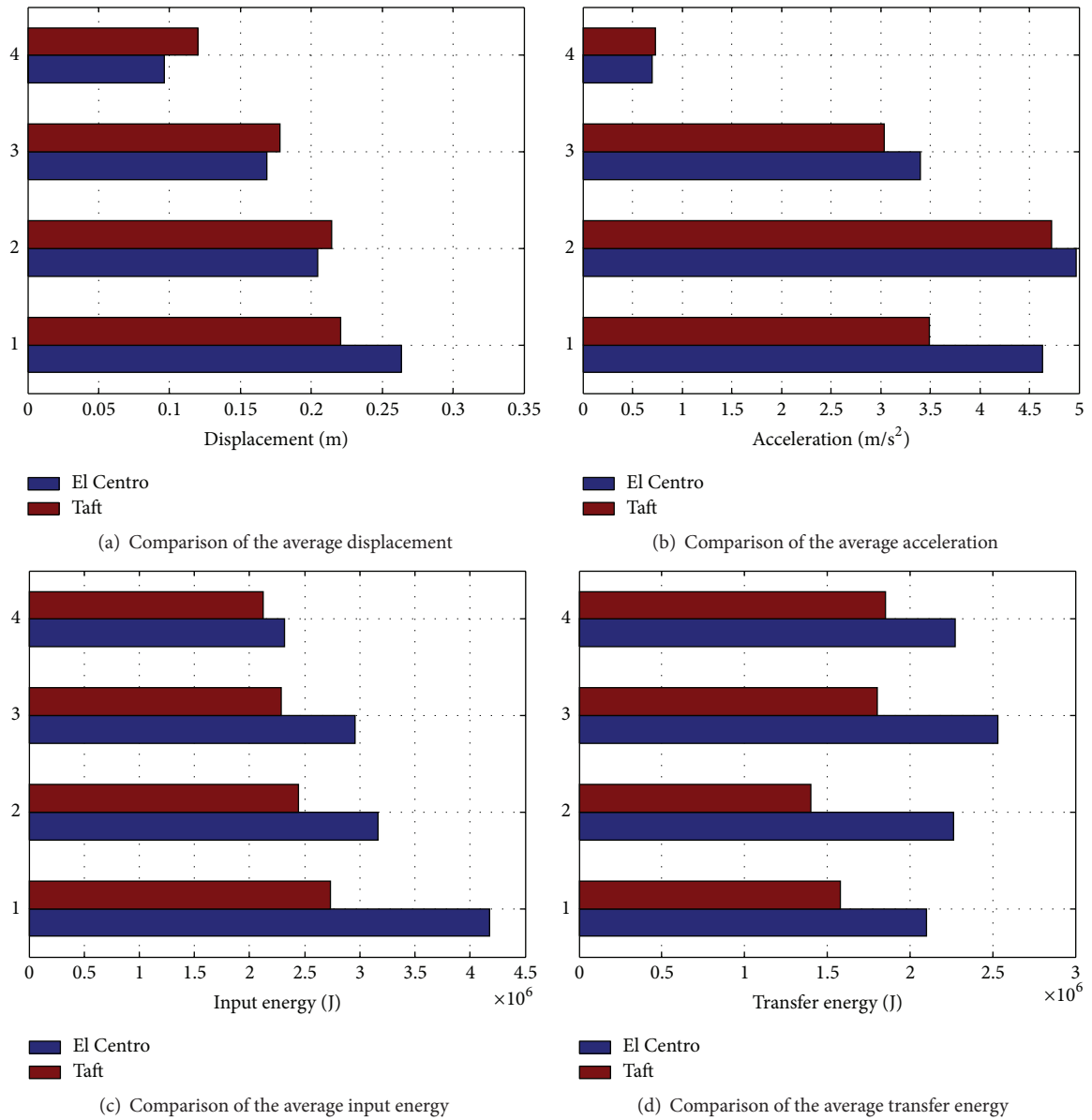


FIGURE 9: Comparison of average values.

the transfer energy of the substructure with the changes of the number of isolated substructures. The number in y -axis represents the number of the isolated substructures. From Figure 9, it can be confirmed that the number of isolated substructures can influence the control performance of the mega-sub-isolation system greatly and, with the increasing number of isolated substructures, the average values of maximum displacement of top megastructure and the total input energy show a decreasing trend, while the average value of the transfer energy presents the opposite trend. That is, when the number of isolated substructures increases, the total input energy can be reduced and larger energy can be transferred to the substructure which is consumed by the isolation devices, and then the energy consumed by the megastructure itself becomes less. Therefore, in practical engineering applications, all the substructures should be connected with the megastructures by isolation devices in order to achieve the best control performance.

6. Conclusions

The control mechanism of the mega-sub-isolation system has been studied from its dynamic characteristics in this paper, and the parameters optimization and the control performance of a mega-sub-isolation system have also been studied when the number and locations of the isolated substructures are different. The following conclusions can be made.

With increasing substructure mass, the working mechanism of the mega-sub-isolation system changes from tuned vibration absorber and energy dissipation to seismic isolation, which is confirmed by theoretical analysis.

Locations of isolated substructures have little influence on the optimal frequency ratio and have great influence on the optimal damping ratio, while the number of isolated substructures and the mass ratio show great impact on both the optimal frequency ratio and damping ratio. The results of parameter optimization can give some useful design suggestions to this novel system.

When the number of isolated substructures is given, locations of the isolated substructures have little effect on the maximum displacement of the top megastructure, the maximum acceleration of the top substructure, and the total input energy, but they have great impact on the transfer energy of substructure, and the transfer energy of substructure is larger when the isolated substructures are located in the upper part of the system. That is, when the isolated substructures are located in the upper part of the structure, more energy will be consumed by the isolation devices. With the increase of the number of isolated substructures, the maximum displacement of top main structure and the total input energy show a decreasing trend, but the transfer energy presents the opposite trend. That is, the more the isolated substructures are, the better the control performance can be achieved. Hence, in practical engineering applications, when the number of isolated substructures is determined, the isolation devices should be installed in the upper substructures and, in order to achieve the best control performance, all

the substructures should be connected to the megastructures with isolation devices.

Competing Interests

The authors declare that there are no competing interests regarding the publication of this paper.

Acknowledgments

The work was primarily supported by the National Basic Research Program of China (2011CB013601) and the Major Research Plan of the National Natural Science Foundation of China under Grant no. 91315301-07, partially by the National Science Foundation under Grants nos. 51408560 and 51578514, and also in part by the Basic Research and Business Projects of Public Welfare Institutes under Central Level by Grant no. DQJB15B11.

References

- [1] F. Khoshnoudian and B. Mehrparvar, "A new control algorithm to protect nonlinear base-isolated structures against earthquakes," *The Structural Design of Tall and Special Buildings*, vol. 22, no. 18, pp. 1376–1389, 2013.
- [2] F. Mollaioli, A. Lucchini, Y. Cheng, and G. Monti, "Intensity measures for the seismic response prediction of base-isolated buildings," *Bulletin of Earthquake Engineering*, vol. 11, no. 5, pp. 1841–1866, 2013.
- [3] A. Leopa, S. Nastac, and C. Debeleac, "Researches on damage identification in passive vibro-isolation devices," *Shock and Vibration*, vol. 19, no. 5, pp. 803–809, 2012.
- [4] V. Briman and Y. Ribakov, "Using seismic isolation columns for retrofitting buildings with soft stories," *The Structural Design of Tall and Special Buildings*, vol. 18, no. 5, pp. 507–523, 2009.
- [5] Y. Ribakov, "Base-isolated structures with selective controlled semi-active friction dampers," *The Structural Design of Tall and Special Buildings*, vol. 20, no. 7, pp. 757–766, 2011.
- [6] Y. D. Shi, M. Kurata, and M. Nakashima, "Disorder and damage of base-isolated medical facilities when subjected to near-fault and long-period ground motions," *Earthquake Engineering and Structural Dynamics*, vol. 43, no. 11, pp. 1683–1701, 2014.
- [7] G. Y. Yan and F. Q. Chen, "Seismic performance of midstory isolated structures under near-field pulse-like ground motion and limiting deformation of isolation layers," *Shock and Vibration*, vol. 2015, Article ID 730612, 17 pages, 2015.
- [8] G. Ozdemir and U. Akyuz, "Dynamic analyses of isolated structures under bi-directional excitations of near-field ground motions," *Shock and Vibration*, vol. 19, no. 4, pp. 505–513, 2012.
- [9] F. Oliveira, P. Morais, and A. Suleman, "A comparative study of semi-active control strategies for base isolated buildings," *Earthquake Engineering and Engineering Vibration*, vol. 14, no. 3, pp. 487–502, 2015.
- [10] P. Castaldo, B. Palazzo, and P. Della Vecchia, "Seismic reliability of base-isolated structures with friction pendulum bearings," *Engineering Structures*, vol. 95, pp. 80–93, 2015.
- [11] M. Q. Feng and A. Mita, "Vibration control of tall buildings using mega subconfiguration," *Journal of Engineering Mechanics*, vol. 121, no. 10, pp. 1082–1088, 1995.

- [12] W. Chai and M. Q. Feng, "Vibration control of super tall buildings subjected to wind loads," *International Journal of Non-Linear Mechanics*, vol. 32, no. 4, pp. 657–668, 1997.
- [13] Y. J. Tian, *Vibration Damping Theory and Optimization Design Method for Multifunctional Vibration-Absorption of RC Megaframe Structures*, College of Civil Engineering, Southeast University, Nanjing, China, 2002.
- [14] Z. J. Lan, Y. J. Tian, S. Y. Cao, and H. H. Wang, "The mechanism and efficiency of multifunctional vibration absorption for megaframe structures," *China Civil Engineering Journal*, vol. 35, no. 6, pp. 1–5, 2002.
- [15] X.-Z. Pei and L. Wang, "Earthquake response analysis of mega-suspended braced frame attached with damper," *Journal of Vibration and Shock*, vol. 30, no. 11, pp. 190–197, 2011.
- [16] X. J. Qin, X. A. Zhang, L. Zou, Q. Q. Wang, and P. Jiao, "Research on active control of mega-sub controlled structure with dampers subjected to seismic loads," in *International Multi-Conference of Engineers and Computer Scientists (IMECS '10)*, pp. 1055–1060, March 2010.
- [17] X. J. Qin and X. A. Zhang, "Vibration controlling characteristics of a new improved mega-sub controlled structure subjected to random wind loads," in *Proceedings of the International Multi-Conference of Engineers and Computer Scientists (IMECS '09)*, pp. 1342–1347, Hong Kong, March 2009.
- [18] Z. Xun'an, W. Dong, and J. Jiesheng, "The controlling mechanism and the controlling effectiveness of passive mega-sub-controlled frame subjected to random wind loads," *Journal of Sound and Vibration*, vol. 283, no. 3–5, pp. 543–560, 2005.
- [19] X. A. Zhang, X. J. Qin, S. Cherry, Y. D. Lian, J. L. Zhang, and J. S. Jiang, "A new proposed passive mega-sub controlled structure and response control," *Journal of Earthquake Engineering*, vol. 13, no. 2, pp. 252–274, 2009.
- [20] Y. D. Lian, X. A. Zhang, and C. Sheldon, "Damping characteristics of friction damped braced frame and its effectiveness in the mega-sub controlled structure system," *Earthquake Engineering and Engineering Vibration*, vol. 6, no. 2, pp. 171–181, 2007.
- [21] Y. D. Lian, X. J. Wang, and T. Li, "Analysis of seismic response for the mega-sub controlled frame with friction damper," in *Chapter 6: Landscape Planning and Design*, vol. 450–451 of *Advanced Materials Research*, pp. 1269–1273, 2012.
- [22] T. Limazie, X. A. Zhang, and X. J. Wang, "Vibration control parameters investigation of the mega-sub controlled structure system (MSCSS)," *Earthquake and Structures*, vol. 5, no. 2, pp. 225–237, 2013.
- [23] X. J. Qin, X. A. Zhang, and S. Cherry, "Study on semi-active control of mega-sub controlled structure by MR damper subject to random wind loads," *Earthquake Engineering and Engineering Vibration*, vol. 7, no. 3, pp. 285–294, 2008.
- [24] F. L. Zhou, Y. Zhang, and P. Tan, "Theoretical study on story isolation system," *China Civil Engineering Journal*, vol. 42, no. 8, pp. 1–8, 2009.
- [25] J. P. Ou and G. Y. Wang, *Structural Random Vibration*, High Education Press, Beijing, China, 1998.